Investigations of Environmental Effects on Freeway Acoustics

by

Stephen Richard Shaffer

A Dissertation Presented in Partial Fulfillment
of the Requirements for the Degree
Doctor of Philosophy

Approved November 2014 by the
Graduate Supervisory Committee:

Mohamed Moustaoui, Chair
Alex Mahalov
Harindra J.S. Fernando
Nicholas C. Ovenden
Huei-Ping Huang
Ronald Calhoun

ARIZONA STATE UNIVERSITY

December 2014

ABSTRACT

The role of environmental factors that influence atmospheric propagation of sound originating from freeway noise sources is studied with a combination of field experiments and numerical simulations. Acoustic propagation models are developed and adapted for refractive index depending upon meteorological conditions. A high-resolution multi-nested environmental forecasting model forced by coarse global analysis is applied to predict real meteorological profiles at fine scales. These profiles are then used as input for the acoustic models. Numerical methods for producing higher resolution acoustic refractive index fields are proposed. These include spatial and temporal nested meteorological simulations with vertical grid refinement. It is shown that vertical nesting can improve the prediction of finer structures in near-ground temperature and velocity profiles, such as morning temperature inversions and low level jet-like features. Accurate representation of these features is shown to be important for modeling sound refraction phenomena and for enabling accurate noise assessment. Comparisons are made using the acoustic model for predictions with profiles derived from meteorological simulations and from field experiment observations in Phoenix, Arizona. The challenges faced in simulating accurate meteorological profiles at high resolution for sound propagation applications are highlighted and areas for possible improvement are discussed.

A detailed evaluation of the environmental forecast is conducted by investigating the Surface Energy Balance (SEB) obtained from observations made with an eddy-covariance flux tower compared with SEB from simulations using several physical parameterizations of urban effects and planetary boundary layer schemes. Diurnal variation in SEB constituent fluxes are examined in relation to surface layer stability and modeled diagnostic variables. Improvement is found when adapting parameterizations for Phoenix with reduced errors in the SEB components. Finer model resolution (to 333 m) is seen to have insignificant

($< 1\sigma$) influence on mean absolute percent difference of 30-minute diurnal mean SEB terms. A new method of representing inhomogeneous urban development density derived from observations of impervious surfaces with sub-grid scale resolution is then proposed for mesoscale applications. This method was implemented and evaluated within the environmental modeling framework. Finally, a new semi-implicit scheme based on Leapfrog and a fourth-order implicit time-filter is developed.

DEDICATION

To my son, Evan. May you never stop asking questions, especially of the answers.

Also,
to my parents and brother,
for their support,
and,
most importantly,
for their patience.

ACKNOWLEDGEMENTS

I thank Prof. M. Moustaoui, for taking me as his first doctoral student in 2010, and for the many discussions we have had during my time at ASU. I also thank my other committee members Prof. A. Mahalov, Prof. H.J.S. Fernando, Prof. N.C. Ovenden, Prof. H.-P. Huang, and Prof. R. Calhoun, for their useful discussions and feedback during my course of study.

I am grateful to Prof. H.J.S. Fernando for accepting me into the Program in Environmental Fluid Dynamics at ASU. Under his direction, the EFD group provided a research environment highly conducive to stimulating intellectual pursuits within the field and made possible the collaboration with various global researchers.

Thank you to Prof. A. Mahalov for supporting me throughout my graduate studies, and also for the opportunity to explore and develop applications for topics beyond the content of this dissertation.

Grants and projects that provided support: ADOT grant JPA06014T with Prof. H.J.S. Fernando, with project manager Christ Dimitroplos at ADOT under ADOT projects SPR 605-1, SPR 605-2, and now continuing with SPR-699 and soon hopefully SPR-730. Also, NSF CMG grant ATM-0934592 with A. Mahalov et al., and NSF EaSM grant EF-1049259 with Prof. B.L. Ruddell. Some chapters contain project-specific acknowledgements.

The words of wisdom of Dr. Elizer Kit were quite instructive during my first year of study. Particulary, that “theorists need to remember that water is wet”, and “everyone believes the experiments except for the experimentalist, while noone believes the model except for the theorist”.

Thank you to Prof. J.C.R. Hunt, for all the lectures, conversations, and inspiration, during your visits to ASU. Also, the car is still running well and taking Evan and I on various adventures in the mountains of the Southwest.

I am grateful to have had the opportunity for many discussions with various colleagues on

topics beyond the scope of what is presented in this dissertation. Notably, P. Hyde and Prof. J. Anderson on urban air quality; Tom Volo, Prof. Enrique Vivoni, and Prof. Ben Ruddell, on vegetation and hydrological considerations; and Dr. Francisco Salamanca on urban schemes.

Thanks to all the MCs and BCs and fellow EFD students throughout the years that enriched my graduate school experience. Also, thank you to the many friends I've made, especially at local climbing facilities, for the great times, and many belays that provided necessary stress-relief. Most notably, Tim and Scott, the Thursday regulars.

I am also grateful for the two long-term landlords I've had while at ASU, Margaret (and family) while in Tempe, and Larry while in Scottsdale. Especially in that they both allowed me to continue developing my green-ish thumb on thier properties, which included a lot of radical experimentation and digging.

Thank you to Tomohiro for enabling the serendipitous discovery of the EFD program, when he simply asked for a ride from Tucson to Tempe and suggested that I also look at the programs offered at ASU. And to Josh, Sanae, and Erin, for encouraging me along the way, and other friends, colleagues, and teammates, from the days at UofA before I arrived at ASU, and in CT from before I left for AZ, since I didn't have the formal forum to say "thank you" then, as I do here with this transition.

TABLE OF CONTENTS

APPENDIX Page

LIST OF TABLES

Table Page

LIST OF FIGURES

PREFACE

This dissertation presents a selection of the research topics investigated in relation to environmental effects on freeway acoustics. An extended abstract is now given.

The role of environmental factors that influence atmospheric propagation of sound originating from freeway noise sources is studied with a combination of field experiments and numerical simulations. Acoustic propagation models are developed and adapted for refractive index depending upon meteorological conditions within both homogeneous and heterogeneous horizontal approximations. Acoustic models are used to compute the refracted sound field up to 600 m from the freeway to predict the noise exposure of residential areas nearby. The model was used in conjunction with meteorological and sound-level measurements taken at freeway sites in Phoenix, AZ. From the data collected, test cases of varying levels of atmospheric stratification and wind shear are presented and discussed. The acoustic model demonstrates that atmospheric effects are able to raise sound levels by 10–20 dB at significant distances away from the highway, causing violations of acceptable limits imposed by the Federal Highway Administration in residential areas that are normally in compliance. Sound propagation in settings with terrain and back-scatter from walls are investigated. Simplified terrain cases without meteorological effects are presented to illustrate the capabilities of the new model with emphasis on effects of terrain. A reflection scheme for 1-way parabolic-type acoustic models is derived based upon the normal impedance ground boundary condition and tested.

A high-resolution multi-nested environmental forecasting model forced by coarse global analysis is then applied to predict real meteorological profiles at finer scales. These profiles are then used as input for the acoustic models. Numerical methods for producing higher resolution acoustic refractive index fields are proposed. These include spatial and

temporal nested meteorological simulations with vertical grid refinement; and also a Lagrangian technique of reverse domain filling trajectories which have the ability to resolve structures at scales that are much finer than those of the wind fields used for advection. It is shown that vertical nesting can improve the prediction of finer structures in near-ground temperature and velocity profiles, such as morning temperature inversions and low level jet-like features. Accurate representation of these features is shown to be important for modeling sound refraction phenomena and for enabling accurate noise assessment. Comparisons are made using the acoustic model for predictions with profiles derived from meteorological simulations and from field experiment observations in Phoenix, Arizona. The challenges faced in simulating accurate meteorological profiles at high resolution for sound propagation applications are highlighted and areas for possible improvement are discussed.

A detailed evaluation of the environmental forecast is conducted by investigating the Surface Energy Balance (SEB) obtained from observations made with an eddy-covariance flux tower compared with SEB from simulations using several physical parameterizations of urban effects and planetary boundary layer schemes. Diurnal variation in SEB constituent fluxes are examined in relation to surface layer stability and modeled diagnostic variables. Improvement is found when adapting parameterizations for Phoenix with reduced errors in the SEB components. Finer model resolution (to 333 m) is seen to have insignificant ($< 1\sigma$) influence on mean absolute percent difference of 30-minute diurnal mean SEB terms. A new method of representing inhomogeneous urban development density derived from observations of impervious surfaces with sub-grid scale resolution is then proposed for mesoscale applications. This method was implemented and evaluated within the environmental modeling framework.

Finally, a new semi-implicit scheme based on Leapfrog and a fourth-order implicit

time-filter is developed. Formal stability analysis and benchmark tests demonstrate that this scheme has third-order accuracy for amplitude errors while damping non-physical modes inherent in time-filtered Leapfrog methods. The scheme can be implemented explicitly, only uses one function evaluation per timestep and gives a factor of three speed-up over the third-order Runge-Kutta scheme. This method has many applications including acoustic, atmospheric, oceanic, and climate modeling.

Chapter 1

INTRODUCTION

1.1 Motivation

The issue of anthropogenically generated noise pollution, particularly within a metropolitan setting, is within the purview of the concept of a "tragedy of the commons," discussed by Hardin 1968 and provides a broader context within which the content of this dissertation resides. Namely, the perceived individual cost-to-benefit of an activity that produces noise is often low, such as the personal decision to drive a vehicle on the freeway. Yet the emergent effect of many similar such decisions within an metropolitan area produces a nuisance much larger than the actions of any single agent. Management strategies of common-pool resources (e.g. for unintentional freeway noise) are often within the realm of engineering solutions as described in De Young 1999. These include to mitigate generation of noise at or near the source, such as with quiet pavement Scofield and Donavan 2005, or to determine recommendations for noise barrier placement and other such strategies. Evaluation and development of tools to understand the optimal implementation and efficacy of such strategies is thus needed to ensure cost effectiveness. However, there is no current framework that can forecast real environmental effects on the propagation of noise for a roadway network for an entire metropolitan area. The work presented herein attempts to develop necessary components toward such a goal.

The aggregate global-scale impact of human activities is suggested to have brought about a geological epoch known as the Anthropocene (Crutzen 2002, Smith and Zeder 2013). Most noticeable since the industrial revolution, anthropogenic influence may result

in adverse transitions beyond critical thresholds, triggering ecosystem collapse, as discussed by Barnosky et al. 2012. The world population is rapidly increasing and urbanizing while also increasing energy use and emissions ((Moreno et al. 2008), Cohen 2004, Seto et al. 2011, Mattick, Williams, and Allenby 2009, Webster et al. 2002). The pre-eminent influence of anthropogenically determined local-scale urban microclimate is thus becoming ever more important within hot arid cities (e.g. Coutts, Beringer, and Tapper 2007). These cities are growing worldwide and are particularly vulnerable to climate change and water resource availability ((Golden 2004), Luber and McGeehin 2008, Vörösmarty et al. 2000, Vörösmarty et al. 2010). These issues motivate the development of fine resolution modeling tools for studying effects of urban design on a regional scale to mitigate adverse effects and optimize urban microclimate. Modeled values of temperature and moisture provide key results to inform policy making and decisions regarding human-ecosystem interaction (Fernando 2008, Chow, Brennan, and Brazel 2012, M Georgescu et al. 2013), though lack of available observations, particularly of surface energy balance (SEB) fluxes within urban settings, often leaves such predictions unvetted. Furthermore, many features of urban microclimate are determined at scales below 1 kilometer (Grimm et al. 2008, Rosenzweig et al. 2010, Hunt et al. 2012, Ching 2013).

1.2 Environmental and Health Impacts of Noise Pollution

Noise pollution, deemed as undesired sound and largely of anthropogenic origin has many adverse effects in both atmospheric and marine environments. These range from human health and stress, as reported in e.g. Babisch et al. 2012, Ising, Kruppa, et al. 2004, Babisch et al. 2005, Goines and Hagler 2007, Moudon 2009, Stansfeld and Matheson 2003, Passchier-Vermeer and Passchier 2000. Especially for newborns Etzel 1997, Bremmer,

Byers, and Kiehl 2003, issues with learning, health and cognition in school children, particularly from railways A. Bronzaft 1981, Bronzaft and McCarthy 1975, aircraft Haines et al. 2002, Hygge, Evans, and Bullinger 2002 and wind turbine sources in A. L. Bronzaft 2011.

Wildlife is also the recipient of adverse anthropogenic noise influences. Freeway noise has been shown to influence success of bird reproduction by interfering with communication between parents and the nest Halfwerk et al. 2011. Remote areas are also influenced Rheindt 2003, Forman and Deblinger 2000. Other studies have shown that marine habitat is also strongly influenced from anthropogenic activities Hildebrand 2009 including offshore oil prospecting Parsons et al. 2009, shipping Hatch et al. 2008, construction and operation of offshore wind farms Madsen et al. 2006 and naval activities Parsons et al. 2008; Zirbel, Balint, and Parsons 2011, to highlight just a few.

Predictability of the ambient acoustic environment implicated in the aforementioned adverse effects within a metropolitan setting is of interest given the rate of urban growth both in terms of population and land-use modifications as the current world population is rapidly moving away from rural lifestyles Moreno et al. 2008. Human activity is increasing ambient noise conditions worldwide, reducing access, extent, and quality of quiet locations (e.g. McGregor et al. 2013, Votsi et al. 2012), and the extent and quietness of remote areas (e.g. Iglesias Merchan, Diaz-Balteiro, and Soliño 2014 and references therein). Tyes of sources include transport (vehicular on land, car/truck/motorbike/recreational, vessel at sea, aircraft), and industrial (construction, building machinery, wind turbines). Though this is not an exhaustive listing. The main anthropogenic sources of topical study for atmospheric propagation are aircraft, transportation, and wind turbines.

The growing concern to residents poses a particular challenge to land managers and city planners to account for noise or in preserving quiet areas Votsi et al. 2012, specifically

when designing highway transportation systems Stewart et al. 2011; Pry and Andersen 2011. Additionally, housing prices in populated urban and suburban settings are influenced by noise Nelson 1982.

Studies on the effects of chronic noise exposure are reviewed by Hygge 2011, and suggest that there is no critical threshold demarking impact, rather that there is a significant difference on impairment of memory and learning with exposure to ambient outdoor noise levels above L_{eq} =60 dBA compared to around 55 dBA. A recent study by Hart et al. 2014 finds that the dose-response relationship between major roadway proximity and risk of sudden cardiac death for middle-age women was linear for distances between 50 m and 500 m, and that each 100 m reduced proximity was associated with a 8% increased risk (95% confidence interval 3-14%).

Engineering considerations are used to inform how best to design and implement mitigation strategies to improve areas already receiving complaints of traffic noise, or for being in violation local regulations. Guidelines for traffic noise in the United States, for instance, are set by the Federal Highway Noise Abatement Criterion with a limit of 67 dB(A)[1], where human sensitivity to hearing is represented by applying a band-pass filter called A-weighting following International Standard IEC 561 (1993-09). More restrictive levels for mitigation are suggested by the World Health Organization (WHO) deeming 55 dB(A) as a level of serious annoyance during daytime and evening (Berglund, Lindvall, and Schwela 1999, WHO 2007) and are being considered in Europe (Boer and Schroten 2007).

[1]Title 23: Highways - Part 772-Procedures for Abatement of Highway Traffic Noise and Construction Noise

1.3 Field Experiments

Several field experiments were conducted during the course of this work. For the ADOT acoustics studies, experimental configuration is described in Chapter 2. Additional data is described and provided in Appendix A. In short, these experiments included three several-day deployments of balloon-tethersonde, SODAR-RASS, and towers with sonic anemometers.

Additionally, an eddy-covariance flux tower was recently installed in a Phoenix residential neighborhood and is described in detail in Chow et al. 2014. These data are used in Chapter 5 for WRF model evaluation. Additional data is presented in Appendix C. Ongoing work to study the influence of freeway noise walls is being conducted but is beyond the scope of the present dissertation. Further field experiments are needed with both detailed meteorological and acoustic measurements, to enable validation of the acoustic models to large distances, and also to evaluate or provide input profiles for high-resolution micro-meteorological predictions and simulations.

1.4 Acoustic Modeling

1.4.1 Context and Assumptions

Focus will now be on atmospheric acoustics, basic mathematical theory and determining important factors. In particular, how does noise propagate from source to receiver? The role of propagation medium via temperature/density gradients, wind shear, turbulence, and relative humidity role in attenuation. Boundary effects, such as acoustic reflections, distortion of flow and feedback onto the acoustic propagation. Ranges

considered are up to 1 km. As such, we can assume that the medium is "frozen" and examine mean field propagation. This is because the propagation timescale is much smaller than atmospheric timescales. To be explicit, consider the acoustic propagation timescale, τ_{sound} obtained as the ratio of the lengthscale of consideration Λ to the mean sound speed $\bar{C_{\text{eff}}}$, as,

$$\tau_{\text{sound}} = \frac{\Lambda}{\bar{C_{\text{eff}}}} \sim \frac{1000 \text{ m}}{330 \text{ m s}^{-1}} \sim 3 \text{ s}.$$

Near the ground, the eddy turnover timescale τ_{eddy} is found as

$$\tau_{\text{eddy}} = \frac{z_i}{v*} \sim \begin{cases} \frac{1000 \text{ m}}{1 \text{ m s}^{-1}} \sim 1000 \text{ s}, \text{ for } w* \\ \frac{100 \text{ m}}{.1 \text{ m s}^{-1}} \sim 1000 \text{ s}, \text{ for } u* \end{cases},$$

where z_i is the boundary layer depth and $v*$ is a velocity scale. For neutral or unstable PBL the convective velocity scale $w*$, and friction velocity scale $u*$ for stable PBL, with typical order-of-magnitude values (e.g. Stull 1988). Clearly $\tau_{\text{sound}} \ll \tau_{\text{eddy}}$. Investigations will include boundary layer stability considerations, turbulence considerations, and synoptic forcing considerations. There are several methods to incorporate turbulent fields as an ensemble of perturbations about the mean, since smaller eddies have much smaller timescales than for τ_{eddy} given above. The scattering by turbulent media is beyond immediate scope of this work and will be covered in future work. Inhomogeneities within the medium are accounted for by updating the effective sound speed profile at each range step, within the frozen-field approximation, as will be discussed below and in Appendix B.

1.4.2 General Modeling Background Details

We use the same acoustic model as presented in Ovenden, Shaffer, and Fernando 2009, called the wide-angle Parabolic Equation (PE) model, a summary of which is provided here with emphasis placed on the PE model equations and the effective sound

speed. When considering 20 minute time-averaged sound levels a straight highway-segment can be treated as a series of mono-frequency coherent effective line-sources placed at some position above the travel lane of the roadway. Stability of the PE model requires 10 points per wavelength, so high frequencies become costly to compute. Fortunately, due to A-weighting, restricting the acoustic spectrum to 17 standard third-octave frequency bands incurs less than 1% error when compared to the sum over any larger bandwidth and speeds computation time by eliminating higher frequencies.

The ground is treated as a locally reacting impedance plane using boundary conditions for the complex pressure amplitude p_c,

$$\frac{-1}{i\omega}\partial_z p_c = \frac{p_c}{Z}, \tag{1.1}$$

at $z = 0$, with an empirically derived relation for complex impedance,

$$Z = 1 + 0.0511\left(\frac{\sigma}{f}\right)^{0.75} + i0.0768\left(\frac{\sigma}{f}\right)^{0.73}, \tag{1.2}$$

dependent upon acoustic frequency and a model of flow porosity, an intrinsic property of the material Delany and Bazley 1970; Attenborough, Li, and Horoshenkov 2007. Here ω is the Helmholtz number defined below. We used a Green's function solution for homogeneous atmosphere above an impedance plane based upon Chandler-Wilde and Hothersall 1995 to derive a starting field for the PE domain at the edge of the road using porosities $\sigma = 3x10^7$, and $4x10^5$ Pa s m^{-2} representative of asphalt and sandy soil, respectively. The source strengths and heights were derived by minimizing a cost function using measured values of sound pressure, a penalty for height to keep the sources near the ground, and using the Green's function at the sound meter locations.

The PE model is an approximation to the elliptic Helmholtz equation E. Salomons 2001 which governs acoustic pressure fluctiations, $p_c(\vec{x})exp(-i\omega t)$, of angular frequency $\omega = 2\pi/f$, for frequency f and complex amplitude scalar field p_c. Using the assumption of

a stationary atmosphere with effective wavenumber, $k_{eff,i} = \omega/(c+u_i)$, in direction x_i to account for wind u_i and adiabatic sound-speed c from an isentropic equation of state $P = c_0^2\rho$, a harmonic perturbation to the mean for the Euler equations results in,

$$(k_{eff}^2 \nabla \cdot k_{eff}^{-2} \nabla + k_{eff}^2) p_c = 0. \tag{1.3}$$

The PE model variant we use is derived by reducing the two-way hyperbolic Helmholtz wave equation in cylindrical coordinates into a one-way parabolic equation approximation. The propagation direction is taken as being in the plane transverse to a line source of strength S_0 at position $\vec{x}_s$, representation of the roadway. The derivation we use assumes that the complex pressure varies slowly with range so that second derivative terms can be dropped, i.e. $\partial_{xx} p_c \ll \partial_x p_c$. Then treating the remaining terms as an operator and using a rational Padé expansion to higher order yields a wide angle form for the PE method given as equation 6 in Ovenden, Shaffer, and Fernando 2009. An alternate derivation is to split the Helmholtz equation into two one-way propagation operators and considering only waves moving in one direction within a 2-D plane,

$$\left(\partial_x + i\sqrt{H}\right)\left(\partial_x - i\sqrt{H}\right) p_c = S_0 \delta(\vec{x} - \vec{x}_s). \tag{1.4}$$

This is valid if $[H, \partial_x] = 0$, and an approximation if H varies slowly with range x.

Taking $p_c = \psi(x,z) exp(ik_0 x)$ as a complex acoustic pressure for a plane wave of representative wavenumber k_0 (i.e. surface value) and complex amplitude modulation ψ. From a finite difference approximation to the differential operators we obtain an equation of the form,

$$M\psi^{i+1} = N\psi^i, \tag{1.5}$$

relating the complex pressure amplitude at range $i+1$ to that at range step i, where M and N can be expanded in terms of E,D, and O viz, $M = \Delta_z^2(E - D + O)$ and

$N = \Delta_z^2(E + D - O)$. These diagonal matrices for the interior of the domain on vertical coordinate $z = j\Delta_z$, $j = 2, \ldots, n = n_z - 1$, with horizontal grid spacing Δ_x, are defined by,

$$E = \begin{pmatrix} E_{22} & \alpha + \gamma_2 - \Omega_b(\alpha - \gamma_2) & & & \\ \alpha - \gamma_j & -2\alpha + \frac{\kappa_j}{4k_0^2\Delta_x} + \frac{1}{\Delta_x} & \alpha + \gamma_j & & \\ & \ddots & \ddots & \ddots & \\ & & & \alpha - \gamma_n - \Omega_t(\alpha - \gamma_n) & E_{nn} \end{pmatrix} \tag{1.6}$$

With $E_{22} = -2\alpha + \frac{\kappa_2}{4k_0^2\Delta_x} + \frac{1}{\Delta_x} + 4\Omega_b(\alpha + \gamma_2)$ and $E_{nn} = -2\alpha + \frac{\kappa_{n_z-1}}{4k_0^2\Delta_x} + \frac{1}{\Delta_x} + 4\Omega_t(\alpha + \gamma_{n_z-1})$ and using shorthand $n = n_z - 1$ to avoid confusion with the subscripts. The diagonal matrix D has entries,

$$D_j = \frac{i\kappa_j}{2k_0}. \tag{1.7}$$

Lastly we have,

$$O = \begin{pmatrix} O_{22} & \beta - \delta_2 - \Omega_b(-\beta + \delta_2) & & & \\ -\beta + \delta_j & 2\beta & -\beta - \delta_j & & \\ & \ddots & \ddots & \ddots & \\ & & & -\beta + \delta_n - \Omega_t(-\beta - \delta_n) & O_{nn} \end{pmatrix}. \tag{1.8}$$

Where, $O_{22} = 2\beta + 4\Omega_b(-\beta + \delta_2)$ and $O_{nn} = 2\beta + 4\Omega_t(-\beta - \delta_n)$ are used as shorthand to represent the matrix when typesetting. For the above equations, the dimensionless Helmholtz number is $\omega = 2\pi fL/c_0$, the reference wavenumber is $k_0 = \omega/c_{eff,0}$, the density, where gravitational effects be included, is $\rho_0 = 1/c_0^2$, and we have the following relations,

$$\alpha = (4k_0^2\Delta_z^2\Delta_x)^{-1}, \tag{1.9}$$

$$\beta = i(4k_0\Delta_z^2)^{-1}, \tag{1.10}$$

$$\gamma_j = \frac{\partial_z C_{eff,j}}{4k_0^2 \Delta_z \Delta_x C_{eff,j}}, \tag{1.11}$$

$$\delta_j = \frac{i\partial_z C_{eff,j}}{4k_0 \Delta_z C_{eff,j}}, \tag{1.12}$$

$$\kappa_j = \frac{\omega^2}{C_{eff,j}^2} - k_0^2. \tag{1.13}$$

Beginning with the Green's function solution at the edge of the road, a Crank-Nicholson scheme is used to march the starting field of complex acoustic pressure perturbations across the PE domain in equation 1.5. An exponential attenuation layer at the top third of the domain, combined with the Sommerfeld radiation condition, was used to prevent artificial numerically reflected waves.

Each third-octave band's central frequency is assumed to represent the entire band, so the logarithmic-sum of the PE calculations for each band gives the resultant total field using,

$$L_{eq} = 10\log_{10} \sum_{n=1}^{17} 10^{L_A(f_n)/10}, \tag{1.14}$$

where $L_A(f_n) = L_{A,f_n}(x,z)$ is the A-weighted spectral contribution of frequency f_n at point (x,z) within the domain. It may be written in terms of the complex pressure and source strength by, $L_{A,f_n} = 10\log_{10}(.5|\eta\,\psi|^2) + 20\log_{10} S_{0,f_n}$, where $\eta^{-1} = \max_{i,j}|\psi|$ is a normalization factor since we effectively calculate the attenuation with respect to the Green's function starting field and still need to account for the amplitude of the source. Lastly, atmospheric absorption can be applied to each frequency band after the PE model gives output by using a constant attenuation factor with range dependent upon frequency and humidity (see Ovenden, Shaffer, and Fernando 2009).

In summary, the model input is the starting pressure field derived from the source strength and height along with the effective-sound-speed profile, defined as,

$$C_{eff}(z) = \sqrt{\gamma RT(z)} + U_{\|}(z), \tag{1.15}$$

which we normalize with respect to the surface value. Here γ is the ratio of specific heats, R is the gas constant, $T(z)$ is the temperature profile and $U_{\|}(z)$ is the profile of wind speed parallel to the direction of propagation. The first term is commonly referred to as the adiabatic sound speed, C_{ad}, is also given by $C_{ad}(z) = 331.3\sqrt{T(z)/273.15}$ m s^{-1} for temperature T in Kelvin. The second term accounts for advection and compensates for the assumption of a stationary medium.

1.5 Atmospheric Modeling

Acoustic models need profiles of acoustic refractive index, or effective sound speed, as described (e.g. Eqn. 1.15), from temperature and velocity. These profiles can be obtained by observation only for limited areas, and clearly only for the period of observation. However, with the capability of employing numerical weather prediction techniques, profiles may be forecast for entire regions, at any time, and in advance. Thus, in combination with suitable acoustic source models (beyond the scope of the present work), such tools provide a key step in scaling up efforts from studies of specific sites to larger regions.

For the following discussion, the Advanced Research Weather Research and Forecasting (ARW-WRF) model will be assumed, and is described in further detail in Skamarock and Klemp 2008. Background material related to subsequent chapters will now be described.

1.5.1 Parameterizations of Turbulence Closure

For mesoscale applications, the horizontal grid scale (Δ_H) is typically larger than 1 km, with 1 km considered to be high resolution. As such, eddy structure responsible for mixing within the planetary boundary layer (PBL) is not explicitly resolved and must be parameterized. When employing a PBL scheme, the ARW-WRF model separates horizontal mixing from vertical mixing, with the PBL scheme accounting for vertical mixing for the entire vertical column. Flux exchange between the land surface model (LSM) and PBL are incorporated by a surface layer scheme (SLS) within the model's first vertical level. Here, we describe two PBL schemes employed in later chapters without delving into the details of turbulence closure, which can be found in e.g. Tennekes and Lumley 1972 and Stull 1988.

The non-local scheme of Yonsei-University (YSU) Hong, Noh, and Dudhia 2006, explicitly treats entrainment between the free atmosphere and top of the boundary layer, in addition to a non- local gradient flux term to account for large eddies. The YSU PBL scheme couples with the 5th generation Mesoscale Model (MM5) SLS (Hong, Noh, and Dudhia 2006), a first-order closure gradient transport model. The MM5 SLS is implemented in WRF based on stability functions given in Paulson 1970, Dyer and Hicks 1970, and Webb 1970, for four stability regimes following Zhang and Anthes 1982, and with a convective velocity following Beljaars 1995.

The local scheme of Mellor-Yamada-Janjic (MYJ) Janjic 1994, 2001 is a 1.5 order scheme following Mellor and Yamada 1982 where closure is based on TKE. The MYJ PBL scheme requires the Eta SLS (Janjic 1996, 2001), is a zero-order similarity scaling based upon Monin-Obukhov Similarity Theory (MOST) (Monin and Obukhov 1954). A 1 cm deep viscous sub-layer over land surface is parametrized in terms of a variable roughness length for moisture and humidity following Zilitinkevich 1995. Friction velocity is limited

in unstable conditions with low wind speeds so that $u^* > 0$ holds, following Beljaars 1995. The Obukhov stability parameter and stability functions are derived iteratively and are determined for stable and unstable conditions following Holtslag and de Bruin 1988 and Paulson 1970, respectively.

Although Δ_H near 1 km is considered high resolution, PBL schemes are typically still employed since the domain is typically being forced by coarser nests that also employ the scheme. However, this scale of Δ_H is encroaching upon the so-called "Terra-Incognita" of Wyngaard 2004, where the Δ_H (and model filter length scales) become small enough where they should resolve the energetic PBL eddies. With smaller Δ_H, the PBL scheme method of parameterization by separating horizontal and vertical mixing is no longer valid. Here, methods such as large eddy simulation (LES) (e.g. Moeng 1984, Moeng et al. 2007, F. Chen et al. 2011, Mirocha, Kosović, and Kirkil 2014), are typically employed since PBL eddies are explicitly resolved. Thus, several model parameterization scheme assumptions are expected to break down as grid resolution is refined, both vertically and horizontally, while using a PBL scheme.

Forecasting at smaller scales has become computationally possible by advances in technology (Schaller 1997), and by advances in numerical technique, such as nesting within a limited area (Davies 1983; Smolarkiewicz and Grell 1992; Skamarock and Klemp 2008; Alex Mahalov and Mohamed Moustaoui 2009). Yet theoretical issues regarding turbulence closure and parameterization of PBL eddies remain a challenge as resolution approaches what Wyngaard 2004 describes as the Terra-Incognita, beginning near order of 1 km (Mirocha, Kosović, and Kirkil 2014). At scales finer than the Terra-Incognita, methods such as large eddy simulation (LES) ([ )e.g.][]Moeng1984,Moeng2007, are typically employed since PBL eddies are explicitly resolved. Recently, model development efforts have been focused on enabling transiting the Terra-Incognita by combining these computational

methods, (Mirocha, Kosović, and Kirkil 2014; Wyszogrodzki, Miao, and Chen 2012; F. Chen et al. 2011). Yet computational feasibility often limits applications to research rather than real-time operational forecasting. Furthermore, there has been limited assessment of model error as nested simulation resolution approaches the Terra-Incognita regime. Studies often avoid the Terra-Incognita issues by limiting resolution to around 1 km, some of which have been reviewed by Loridan et al. 2013.

In addition to the need of transitioning from employing a PBL scheme to LES with decreased Δ_H, the influence on turbulent fluxes from resolving groups of building are expected to complicate the currently available schemes (Bou-Zeid et al. 2009). Although this is not considered in this work it is mentioned for completeness of discussion. One such solution to incorporate building-resolved flow can be achieved by coupling WRF with the EULerian LAGrangian (EULAG) model (Prusa, Smolarkiewicz, and Wyszogrodzki 2008), and is being added to the WRF system by F. Chen et al. 2011. Combining EULAG with fine scale digital elevation model data and building data could yield powerful simulation methods. One goal is to inform development of sub-grid parameterizations for coarser resolution models yet still within Terra-Incognita. Furthermore, each simulation should be considered as a single realization of expected eddy structure, not a forecast of the actual eddies. Therefore, averaging is typically applied to determine flow structure results. These techniques may be adapted for e.g. flow over noise walls and groups of buildings for sound propagation applications.

1.5.2 Parameterizations of Land Surface and Urbanization

The capability of atmospheric modeling in urban environments is influenced by land-atmosphere coupling within models (Ching 2013; F. Chen et al. 2012, 2011; Fernando

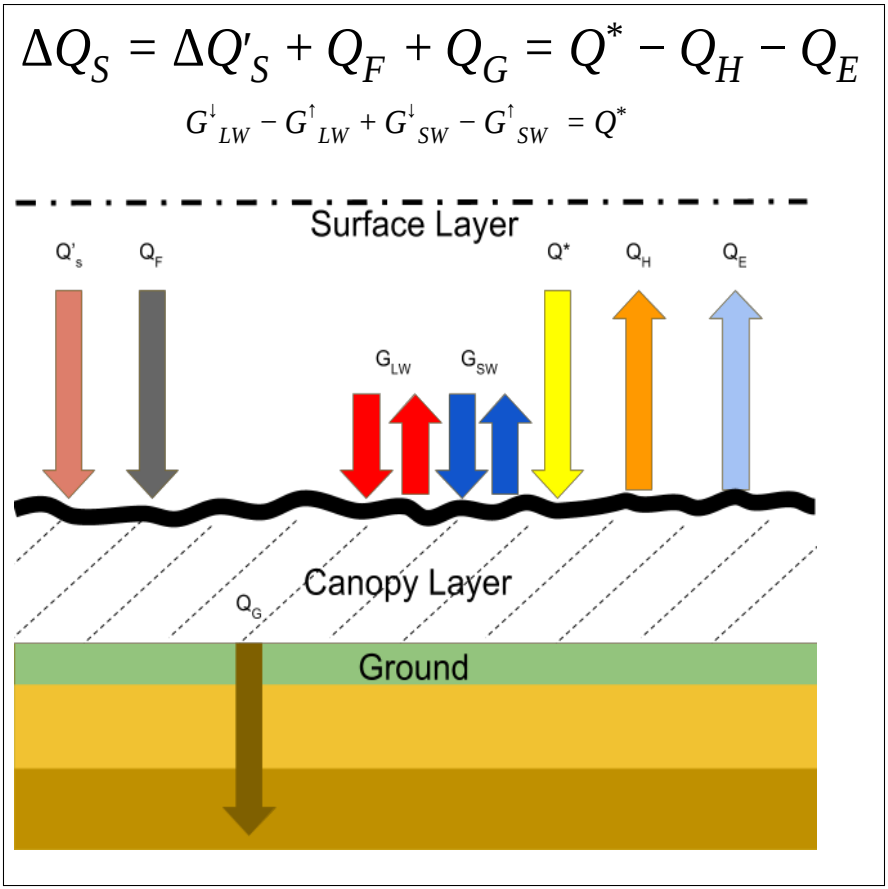

Figure 1: Schematic depiction of SEB relationship given in Eq. 1.16.

2010; Sailor and Lu 2004). The Surface Energy Balance (SEB) is intimately related to the atmospheric surface-layer (ASL), or region closest to the ground, which provides via a surface-layer scheme (SLS) the interconnection between the ground, or land surface model (LSM), and lower atmosphere, or, the planetary boundary layer (PBL) (Stull 1988; Arya 1988). In particular, SEB closure error (Foken 2008), has been examined in the context of urban climate for several decades and remains a challenging issue (T. R. Oke 1974, 1979, 1982; Arnfield 2003). In the context of SEB modeling, the role of vegetation, moisture, latent heat flux, and anthropogenic forcing are important areas of active research (Arnfield 2003; Kalma, McVicar, and McCabe 2008; Ching 2013). A systematic evaluation of the

modeled SEB is thus needed before proceeding to address applications such as discussed above. An extensive inter-model comparison and evaluation of contemporary methods for modeling urban effects in off-line models found that not all models explicitly check or force SEB closure, which could result in a source of bias in long-term urban climate modeling (C. S. B. Grimmond et al. 2010).

The SEB relationship as depicted in the schematic (Fig. 1), is defined as,

$$\Delta Q_s = \Delta Q'_S + Q_F - Q_G = Q^* - \langle Q_H \rangle - \langle Q_E \rangle, \tag{1.16}$$

where ΔQ_s, is the residual or storage term within the canopy layer, which can be represented by reduced residual $\Delta Q'_s$, anthropogenic forcing Q_F, ground heat flux Q_G. The net radiation, Q^*, can be written in terms of the longwave (subscript 'LW') and shortwave (subscript 'SW') partitions for upward and downward components, as,

$$Q^* = G^{\downarrow}_{LW} - G^{\uparrow}_{LW} + G^{\downarrow}_{SW} - G^{\uparrow}_{SW}.$$

Within the Noah LSM, the turbulent fluxes of sensible and latent heats are defined by,

$$\begin{aligned} Q_H &= \rho c_p C_H |U_{z_1}|(\theta_s - \theta_{z_1}), \\ Q_E &= \rho C_E |U_{z_1}|(q_s - q_{z_1}), \end{aligned} \tag{1.17}$$

where variables with subscript z_1 are prognostic values (integrated in time) at the first model level, and variables with subscripts s are diagnostic surface-layer values, for air potential temperature θ, air specific humidity q, and magnitude of the horizontal winds $|U|$, along with specific heat at constant pressure for air c_p, heat and moisture exchange coefficients C_H and C_E, respectively (Chen and Dudhia 2001, Chen and Zhang 2009). These fluxes provide the bottom boundary condition to the surface layer and PBL. Fluxes are aggregated from the LSM and urban schemes before forcing the SLS.

Parameterizations of urban processes within atmospheric models typically presume that the city is entirely sub-grid to the ASL. This modeling assumption means that the built

environment should be contained within the surface layer, or first full model level (C. S. B. Grimmond et al. 2010). One main concern is that anthropogenic waste heat and momentum modifications are only supplied to the first model level. However, one method often employed within studies of the surface layer or of lower PBL profiles is to add extra model levels near the ground. Hence, there is a trade-off between explicitly resolving fine structure in the ASL, especially within the urban boundary layer (UBL), also in conjunction with flow dominated by complex terrain, as detailed for Phoenix in Fernando 2010, and the sub-grid requirement for these urban models. Furthermore, parameterizations of the ASL often employ Monin-Obukhov Similarity Theory (MOST) (Monin and Obukhov 1954), wherein horizontal homogeneity is assumed, meaning that individual buildings and land uses at sub-grid scales are not explicitly resolved. This assumption can break down in settings with inhomogeneous land use and land cover (LULC) and variable roughness, such as urban areas (Grimmond and Oke 1999; Nordbo et al. 2013). Arnfield 2003 reviews spatial scale effects where variability between LULC types decreases when transitioning towards larger horizontal spatial scales (e.g. from about 10^1 to 10^4 m, the city-scale), enabling average value parameterization of urban processes at coarser resolutions. However, micro-scale LULC variations may become important when comparing with neighborhood-scale flux-tower measurements.

The National Building Statistics Database 2 (NBSD2) Burian, Velugubantla, and Brown 2002 has been incorporated into the latest release of WRF v3.5 (2013) within the National Urban Database and Access Portal Tool (NUDAPT) described by Ching et al. 2009. However, cities such as Phoenix have limited coverage since emphasis of NUDAPT has been on central business districts. The residential areas have shown impacts on regional climate (e.g. M Georgescu et al. 2013), along with impacts of heterogeneity of urban development Monaghan et al. 2014. Although NUDAPT provides a formulation for

development density, Ching 2013 indicates that more guidance is needed for aggregating subgrid representation to grid scales. This topic is explored in Chapter D.

Chapter 2

IMPACT OF METEOROLOGICAL CONDITIONS ON NOISE PROPAGATION FROM FREEWAY CORRIDORS

Published in: *Journal of the Acoustical Society of America*,
N.C. Ovenden, **S.R. Shaffer**, H.J.S. Fernando (2009) **126**(1)25-35.

This chapter examines the impact of meteorological conditions on the propagation of vehicular noise from urban freeways. A parabolic equation model coupled to an analytical Green's function solution close to the source field is used to compute the refracted sound field up to half a mile from the freeway to predict the noise exposure of residential areas nearby. The model was used in conjunction with meteorological and sound-level measurements taken at two freeway sites over the course of four days in Phoenix, Arizona. From the data collected, three test cases of varying levels of atmospheric stratification and wind shear are presented and discussed. The model demonstrates that atmospheric effects are able to raise sound levels by $10-20$dB at significant distances away from the highway, causing violations of acceptable limits imposed by the Federal Highway Administration in residential areas that are normally in compliance.

2.1 Introduction

Noise pollution is a serious and worsening environmental concern in urban areas. Not only does it diminish the quality of human life Goines and Hagler 2007, Granados 1998, Ward and P. Suedfeld 1973, but it also alters wildlife habitats and breeding sites Forman and Deblinger 2000. Highway traffic, airports, heavy industry, railways and even leisure activities located close to built-up areas all contribute to the noise menace, and thus urban planners and managers pay close attention to mitigate it. This paper concerns a main contributor to noise pollution in urban areas - the freeway noise - which varies considerably in time and space in the proximity of roadways. The noise level therein depends on a myriad of factors, to name a few, the traffic speed and volume, vehicle type, ground conditions, terrain, sound barriers, atmospheric absorption and meteorological variables (e.g. temperature, wind velocity, turbulence) and their spatial and temporal profiles E. Salomons 2001; Attenborough, Li, and Horoshenkov 2007. While a majority of these factors are accounted for in operational sound prediction models, such currently available models do not take all the salient factors into account C. Steele 2001, Lihoreau et al. 2006, Wayson et al. 1995. For example, the latest version of the Federal Highway Administration's (FHWA) Traffic Noise Model (TNM) Version 2.5 released in 2004 does not include the effects of temperature and wind variability; *i.e.* uniform, isothermal atmospheric conditions are assumed in the calculations. The latter is a reasonable assumption for shorter (less than 200m) distances from the sound source, but errors can be substantial when predicting intermediate and far field noise, since refraction of sound due to temperature and wind causes anomalous intensity variations at a significant distance from the source. For example, noise measurements conducted in Scottsdale, Arizona, following complaints by residents living more than about 400m ($\sim$1/4 mile) from the East Loop 101 freeway, suggest that

ground-level inversions (surface stable temperature stratifications) can increase the sound level by as much as 10-15dB J. Chambers et al. 2006. While the noise level therein under neutral atmospheric conditions is well within the FHWA noise abatement criterion (NAC), an inversion can cause the dBA level to exceed it. FHWA-NAC recommends implementing abatement procedures such as noise walls or modified pavement types (quiet pavements) when the energy averaged or equivalent sound level (Leq) approaches an A-weighted value of 67dBA. The challenge, however, is accounting for inversions and wind shear.

The influence of atmospheric factors becomes particularly critical when noise mitigation is realized via a combination of techniques, for example, noise walls and quiet pavements. The Arizona Department of Transportation (ADOT) has received approval from the FHWA for the Quiet Pavement Pilot Program (QPPP) to investigate the usefulness of pavement surface type as a noise mitigation strategy, subject to the condition that Arizona would be a pilot program with specific research objectives and requirements Scofield and Donavan 2005. This research is intended to validate the efficacy of Asphalt Rubber Friction Courses (ARFC) as a noise mitigation method. ADOT would overlay Portland Cement Concrete Pavement (PCCP) in the Phoenix valley with a one-inch thick ARFC surface. Where the ARFC is placed and noise walls are required the walls may be reduced in height in view of the extra mitigation offered by ARFC surfacing Scofield and Donavan 2005. Beginning in 2003, ADOT has been monitoring six sites across the Phoenix Metropolitan Area for traffic-generated noise to evaluate the effectiveness of ARFC. While measurements show that ARFC has reduced freeway noise appreciably (8-10dB) at close-in community locations, sound refraction due to environmental conditions can defeat the noise abatement approaches (e.g. the use of walls) at some distances away. Noise walls are expensive and typically cost $\sim$ \$1M/mile, and hence merits of their installation should be carefully evaluated *a priori*.

The effectiveness of AFRC pavements, sound walls and environmental factors become dominant only at certain intrinsic frequency ranges. The relationships between these variables and A-weighted noise levels in the field thus are intricate and can only be delineated via models that properly quantify fundamental relationships and their complex interactions. To develop such models will help in design, interpretation of measurements taken at different positions/times and in placing results on a unified scientific basis. The only viable method for predicting sound in complex field situations is the use of a numerical model that incorporates salient governing factors. A straightforward (yet onerous, because of computational expense) method is the nesting of an acoustic model with an environmental forecasting model. A simpler methodology is to use available representative atmospheric data from the area to feed the acoustic model, assuming local smaller scale variations are unimportant. The research reported herein is of this ilk and includes a meteorological measurement component. The aim is to examine how different meteorological conditions, especially ground based inversions and shear, can affect freeway noise, by taking Phoenix as a case of interest J. Wang and J. Angell 1999; H. Fernando et al. 2001.

A suite of computational approaches are presently being used for atmospheric sound propagation studies E. Salomons 2001, which include (i) Gaussian-beam methods, (ii) Fast-Field Program (FFP) models and (iii) Parabolic Equation (PE) models. Ray theories, although robust for indoor acoustics, rapidly become highly cumbersome to compute in downward refracting media where many rays are needed and caustics are problematic. Additional complications, such as diffraction by obstacles, turbulence and prediction of acoustic shadow regions, further urge the use of alternative methods. The key to PE models is the use of an effective sound speed based upon temperature and wind speed of the actual mean flow field that both modify the isotropic adiabatic sound speed Gilbert and White

1989; West, Gilbert, and Sack 1992. When assuming a line (or an axisymmetric) source, the two dimensional wave operator is factored into left- and right-traveling components transverse to the source. The unsteady pressure field due to a source can then be resolved by marching the computation across the domain away from the source by discounting any waves that propagate towards the source. Major disadvantages of this method are that it becomes inaccurate at high elevation angles and cannot directly account for back scatter unless the more difficult task of handling propagation in both directions is addressed. It has many advantages, however, including the ease of incorporating atmospheric absorption, varying boundary conditions and geometries (e.g. complex terrain) along with actual spatially varying meteorological profiles. For these reasons, methodologies based on the PE equation prove highly popular Gilbert and X. Di 1993, X. Di and Gilbert 1994; R. Sack and M. West 1995; M. West and Y. Lam 2000; Wilson 2000; Wilson, Brasseur, and Gilbert 1999; P. Chevret, P. Blanc-Benon, and D. Juve 1996, although it is common practice to use hybrid models combining several methods to exploit features of the problem at hand in an attempt to circumvent potential caveats of any individual method E. Salomons 2001, Ostashev 1997; Ostashev, V. Mellert, et al. 1997; Ostashev, F. Gerdes, et al. 1997; Ostashev et al. 2005; F. de Roo and I. Noordhoek 2003.

In order to understand and quantify the effects of atmospheric temperature and velocity profiles on sound propagation, we have combined a field measurement campaign (section 2.2) with modeling efforts (section 2.3). The field measurements are to provide realistic vertical profiles of temperature and cross wind velocities to the model and were performed over four days at two freeway sites in Scottsdale, AZ and Mesa, AZ, where meteorological and sound data were taken and recorded over roughly a six-hour period between 6 a.m. and 12 p.m. (section 2.4). For the modeling, the sound data is input into a Green's function model to evaluate the near source field generated from the freeway traffic

(section 2.5). This source field along with the meteorological data is then input into a parabolic equation (PE) model to compute the refracted sound field out to a distance of 600m. The results are compared to neutral atmospheric conditions, and the effect of stratification and wind shear are separated and quantified in three twenty-minute time-averaged cases selected from the field data (section 2.6). The conclusions of the study are given in section 2.7.

2.2 Experiments

In order to study the influence of meteorological conditions on noise propagation from Phoenix highways, the Center for Environmental Fluid Dynamics at Arizona State University (EFD-ASU) conducted a joint field campaign with ADOT and Illingworth & Rodkin, Inc. The EFD-ASU team made detailed measurements of atmospheric meteorological conditions, Illingworth & Rodkin Inc. provided sound measurements and ADOT videotaped the traffic and recorded its speed.

The field experiments were conducted on October 10th and 11th, 2006, in a location just on the west side of Phoenix loop 101 (ADOT location 3E, $33^o30'05.95$" N $111^o53'17.09$" W) and on November 7th and 8th, 2006, just on the north side of Phoenix loop 202 (ADOT location 3D: $33^o28'56.65$" N $111^o45'48.16$" W). The details of motivation for site selection are outlined in Chambers *et al.* (2005) J. Chambers et al. 2006. Although both sites are situated in urban locations, the freeways are relatively new so that housing and other buildings are located some distance (at least 0.5km) away. Hence, the terrain neighboring both freeways is relatively flat and homogeneous with hard sandy soil and sparse bushes. A cross section of the terrain for the route 202 site is shown in figure 2.

Measurements were taken from 7 a.m. to 11 a.m. in order to better understand how

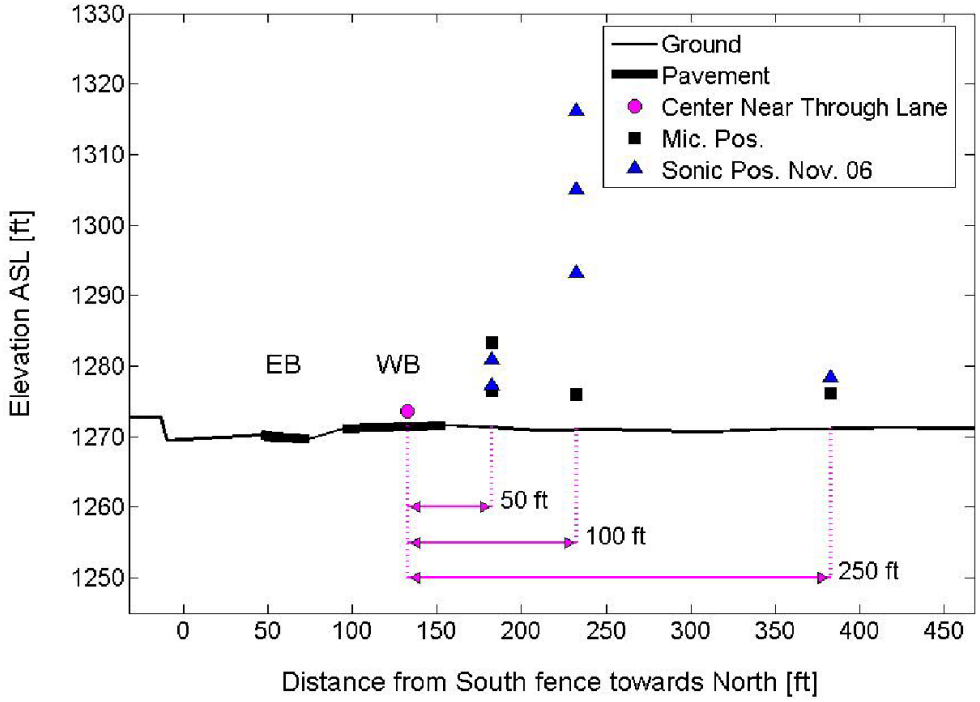

Figure 2: Cross section of loop 202 site as elevation above sea level. Horizontal distance is measured in feet from the fence on the south side. Positions of instruments are shown as squares for microphones and triangles for sonic anemometers in the November 2006 field campaign. Arrows indicate distances from the center of the nearest travel lane (filled circle) on the West Bound (WB) side.

noise levels change during a period of a temperature inversion, typical daytime adiabatic lapse conditions and during the morning transition period. It is interesting to note that the temperature conditions near the surface were found to be unstable even in the early morning hours, and this is believed to be due to retention of heat by the roadway surfaces even after the sunset, because of the high thermal capacity of road surfaces.

A number of instruments were employed, which included 3D sonic anemometers and a SODAR (SOund Detection And Ranging) with RASS (Radio Acoustic Sounding System). SODAR measures vertical wind profiles of all three components whereas RASS measures the vertical temperature profile. Sound measurement instruments at the 3E site

were also located at the following positions, where range is the horizontal distance from the center of the nearest travel lane and height is measured above ground level (agl):

Location	Range	Height
1	15.24m(50ft)	1.52m(5ft)
2	15.24m(50ft)	3.66m(12ft)
3	30.48m(100ft)	1.52m(5ft)

Note at the 3D site there was an additional meter at 76.22m (250ft) from the center of the nearest travel lane at a height of 1.52m (5ft) above ground level. The sonic anemometers were located on towers at the same distance from the highway as the sound measurement instruments, while the SODAR/RASS systems were located further away to avoid possible contamination of the sound level measurements (figure 2).

The sonic anemometers were operated at a frequency 10 Hz, providing all three velocity components and temperature. The data collected enables us to obtain detailed information on mean flow and temperature close to the surface, as well as turbulent statistics. During October 10th and 11th two sonic anemometers were located on a tripod 15.24m (50 ft) from the center of the nearest travel lane and three on a tower 30.48m (100 ft) from the center of the nearest travel lane. The heights of instruments on the tripod were 1.8 and 2.9 m agl (above ground level) and the height of those on the tower were 2, 4 and 6 m agl. During measurements on November 7th and 8th, an additional tripod was also located at 15.24m (50 ft) where the heights of the sonics were 1.8 and 2.9 m agl, while sonics at the tower were placed at levels 6.8, 10.4 and 13.8 m agl. On November 8th, one more sonic was placed on a tripod at a location 76.22 m (250 ft) from the center of the nearest travel lane at 2.2m agl to measure atmospheric conditions close to the furthest sound measurement point.

The SODAR/RASS system was utilized to measure wind speed and temperature profiles, respectively, between roughly 20m to 600m agl. during the October and November

deployments. This system provided more details on the structure of the atmospheric boundary layer during the periods of measurements at high altitudes, but for the present study the most important is the data taken up to 200m or so in height. Both the SODAR/RASS and the sonic anemometers were set up to enable the wind velocity component across the highway to be separated from the wind velocity component parallel to the highway. Only the component perpendicular to the highway is input into the sound propagation model.

2.3 Modelling

Based on the initial sound data from the field experiments, we construct a two-dimensional model of acoustic propagation from a single monofrequency coherent line source in a vertically layered atmosphere. A rectangular xy coordinate system is used with y measuring the vertical height and x measuring the horizontal range from the centre of the nearest travel lane. All lengths are non-dimensionalised on a typical source height L_0, velocities are non-dimensionalised on the sound speed measured at ground level C_0, density is non-dimensionalised on the density of air at 1 atmosphere ($\rho_0 = 1.2\text{kgm}^{-3}$) and pressure p is non-dimensionalised on $\rho_0 C_0^2$. For a given frequency f[Hz], we define the Helmholtz number as $\omega = 2\pi f L_0/C_0$ and by writing the acoustic pressure perturbation as $p(x,y,t) = p_c(x,y)\,\mathrm{e}^{-i\omega t}$ the Helmholtz equation for a line source at $\mathbf{x} = \mathbf{x_0}$ of strength S in a vertically layered atmosphere is obtained:

$$\frac{\partial^2 p_c}{\partial x^2} + \frac{\omega^2}{\tilde{c}^2(y)}\frac{\partial}{\partial y}\left(\frac{\tilde{c}^2(y)}{\omega^2}\frac{\partial p_c}{\partial y}\right) + \frac{\omega^2}{\tilde{c}^2(y)}p_c = S\delta(\mathbf{x}-\mathbf{x_0}). \tag{2.1}$$

Here, $\tilde{c}$ is the non-dimensional *effective* sound speed which includes the effects of both temperature and crosswind. Given measured vertical temperature $T(y)$ and crosswind $U_0(y)$

profiles, the effective sound speed is defined in a standard manner to be

$$\tilde{c}(y) = \frac{\sqrt{\gamma RT(y)} + U_0(y)}{C_0},$$

where γ is the ratio of specific heats and R the ideal gas constant. The boundary conditions imposed are a far-field Sommerfield radiation condition as $r = \sqrt{x^2 + y^2}$ becomes large, which takes the form

$$\frac{\partial p_c}{\partial r} - \mathrm{i}\frac{\omega}{\tilde{c}} p_c = o(r^{-1/2}) \text{ and } p_c = \mathrm{O}(r^{-1/2}) \quad \text{as } r \to \infty, \tag{2.2}$$

and an impedance boundary condition at the surface

$$-\frac{1}{\mathrm{i}\omega}\frac{\partial p_c}{\partial y} = \frac{1}{Z} p_c \quad \text{at } y = 0. \tag{2.3}$$

Throughout this paper, the empirical impedance model of Delany and Bazley Delany and Bazley 1970 is used where, for a ground surface with flow resistivity σ [Pa s m^{-2}], the impedance Z is given by

$$Z = 1 + 0.0511 \left(\frac{\sigma}{f}\right)^{0.75} + \mathrm{i}\, 0.0768 \left(\frac{\sigma}{f}\right)^{0.73}. \tag{2.4}$$

Two models are used in tandem to compute the far-field sound propagation: (i) a near-field analytic Green's function solution assuming a homogeneous atmosphere and (ii) a parabolic equation approximation. Figure 3 shows the regions of the x-y domain where each model is used.

The near-field Green's function solution Chandler-Wilde and Hothersall 1995 is used to obtain the acoustic field in the vicinity of the line source where the refractive effects of atmospheric factors are assumed to be negligible. In other words, the Green's function solution assumes a constant effective sound speed $\tilde{c} = 1$ and solves (2.1) to (2.3) with this

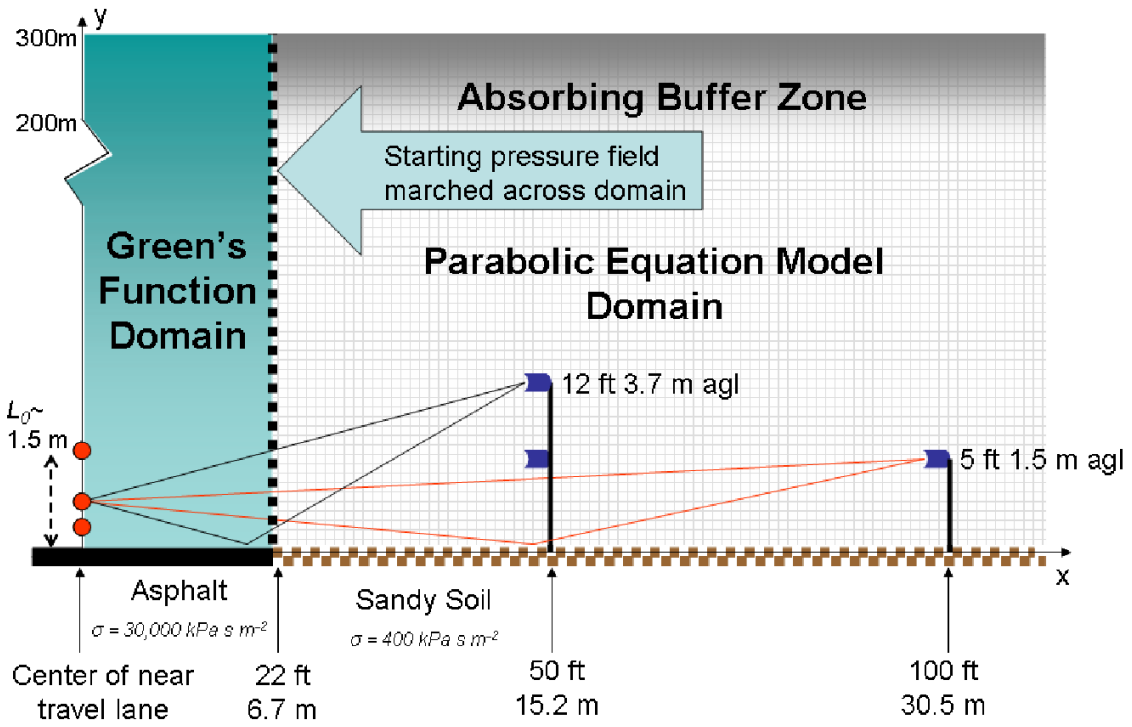

Figure 3: A schematic of the coupled models used to resolve the far-field propagation of traffic noise from a freeway corridor. The filled circles represent monofrequency coherent effective line sources above the centerline of the nearest lane of traffic. A Green's function method is utilized both to determine virtual source heights and strengths from the sound meter data and also to initialize the sound field along the vertical dashed line at the edge of the pavement. A parabolic equation model then marches this input pressure field across the domain, handling each frequency component separately.

assumption up to the edge of the highway, at 6.7m (22ft), obtaining the sound field

$$\begin{aligned}\frac{p_c(x,y;y_0)}{S} &= -\frac{\mathrm{i}}{4}H_0^{(1)}(\omega\sqrt{x^2+(y-y_0)^2}) \\ &\quad -\frac{\mathrm{i}}{4}H_0^{(1)}(\omega\sqrt{x^2+(y+y_0)^2}) \\ &\quad +P_Z(x,y;y_0), \end{aligned} \tag{2.5}$$

where $H_0^{(1)}$ is the zeroth order Hankel function of the first kind, and the term $P_Z(x,y;y_0)$ represents the correction to the hard-wall solution for Z finite. This correction is derived by

Chandler-Wilde and Hothersall 1995 and is given in terms of

$$\begin{aligned}
\lambda &= \omega\sqrt{x^2+(y+y_0)^2}, \\
\gamma &= (y+y_0)/\sqrt{x^2+(y+y_0)^2}, \\
a_+ &= 1+\frac{\gamma}{Z}-\left(1-Z^{-2}\right)^{1/2}\left(1-\gamma^2\right)^{1/2},
\end{aligned}$$

with the result

$$\begin{aligned}
P_Z(x,y;y_0) &= \frac{\mathrm{e}^{\mathrm{i}\lambda}}{\pi Z\sqrt{\lambda}}\int_0^\infty s^{-1/2}\mathrm{e}^{-s}\,g(s/\lambda)\mathrm{d}s \\
&+ \frac{\mathrm{e}^{\mathrm{i}\lambda(1-a_+)}}{2\sqrt{Z^2-1}}\mathrm{erfc}(\mathrm{e}^{-\mathrm{i}\pi/4}\sqrt{\lambda a_+})
\end{aligned}$$

where

$$\begin{aligned}
g(t) &= -\frac{\left[Z^{-1}+\gamma(1+\mathrm{i}t)\right]}{(t-2\mathrm{i})^{1/2}\left[t^2-2\mathrm{i}(1+\gamma/Z)t-(Z^{-1}+\gamma)^2\right]} \\
&- \frac{\mathrm{e}^{-\mathrm{i}\pi/4}\sqrt{a_+}}{2(1-Z^{-2})^{1/2}(t-\mathrm{i}a_+)}.
\end{aligned}$$

The first integral expression is calculated using Gauss-Laguerre Quadrature and the second *surface wave* term (due to its strong exponential decay away from the ground) is evaluated using the formula given in Attenborough K. Attenborough 2002. We assume over the near-field calculation that the ground impedance is typically of porous asphalt with $\sigma = 3\times10^7$Pa s m^{-2}, which is given in Table 4.9 of Attenborough, Li, and Horoshenkov 2007.

The near-field Green's function solution provides an acoustic field at the edge of the freeway $p_{\mathrm{ini}}(y) = p_c(x_{\mathrm{edge}},y)$, which is subsequently used as an initial condition for a two-dimensional cartesian variant of the standard axisymmetric parabolic equation (PE) model, first derived by Gilbert and White Gilbert and White 1989.

The PE model used is the parabolic wide-angle approximation of (2.1) assuming a two-dimensional line source. The pressure field is rewritten as $p_c(x,y) = \psi(x,y)\,\mathrm{e}^{\mathrm{i}\omega x}$ and

$\psi(x,y)$ is obtained by solving the equation

$$\begin{aligned} \frac{\partial \psi}{\partial x} &+ \frac{1}{4\omega^2}\left[\frac{1}{\tilde{c}^2}\frac{\partial}{\partial y}\left(\tilde{c}^2\frac{\partial^2\psi}{\partial y\partial x}\right)+\omega^2\left(\frac{1}{\tilde{c}^2}-1\right)\frac{\partial\psi}{\partial x}\right] \\ &= \frac{\mathrm{i}}{2\omega}\left[\frac{1}{\tilde{c}^2}\frac{\partial}{\partial y}\left(\tilde{c}^2\frac{\partial\psi}{\partial y}\right)+\omega^2\left(\frac{1}{\tilde{c}^2}-1\right)\psi\right]. \end{aligned} \tag{2.6}$$

The equation (2.6) and the impedance boundary condition (2.3) are finite-differenced and the solution is obtained by marching forward in the x direction. Sandy soil is taken to be the ground surface type beyond the freeway with $\sigma = 4\times10^5$Pa s m^{-2} and we assume the ground to be completely flat to concentrate strictly on atmospheric effects in this study.

The radiation condition (2.2) is dealt with numerically by a buffer zone West, Gilbert, and Sack 1992; E. M. Salomons 1998; Robertson, Seigmann, and Jacobson 1995 occupying approximately the upper one third (100m) of the grid domain, $y_{\text{att}} < y < y_{\max}$, where the effective sound speed $\tilde{c}$ in (2.6) is replaced by

$$\bar{c}(y) = \tilde{c}(y)\left[1+\mathrm{i}A\left(\frac{y-y_{\text{att}}}{y_{\max}-y_{\text{att}}}\right)^3\right]^{-1}.$$

Here, A is a real parameter that can be optimised for each frequency component. To ensure the effectiveness of the buffer zone, the initial pressure profile obtained from the near-field Green's function method $p_{\text{ini}}(y)$ must also be smoothly reduced to zero within the buffer zone to prevent spurious reflections from the truncated top of the grid domain. Thus,

$$\psi(x_{\text{edge}},y) = p_{\text{ini}}\exp\left(-\frac{B\omega^2}{2}\left(\frac{y-y_{\text{att}}}{y_{\max}-y_{\text{att}}}\right)^2-\mathrm{i}\omega x_{\text{edge}}\right)$$

where $1 \leqslant B \leqslant 4$ is another optimised parameter dependent on frequency.

Effects of atmospheric absorption are additionally incorporated following the method outlined in E. Salomons 2001 (section B.5) by applying an attenuation rate dependent on the local humidity, temperature and atmospheric pressure in dB m^{-1} to each frequency band at 1m agl before summing to form the L_{eq} versus range plots (figures 9, 11

and 13). This method follows the International Standard ISO 9613-1:1993(E). The attenuation rate used here is based a relative humidity of 20%, which is typical for the city of Phoenix, and the temperature profiles obtained from the measurements taken. The pressure in the absorption calculation is assumed to be 101.325kPa.

2.4 Chosen Test Cases and Modelling Parameters

Based on the large amount of meteorological and sound data collected, three test cases are presented here for long-scale sound transmission modeling. To exclusively illustrate the strong dependence of acoustic properties on environmental conditions, the main focus will be on one site (Rt. 202). Temperature and crosswind profiles above 40 metres are obtained from the SODAR/RASS measurements in 10 meter increments, whereas data at lower altitudes is gleaned from the sonic anemometers. The meteorological profiles are time-averaged over a period of 20 minutes. To obtain the surface-layer velocity profile for an unstable convective boundary layer (below 60m), theoretical curves of the Monin-Obukhov (MO) stability theory are fitted to the sonic data. The MO theory suggests that near the ground both vertical temperature and velocity gradients have the form

$$\frac{\partial \bar{\zeta}}{\partial y} \sim A_{\bar{\zeta}} \left(1 - B_{\bar{\zeta}} y\right)^{2/3} y^{-4/3} \quad \text{for } \bar{\zeta} = U_0(y),\ T(y). \tag{2.7}$$

where $A_{\bar{\zeta}}$ and $B_{\bar{\zeta}}$ are parameters fitted to the data Stull 1988. Since $\frac{\partial \bar{\zeta}}{\partial y}$ diverges like $y^{-4/3}$ as $y \to 0$, the chosen temperature profile is made linear near the ground so that $T(y) \sim Ay + B$ and the velocity takes instead a standard logarithmic form, $U_0(y) \sim A \log(z/z^*)$, where z^* is the aerodynamic roughness length. Above 60m the theoretical curve smoothly transitions into the SODAR-RASS data. If the useful range of data from the SODAR-RASS is less than 300m, the theoretical curve is held constant at the last entry from the SODAR-RASS. Measurements and theoretical profiles for the three

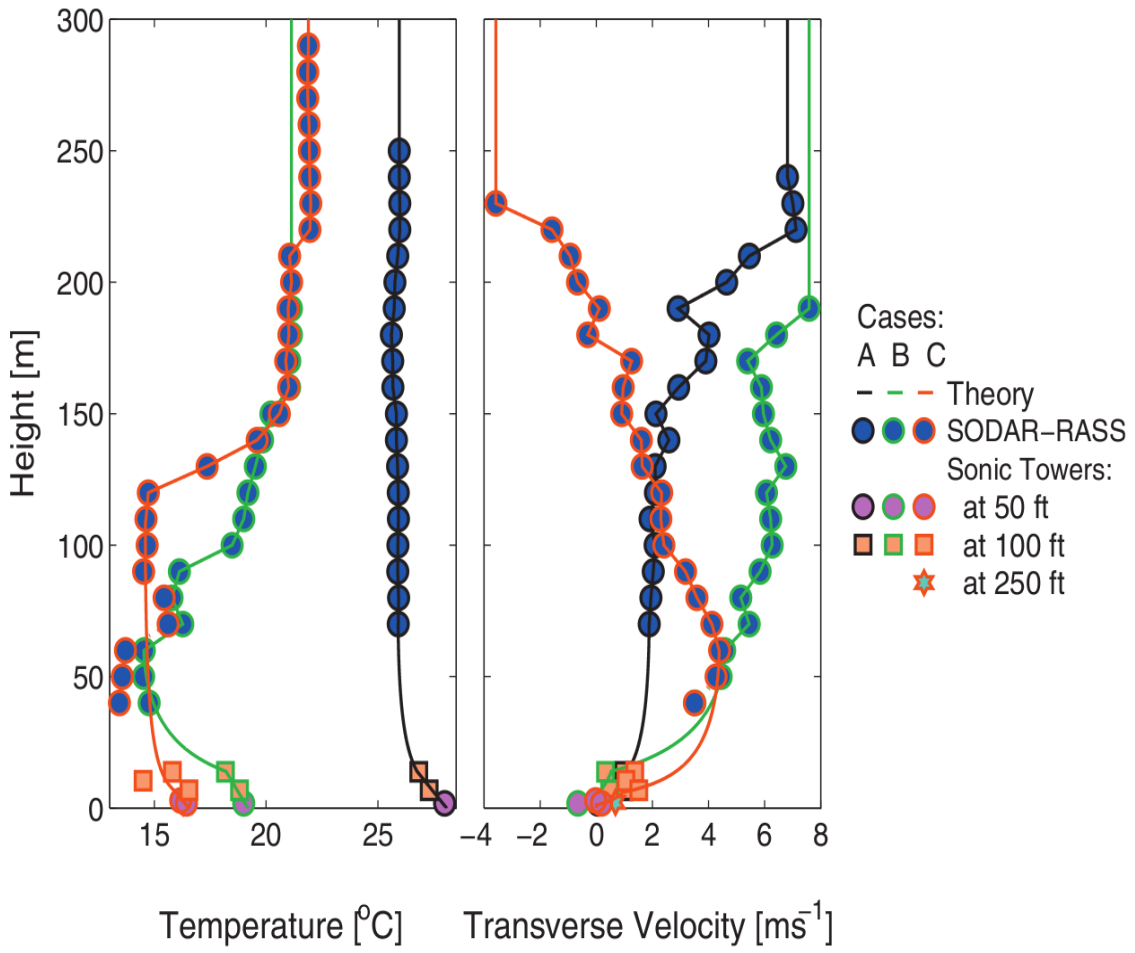

Figure 4: Temperature and crosswind (to the freeway) data with fitted theoretical profiles for the three cases. All data points above 20 m are given by the SODAR-RASS with lower height information obtained from the sonic anemometers as shown in the legend.

chosen cases are shown in figure 4. The following representative cases were selected for study:

A Nov 7th 2006 (Rt 202) 11am - wind shear at very high altitudes but little temperature stratification. Note that in this case, the SODAR-RASS data was usable up to 250 m compared with 200 m in the other cases.

B Nov 7th 2006 (Rt 202) 8am - significant stratification and shear flow.

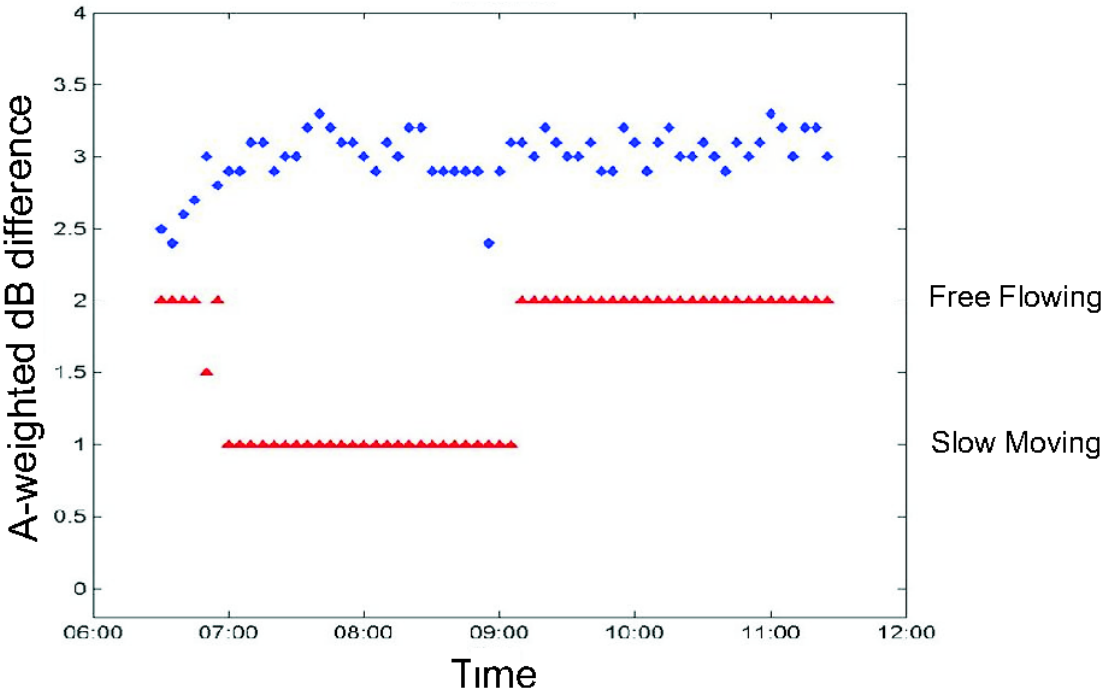

Figure 5: The difference in overall A-weighted sound level on 11 October 2006, measured between the sound meter located 15.2 m (50 ft) from the center of the nearest lane of traffic at a height of 1.5 m (5 ft) and the sound meter located 30.5 m (100 ft) from the center of the nearest lane of traffic at a height of 1.5 m (5 ft). The triangles merely display an indication of the traffic conditions at the time (either free flowing, slow moving or intermediate). A decrease of 3 dB with a doubling of distance corresponds to what is expected for a line source as $P_{\text{line}} \sim r^{-1}$ in a neutral atmosphere.

C Nov 8th 2006 (Rt 202) 8am - strongly stratified with a sharp change in temperature at approx 120m above the ground and a crosswind jet at approximately 50m above the ground.

2.5 Analysis of Traffic Spectra Taken by Noise Meters

The overall acoustic source field we are attempting to replicate consists of a six-lane highway (three lanes in each direction) with multiple moving sound sources that vary

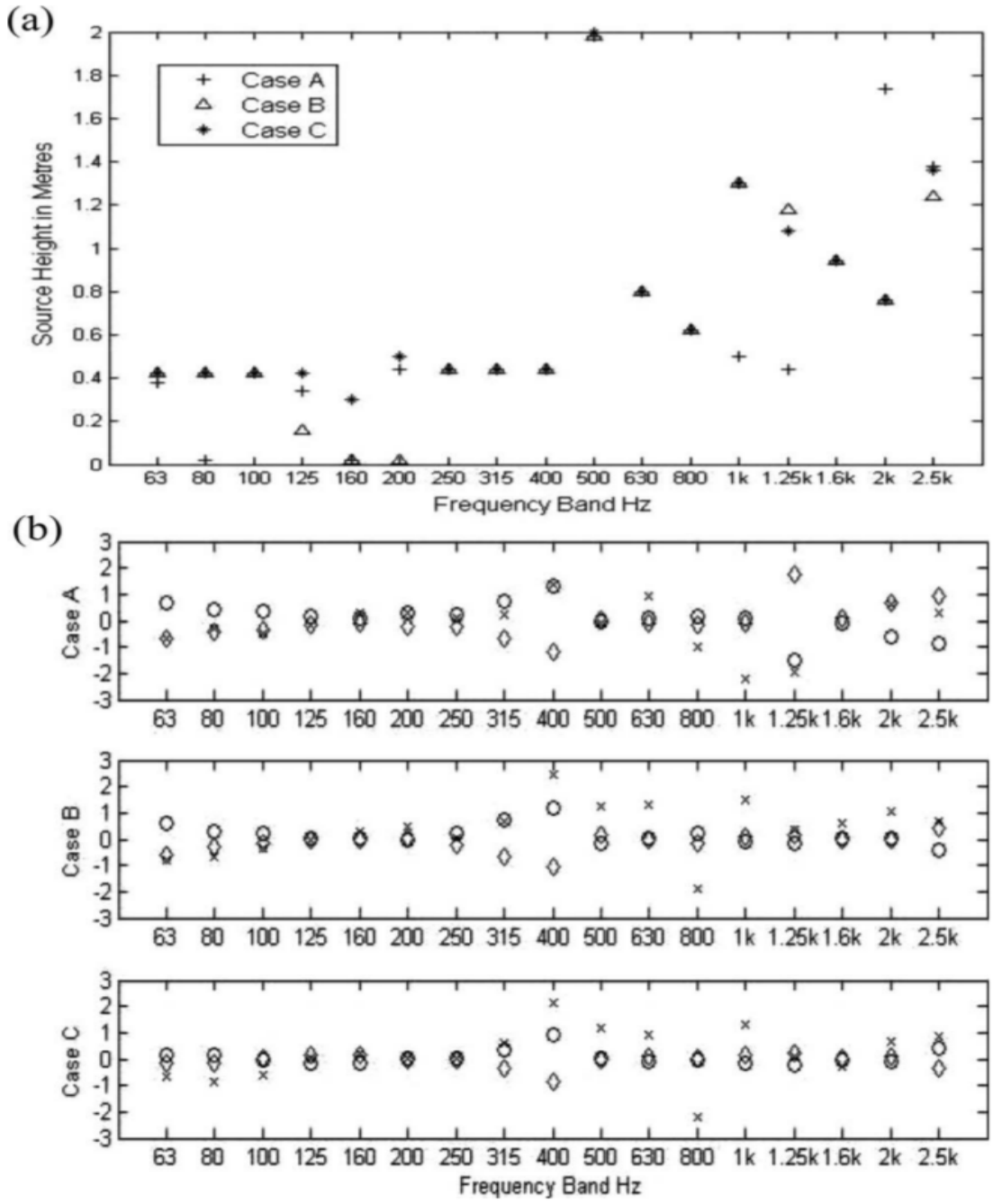

Figure 6: (a) Virtual source heights for the three cases obtained by minimising an error norm based on dB differences between sound meters. (b) Measured dBA minus the dBA obtained from the Green's function solution for each virtual line source at the three sound meter locations. Circles show measured minus computed dBA for the meter at location 1, diamonds for the meter at location 2 and crosses for the meter at location 3.

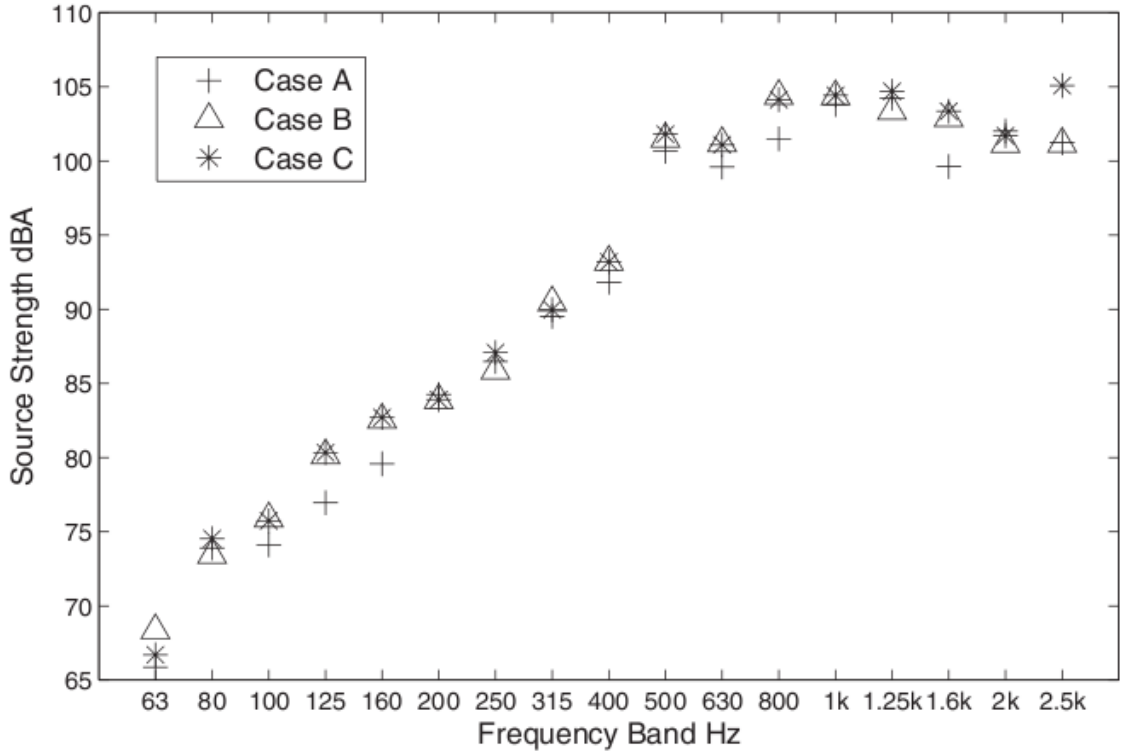

Figure 7: Virtual source strengths for the three cases obtained by minimising an error norm based on dB differences between sound meters.

according to their speed, traffic density and vehicular type. Without knowledge of the exact acoustic signature of every car and truck, a number of severe but unavoidable assumptions need to be made about the nature of the sound sources. We emphasise here that the focus of this paper is on the meteorological aspect of noise transmission from freeways as opposed to understanding the composition of sound sources emitted.

Our sound data consists of five-minute time-averaged $1/3$rd octave data from three sound meters placed close to the highway. We have no information about the sound generated from separate lanes of traffic or the frequency output of different vehicle types traveling at different speeds. Hence, the principal aim of our model noise source must be to generate a *representative* sound field that matches the three sound meter measurements

taken at the site. Figure 5 shows the difference between the five-minute averaged dBA level taken from the sound meter at 1.5m (5ft) above the ground and located 15.2m (50ft) away from the center of the nearest travel lane and the sound meter at 1.5m (5ft) above the ground and located 30.5m (100ft) away from the center of the nearest travel lane. This clearly shows a geometric attenuation of 3dB as the distance from the source doubles, providing some justification to the assumption that the freeway can be treated as series of line sources. We assume that this holds true for the entire study domain.

For the purpose of our model, the traffic noise is approximated as a series of monofrequency coherent line sources positioned vertically above the center of the nearest travel lane (see figure 3). The strength and effective height of these *virtual* sources are unknowns that are determined by replicating as closely as possible the $1/3$rd octave data obtained from the three closest sound meters. As the sound meters are positioned relatively close to the source, the influence of meteorological conditions is regarded as negligible over the range up to the furthest sound meter, and a neutral atmosphere is therefore assumed in the near field. This enables the unknown line source parameters to be determined by using the Green's function model for acoustic propagation from a line source above an impedance plane as detailed in section 2.3. As mentioned before, the flow resistivities chosen are $\sigma = 3 \times 10^7$Pa s m^{-2} for the asphalt and $\sigma = 4 \times 10^5$Pa s m^{-2} for the sandy soil where, for the loop 202 experimental site (figure 2), the surface is assumed to be asphalt out to a range of 6.7m (22ft) from the virtual line sources with sandy soil beyond, as shown in Figure 3. Repeating the calculation for other flow resistivities suggests that neither representating the asphalt as a hard wall ($Z = \infty$) nor varying the sandy soil flow resistivity between 2×10^2 to 6×10^5 Pa s m^{-2} change the results significantly.

For a given $1/3$rd octave interval, the height of a representative line source can be calculated by accurately trying to replicate the differences between the dBA values recorded

by the three sound meters. This is done by varying the source height to minimise the sum of the absolute errors between the differences obtained by the Green's function model in the meter locations and the actual measured differences. However, this can lead to unrealistic virtual source heights and so an additional height penalty is also imposed. A norm based on this premise can be obtained by defining $\Delta \mathrm{M}_{ij}^{f}$ to be the dBA difference actually recorded at frequency band f between meter locations i and j (as numbered in section 2.2) and $\Delta \mathrm{G}_{ij}^{f}(H)$ to be the dBA difference obtained between meter locations i and j from a virtual monofrequency coherent line source at frequency f and at height H above the surface. Our virtual source height H is then determined by minimising

$$\sum_{i \neq j, i<j} \left| \Delta \mathrm{M}_{ij}^{f} - \Delta \mathrm{G}_{ij}^{f}(H) \right| + 3H.$$

where the term $3H$ represents the additional height penalty mentioned above. Once the height is determined, the source strength can be obtained by averaging the source strengths required to reproduce the three meter readings. The source heights calculated for each frequency band in Cases A-C are plotted in Figure 6(a) and Figure 6(b) shows for all three cases the difference between the dBA measured at each sound meter and that determined from the virtual source obtained through the optimisation process described above. Observe that the virtual line sources replicate the measured sound field accurately, to well within 1dBA error for most frequencies and meter readings. Note additionally that there is generally very good agreement on the source heights obtained in each case for all frequencies (using data taken on different days at different times) although three obvious exceptions are the significant virtual source height differences for the 1kHz, 1.25kHz and 2kHz components between Case A and the other cases. We point out, however, that local norm minima are obtained for Case A at approximately the same heights as the virtual heights obtained for the two other cases but these are not optimal with the chosen norm. Other small discrepancies in figure 6(b) for the lower frequencies can be explained as the

dBA difference errors do not vary that much with height due to the large wavelengths so that variations of source height do not significantly alter spatially the sound field generated. Perhaps in fact the most problematic difficulty in selecting source height here occurs around 400 to 500 Hz range where the norm error at small heights takes unacceptably high values (possibly 7 dB) but only approaches zero again at source heights of well over 2m or so. This can be observed in the increase in measured minus computed errors at around 400Hz and providing some justification for imposing a height penalty.

Following the determination of source heights, it is relatively straightforward to use the Green's function near-field model to obtain the A-weighted source strengths and these are shown for Cases A-C in figure 7. Note the good agreement in the source strength profile across the frequency ranges 63Hz to 2.5kHz for the three cases. The sound signature is almost identical for Cases B and C, both taken at the same time during rush hour on consecutive days, whereas Case A has lower sound levels particularly in the $100-160$Hz and 630Hz to 1.6kHz bands, possibly due to the lower traffic levels occuring in the late morning.

2.6 Construction of L_{eq} Plots

In each chosen case, the model is run for each frequency component, based on the central frequency of the $1/3$rd octave band, with and without the influence of meteorological effects for comparison. For efficiency, the frequency range of the computation is reduced from spanning the entire range of 25Hz to 20kHz to only include those bands between 63Hz and 2.5kHz (17 components in all). Such a restriction produces an error of less than 0.2% in terms of the final overall sound pressure level when compared to the actual values measured by the sound meters.

The spatial A-weighted sound pressure level distribution for each frequency component is resolved by the PE model on a grid of size and spacing dependent on the wavelength (based on a usual ten grid points per wavelength). These results are subsequently interpolated onto a grid of one metre spacing with a range of $0-600$m horizontally and $0-300$m vertically. Then at each grid point the A-weighted frequency contributions $L_A(f_n)(x,y)$ are combined to produce the overall L_{eq} sound pressure level by the formula

$$L_{\text{eq}} = 10\log_{10}\sum_{n=1}^{17} 10^{L_A(f_n)/10},$$

with

$$f_n = \left\{ \begin{array}{cccccc} 63, & 80, & 100, & 125, & 160, & 200, \\ 250, & 315, & 400, & 500, & 630, & 800, \\ 1000, & 1250, & 1600, & 2000, & 2500 & \end{array} \right\}.$$

Results of the spatial sound pressure levels are presented in figures 8 and 9 for Case A, figures 10 and 11 for Case B, and figures 12 and 13 for Case C. For each case, figures 8, 10 and 12 show a contour plot of the equivalent spatial sound field obtained in a neutral atmosphere directly above the contour plot of the resolved spatial sound field when the temperature and crosswind velocity effects are included. Note that the downwind side of the freeway is always shown and the vertical range displayed is only up to 20m in height agl. It is clear from these figures that the overall impact of the meteorological effects is significant in all three cases examined. Indeed, significantly higher noise levels are predicted near the ground downwind for all cases. For guidance, FHWA's noise abatement criteria threshold of 67 dBA is shown as a thick contour line on the spatial contour plots of L_{eq} (figures 8, 10 and 12). Furthermore, on the range plots (the top plot in figures 9, 11 and 13), the shaded area also represents sound pressure levels exceeding the 67dBA threshold. Below each case is examined in more detail.

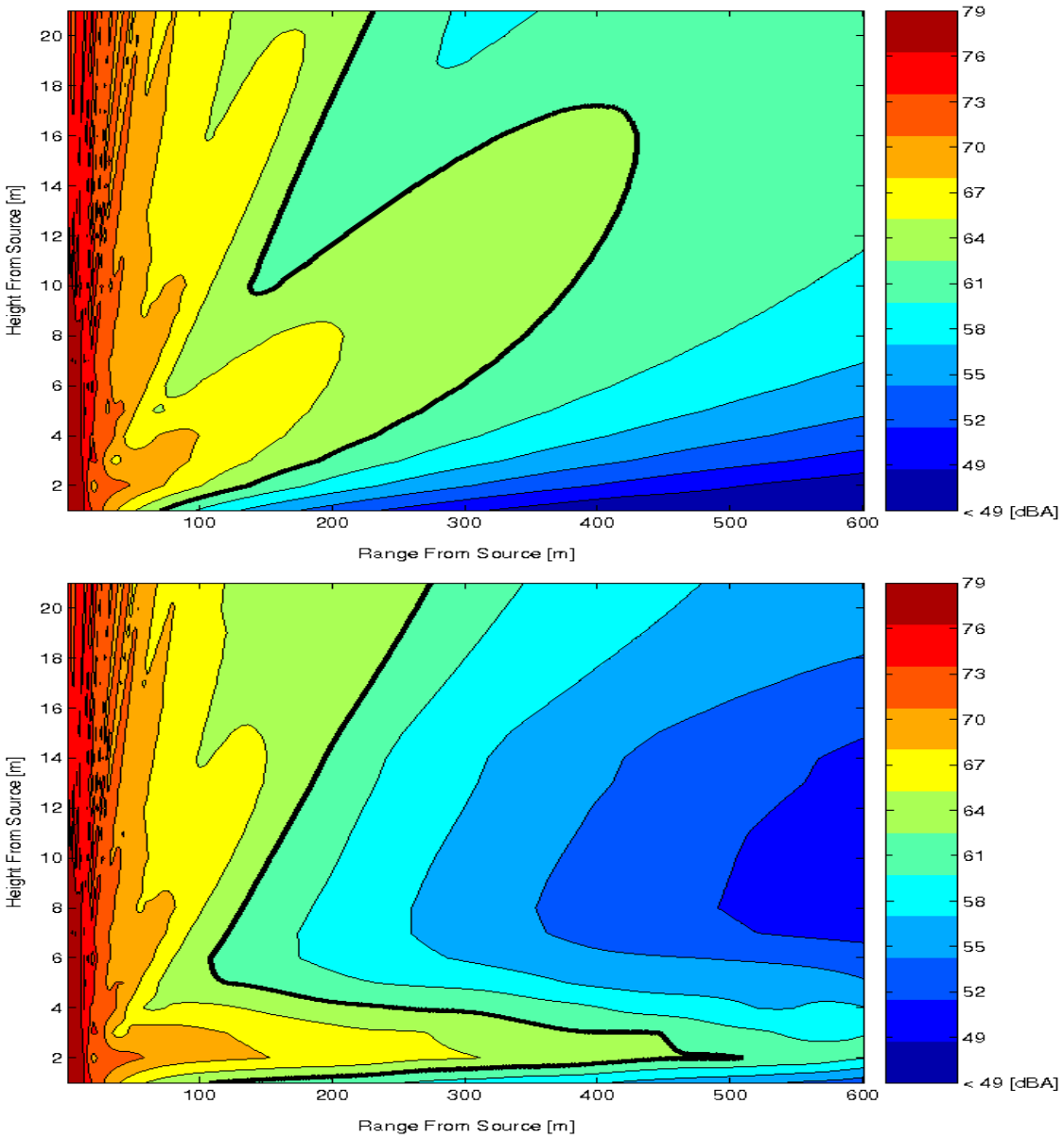

Figure 8: Case A: A-weighted sound pressure level contours without meteorological effects (top) and with meteorological effects (bottom). The effect of atmospheric absorption is not included here. Each contour line represents a change of 3 dBA. The bold contour represents the 67 dBA level.

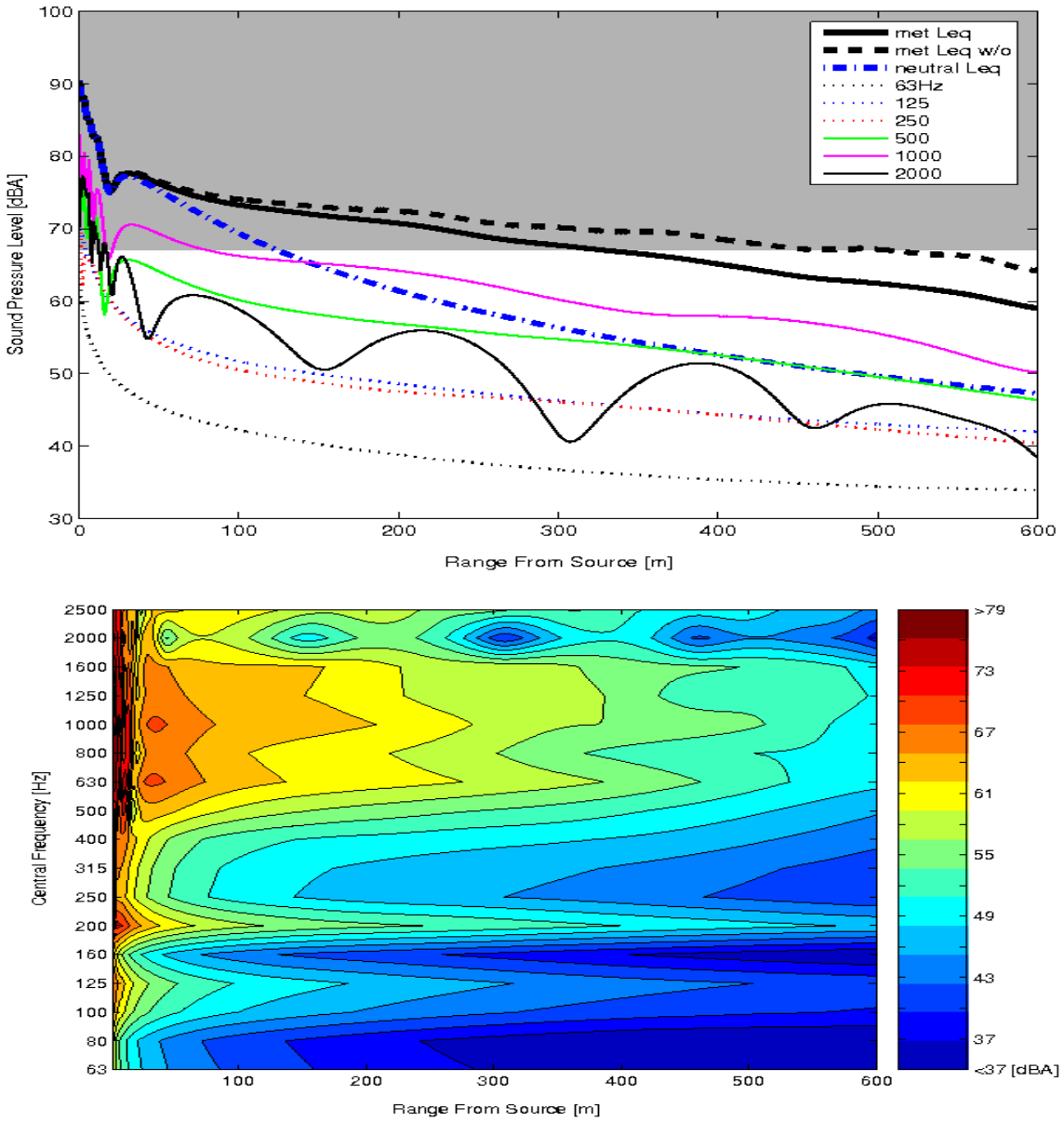

Figure 9: Case A: Overall A-weighted sound pressure level (SPL) and the SPL of each frequency component at a height of 1 meter above the ground. The top figure shows the SPL for neutral conditions (bold blue dotted line), with meteorological effects but without atmospheric absorption (bold black dotted line) and with both meteorological effects and with atmospheric absorption (bold black solid line and frequency bands). The shaded area in the top figure represents the region where the SPL range exceeds the 67 dBA threshold. The bottom figure shows contours of A-weighted sound pressure level with meteorological effects for each frequency component at an altitude of 1 meter neglecting atmospheric absorption. Each contour line represents a change of 3 dBA.

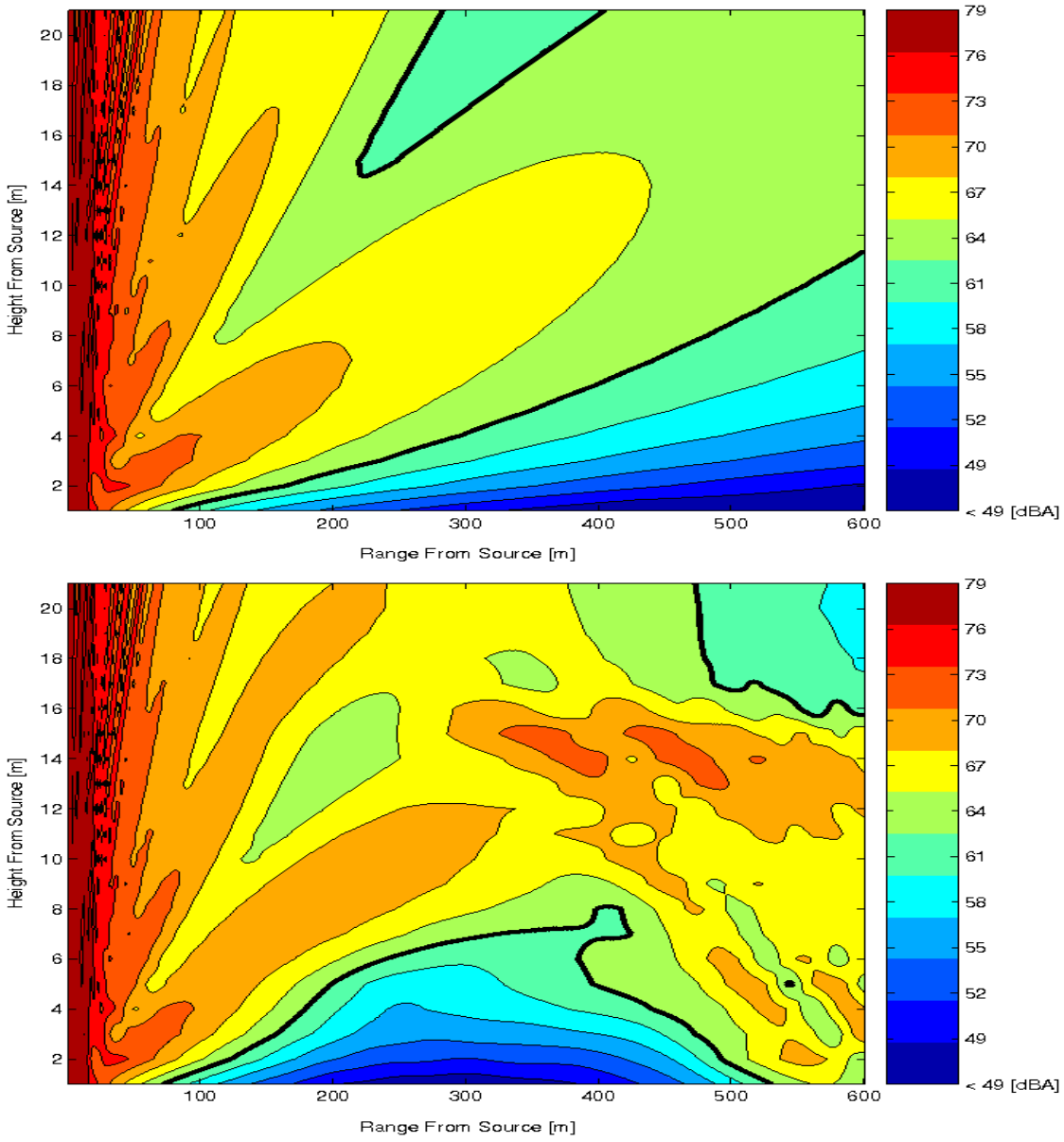

Figure 10: Same caption as for figure 8, but for case B.

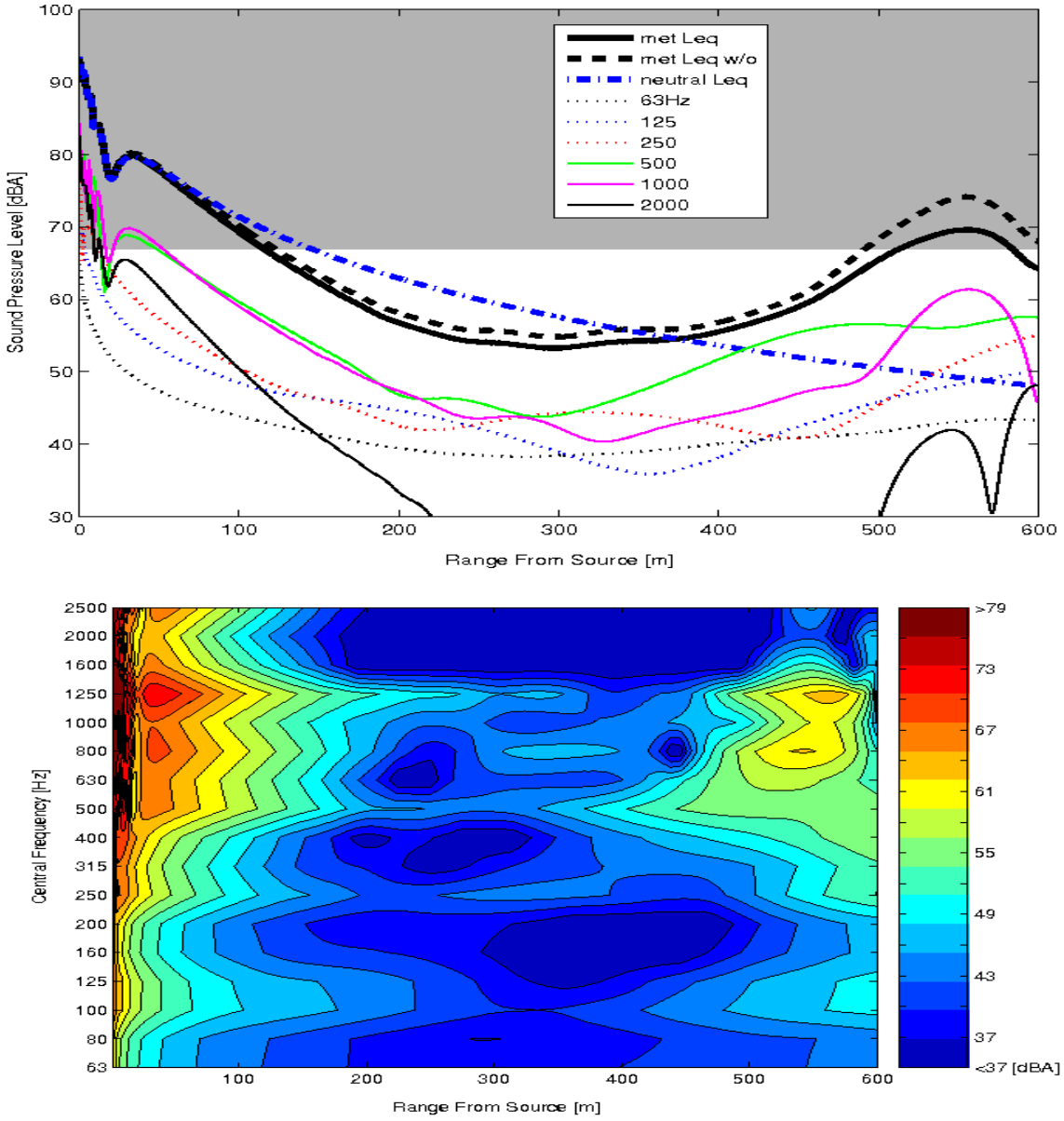

Figure 11: Same caption as for figure 9, but for Case B.

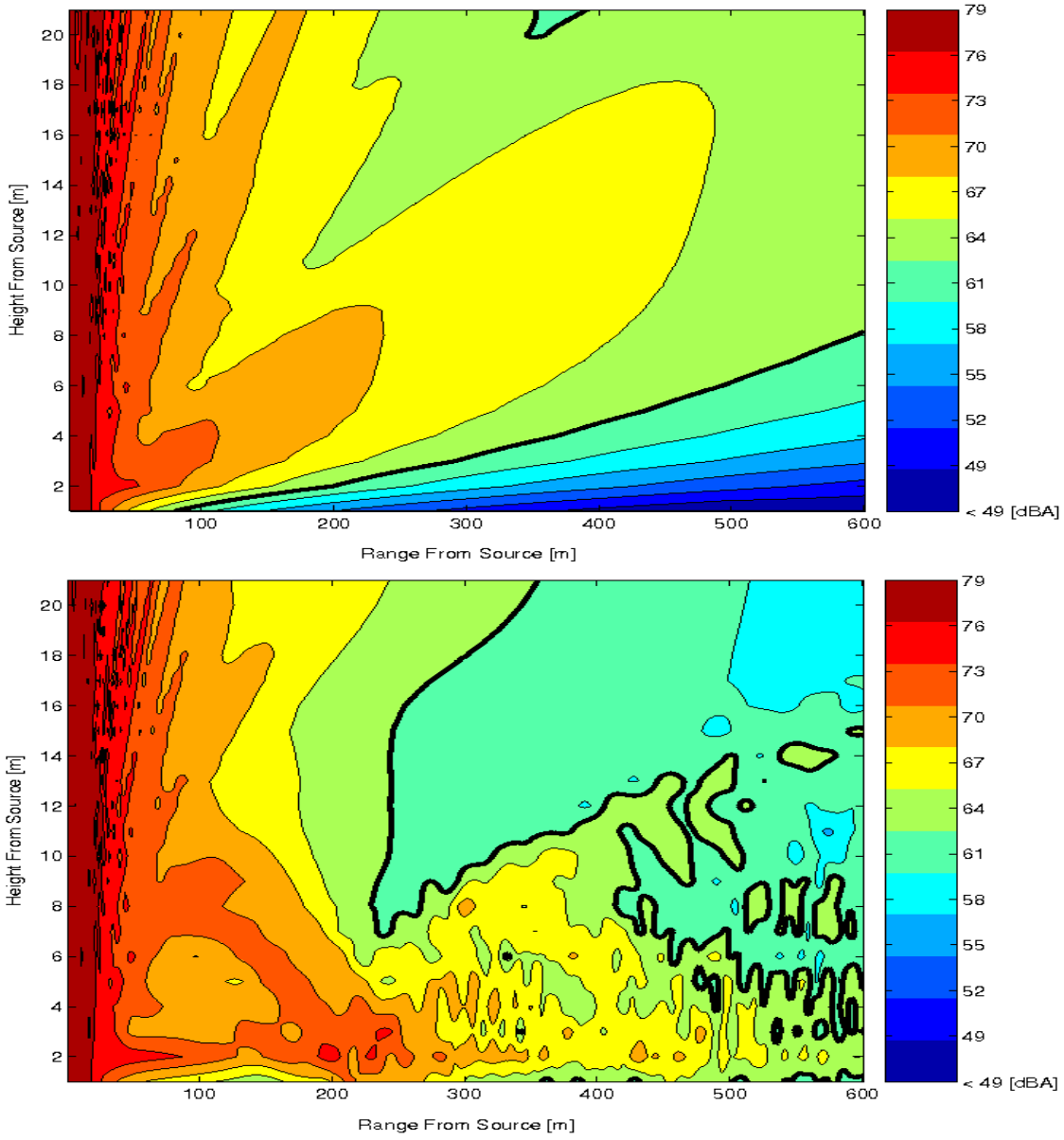

Figure 12: Same caption as for figures 8 and 10, but for Case C.

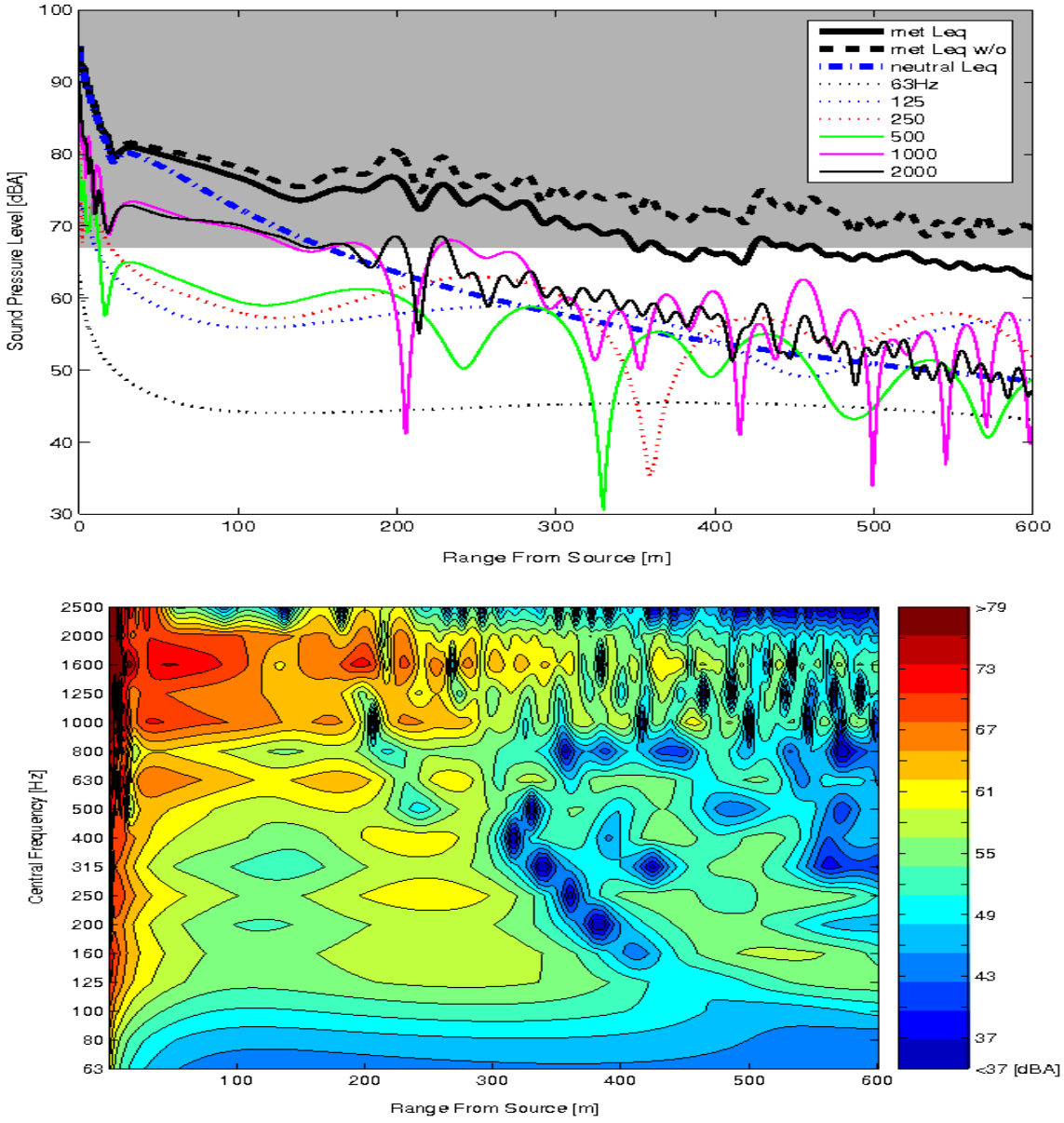

Figure 13: Same caption as for figures 9 and 11, but for Case C.

The meteorological effects are weakest for Case A with little temperature stratification and a crosswind of the order of $2ms^{-1}$ persisting from about 30 metres to around 150 metres in altitude. However, figure 8 clearly shows how the crosswind shear flow present up to 30 metres above the surface focuses sound into a thin layer of 3-5 metres in height, where the sound intensity is raised by roughly 10-15 dB. As a result, the sound level close to the ground does not fall below 67 dBA until a horizontal distance of approximately 220m from the freeway is reached, as opposed to approximately 110m predicted for a neutral atmosphere (see figure 9). A close examination of the impact of the meteorological effects on individual frequency components (figure 9 bottom) reveals that the frequency bands 200-250Hz and 1kHz to 2.5kHz remain the most intense out to the far-field.

Case B occured during rush-hour traffic on Loop 202 with a stronger wind shear from the ground attaining a crosswind speed $6ms^{-1}$ at 60 metres in height. More severe temperature gradients can be observed, with the temperature falling 5 degrees with increasing altitude before rising back to its ground level value at an altitude of 100 m. The competition between the near-ground negative temperature gradient and positive wind shear means that overall near-ground sound levels drop more rapidly than they would in neutral atmospheric conditions over the first 150 metres or so from the freeway. However, the refractive effects due to wind shear and to the presence of a temperature inversion at higher altitudes lead to sound rays being refracted back towards the ground from above and sound focussing at around 550m from the freeway. Indeed, figures 10 and 11 indicate that the A-weighted sound pressure level starts to exceed the 67 dBA threshold close to the ground at a range of 500 metres before continuing to exceed 67 dBA almost up to the edge of the calculation domain. It would appear that the frequency range 800Hz to 1.6kHz is particularly influenced and focussed most intensely by the combination of wind shear and

temperature gradients (see bottom of figure 11) although all frequency ranges appear to be subject to some degree of near-ground focussing at the 500m range. It is especially interesting to note that the most intensely focused frequency range components appear, in fact, to fall to perceptively low sound levels (below 40dBA) in the range 200m - 400m from the freeway. The spatial contours in figure 10 thus strongly suggest that this case could be a typical example of excessive sound levels occuring far from the freeway which are unlikely to be abated by the use of a sound barrier.

Case C is also taken during rush-hour traffic and has the more severely altering meteorological profiles, being strongly stratified and having a crosswind jet peaking at $4ms^{-1}$ at a height of 50 m above the ground. Figures 12 to 13 show a concentration of sound rays and pockets of constructive and destructive interference between the rays in a roughly 5-6m wide layer close to the ground, particularly beyond the 300m range. As a result, the effect of the wind shear with only a mild negative temperature gradient close to the ground leads to the near-ground sound pressure level persisting in excess of the 67 dBA threshold up to almost 350 metres from the freeway. Once again the dominant frequencies responsible appear to be 1 kHz and 1.25 kHz with other neighbouring frequencies also being strongly influenced by the meteorological conditions.

2.7 Conclusions/Further Comments

This work represents a combined experimental and theoretical study on the impact of meteorological conditions on the propagation of traffic noise from a freeway corridor. Clear indications from the results obtained are that traffic noise models used to judge the environmental noise impact on nearby communities must incorporate the usual or expected meteorological conditions that occur in that geographical location. This is of particular

importance for the case of ARFC that motivated this study, wherein the reduction of the effectiveness of the pavement with use is deduced via measurements made over certain time periods of different years. Without corrections for the effects of meteorology, the validity of such assessments is highly questionable unless only the near field data is utilized. It should also be added that some of the atmospheric effects observed in this paper appear to offer the possibility of rendering traditional mitagation techniques, such as noise walls, ineffective. However, this would not occur with strategies based on controlling the traffic noise at source, by developing quiet pavement materials such as ARFC for instance.

The combined Green's function and PE model has shown its capabilities in taking meteorological data and near-field sound measurements to generate a spatial map of predicted noise levels. The model also enables analysis of individual frequency components (e.g. as in Figure 9 for Case A), and there is a some indication in this study that the frequency range 1kHz to 1.6kHz is the most significantly influenced by meteorological conditions and thus provides the principal contribution to far-field traffic noise levels; however, this requires experimental confirmation. If such further evidence arises, mitigation strategies targeting this frequency band would be the most effective in preventing excessive noise levels at large distances from the freeway corridor.

Acknowledgments

We are extremely grateful to Arizona Department of Transportation (ADOT), Arizona State University (ASU) and University College London (UCL) for their support of this ongoing collaborative research. In particular, we thank Christ Dimitroplos and Fred Garcia at ADOT for their interest and encouragement. The consultants Illingworth-Rodkin assistance in the project in measuring and processing the sound data is also gratefully

acknowledged. We also thank Dragan Zajic, Leonard Montenegro and Adam Christman for their help with the field experiments and subsequent data analysis and the referees for their very constructive and encouraging comments.

Chapter 3

INCORPORATING TERRAIN AND VERTICAL WALLS INTO A FREEWAY NOISE PROPAGATION MODEL

Material from this chapter is published in:
Arizona Dept. of Transportation, Final Report: Project ID - R060518P (JPA 06-014T), SPR 605-2, **S.R. Shaffer**, H.J.S. Fernando and N.C. Ovenden (2012). "Investigations of environmental effects on freeway acoustics".

A generalized terrain PE (GTPE) model for sound propagation in an atmosphere bounded by non-uniform terrain is presented, following the work of R. Sack and M. West 1995. Simplified terrain cases without meteorological effects are presented to illustrate the capabilities of the new model with emphasis on effects of terrain. The GTPE model is extended by deriving a reflection scheme for PE-type models based upon the normal impedance ground boundary condition to account for two-way propagation. Thus this new model enables the study of backscatter from vertical terrain features in addition to the forward propagation of traffic noise in settings with complex terrain. Future model developments will extend the reflection scheme to terrain features with arbitrary angles. Future possibilities also include coupling the sound model with flow calculation software to determine the flow response to terrain and the sound field response to perturbed flow, along with model evaluation with field and lab experiments.

3.1 Introduction

Typical results of PE modeling have only been one-way calculations ignoring backscatter from terrain features. We have derived a simple method for calculating the back-reflected field using the normal impedance boundary condition and the first order PE approximation. Utilizing the reflected component in a reverse running calculation and iterating over several subsequent back reflections, a more representative prediction for the effects of terrain features of various impedances and geometries on the 2D sound field from a line source can be made. Furthermore, the relevent meteorological parameters of temperature and flow velocity can be incorporated into the model via the 2D scaler field of an effective sound speed either through prediction with numerical techniques or derived from field experiment measurements. Thus this new model enables assessment of the sound field under both varying terrain boundary conditions and the additional influence from the response of the meteorological field to the varying terrain through the effective sound speed.

The organization of this chapter is as follows. The GTPE and reflection model is presented in Section 3.2 with the terrain following transformation and boundary condition given in Section 3.2.1. A derivation of our vertical terrain backscatter approximation is given in Section 3.2.2. We then present several model validation and application experiments to demonstrate the model capabilities in Section 3.3. A discussion and conclusions follow in Section 3.4with future directions proposed in Section 3.5.Note that some figure numbers and references of this preliminary draft are still in a format using roman numerals, the reader is cautioned to not be confused by this.

3.2 GTPE and Reflection Model

We follow the development presented in Sack and West (1995) for the General Terrain Parabolic Equation (GTPE) model and apply it to a Gaussian hill, an escarpment with and without a wall, and to a symmetric canyon treating the reflection from a theoretical wall placed atop the escarpment. In general, it is desirable to determine the back-reflected field at all points in the range, but a first approximation can be made by only considering the reflection from vertical boundaries. This can then be enhanced to account for boundaries tilted slightly from vertical, and also for general terrain boundaries. In this report we only show results for reflection from vertical barriers.

It is desirable to determine the back-reflected field at all points in the range, but a first approximation can be made by only considering the reflection from vertical boundaries. This can then be enhanced to account for boundaries tilted slightly from vertical, and also for general terrain boundaries. The methods will be derived in this order. We begin with the simplest case in Section 3.2.2 where we will show the derivation for backscatter from a perfectly vertical wall or terrain obstacle with complex impedance Z. We then propose a method to account for terrain with small variations from vertical and then for backscatter from a general smooth terrain. Future considerations could explore constraints on the smoothness of H and comparison of diffraction calculations for non-continuous H' and with analytical ray-based approaches Robertson 1999.

3.2.1 Terrain Following Coordinates and Boundary Conditions

The (x,z) Cartesian coordinate system is transformed into terrain-following eta-coordinates defined here by $\xi = x$ and $\eta = z - H(x)$, where the terrain height above

some reference datum is given by the function $H(x)$. The core of our method is to apply the normal impedance boundary condition (eqn 24 of R. Sack and M. West 1995)

$$\partial_{\vec{n}}\psi = \frac{\partial\psi}{\partial\vec{n}} = -ik_0\hat{\beta}\,\psi, \tag{3.1}$$

for an appropriate representation of the normal derivative $\partial_{\hat{n}}$. The ground normal vector, $\vec{n}$ is away from the ground, $\hat{\beta} = \rho_0 c Z^{-1}$ is the complex admittance defined in terms of a reference fluid density ρ_0, characteristic sound speed c and representative complex ground impedance Z, which can be represented in terms of the frequency of interest and an effective flow resistivity representative of the ground materials Attenborough, Li, and Horoshenkov 2007; Delany and Bazley 1970. The complex velocity potential, $\psi = \varphi e^{ik_0\xi}$ is written in terms of a complex modulator φ multiplied by an exponential carrier term with reference wavenumber k_0 and horizontal coordinate ξ. In general, the outward normal derivative $\partial_{\vec{n}}$ to a slope at an angle δ from vertical is defined in transformed coordinates by,

$$\partial_{\vec{n}} = -(\sin\delta)^{-1}\partial_\eta - (\cos\delta)\partial_\xi. \tag{3.2}$$

3.2.2 Vertical Terrain Backscatter

We begin with the simplest case for a vertical wall and set $\delta = 0$ at the postion of the wall, $\xi = \xi_w$, so equation 3.2 becomes,

$$\partial_{\vec{n}} = -\partial_\xi. \tag{3.3}$$

We now should write the total field as the sum of the left and right traveling components, $\psi = \overleftarrow{\psi} + \overrightarrow{\psi}$. Upon substitution of equation 3.3 into equation 3.1 we have,

$$\partial_\xi(\overleftarrow{\psi} + \overrightarrow{\psi}) = ik_0\rho_0 c Z_w^{-1}(\overleftarrow{\psi} + \overrightarrow{\psi}) \text{ at } \xi = \xi_w, \tag{3.4}$$

as the boundary condition for the total field on the face of the vertical obstacle (wall) with surface impedance Z_w. Next, the wavenumber for the left (right) traveling components are written as $\overleftarrow{k_0} = -k_0$ ($\overrightarrow{k_0} = k_0$). Separating the left from the right components, we arrive at,

$$\left[ik_0\rho_0 c Z_w^{-1} + ik_{0w} - \partial_\xi\right]\overleftarrow{\varphi} = \exp(2ik_{0w}\xi_w)\left[\partial_\xi + ik_{0w} - ik_0\rho_0 c Z_w^{-1}\right]\overrightarrow{\varphi}, \tag{3.5}$$

where k_{0w} and Z_w are the wavenumber and complex impedance at the face of the wall.

The next key step to our method uses equations 10-12 from Sack and West 1995 for the first-order or narrow angle PE operator. Written here in the notation of the left-traveling component as,

$$\partial_\xi \overleftarrow{\varphi} = \frac{-i}{2k_0}\overleftarrow{L}_1[\overleftarrow{\varphi}]. \tag{3.6}$$

Where the left traveling first order (narrow angle) PE operator $\overleftarrow{L}_1$, is defined in general (without direction) as,

$$L_1[\varphi] = (1+(H')^2)\partial_{\eta\eta}\varphi - (H'' - 2ik_0H')\partial_\eta\varphi + k_{0w}^2 - k_0^2. \tag{3.7}$$

For a vertical wall, we assume nearly flat terrain in front of the discontinuity and set $\lim_{\xi\to\xi_w} H' = H'' = 0$ to obtain the approximation (for the left traveling component),

$$\overleftarrow{L}_1^{(v)}[\overleftarrow{\varphi}] \approx \partial_{\eta\eta}\overleftarrow{\varphi} + k_{0w}^2 - k_0^2, \tag{3.8}$$

where the superscript (v) is used to denote the L_1 operator for the vertical terrain case.

3.2.3 Nearly Vertical Terrain Backscatter

The motivation for a nearly vertical approximation would be to allow application to fascade features for a wall which only varies slightly from vertical and typically less than grid resolution $\delta \sim \lambda/10$, without the need for modifying the resolution or making

assumptions about varying the impedance value. This enhancement is made by applying a small angle approximation to equation 3.2 resulting in,

$$\frac{\partial}{\partial \vec{n}} \approx \left(\frac{6\delta^{-1}}{\delta^2-6}\right)\frac{\partial}{\partial \eta} - \left(1-\frac{\delta^2}{2}\right)\frac{\partial}{\partial \xi}. \tag{3.9}$$

Which, with the same approximation used in equation 3.8 gives a model equation simalar to equation 3.5 viz,

$$\begin{aligned}&\left[\left(\tfrac{6\delta^{-1}}{\delta^2-6}\right)\tfrac{\partial}{\partial \eta} - \left(1-\tfrac{\delta^2}{2}\right)\left(ik + \tfrac{i}{-2k_0}\overleftarrow{L}_1^{(v)}\right) + \tfrac{ik_0}{Z_0}\right]\overleftarrow{\varphi} \\ &= e^{2ik\xi}\left[\left(\tfrac{-6\delta^{-1}}{\delta^2-6}\right)\tfrac{\partial}{\partial \eta} + \left(1-\tfrac{\delta^2}{2}\right)\left(ik + \tfrac{\partial}{\partial \xi}\right) - \tfrac{ik_0}{Z_0}\right]\overrightarrow{\varphi}.\end{aligned} \tag{3.10}$$

3.3 GTPE Model Test Cases

The general domain configuration used in these test cases was a 300 meter high by 300 meter in range grid with 10 points per wavelength for several frequency bands. The only case with a different range was the symmetric canyon, which is the same as for the escarpment with barrier and symmetric about the origin but not extending beyond the barriers. For all but the reflected field case in Section 3.3.4, a road section of width 6.7 meters using the one parameter ground impedance model of Delany and Bazley (1970) with a flow resistivity representative of asphalt $\sigma = 3$ x 10^7 Pa s m^{-2} (Attenborough 2007). This was used in conjunction with a Green's function solution for an infinite line source above an impedance plane to obtain the starting complex pressure field at the edge of the road in a manner identical to Ovenden et al. (2009). For the remainder of the domain, the ground flow resistivity value was changed to 4 x 10^5 Pa s m^{-2}, which is a value representative of hard sandy soil. The flow resistivity model variable can be vectorized to enable variations with range, but the creation of artificial diffraction at impedance discontinuities within the

PE model needs to be explored. The terrain function was also constrained to vary smoothly after the edge of the road to avoid artificial diffraction. In all cases, an attenuating layer was placed at the top third of the PE model domain to eliminate numerically reflected waves. The source heights and frequencies are described for each case.

3.3.1 Gaussian hill

Owing to smoothness constraints to minimize possible artificial diffraction at terrain discontinuities when the function is discretized onto the computational grid, we chose to use a Gaussian profile over the sine-squared profile used in Sack and West (1995). We also significantly scaled down the domain size in comparison, yet the results are qualitatively similar.

3.3.1.1 Model and Domain Setup

The terrain function used for this case is,

$$H(x) = 40e^{-((x-206)/50)^2}[\text{m}],$$

giving a hill of 50 m half-width centered at 206 m in range (200 m from the edge of the pavement) with a height of 40 m. The source height was placed at 5 m AGL with a source strength of S=1 since log10(1)=0, so that the output SPL field would then be attenuation with respect to the source. However, there is a shift in the results shown by -20 dB in the terrain case and +52 dB in the flat comparison (which can be revised as appropriate). The meteorological fields were held constant with $T = 25°\text{C}$ and U=0 m s-1 giving a neutral atmosphere. This case was run for a set of 17 frequency bands listed in figure 14.

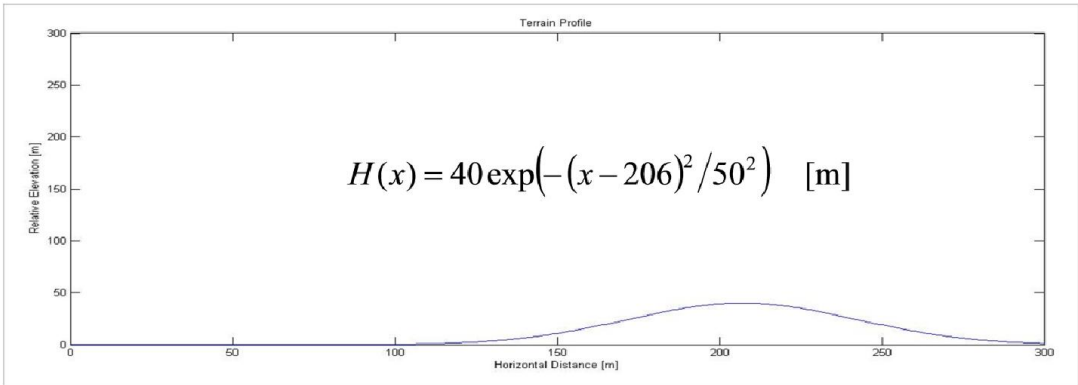

T=25 [°C]
U=0 [ms^{-1}]
$\log_{10}$(Source Strength)=0
L_0=5 [m]

$$f \in \begin{Bmatrix} 63 & 125 & 250 & 500 & 1000 & 2000 \\ 80 & 160 & 315 & 630 & 1250 & 2500 \\ 100 & 200 & 400 & 800 & 1600 & \end{Bmatrix} \quad [\text{Hz}]$$

Figure 14: Terrain profile used for the Gaussian hill case along with parameters of the setup configuration. The set of frequencies for which output was created are also given.

3.3.1.2 Model Results

Shown in (Fig. 15) and (Fig. 16) are the cases for no terrain and with terrain, respectively. In (Fig. 16), the terrain following transformation has been inverted to give display, and so the black region at the top was above the computational grid and the brown region is the ground below the computational grid. Regions of white contours are below the minimum contour level. The attenuating layer is visible most notably above 250 m in height, and this is the reason that contours above 200 meters in height are diminished. Note that high angles in the PE and GTPE models lose accuracy. Observe the region of constructive and destructive interference on the near side of the hill, the diffraction pattern from the top of the hill and down range and the acoustic shadow region down range. Shown in (Fig. 17) (top) is a zoom in the lowest 60 m height showing the detail of the sound field

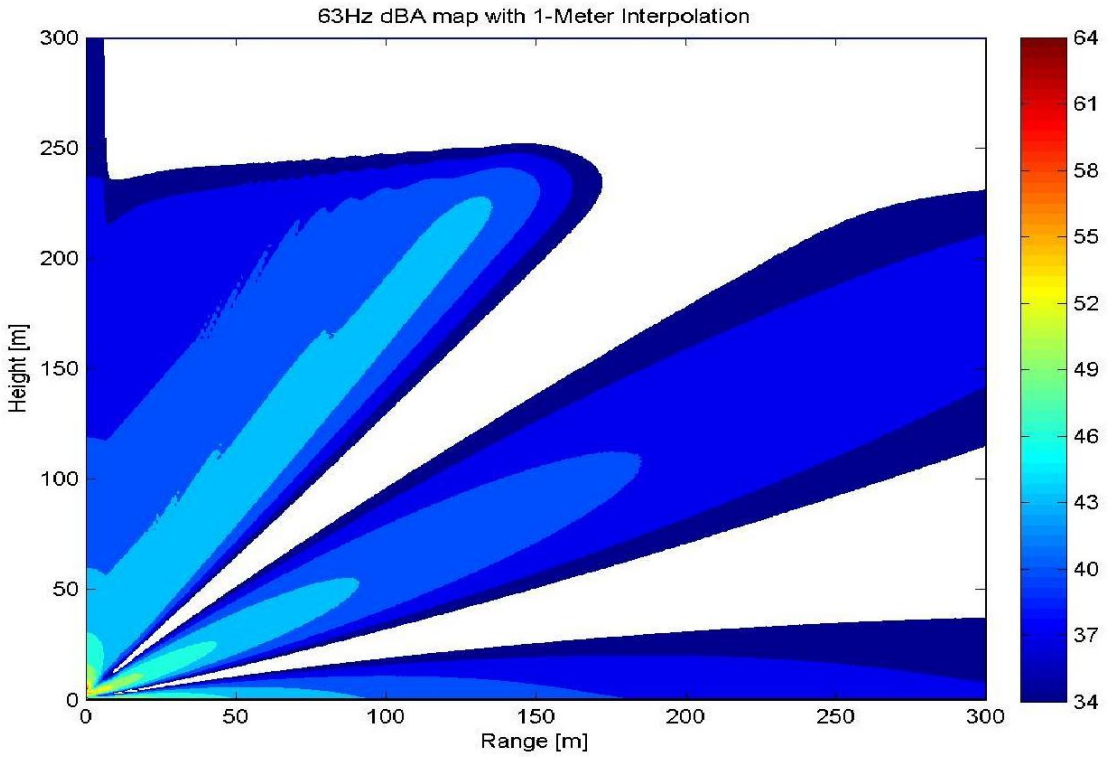

Figure 15: Flat terrain comparison for 63 Hz, $T = 25°$C and U=0 m s^{-1} for the entire domain.

near the terrain. Also shown in (Fig. 17) (bottom) is an attenuation versus range plot at 2 m AGL, comparing sound levels in range against the value at 50 m in range. The dotted curve is the case with terrain and the dashed curve is without for evaluation of the terrain effect. Shown in (Fig. 18) are results for 7 of the 17 frequency bands computed, showing how each frequency responds to the terrain. Since the model is to be extended accounting for meteorological profiles, a useful nondimensionalization is difficult to define, though for the neutral case one might explore nondimensionalization based on the wavelength. We do not pursue this aspect.

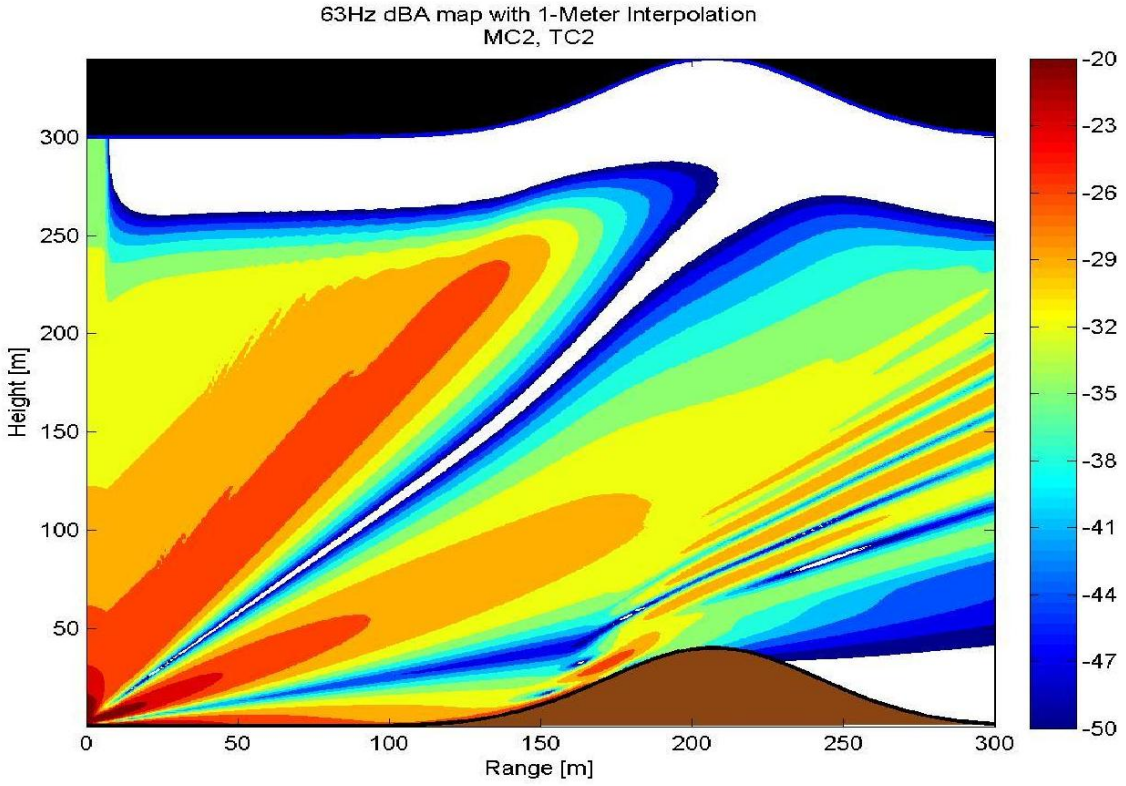

Figure 16: Gaussian hill results for 63 Hz, $T = 25°$C and U=0 m s^{-1} for the entire domain.

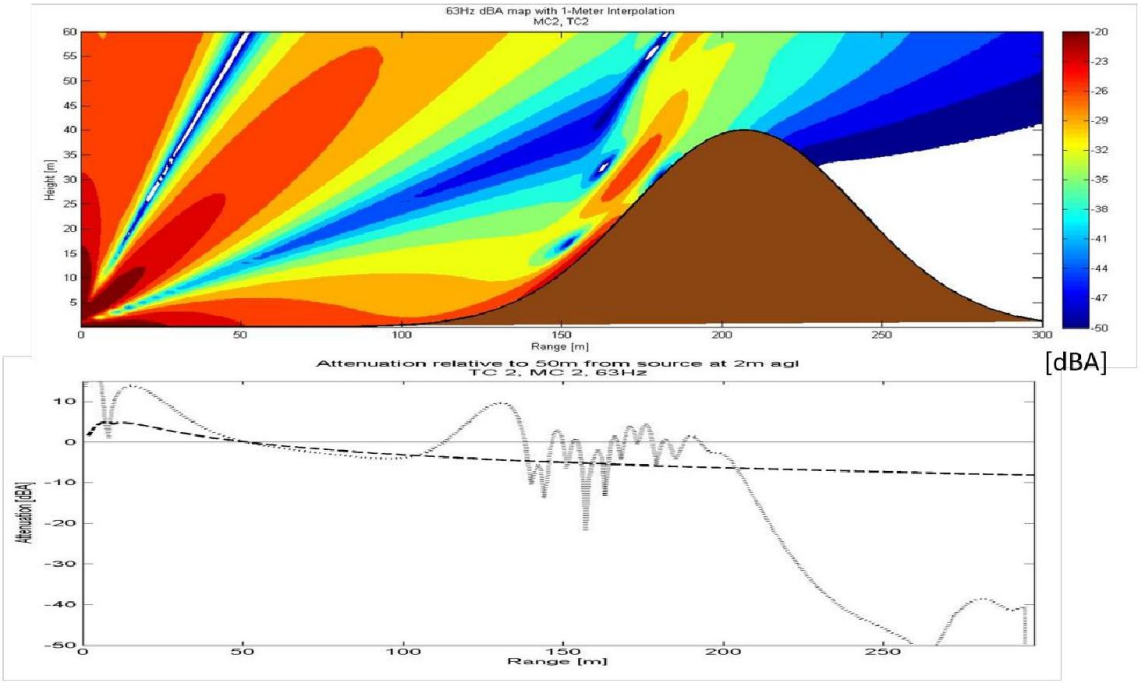

Figure 17: Gaussian hill results for 63 Hz zoomed to the lowest 60 m (top) and attenuation versus range at 2 m AGL (bottom) for the flat comparison (dashed) and with terrain (dotted).

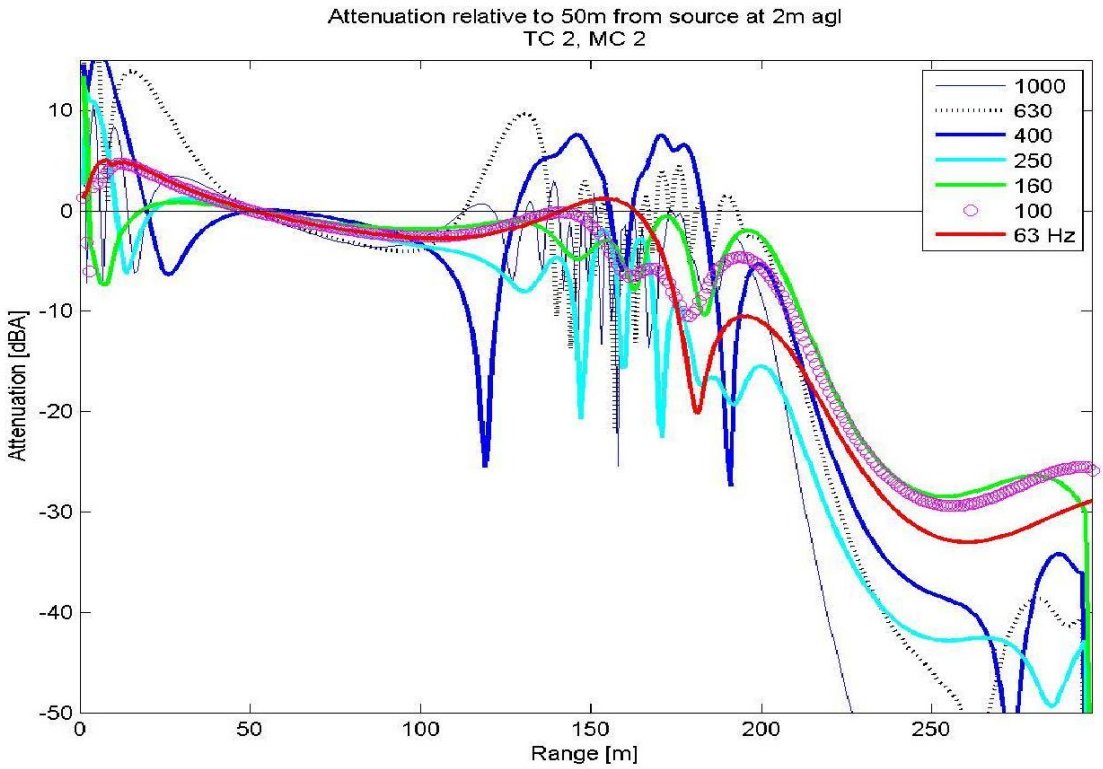

Figure 18: Gaussian hill attenuation with respect to 50 m range at 2 m AGL for select frequencies.

3.3.1.3 Comparison to Literature Benchmarks

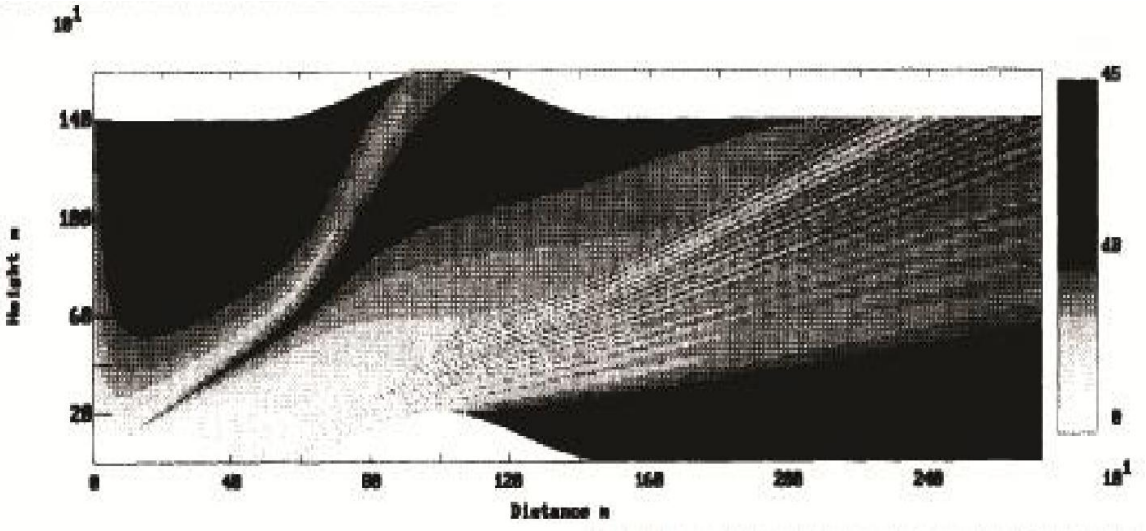

Figure 19: From R. Sack and M. West 1995 Figure 7 showing the terrain comparison given by Eq. 3.11 showing qualitative agreement with Figure 16.

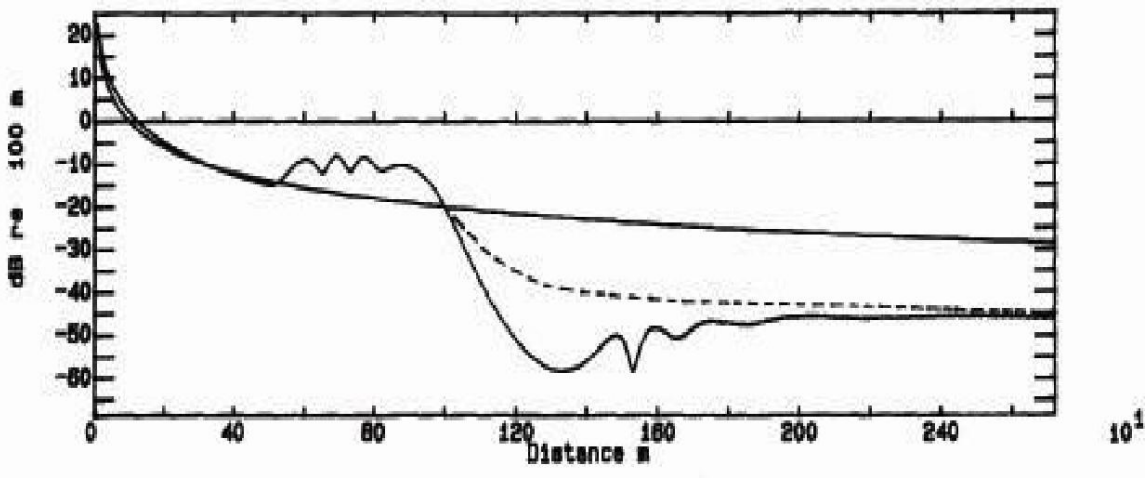

Figure 20: From R. Sack and M. West 1995 Figure 6 showing attenuation at 2 m AGL relative to 100 m from source for geometric attenuation (solid smooth) GTPE results for their terrain case (solid wiggly) using Maekawa barrier diffraction approximation (dashed).

For comparison with the Gaussian hill, we present the results from Sack and West

(1995). The terrain function used in their work is,

$$H(x) = \begin{cases} a\cos^2\left[\frac{\pi x_{top}}{W}\left(1-\frac{x}{x_{top}}\right)\right] & , \frac{W}{2} \leq x \leq W = 1[\text{km}] \\ 0 & , \text{elsewhere} \end{cases}, \tag{3.11}$$

where the hill height a = 200 m, the width W = 1 km and the center $x_{top} = 1$ km. They use a 50 Hz source at 2 m height with U=0 and T=constant. Reproduced in (Fig. 19) is Figure 7 from their work showing the resultant sound field for this case. Comparing the qualitative features with those in (Fig. 16) indicates good agreement.

3.3.2 Escarpment

To explore a terrain configuration similar to a highway canyon, a smooth escarpment was chosen. Note that we still use a scale much different from the actual cases to show the general effect of including terrain.

3.3.2.1 Model and Domain Setup

The terrain function used in this case is,

$$H(x) = .5A\left(\tanh(\frac{x-x_c}{W})+1\right), \tag{3.12}$$

where A = 10 m scales the height of the escarpment, $x_c = 30+7$ m shifts the center of the feature by 30 m plus accounting for the Green's function domain of 6.7 m (and rounding up), while the slope angle is controlled by varying W, which is set to 20 m in this case. The other model parameters are identical to the case outlined in Section 3.3.1, namely $U = 0$ m s^{-1} and $T = 25°$C, $S = 1$ and has a height of 1 m.

3.3.2.2 Model Results

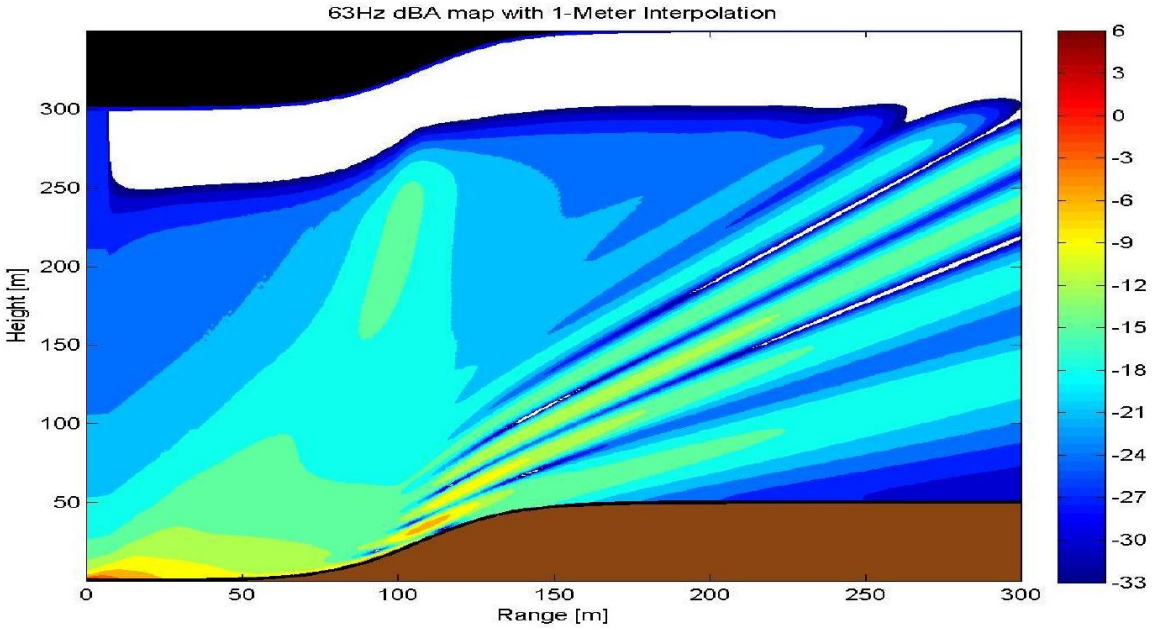

Figure 21: GTPE output for right propagating field from a 63 Hz line source of unit strength at coordinate (0,1) [m] with zero wind and uniform temperature (25 °C) interpolated onto a 1m grid.

The PE starter field is computed with a Green's function solution initialized at 6.7 m from the line source with a ground porosity representative of asphalt transitioning to hard sandy soil in the PE domain ($\sigma = 3 \times 10^7$ and 4×10^5 Pa s m^{-2}). The escarpment is defined by equation 3.12.The dimensions of the escarpment were chosen to be quite large to demonstrate the effects of terrain as a first step. A large set of values will be tested in the future. Shown in (Fig. 21) are the contours representing the attenuation from the source, shown in increments of -3dB normalized based upon the PE starting field. The brown shaded region represents ground, and along with the black shaded region, are cells outside of the computational domain. Similar to results from Section II.C.1, the diffraction pattern

from the slope along with the constructive and destructive interference patterns on the near side are quite evident. Also present is an acoustic shadow region on top of the escarpment.

Contour levels of -3dB are the attenuation one expects from geometrical spreading of a line source when doubling distance in a neutral atmosphere. As in figure 16, regions outside the computational domain are shaded black (above) and brown (ground) and white regions represent values below the minimum contour level. The Green's function starting field is present out to 6.7 m and the exponentially attenuating layer above 200 m is evident beyond 6.7 m.

3.3.3 Escarpment With Barrier

To explore the effects of placing a wall in the domain, we placed a perfectly absorbing wall by setting the forward pressure field to zero at the wall position. This allows determining the absolute best effect that placing such a wall would have on attenuating the sound field on the far side of the barrier.

3.3.3.1 Model and Domain Setup

The model configuration is the same as for Section 3.3.2 with a wall at the top of the escarpment. Keep in mind that the large scale used in the terrain configuration is intended to demonstrate the effects of the terrain. The wall was placed at $x_w = 170$ meters with a height $H_w = 25$ meters. The height was chosen to knock out the first diffracted constructive lobe pattern. The pressure field at the wall position was set to zero to obtain the best theoretical wall possible.

3.3.3.2 Model Results

The effects of placing a wall are evident in figure 22 in contrast to not having a barrier.

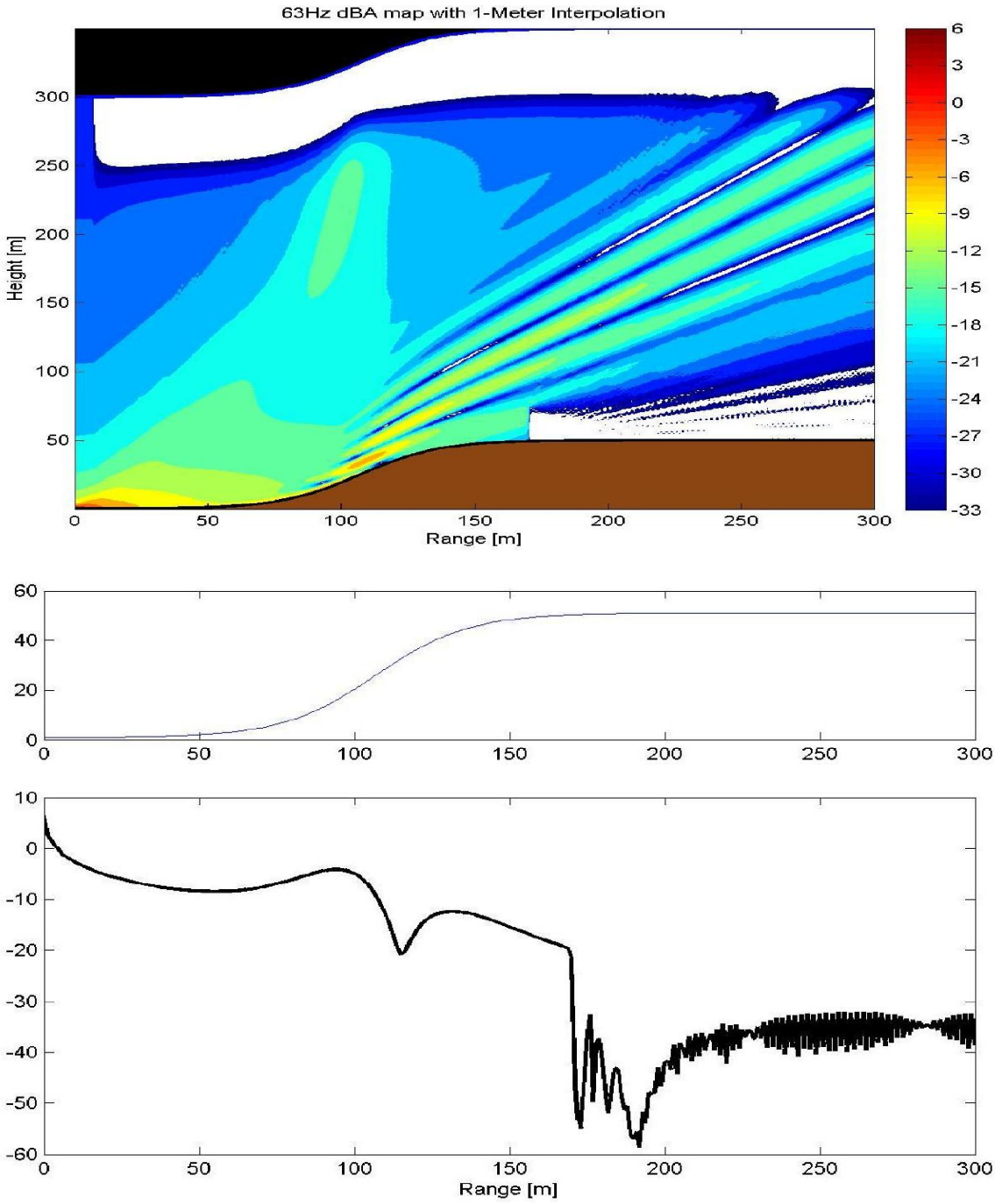

Figure 22: (Top) Same configuration as for (Fig. 21) with the additional inclusion of a 25 m high barrier with zero transmission placed 170 m from the source position. The pressures were set to zero "within" the barrier of single computational-cell width for the continuation of the PE marching loop. (Middle) The terrain profile is in meters (Bottom). The sound pressure level at 1 meter above ground level versus range.

3.3.4 Symmetric Canyon with Barrier and Reflected Field

The complex pressure field which was incident on the wall in Section 3.3.3was used in equation 3.5to compute a reflected field for the left traveling component of the total field. For this purpose, the impedance was set such that the barrier would be partially reflecting by setting $\sigma_w = 10^5$ Pa s m^{-2}.

3.3.4.1 Model and Domain Setup

The domain is identical to Section 3.3.3, only symmetric about the origin extending from -170 m to 170m, from the source. There was no change in the ground impedance to represent crossing the asphalt section as we want to focus on the reflected field in this neutral case. The starting pressure field for the GTPE model was calculated using the reflected field in equation 3.8 to the top of the wall, and set to zero above the wall to the top of the domain.

3.3.4.2 Model Results

For the left running GTPE calculation, we reverse the x coordinate and show the reflected field as starting at x = -170 m and propagating to the right, shown as attenuation relative to the initial starting field (from (Fig. 22)) in (Fig. 23). Since the outline of the contours is quite jagged, the contour filling patching algorithm could not properly render the image; thus only the contour levels without solid fill are shown. The reflected field initially decreases in intensity as the waves spread, but then begins to increase in intensity on the far side of the canyon as reflected waves superimpose constructively to refocus the

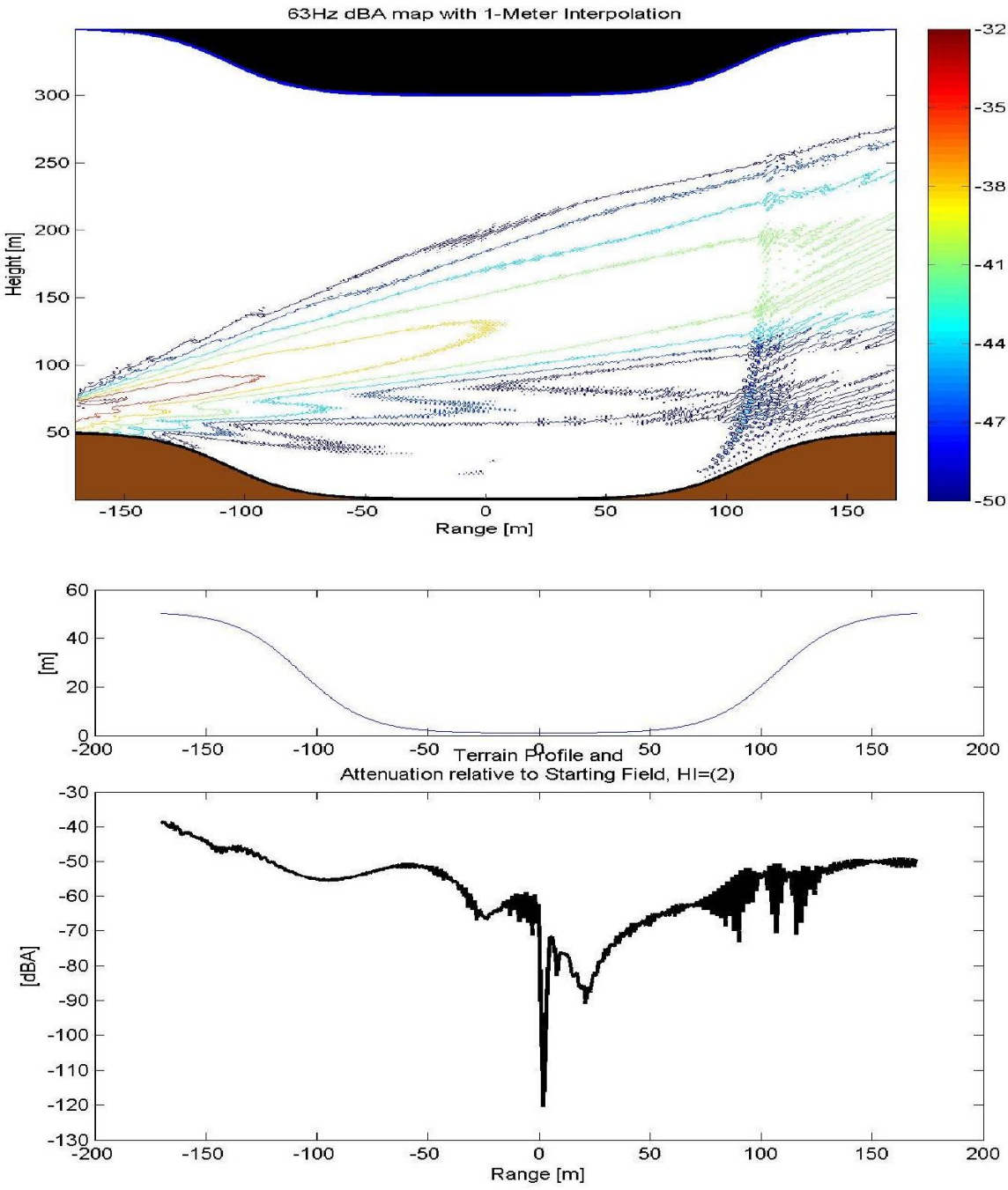

Figure 23: Same as for (Fig. 22), only showing the reflected field by reflecting the x-axis and applying the right traveling GTPE model to the starting field reflected from the barrier. Contours levels without filling due to irregular boundaries are shown. Note that the ground impedance remains that of hard sandy soil and does not account for the asphalt section from the starting field of (Fig. 22). The start and end position of the middle panel is bounded by the reflecting barriers and is symmetric about the origin. The attenuation of the bottom panel is with respect to the original starting field of (Fig. 22) and is for 1 m AGL.

acoustic energy. The net effect results in less than 10 dB attenuation to the symmetrically opposite side of the canyon (seen in the bottom of figure II.10), where at the midpoint of the canyon nearly 30 dB of attenuation along with periodic destructive interference drops, or quiet zones, was achieved. Subsequent reflections, resulting in reverberation of the sound field due to two walls in a symmetric canyon, could be calculated to determine if this trend continues with each echo.

3.4 Discussion and Conclusions

The performance of the GTPE code was demonstrated for a general Gaussian terrain bump and compared against expectations for similar terrain from Sack and West (1995). A second numerical terrain profile test case was created for a symmetric recessed canyon both with and without vertical walls placed at the top of an escarpment. Owing to smoothness constraints on the terrain function H(x) and to eliminate artificial numerical diffraction from discontinuities in H'(x), the shape of the canyon is generated with a hyperbolic tangent function (see (Fig. 22) and (Fig. 23) middle panel). A routine to determine the reflected pressure wave field from vertically oriented terrain features (e.g. noise barrier walls) was derived from the normal impedance boundary condition and incorporated into the model. Several cases were then run both without and with barriers atop the escarpment for the 63 Hz band. In the case with a barrier, the reflected field was then calculated back to a symmetrically opposing barrier. Calculating multiple reflections is now possible but first the single reflection needs to be validated. Issues were encountered using the contourf routine in Matlab, which are believed to be due to the patch algorithm that has difficulties with the irregular contour morphology. Thus, simple contour plots without solid level set filling are presented for the reflected field. Additionally, range plots at 1 meter AGL are generated for

all cases. It is difficult to justify summing the incident and reflected fields because the path lengths vary, and so the phase of each wave will be difficult to account for when computing their sum. Instead, the reflected field should be used as a guideline for understanding the intensity of the reflected field, and presented separately from the incident field. A worst case could then be constructed by summing the magnitudes of the two fields, accounting for phase by distance along the ground from the source, including reflected distances.

3.5 Future Work

In the review of Li, Franke, and Liu 1993, a method was proposed for determining the analytical prediction of sound field over a terrain with a Gaussian shaped hill in the presence of a uniform or linearly varying sound speed profile. The method substitutes a Green's function solution for the field from a line source into the Helmholtz-Kirchoff integral equation yielding an exact closed form solution. This method could be extended for the hyperbolic tangent terrain profile without barrier for comparison with the neutral cases presented herein. Literature was reviewed to find methods for benchmark comparisons and calculations of diffraction from simple terrain features. Some potentially useful publications include Gauvreau et al. 2002; Robertson 1999; Rasmussen 1985; Bowman, Senior, and Uslenghi 1987.

Additionally, a formulation was derived for calculating the backscattered field from terrain with arbitrary angle and for barriers with facades tilted slightly from vertical. The formulation is similar to that derived for vertical barrier reflection, resulting from combining the first order parabolic equation operator with the normal impedance ground boundary condition of Sack and West 1995. A numerical implementation has been outlined and will soon be implemented. Computational fluid dynamics software such as FLUENT or

WRF-LES could be utilized for generating simulated input meteorological fields for the case of flow over fine terrain features.

Chapter 4

SIMULATING METEOROLOGICAL PROFILES TO STUDY NOISE PROPAGATION FROM FREEWAYS

Accepted for publication in: *Applied Acoustics*,

S.R. Shaffer; N.C. Ovenden; H.J.S. Fernando; M. Moustaoui; A. Mahalov (Accepted, Oct. 2014).

The capability of vertical nesting in version 3.2 of the Weather Research and Forecasting model (ARW-WRF) is utilized for studies in highway noise pollution. The ARW-WRF is used to produce a limited area forecast with 1 kilometer horizontal resolution and near-ground vertical resolution finer than 20 meters for input into a sound propagation model to produce forecasts of noise pollution from a highway line segment noise source. It is shown that vertical nesting can improve the prediction of finer structures in near-ground temperature and velocity profiles, such as morning temperature inversions and low level jet-like features. Accurate representation of these features is shown to be important to modeling sound refraction phenomena and for enabling accurate noise assessment. Comparisons are made with parabolic equation model predictions using profiles derived from field experiment observations [Ovenden et al. J. Acoust. Soc. Am. **126**(1):25-35 (2009)] during mornings on November 7 and 8, 2006 in Phoenix, Arizona.

4.1 Introduction

Since early work of Reynolds Reynolds 1875a, 1875b, the importance of atmospheric structure on sound propagation is well recognisedEmbleton 1996; E. Salomons 2001. In a previous study(Ovenden, Shaffer, and Fernando 2009), hereafter OSF09, the effects of measured near-ground profiles of temperature and wind speed on sound propagation from a highway noise source were quantified and a high sensitivity to temperature and wind profiles was found. For this reason it is desirable to accurately replicate temperature and wind velocity profiles in sound propagation models using either careful measurements or detailed simulations. Simulations are applicable for future situations as a forecast (derived from observations of an initial state at the current time or a future state based on models of global change), or for previous situations using either hind-casting (derived from observations of an initial state at a previous time) or reanalysis (hind-casting combined with periodic assimilation of in-situ data). Obviously, in combining the meteorological model with an acoustic model, the mode of forecasting requires additional modeling/forecasting of the acoustic sources which is not considered here.

OSF09 used a few surface measurements coupled to Monin-Obukhov similarity theory (MOST) to derive near-surface meteorological profilesStull 1988. However, the appropriateness of such approaches to settings with varying terrain and land-cover must be viewed with caution because the theory is only suitable for flat horizontally homogeneous terrain and land-cover. Furthermore, stable conditions can lead to decoupling of the surface layer from dynamics aloft which can host rich complexity including intrusions, low level jets or katabatic/adabatic valley flows typical of cities set within mountainous terrain(Fernando 2010; Whiteman 2000). The inadequacy of Monin-Obukhov scaling in the

presence of a katabatic jet has been discussed previously as well as for flat terrain stable flowsSun et al. 2012.

A second criticism of assuming MOST for sound propagation is that it is applicable only for mean profiles and hence will not capture transient atmospheric events that may influence sound propagation even from steady sources leading to strong fluctuations in sound levels at far field locations. Such transient atmospheric events have been reported in cities such as Salt Lake City, UtahBanta et al. 2004 and Phoenix, ArizonaFernando 2010, where morningLee et al. 2003; Shaw, Doran, and Coulter 2005 and eveningBrazel et al. 2005 transitions occur during frequent high pressure/weak synoptic forcing. Similarly, coastal cities, especially with adjoining mountains such as in California, have added influences of marine intrusions in the local dirunal circulation patternsZaremba and Carroll 1999; Bao et al. 2008.

There have been scarce previous studies where real regional-scale meteorological conditions are simulated for use in near-ground acoustic models for noise pollution. Most notably, Hole and HaugeHole and Hauge 2003 predicted the influence on transmission loss of a 100 Hz source due to a temperature inversion breakup during low wind conditions. They derived vertical profiles using the Fifth-Generation NCAR / Penn State Mesoscale Model (MM5)(Grell, Dudhia, and Stauffer 1994) model, where their highest resolution domain had a 500 m horizontal grid spacing with 31 vertical levels, 6 of which being below 100 m above ground level (AGL). In the same paper, the authors explored special considerations for the influence of topographic shading on the surface energy budget and concluded that doing so improved prediction of temperature profiles in comparison with balloon-tethersonde observations. Such an improvement potentially makes such model applications for sound predictions more reliable. Other efforts focus on large-eddy

resolving scales (horizontal length scales less than 500 m) and are beyond the scope of the present manuscriptLihoreau et al. 2006.

In this paper, we employ the Weather Research and Forecasting (WRF) model, a software framework developed and currently maintained by the National Center for Atmospheric Research (NCAR)Michalakes et al. 2004; Skamarock and Klemp 2008, which is a successor to the MM5 model mentioned above. Like MM5, WRF makes use of horizontal nesting, which is a method of grid refinement wherein a child domain with increased horizontal resolution derives initial and lateral boundary conditions from a parent domain, thus making it possible to study detailed phenomena within a limited area without the computational expense of running all nests at the higher resolutionSkamarock et al. 2008. Moreover, since the release of version 3.2 in April 2010, the Advanced Research core of WRF (ARW) has the added capability of refining the vertical grid resolution within a child domain. Doing so has demonstrated the ability to resolve dynamics not present in the coarser simulations, thus more closely predicting observations for phenomena within the upper troposphere and lower stratosphereAlex Mahalov and Mohamed Moustaoui 2009; A. Mahalov and M. Moustaoui 2010; Mahalov, Moustaoui, and Grubišić 2011.

In this study, we examine the degree to which the refractive effects of actual measured wind and temperature profile can be represented by utilizing vertical nesting within ARW-WRF V3.2, in contrast to unrefined simulations, for deriving profiles below 400 m AGL. Such an investigation then enables us to judge how useful such models might be in assessing environmental noise impact from near-ground sources. A baseline configuration of WRF is used to derive vertical profiles of temperature and velocity to be used in an acoustic propagation model described in our previous paperOvenden, Shaffer, and Fernando 2009. Field experiment data and subsequent results from the original paper are then used to evaluate the simulation improvements. We perform a reanalysis of the

meteorological conditions for the November 2006 Arizona Department of Transportation (ADOT) field experiment using a 1 km horizontal grid as the finest domain. Diffraction and reflection effects from buildings are not incorporated into our models since they are not present in the meteorological code nor in the vicinity of the highway section of field experiments.

4.2 Acoustic Model

The same acoustic model is used in this paper as that presented in our previous workOvenden, Shaffer, and Fernando 2009, but using sound speed profiles derived from WRF simulations rather than observations. A brief description of the model is provided here. The two-dimensional vertical plane transverse to the highway is divided into two sub-domains: a near-field domain where refractive effects are ignored, and a far-field domain beyond. The traffic noise is represented by 17 monofrequency coherent line sources, with each frequency representing a standard one-third octave band. Within the near-field domain where a homogeneous atmosphere is assumed, a Green's function solution adapted from the work of Chandler-Wilde and HothersallChandler-Wilde and Hothersall 1995 for a line source above a horizontal plane of spatially varying acoustic impedance is used. The Green's function solution is solved to obtain a vertical profile of the acoustic pressure field at the edge of the roadway. The same virtual line source strengths and positions as derived in our previous paperOvenden, Shaffer, and Fernando 2009 were applied for each case.

The acoustic pressure profile is then used as the starting field for a wide-angle parabolic equation (PE) model that incorporates a varying vertical effective sound speed profileGilbert and White 1989; West, Gilbert, and Sack 1992. This sound speed profile used in the PE model is derived from profiles of the wind component in the direction of

propagation, $U_{\parallel}(z)$, and the potential temperature $T(z)$ in Kelvin. The effective-sound-speed profile is then given by,

$$C_{\text{eff}}(z) = \sqrt{\gamma R T(z)} + U_{\parallel}(z), \tag{4.1}$$

where γ is the ratio of specific heats, and R is the gas constant. The first term in Equation 4.1 is the adiabatic sound speed, C_{ad}, and the second term accounts for motion of the medium in the direction of propagation. A key assumption within the PE model is that the medium is stationary, which this form of C_{eff} enables. Within the PE model, a Crank-Nicholson scheme is used to march the starting acoustic field horizontally out to the far-field and an exponentially attenuating layer at the top third of the domain, combined with the Sommerfeld radiation conditionWest, Gilbert, and Sack 1992; K. Attenborough 2002; E. M. Salomons 1998, is applied to prevent artificial numerically reflected waves.

The ground boundary condition is represented by the Delany and Bazley impedance modelDelany and Bazley 1970 with flow resistivities representative of asphalt ($\sigma = 3 \times 10^7$ Pa s m^{-2}) for the near-field ray domain, and hard sandy soil ($\sigma = 4 \times 10^5$ Pa s m^{-2}) for the PE domain. The PE model is run for each single one-third octave band. Stability and accuracy of the PE model requires 10 points per wavelength, so high frequencies become costly to compute. However, only 17 bands are needed since each frequency's contribution to the sound pressure level is A-weightedOvenden, Shaffer, and Fernando 2009. Acoustic model output for each frequency band is then interpolated onto a uniform 0.25 m by 0.25 m grid and summed in the usual fashion to obtain an overall A-weighted sound pressure level.

	Observational Periods		
Case	Date	Local Time (MST)	Remarks on Profiles
A	7 Nov 2006	1040 to 1100	Shear aloft, little stratification
B	7 Nov 2006	0740 to 0800	Shear , stratified
C	8 Nov 2006	0740 to 0800	Shear and cross-wind jet, stratified

Table 1: Specific cases used from OSF09. Note: MST=UTC-7 and the sunrise/set times for these dates was 0653/1730 MST. See timeline in Figure 1c.

4.3 WRF Numerical Experiment

4.3.1 Study Domain of Coupled Acoustic Model

The vertical profiles derived from the WRF simulation were evaluated against those taken during the previous field experiments on freeway noise propagation during morning transitionOvenden, Shaffer, and Fernando 2009 conducted during the morning hours of November 7 and 8, 2006 along the Phoenix Loop 202 highway in Mesa, Arizona near coordinates 33.48240°N, 111.76338°W; the exact location is highlighted in Figure 2 (discussed in Section 4.3.3). Instruments deployed included microphones, SOund Detection And Ranging (SODAR) with Radio Acoustic Sounding System (RASS), and sonic anemometers positioned on one meteorological tower and two tripods. Three cases in the observational dataset were selected in the previous paper because they exemplified varying levels of shear and stratification and these are specified in Table 1. The measured wind and temperature profiles obtained in these cases are compared here to profiles computed using WRF in terms of their impact on long-range noise propagation.

4.3.2 WRF Model Configuration

As noted previously, for applications such as highway acoustics studies, we seek to produce vertical profiles of temperature and horizontal velocity in the lowest 400 m above ground with resolution sufficient to contain salient features necessary for deriving representative acoustic fields. Towards this goal, we use nested simulations with initial resolutions finer than what is typically used for real-time forecasting. The benefit of using a new method of vertical refinement of a child domain, described below, is investigated here. Such refinement is adopted as opposed to increasing near-surface resolution because increasing near-surface resolution adds extra model levels to all domains. Four telescoping nested domains, shown in Figure 1a and Figure 1b, centered near Phoenix Arizona, at coordinates 33.45 °N, 112.074 °W, with horizontal grid resolutions of 27, 9, 3 and 1 km were used. The model top is set to 50 mbar (≈20 km MSL).

The vertical coordinate used in ARW-WRF is based on terrain-following hydrostatic-pressure and levels are non-uniformly distributed, being more closely spaced near the model bottom and top. We test refinement of vertical resolution applied for the fourth nest which has 1 km horizontal resolution, from a modest 27 initial vertical levels (domain d04) to 81 (domain d04R). One-way vertical refinement is achieved with the WRF program `ndown.exe` for a vertical refinement factor of 3, which subdivides each initial vertical level spacing while satisfying smoothness of pressureAlex Mahalov and Mohamed Moustaoui 2009. The schematic in Figure 1c illustrates how the refined nest derives lateral boundary conditions from hourly output of the 3 km domain, and was also nested in time by 12 h to allow sufficient spin-up of the parent domains (Skamarock 2004). An unrefined 1 km nested domain was used as a control, being initialized in a similar fashion except it had the vertical refinement factor set to 1.

The simulations are for a 66 h period, initialized using the 1° 6 h Final Operational Global Analysis (FNL) data product from the National Center for Environmental Prediction (NCEP)NCEP beginning at 06:00 UTC on November 6th 2006, as shown in the timeline schematic in Figure 1c. This allows a 20 h spin-up time before the first observational period (OP-1) of the field experiment for the refined nest, which is nested in time by 12 h from the model initialization of the outer three domains. Two-way feedback was used between the first three nests, which were run in concurrent mode. Hourly output was recorded for the entire period, with 5 min output for the 3 km and 1 km domains. The first domain used a 135 s timestep and a parent-to-child timestep ratio of 1:3 was used for all except the 1 km domain, where increased resolution necessitated a 4 s timestep due to Courant number stability constraints Skamarock et al. 2008. The 4 s timestep was also used in the control domain.

All of the model parameterizations were held fixed to the following settings. Physical processes involving moisture were modeled using the WRF single-moment microphysics 3-class scheme (Hong, Dudhia, and Chen 2004). Standard radiation schemes of (RRTM) long-wave (Mlawer et al. 1997) and Dudhia short-wave (Dudhia 1989) were called every 9, 3, 1 and 1 min for domains d01 through d04, respectively. The Kain-Fritsch cumulus parameterization for unresolved convective processes (Kain 2004) was used only for the outer domain, being called every 5 min. We use 5th (3rd) order horizontal (vertical) advection methods. The split-step scheme uses 4 acoustic timesteps per model timestep for each domain(Wicker and Skamarock 2002; Klemp, Skamarock, and Dudhia 2007). The base temperature was set to 300 K and the non-hydrostatic option was used with no vertical damping imposed.

The geographic land-use classifications and terrain elevations were obtained from the U.S. Geological Survey (USGS) 24-category 30° resolution data supplied with the

standard WRF Preprocessing System (WPS) V3.2. The legacy MM5 5-layer thermal diffusion land surface model(Grell, Dudhia, and Stauffer 1994) was employed to represent ground temperature response to solar forcing. The coupling between the ground and the atmosphere was parameterized by the MM5 surface layer similarity scheme, which is a form of MOST applied to the first model level, and is connected to the Yonsei University planetary boundary layer (YSU-PBL) scheme(Hong, Noh, and Dudhia 2006). The YSU PBL scheme is a non-local method of turbulence closure and handles the vertical mixing due to unresolved eddies. Horizontally, a 2nd-order diffusion parametrization for turbulence and mixing and a horizontal Smagorinsky 1st order closure scheme are implemented to account for subgrid processes.

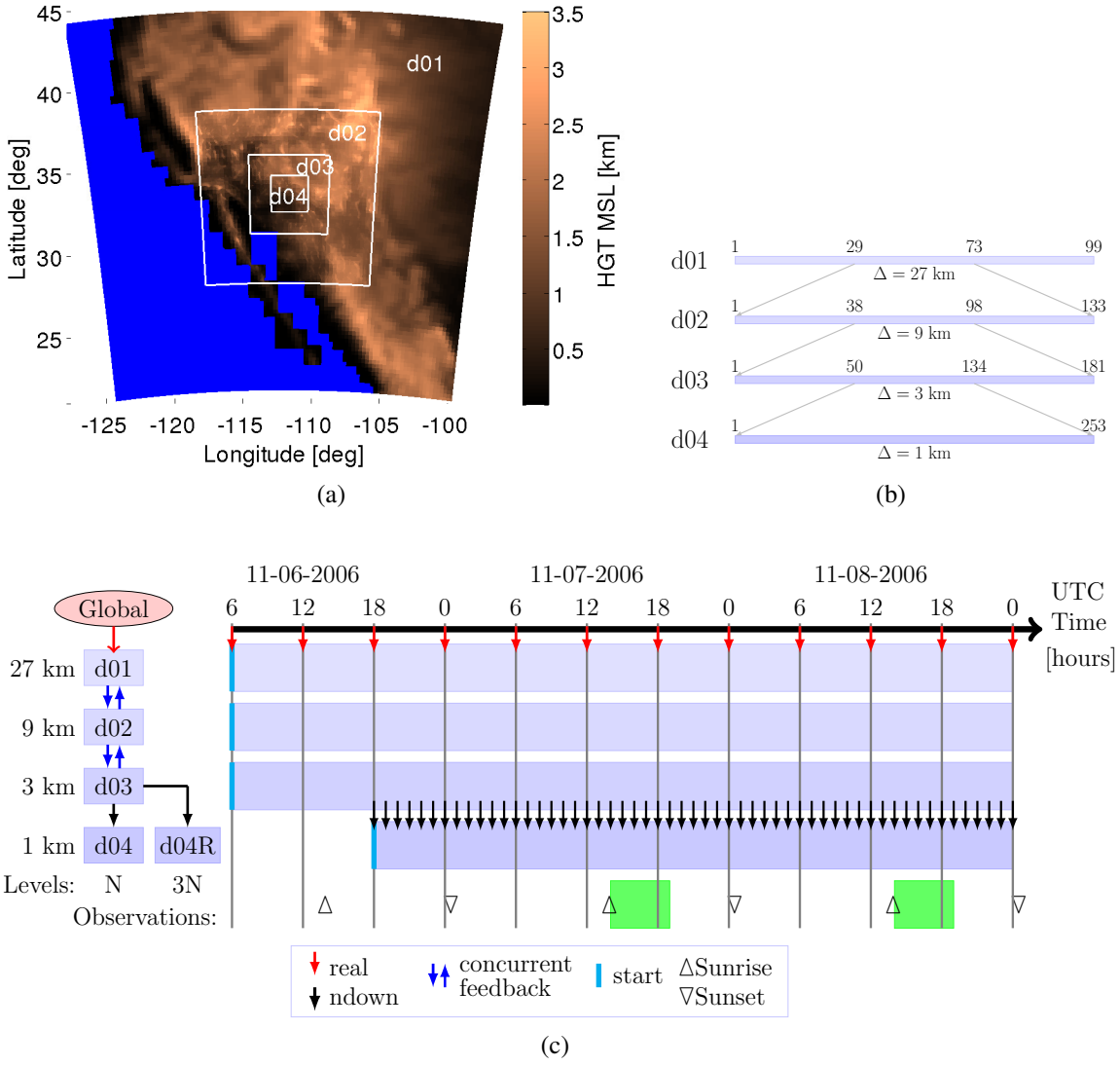

Figure 24: Schematic of WRF Model Domain: (a) Map of terrain height km MSL showing outer perimeter of 4 telescoping nests centered on Phoenix, Arizona. (b) Schematic of nesting by staggered horizontal grid index with nest label d0X, X=1-4, and horizontal grid spacing in km. (c) Schematic of nesting feedback, parent data source, method of nesting and refinement of vertical levels, with corresponding timeline schematic for each nest depicting lateral boundary update and nest initialization times along with observational periods (shaded).

4.3.3 WRF Profile Selection and Coupling With Acoustic Model

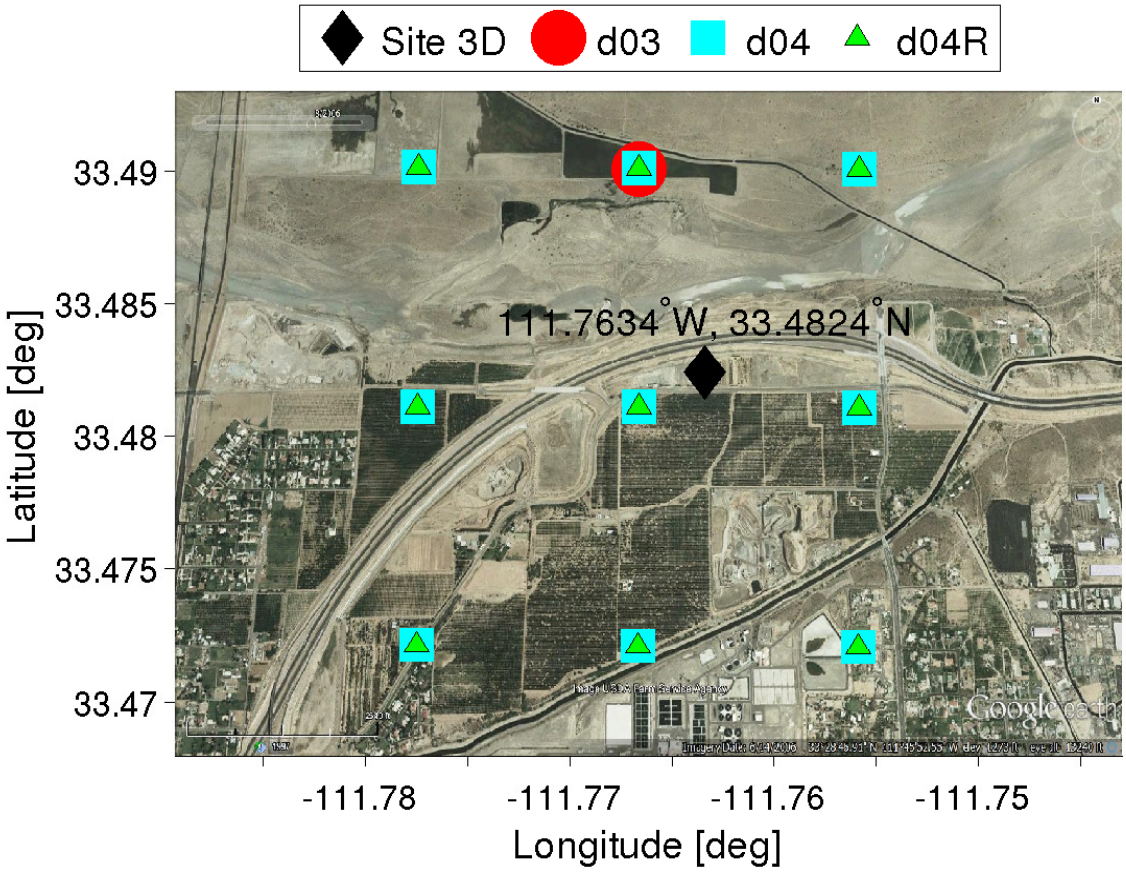

Figure 25: Google Earth image (circa 6/2006) near approximate site location (diamond) and ensemble of WRF Arakawa-C grid cell center locations used in analysis for 3 km (d03, circle), and 1 km (d04, squares; d04R, triangles) horizontal resolution domains.

The ARW-WRF model uses an Arakawa-C grid where scalar variables are at grid cell centers, and vector variable components are on a staggered grid at cell faces. Scalars (e.g. temperature), and horizontal vector components, are at the half-mass level (hereafter level), one-half of the full-mass level (around 60 m for 27 vertical levels). Values at grid centers are interpreted as representative of the cell volume average. Thus, unstaggered

velocities at the grid centers are obtained by a simple arithmetic average between adjacent cell faces.

Shown in Figure 2 are the WRF computational domain non-staggered Arakawa-C grid (cell center) coordinates for the 3 and 1 km domains in the neighborhood of the observational site location used in our analysis. These coordinates are overlaid on a historical Google Earth image to illustrate the land use for the study area near the date of the study. Based upon these grid locations and with the highway running primarily East-West, profiles of potential temperature and the V velocity component (positive to north) are extracted to generate the input $C_{\text{eff}}(z)$ profiles used in the PE model for propagation transverse to the highway. As the field experiment in our previous paperOvenden, Shaffer, and Fernando 2009 typically measured crosswinds from the North and examined downwind impacts, we will look here also at propagation downwind only.

In constructing profiles for the acoustic model, we examine each location in latitude-longitude and time separately. Doing so enables us to check for phase offsets in the timing or localization of phenomena such as low-level jet-like features. In order to directly compare the profiles derived from WRF with the 20 min time-averaged profiles from experimental observationsOvenden, Shaffer, and Fernando 2009, an ensemble of representative profiles from the model domain near the observational site was built by using model output at 5 min intervals during the 20 min observational period on the de-staggered 1 km grid points close to the site, as shown in Figure 2. This is intended to capture both the mean profile shape and to estimate variance in the derived profiles.

Profiles are derived using the geopotential height, given by,

$$z = \frac{\phi}{g} - h, \tag{4.2}$$

where the height above ground level, z, is related to the surface elevation h, gravitational

acceleration $g = 9.81$ m s^{-2}, and the geopotential, ϕ. The model-level temperature values were obtained by,

$$T = \theta \left(\frac{P}{P_0} \right)^{R/c_p}, \tag{4.3}$$

where $\theta = \theta' + \bar{\theta}$ is potential temperature with base value $\bar{\theta} = 300$ K, and prognostic perturbation value θ'. P is total atmospheric pressure, $P_0 = 10^5$ Pa is a reference pressure, and R/c_p is the ratio of the gas constant, $R = 8.3144$ J mol^{-1} K^{-1}, to the specific heat at constant pressure for dry air, $c_p = 29.07$ J mol^{-1} K^{-1}.

The WRF model considers the surface layer as a constant-flux layer linking the land-surface and the first model level, employing similarity theory to obtain diagnostic quantities based upon surface fluxesKlemp, Skamarock, and Dudhia 2007. To allow a fair comparison with the previous method to derive profiles between measurements near-surface and aloftOvenden, Shaffer, and Fernando 2009, we likewise combine the WRF diagnostic 2 m temperature, T_2, and diagnostic 10 m northward wind velocity component, V_{10}, with model level values. The near-ground theoretical wind and temperature profiles, along with prognostic model-level values, are then interpolated for input into the acoustic model using a monotonic cubic spline to a 0.25 m resolution below 10 m and a 2 m resolution above. The acoustic model then subsequently interpolates further for each frequency band to the requisite grid spacing of ten-points per wavelength.

The temperature profile is constructed by holding the value below 2 m constant at T_2, and a linear fit is used to interpolate from 2 m to the lowest model level, z_1. A near-ground logarithmic wind profile was constructed (Stull 1988) of the form,

$$V(z) = \mathrm{sgn}(V_0) \frac{u^*}{\kappa} \log \left(\frac{z}{z_0} \right) + V_0, \tag{4.4}$$

with V_0 based on either $V(z_1)$, or V_{10}, depending on the position of the first level z_1 in the simulation via the following rule:

$$\begin{array}{lll} \text{if } z_1 < 15 \text{ [m]} & V_0 = V(z_1) & , \quad z_0 = z_1 \\ \text{else} & V_0 = V_{10} & , \quad z_0 = 10 \text{ [m]}. \end{array}$$

Here, $\kappa = 0.4$ is the Von Karman constant, u^* the friction velocity, z_0 represents the surface model roughness length, and $\text{sgn}(V_0) = V_0/|V_0|$ ensures that the profile is in the correct direction. Since $\log(z_{\text{sfc}}/z_0)$ diverges as $z_{\text{sfc}} \to 0$, we restrict derived velocity profiles from reversing direction near the ground. This restriction is achieved by setting $V(\tilde{z}) = 0$ for $0 \leq \tilde{z} \leq z_0 10^{-|V_0|\kappa/u^*}$.

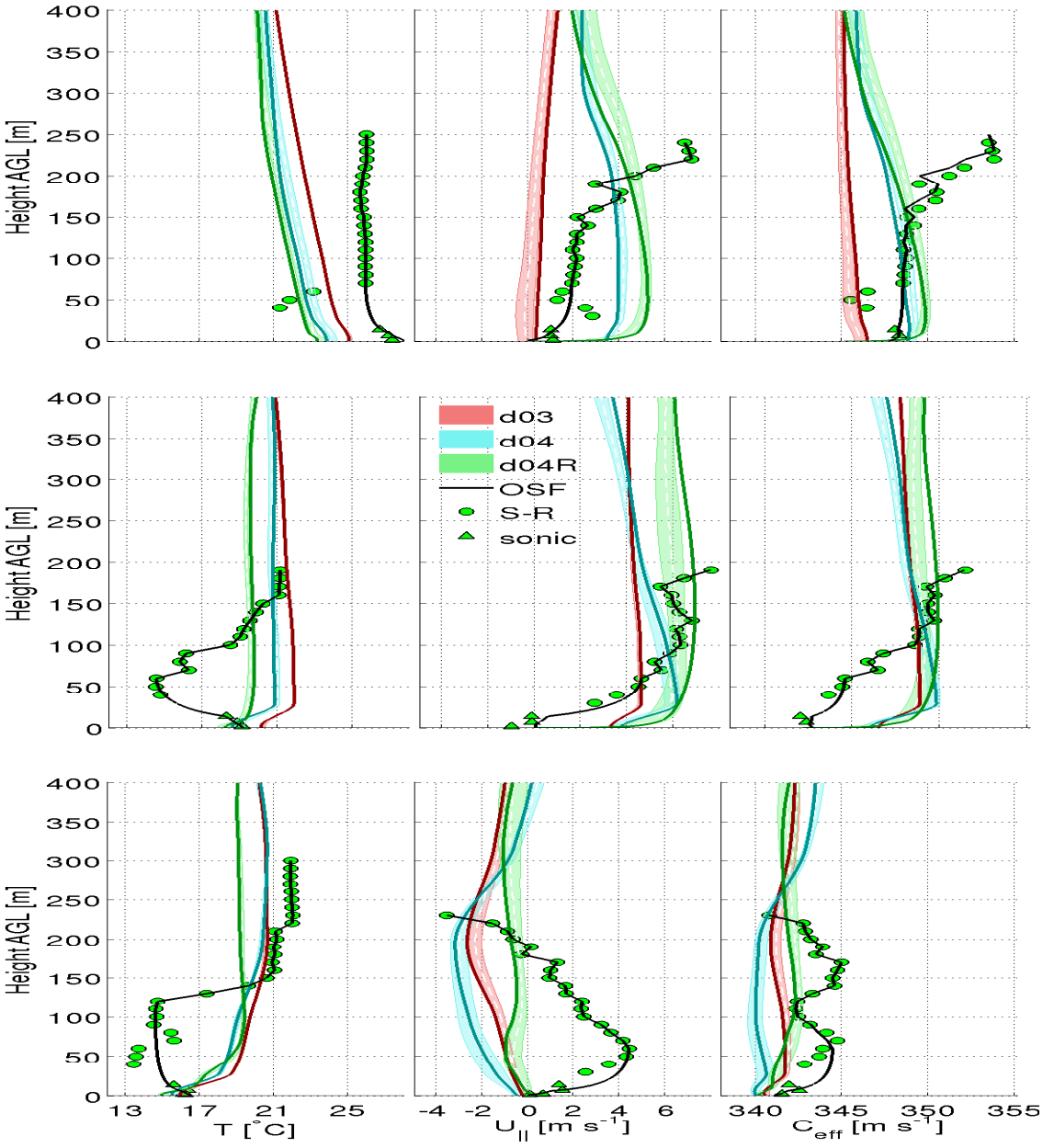

Figure 26: Ensemble of derived WRF profiles of temperature (left column), velocity component parallel to propagation direction (middle column), and effective sound speed (right column), for OSF09 case A (top row), case B (middle row), and case C (bottom row). Shown are curves for domains d03 (red), d04 (cyan), and d04R (blue), at the beginning of the respective observational period at closest site location, and mean (white dashed) with ± 1 standard deviation (shaded) for the ensemble over all 5-minute output times at locations shown in Figure 2 during each case. The green circles and triangles are SODAR-RASS and sonic anemometer observations, respectively, with the black curves being the respective OSF09 theoretical profiles derived from observations.

4.4 Methods of Analysis of Acoustic Model Predictions

The spectral components for each one-third octave frequency band f_n, are defined by,

$$L_{A,f_n}(x,z) = 10\log_{10}(.5|p(x,z)|^2) + 20\log_{10} S_{0,f_n}, \tag{4.5}$$

for acoustic pressure $p(x,z)$ with a virtual source strength given by S_{0,f_n}. Since the observed values used within the optimization procedure described in our previous workOvenden, Shaffer, and Fernando 2009 were A-weighted, so will be the source strengths and resultant spectral components. The L_{A,f_n} results for all frequency bands are then interpolated onto a uniform grid (which here has a spacing of .25 m) and combined to obtain the A-weighted sound pressure level (SPL) given by,

$$L_{eq} = 10\log_{10} \sum_{n=1}^{17} 10^{L_{A,f_n}/10}, \tag{4.6}$$

for the 17 standard one-third octave bands between 63 Hz and 2500 Hz, inclusive.

For a quantative analysis of the influence of different effective sound speed profiles $C_{\text{eff},j}$, we examine the relative SPL with respect to the point $x_0 = 50$ m range at $z = 1$ m AGL, defined for an ensemble of profiles indexed by j as,

$$\Delta L_j(x, z = 1) = L_{eq,j}(x, z = 1) - L_{eq,j}(x = x_0, z = 1). \tag{4.7}$$

Furthermore, PE results for equivalent stationary homogeneous (non-refracting) atmosphere cases, wherein the vertical profiles of crosswind velocity and temperature are set to zero and the ground value, respectively, are used to correct for each ensemble member having different baseline sound speeds. For non-refracting cases the L_{eq} value decays due to geometrical spreading proportional to inverse distance, $L_{eq} \propto x^{-1}$, for a line source. The equivalent relative SPL in the non-refracting atmospheric case (superscript N) can be

written as,

$$\Delta L^N = a(x^{-1} - x_0^{-1}). \tag{4.8}$$

The coefficient, a, will only depend upon the ground-level sound speed (or reference Helmholtz number) for each non-refracting case, which is explicitly denoted by $a = a(C_{0,j})$. Thus, the non-refracting case relative SPL between an ensemble member (subscript j) with respect to an arbitrary reference ensemble member (subscript r), are related by,

$$\frac{\Delta L_r^N}{\Delta L_j^N} = \frac{a(C_{0,r})}{a(C_{0,j})}. \tag{4.9}$$

This non-refracting case relationship enables a fair direct comparison of the relative SPL for an ensemble member, subscript j, with respect to an arbitrary reference member, r, viz,

$$\Delta L_{j,r} = \frac{\Delta L_r^N}{\Delta L_j^N} \Delta L_j, \tag{4.10}$$

arising from PE model predictions using different input $C_{\text{eff},j}$ profiles.

4.5 Results

4.5.1 Influence of Horizontal and Vertical Nest Resolution on Simulated Meteorological Profile Features

Firstly we present the vertical profiles of temperature (T), wind component parallel with propagation direction ($U_{\|} = -V$), and effective sound speed (C_{eff}), derived from WRF and used for input into the acoustic model. These profiles are shown in Figure 3 for OSF09 cases A, B and C, with main features distinguishing observed profile cases summarized in Table 1. The instantaneous profile at the first time of WRF output during the 20 min interval at the nearest horizontal grid location (see Figure 2), which will be employed in later

OSF case	d0X	T °C	U m s^{-2}	V m s^{-2}	$\lvert U_H \rvert$ m s^{-2}	C_{eff} m s^{-2}	ΔL dB(A)
A	3	2.4	6.7	2.3	5.8	3.6	-
A	4	3.3	4.2	1.9	4.0	1.0	4.6
A	4R	3.9	3.0	2.8	2.6	1.1	5.5
B	3	4.1	6.4	1.8	4.9	2.6	-
B	4	3.5	4.6	1.6	3.3	2.9	9.9
B	4R	2.7	1.9	1.5	0.9	2.7	7.9
C	3	3.6	2.5	3.9	2.5	2.3	-
C	4	3.1	3.0	5.0	2.4	3.7	10.7
C	4R	3.4	3.5	3.1	4.2	1.8	4.6

Table 2: RMSE values of profiles for T, V $(= -U_{\|})$, and C_{eff}, shown in Figure 3, using interpolated profiles at 10 m AGL and between 40 m and 190 m AGL at 10 m increments (valid SODAR-RASS levels for all cases), between observations and ensemble mean for each domain, grouped by OSF09 meteorological case. Also for Eastward velocity component (U) and horizontal wind magnitude ($|U_H|$). For relative SPL (ΔL) using the ensemble mean of curves shown in Figure 10 over the entire 600 m range.

examples of acoustic model output, is also shown for each of the domains d03, d04 and d04R.

Additionally, the ensemble spreads (± 1 standard deviation) are shown in Figure 3 as shaded regions for each domain, where the ensemble consists of all 5 min output of instantaneous realizations at profile locations indicated in Figure 2 during the 20 min interval. Each ensemble represents the same spatial and temporal footprint between the different resolution simulation domains, and enables evaluation of spatial and temporal phase errors for a given ensemble member with respect to a representative mean profile within the site neighborhood during the observation period. For comparison, 20 min averaged SODAR-RASS and sonic anemometer observed data obtained from the original experimentsOvenden, Shaffer, and Fernando 2009 are also plotted, along with the OSF09 theoretical curves.

Root-mean square errors (RMSE)Willmott et al. 1985 were derived between each ensemble mean profile and the corresponding OSF09 profile, by interpolating to 10 m height and 10 m increments from 40 m height to 190 m height (limit of SODAR observations), which are summarized in Table 2. Also given in Table 2 are the RMSE values at these same heights for the U velocity component (positive to east) which is perpendicular to the PE model propagation direction and so is not used within the C_{eff} profile, and horizontal wind magnitude $|U_h| = (U^2 + V^2)^{1/2}$. These additional terms enable assessing for wind direction errors within the entire profile, when RMSE for $|U_h|$ is smaller than for each component.

Case A in Figure 3 (top), at 1040 MST (3 h after sunrise), observations show that an unstable layer has formed in the lowest 300 m, with wind shear only present above 150 m. An underprediction bias for all domains is present in predicted temperature, with a 2.4 °C RMSE at 3 km, and larger for the 1 km domains. The V-component winds were underpredicted in the 3 km simulation but overpredicted at 1 km resolution up to the observed shear layer at 150 m, with no corresponding increase in predicted wind speed above 150 m. Meanwhile, horizontal wind magnitude error was reduced at 1 km compared to 3 km resolution, and further reduced by vertical refinement. Also, d04R wind component RMSE values indicate a direction bias. The bias error in constituent terms of C_{eff} partially cancel when constructing profiles, which show reduced RMSE for both 1 km domains compared to 3 km.

For case B in Figure 3 (middle), observations indicate a temperature inversion, warming by nearly 7 °C from 60 m to 160 m AGL, also with a warm surface creating an unstable layer up to $\approx$ 100 m AGL. Wind shear is also present in the same height range, with $U_{\|}$ rising to 6 m s^{-1} at 100 m AGL. The diagnostic 2 m values are all within 2 °C of observations, and better represented at 1 km than at 3 km. However, the lowest prognostic

values all have considerable error below 100 m AGL, failing to capture the observed temperature inversion.

For all domains, the observed temperature variations for the lowest RASS range gates are not well reproduced, with overprediction bias of ≈ 4.5 °C at 50 m AGL for d04R, and increasing bias for coarser resolution domains. Furthermore, the presence of any near-ground temperature inversion in the derived profiles for the unrefined domains is due to the fit between T_2 and $T(z_1)$, which could change with bias in either component. The vertically refined profiles, however, indicate an inversion but not at the same height or magnitude as in observations, and only with the lowest few model levels.

Agreement for $U_{\|}$ between WRF and observed profiles is not encouraging. The d04R $U_{\|}$ profile has closest agreement with observations, showing a gradual shear, whereas $U_{\|}$ derived from d04 has a kink where the profile interpolated from the 10 m value meets the first model level. The $U_{\|}$ RMSE values are comparable for all domains, being between 1.5-1.8 m s^{-1}. The RMSE values also indicate directional errors, where d04R performed best in terms of both reduced errors for wind components and wind speed. However, these profiles combine to produce an incorrect C_{eff} profile below 100 m AGL for all domains.

Case C in Figure 3 (bottom) seems to yield the worst reproduced simulated profiles. The temperature in case C seems quite well reproduced only between 150-210 m AGL for both the unrefined 1 km and 3 km domains. Yet, observations indicate a nearly 6 °C temperature change within the 30 m just below this height, which is not captured at all by the model. The modeled 2 m values are within 1 °C, but then the model exhibits a low inversion of 4 °C over 50 m, then a more gradual inversion of 2-3 °C over the next 150 m, rather than being unstable for the first 140 m followed the aforementioned strong inversion. The observations of $U_{\|}$ indicate a 4.5 m s^{-1} jet with local maxima near a height of 50 m. However, all domains indicate flow in the opposite direction for this velocity component,

with a weak -1 m s^{-1} local maxima in d04R near this height, whereas d04 indicates a local maxima nearly -3 m s^{-1} at 200 m AGL. Furthermore, the observations indicate a reversing of direction above 200 m, coincident with the temperature inversion height range, with speeds approaching -4 m s^{-1} at the limit of the SODAR profile.

4.5.2 Influence of Increasing Vertical Resolution of Meteorological Simulation on Predicted Freeway Noise Propagation

While the analysis of simulating meteorological profiles considered model grid cells in the observational site neighborhood for a stencil with side of 3 km, at each 5 min output during the 20 min period, we now restrict to just the model grid cell containing the site location for each output time. One ensemble member of each meteorological case is shown for the L_{A,f_n} and L_{eq} plots, and the entire ensemble is shown for the ΔL plots. The acoustic model results presented here use the same acoustic source heights and strengths and same propagation model as for the respective cases in OSF09, but the vertical effective sound speed, C_{eff}, is now obtained from the WRF derived profiles for the unrefined and refined 4th WRF domain discussed above (Figure 3). Comparisons are made with the propagation results obtained using experimentally observed profilesOvenden, Shaffer, and Fernando 2009. No atmospheric absorption has been applied to these results.

Individual spectral contributions to SPL at 1 m above the ground versus range, $L_{A,f_n}(x, z = 1\text{m})$, following Equation 4.5, are shown in Figure 4 to Figure 6. With the the total SPL against range and vertical height up to 50 m AGL, $L_{eq}(x,z)$, following Equation 4.6, shown in Figure 7 to Figure 9. The noise abatement criteria threshold value of 67 dBA is emphasized by a change from red to blue contours. The relative SPL, ΔL, following Equation 4.10, is shown in Figure 10 for each case A-C. RMSE results for ΔL are also given

in Table 2 for the entire 600 m range between observations and ensemble mean of 1 km domain predictions without and with vertical refinement.

4.5.2.1 Case A

In case A, since the temperature profiles for the 4th domains are similar, the main differences in outcome will be produced by variations between the velocity profiles. The refined domain's wind profile is somewhat stronger with more shear near the ground. This aspect in the C_{eff} profile leads to ducting close to the ground, most apparent at 500 Hz and above, with multiple loud and quiet interference extrema at the 1 m analysis height.

The L_{eq} in this case fits the experimental observations more closely, and remains above 67 dBA close to the ground up to a range of approximately 300 m, similar to case A in our previous workOvenden, Shaffer, and Fernando 2009. It is unclear if the upward refracting behavior above 150 m in C_{eff}, which is not as pronounced as in the unrefined domain, leads to the reduction in L_{eq} beyond 300 m. Whereas the weaker shear, yet still slightly downward refracting C_{eff} for the unrefined domain, leads to sound focussing around 500 m range. Here, levels exceed 67 dBA, mostly due to contributions from the octave bands between 100-250 Hz, and above 1 kHz.

The aforementioned role of refinement is also manifested within the ΔL. The unrefined domain's values decay with range to a minimum around 300 m range at 12 dBA below 50 m range, before returning to just 5 dBA loss at 600 m range. However, the refined domain displays an irregular and more gradual decay, yet still at a faster rate than for the observed profile. Yet, the RMSE statistic indicates that overall, the unrefined domain performed with nearly 1 dBA reduced error over the refined domain.

4.5.2.2 Case B

For case B, the near-ground shear and inversion were both seen to contribute to downward refraction within the C_{eff} profiles for each domain below 100 m AGL. Based upon standard deviations of ensemble means, there is little difference between C_{eff} profiles for these domains. However, We interpret the resultant near-ground acoustic field differences as being due to the inter-domain C_{eff} variations below 100 m AGL between specific ensemble members. In particular, the fit to the lowest model level in d04R (at $\approx$ 10 m AGL), provides a stronger low-level wind shear than within d04, and creates stronger near-ground ducting of sound, with 500-1000 Hz bands again remaining dominant to larger ranges as in Case A. There is then a more gradual increase in the d04R C_{eff} profile up to $\approx$ 100 m AGL. Whereas, the C_{eff} for d04 peaks near the first model level ($\approx$30 m), with a similar gradient, but more elevated and sustained than in d04R.

These C_{eff} features leads to a near-ground quiet zone centered just after 300 m range before the SPL rises to well above 67 dBA. While this larger scale ducting continues to 600 m range, a smaller scale ducting closer to the ground is apparent in frequencies above 500 Hz after the first near-ground maxima. The decreasing proximity of maxima for higher frequencies supports an interference effect from the ducting by the C_{eff} gradient. Meanwhile, frequency-dependent ground impedance would tend to differentially attenuate the reflected wave amplitude by frequency band, emphasizing the importance of the ground impedance model.

The ΔL for d04 shows that the locations of near-ground maxima are sensitive to the ensemble-member variability, while the higher frequency ducting beyond 300 m range is responsible for the spread in ΔL between ensemble members. Indeed, the unrefined sound field has two near ground constructive maxima in SPL in the first 600 m from the source

whereas the original results based on experimental observations only produces one focusing just before 600 m. The less severe shear and lack of any strong inversion in d04R produces down range ΔL similar to that observed in case A, with 2 dBA better overall RMSE compared to d04.

4.5.2.3 Case C

For case C, all of the WRF-derived T profiles indicate downward refraction below 70 m AGL, whereas $U_{||}$ would cause upward refraction, aside from d04R from 70-130 m AGL. These aspects combine within C_{eff} indicating that below 30 m AGL, both d04 and d04R refract downwards, with d04R having a much stronger gradient in C_{eff} in the lowest 10 m AGL. Suggesting that the method to interpolate between near-ground and first model level values, along with any bias in either value, plays a significant role. From 30 m AGL to around 100 m AGL, C_{eff} profiles indicate that d04 will refract upward whilst d04R refracts downward. The observed profiles, however, show that the wind speed should be causing substantial downward refraction below 50 m, whereas, the unstable temperature profile below 130 m AGL would cause upward refraction below 50 m AGL and otherwise be non-refracting. This scenario is reversed aloft with a second ducting region apparent in C_{eff} between 50-150 m AGL. Here, the strong temperature inversion causes downward refraction from above, and the upper half of a low-level jet causes upward refraction from below.

The spectra and ΔL both indicate near-ground ducting, but with much more gradual refraction than previous cases, having large spacing between near-ground maxima. Ducting within d04R maintains the near-ground SPL above 73 dBA out to 550 m from the source. Whereas d04 exhibits a quiet zone at all frequencies above 250 Hz, with the L_{eq} spatial map indicating a likely second near-ground maxima will occur beyond the PE model's range.

All frequencies contribute to the increased SPL within d04R, with bands above 630 Hz exhibiting two near-ground focusing maxima with just under 300 m spacing at 1 m AGL. The L_{eq} plot indicates that spacing of maxima will shift as L_{A,f_n} is evaluated at different heights, up to 10 m AGL. Lower frequencies begin to exhibit a single quiet zone after 400 m range in d04R, and 300 m in d04, suggesting lower sensitivity than the higher frequencies to the first 10 m of the C_{eff} profile. Lower frequency bands exhibit a near-ground ducting interference pattern similar to that noted for the high frequency bands in case B. The near-ground ΔL suggest that using the vertically-refined C_{eff} profile of domains d04R more closely matched the experimentally derived profiles, with RMSE of 4.6 dBA versus 10.7 dBA, despite the noted issues with C_{eff}.

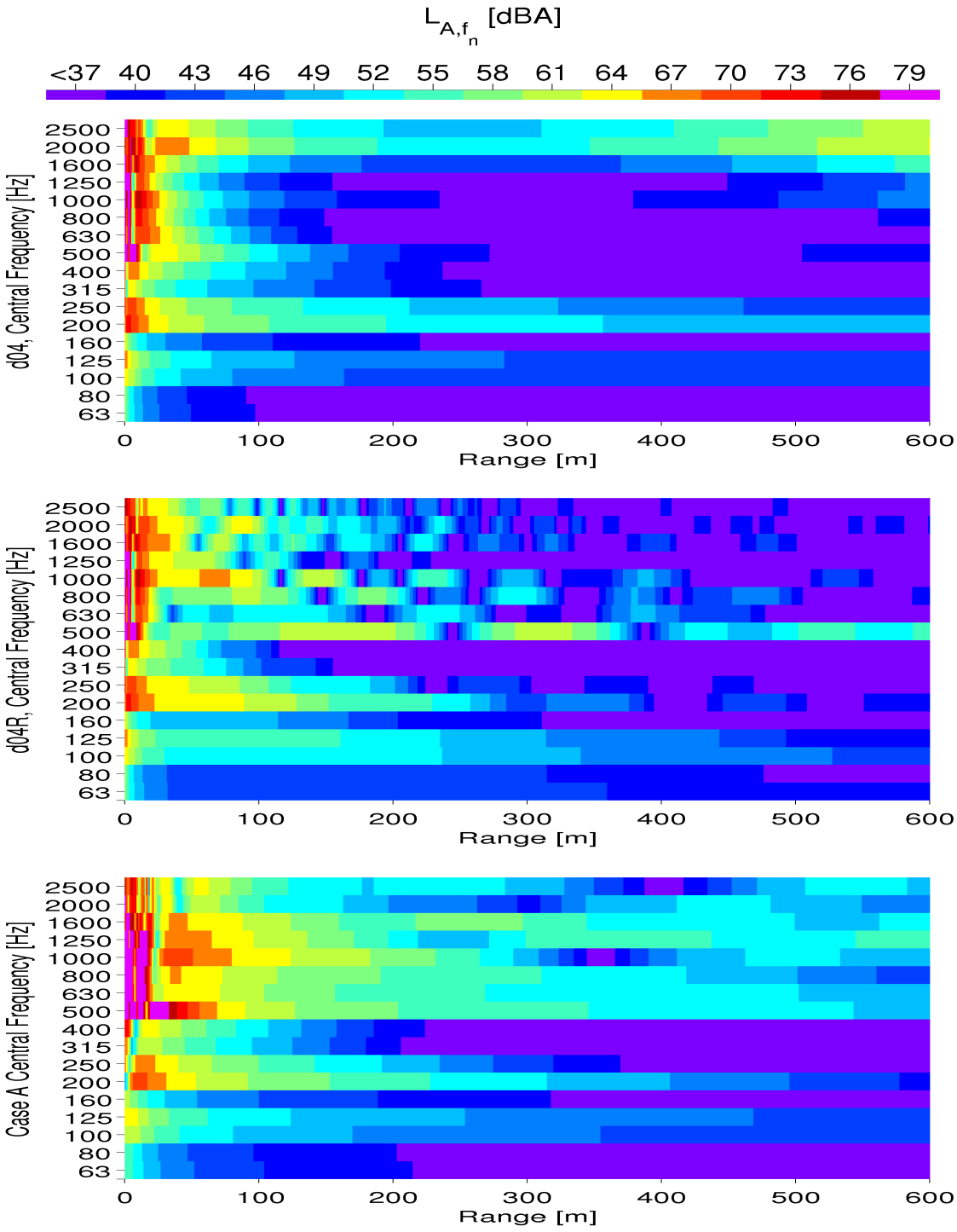

Figure 27: Spectra versus range at 1 meter AGL for d04 (top), d04R (middle) and OSF09 (bottom), for case A. The profiles are from the first of five 5-minute output during the 20-minute observational interval. The color transition from blue to red occurs at 67 dBA denoting noise abatement threshold criteria.

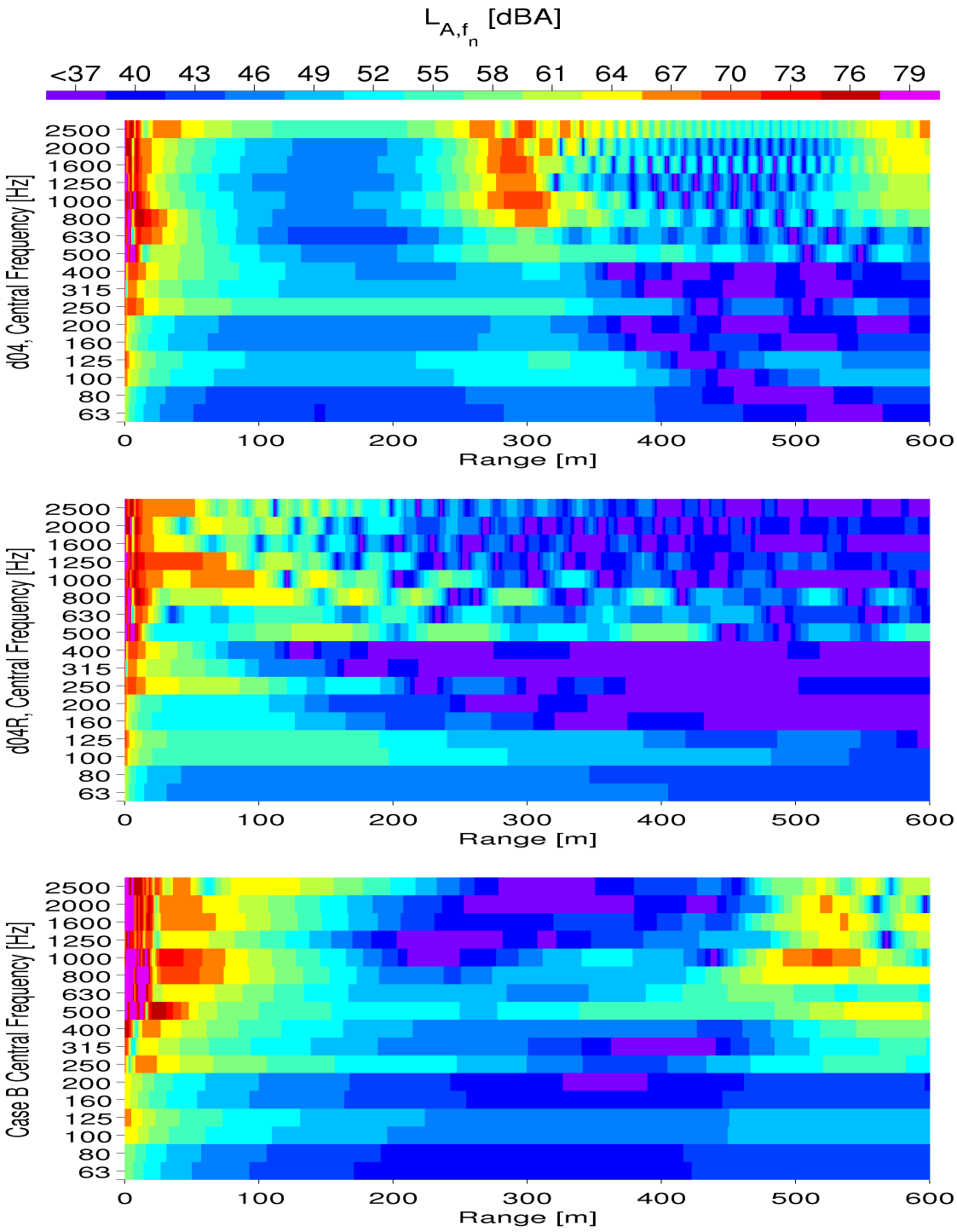

Figure 28: Same as for Figure 27 but for Case B.

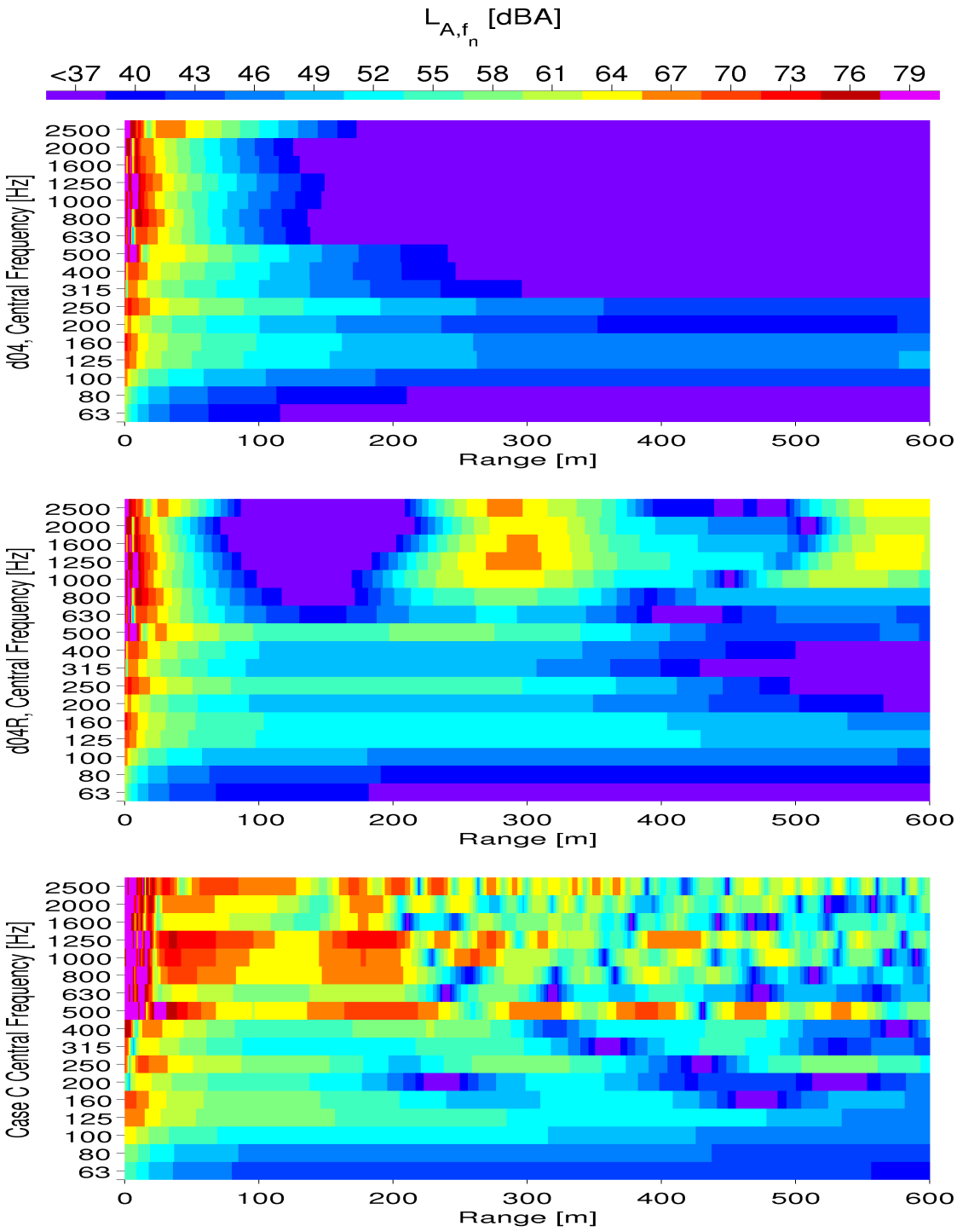

Figure 29: Same as for Figure 27 but for Case C.

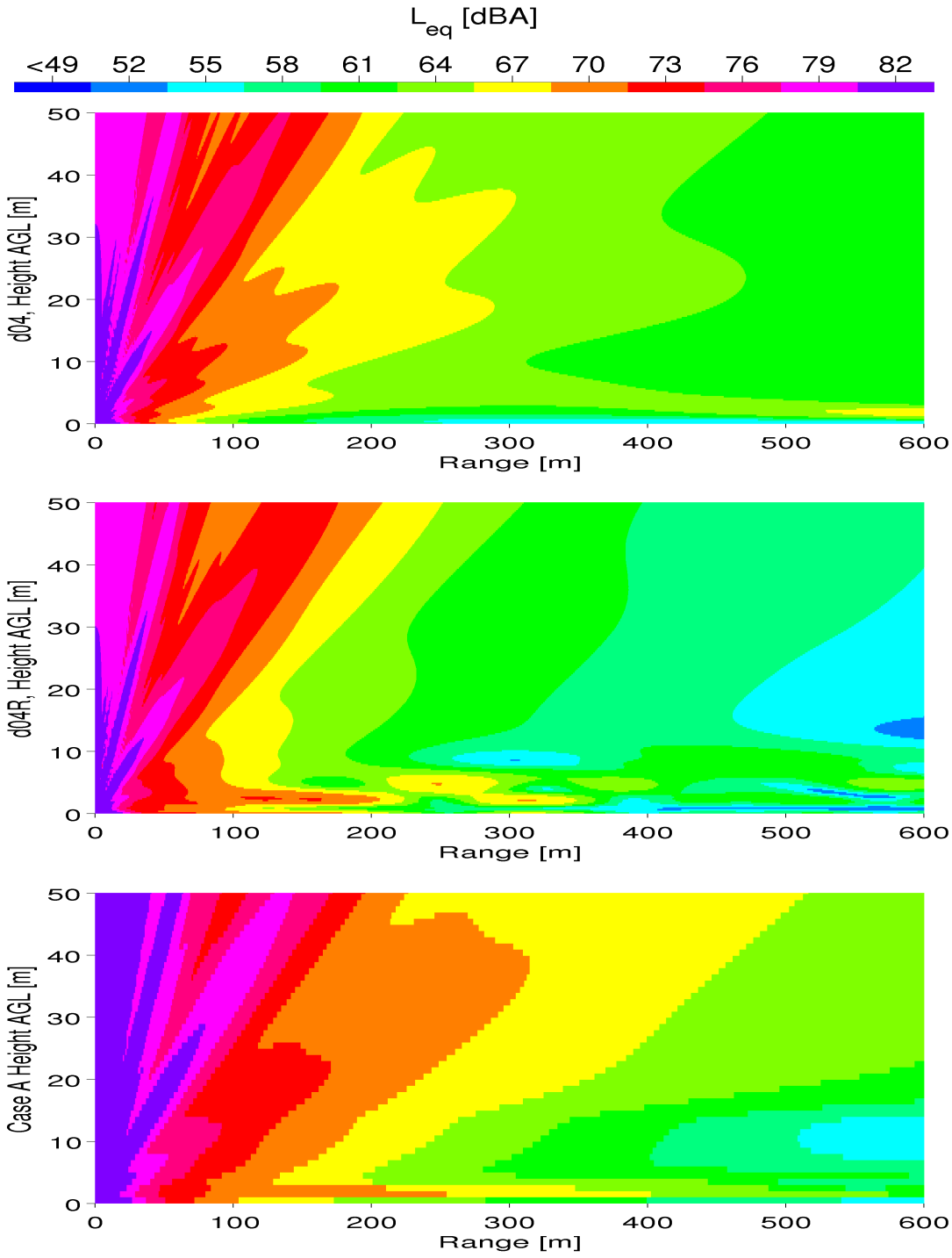

Figure 30: Vertical cross-section up to 50 meters AGL of L_{eq} maps using equation 4.6 for L_{f_n} interpolated onto a 0.25 meter grid for d04 (top), d04R (middle), and 1 meter grid for OSF09 (bottom), for Case A. The C_{eff} profiles are from the first of five 5-minute output during the 20-minute interval. The color transition from blue to red occurs at 67 dBA denoting noise abatement threshold criteria.

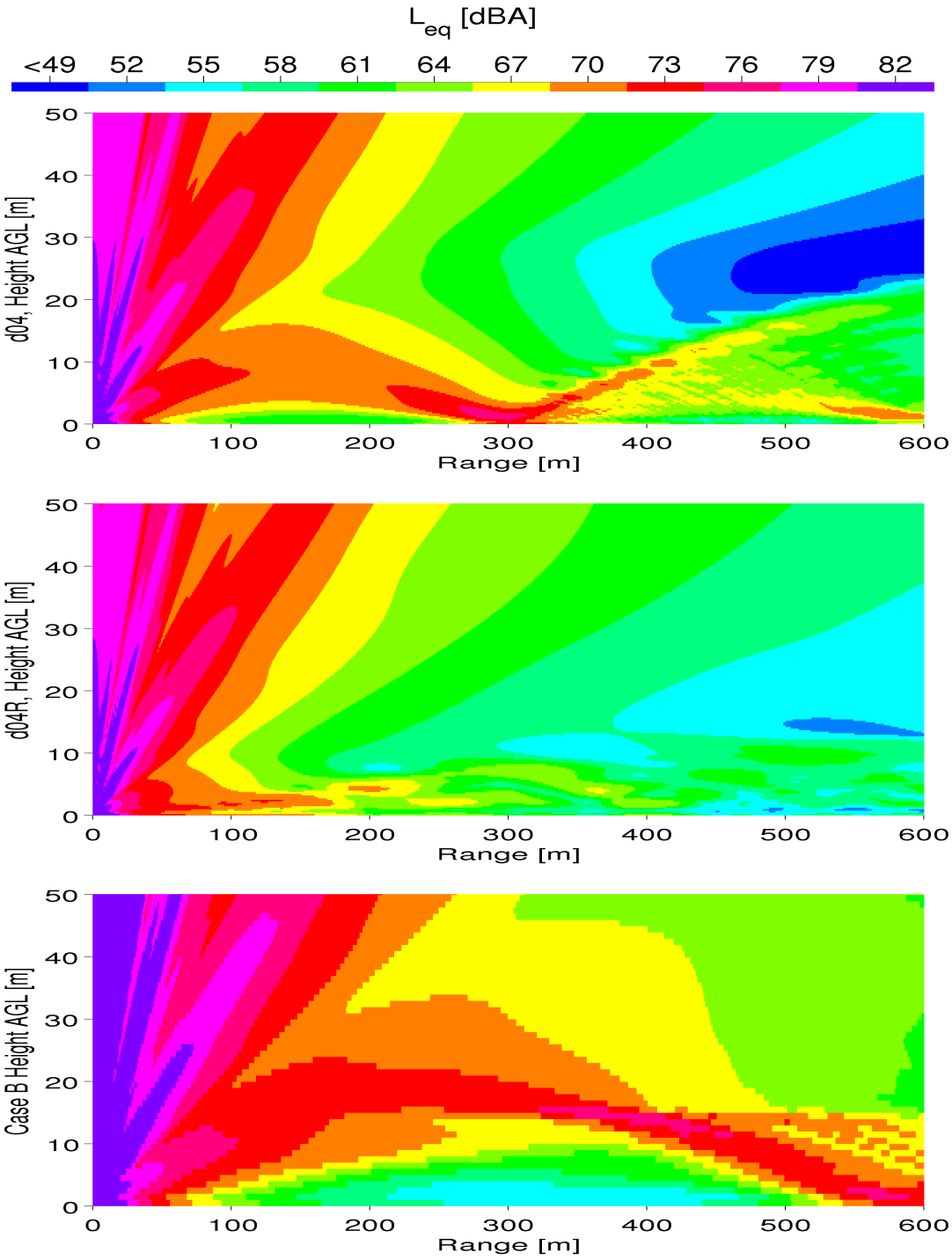

Figure 31: Same as for Figure 30 but for Case B.

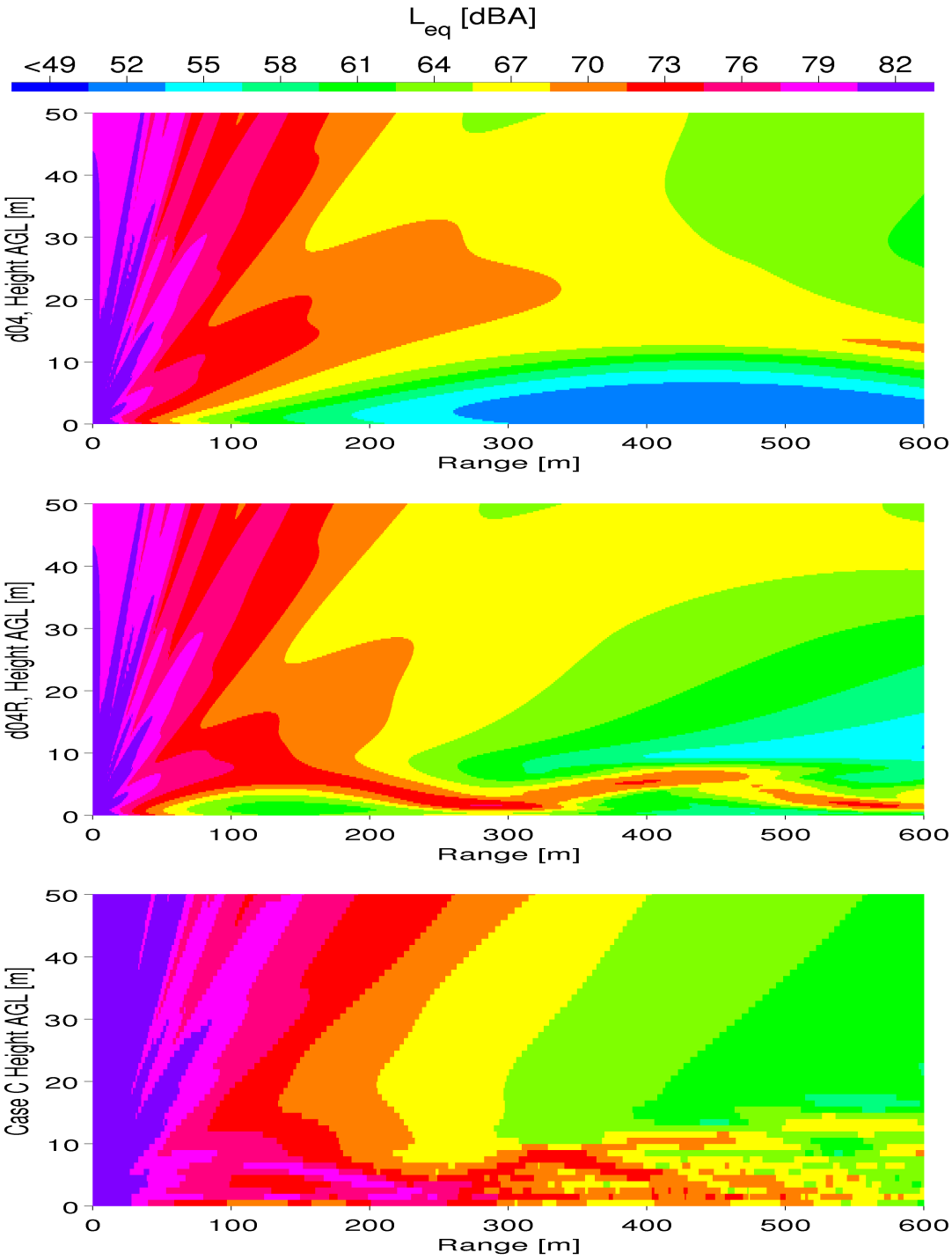

Figure 32: Same as for Figure 30 but for Case C.

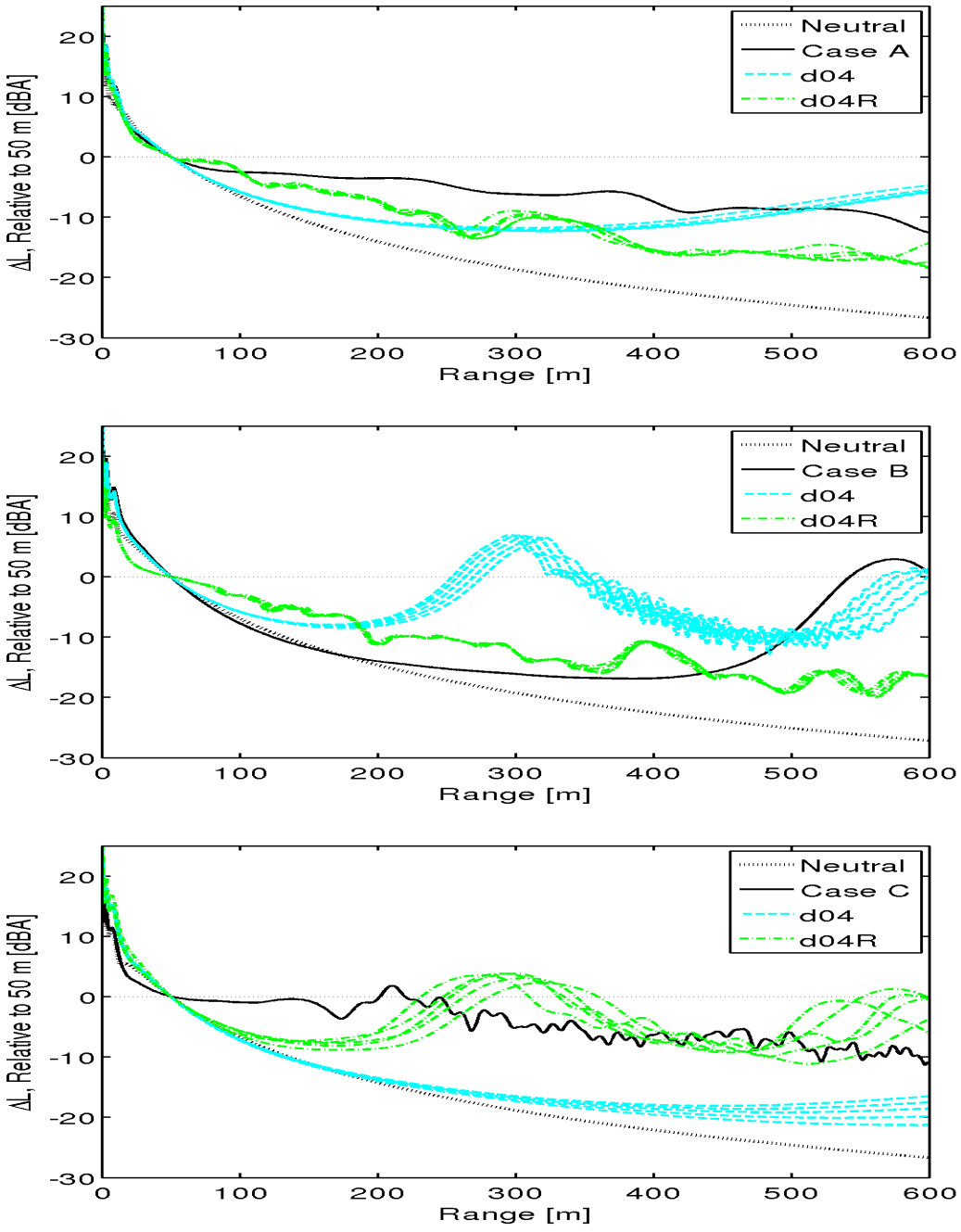

Figure 33: Relative SPL with respect to 50 meters versus range at 1 meter AGL for OSF09 case A (top) case B (middle) and case C (bottom) for OSF09 value (bold solid) non-refracting (dotted) and profiles derived from WRF domains d04 (bold dashed), d04R (bold dash-dot) at closest grid locations shown in Figure 25 for the output times corresponding to the 20 minute observational periods given in Table 1. No atmospheric attenuation has been included. Neutral case reference wavenumber correction has been accounted for following discussion in text.

4.6 Discussion

We have demonstrated a method for simulating meteorological profiles and assessed their suitability for use as input to an acoustic propagation model for freeway noise by examining three case studies in comparison with profiles derived from field measurements. We presented the method of vertical refinement for increasing meteorological simulation child domain vertical resolution, and discussed the influence of increasing the vertical resolution of our meteorological simulation on the predicted freeway noise propagation. We have provided a physically-motivated interpretation of emergent phenomenalogical qualities of spectra, total sound field, and relative SPL, resulting from features within simulated meteorological profiles. We discussed the influence of horizontal and vertical nest resolution on simulated meteorological profile features.

We found that bias within C_{ad} and $U_{||}$ become entangled when constructing C_{eff}, and may mask assessing the true capability and limitations of meteorological forecasting for acoustic application. We recommend investigating forecast skill requirements imposed by the sensitivity of acoustic model predictions of L_{A,f_n} and L_{eq} to variations within C_{eff}, especially below 100 m AGL. Overall RMSE of profiles suggest capability of simulating temperature profiles within around 3 °C, wind speed profiles within around 2 m s^{-1}, and C_{eff} profiles around 2 m s^{-1} in the lowest 190 m AGL.

In the introduction we discussed that a null hypothesis of MOST will fail for real profiles with features such as a jet, variable shear, and temperature inversions, as often is present within valley cities such as Phoenix. We found that a null hypothesis of unrefined profiles being sufficient is not true in all cases, that vertical refinement provides instances of improvement in representation of C_{eff}below 190 m AGL. Though some simulation skill was improved with modification of meteorological model resolutions for 1 km over 3 km, and

vertically refined 1 km over standard 1 km, this study provided a very limited sampling (three 20 min periods) of the entire simulation (several days) and more evaluation is recommended. In particular, detailed observations of profiles below 100 m AGL are key to meteorological model evaluation for this application.

Methods of evaluation established herein may provide means to move forward in assessing profiles for applicability to investigating highway noise pollution. In particular, profiles of sound speed in conjunction with plots of spectra versus range at various heights are useful for interpreting impacts on the spatial plots of total SPL. Examining relative SPL as total sound pressure level with respect to a fixed range location is useful for comparing an ensemble of predicted field results from derived and observed profiles. Improved agreement was seen between vertically refined profiles and observations as opposed to unrefined profiles. However, the RMSE of ΔL is biased by choice of range of evaluation and reference distance. Far-field acoustic obervations are needed to properly assess the validity of these methods. Locations for microphone placement can be considered through identifying range windows with large disagreement between the different methods for several meteorological cases. The experimental setup, however, may be limited by site-specific restrictions or proximity to background sources.

For this WRF model configuration some specific details of the wind and temperature gradients are reproduced quite poorly, in comparison with OSF09 observations, yet other aspects were quite well reproduced. More work needs to be done to assess possible phase errors and effects of localization of phenomena. Further studies are doubtlessly necessary to ascertain what physical processes are either being approximated poorly for this application (model parameterization), what aspects of the observations are just not resolved (influences of terrain resolution, sampling space-time volume, etc), and the added role of urbanization (not included here) on surface meteorology.

The method of producing surface layer profiles, joining near-ground values to the lowest model level, seems to have a strong influence on the sound field. Even though surface values and first model level values cause a gradient to exist, this changes character with increasing resolution, implying that there were unresolved dynamics in the coarser domain. More analysis needs to be performed with detailed flow observations to assess the hypothesis of unresolved dynamics. What we can glean from the current results is that shear is present in both d04 and d04R, and so the sound model is going to be influenced in both cases. However, the vertically refined results allow for dynamics not present in the coarser simulation, enabling a closer agreement with observations in some instances.

In cases A and C, the input effective sound speed profile from the initial unrefined 4th domain WRF simulation, though different from the non-refracting case, is still not as significantly sheared as for the vertically refined simulation. Moreover, although neither refined nor unrefined C_{eff} applied to acoustic simulations reproduce all details in the observations, where near-ground sound levels remain strong for quite some distance due to ducting of sound, they do produce similar results on the sound field intensity. The attenuation versus range results in Figure 10 indicate that near-ground predictions using vertical refinement appear to match more closely the meteorological profiles derived from observations (in comparison to profiles derived from the unrefined domain).

In case B, near-ground upward refraction is eventually overcome further away from the source due to stronger elevated downward refracting conditions. In this case, the shear is well captured. However, the method employed to interpolate between the lowest model level value and the near-ground value, along with bias in either term, can cause strong gradients in C_{eff}, to which the acoustic field appears quite sensitive. The sensitivity and relative contribution of the interpolation method towards the total refracted field, in

comparison with the profile features higher above ground level, needs to be explored for various ranges of propagation.

4.7 Conclusions

In summary, our work shows that conditions of morning temperature inversion and low-level jet or wind shear can be simulated by the WRF model to a certain degree, but that their magnitudes at a given location and time of comparison may disagree with field observations. As observed in case C, the velocity and temperature components within the effective sound speed can counteract each other and make an otherwise poor representation of the medium yield a C_{eff} profile which produces a sound field not too unlike what might be observed. Some of these effects measured in the field could be due to smaller-scale ground boundary conditions not realized in the 1 km x 1 km grid used in the WRF model. For instance, details of the flow modification due to terrain and land-use and land-cover may not be present, which, if accounted for, may lead to a closer representation of the actual measured profiles. Furthermore, sub-grid influence of the roadway and terrainDi Sabatino et al. 2008, and traffic produced turbulenceEskridge and Hunt 1979, in the local meteorology on acoustic propagation was also not explored in our study.

We recommend further work to consider sensitivities in the models, both of the PE model to differing levels of sound speed gradient, and also of WRF to various parameterizations of physical processes, such as land surface, urbanization and potential feedback on circulation and dynamics, representation of subgrid turbulence and surface layer profiles. Assessing the skill of these models for a variety of configurations would provide valuable insight into model prediction capability for acoustics applications. Furthermore, sensitivity of meteorological model to physical parameterization,

understanding unresolved subgrid aspects and their importance on acoustic field predictions, and possible areas for improvement of meteorological models, are all topics which could be motivated by demands within applications such as acoustics. In particular, nocturnal inversion and morning transition are notoriously difficult to accurately simulate. These are key periods that exhibit downward refraction and wind shear, which are ubiquitously neglected or misrepresented in many acoustic assessments.

Acknowledgements

This material is based upon work supported by the National Science Foundation (NSF) under EaSM grant EF-1049251 awarded to Arizona State University (ASU), NSF grant DMS 1419593 awarded to ASU, and by the Arizona Department of Transportation grant ADOT JPA06014T awarded to ASU. We would also like to thank Christ Dimitroplos for his support of this work along with Mr. Peter Hyde and Prof. J.C.R. Hunt for their valuable feedback in preparation of the manuscript. We thank the WRF group at the National Center for Atmospheric Research (NCAR) for providing the WRF code. We also acknowledge the support of the staff at ASU Advanced Computing Center (A^2C^2) for maintaining the Saguaro cluster.

Chapter 5

MULTI-SCALE MODELING AND EVALUATION OF URBAN SURFACE ENERGY BALANCE IN THE PHOENIX METROPOLITAN AREA

Accepted for publication in: *Journal of Applied Meteorology and Climatology*,
S.R. Shaffer; W.T.L. Chow; M. Georgescu; P. Hyde; G.D. Jenerette; A. Mahalov; M. Moustaoui; B.L. Ruddell (Accepted, Oct. 2014).

Physical mechanisms of incongruency between observations and Weather Research and Forecasting (WRF) model predictions are examined. Limitations of evaluation are constrained by: i) parameterizations of model physics, ii) parameterizations of input data, iii) model resolution, and, iv) flux observation resolution. Observations from a new 22.1 meter flux-tower situated within a residential neighborhood in Phoenix, Arizona, are utilized to evaluate the ability of the urbanized WRF to resolve fine scale Surface Energy Balance (SEB) when using the urban classes derived from 30 meter resolution National Land Cover Database. Modeled SEB response to a large seasonal variation of net radiation forcing were tested during synoptically-quiescent high-pressure periods in Winter 2011 and Pre-monsoon Summer 2012. We present results from simulations employing five nested domains down to 333 meter horizontal resolution. A comparative analysis of model cases testing parameterization of physical processes comprised of four configurations of urban parameterization, for the bulk urban scheme versus three representations with the Urban Canopy Model (UCM) scheme, and also for two types of planetary boundary layer parameterization, with the local Mellor-Yamada-Janjic scheme, and the non-local Yonsei University scheme. Diurnal variation in SEB constituent fluxes are examined in relation to surface layer stability and modeled diagnostic variables. Improvement is found when

adapting UCM for Phoenix with reduced errors in the SEB components. Finer model resolution is seen to have insignificant ($< 1\sigma$) influence on mean absolute percent difference of 30-minute diurnal mean SEB terms.

5.1 Introduction

The aggregate global-scale impact of human activities is suggested to have brought about a geological epoch known as the Anthropocene (Smith and Zeder 2013). Most noticeable since the industrial revolution, anthropogenic influence may result in adverse transitions beyond critical thresholds, triggering ecosystem collapse (Barnosky et al. 2012). The world population is rapidly increasing and urbanizing while also increasing energy use and emissions (i.e. Ching 2013). The pre-eminent influence of anthropogenically determined local-scale urban microclimate is thus becoming ever more important within hot arid cities (e.g. Coutts, Beringer, and Tapper 2007). These cities are growing worldwide and are particularly vulnerable to climate change and water resource availability (i.e. Vörösmarty et al. 2010). These issues motivate the development of fine-resolution modeling tools for studying effects of urban design on a regional-scale to mitigate adverse effects and optimize urban microclimate. Modeled values of temperature and moisture provide key results to inform policy making and decisions regarding human-ecosystem interaction (Fernando 2008; Chow, Brennan, and Brazel 2012; M Georgescu et al. 2013), though lack of available observations, particularly of Surface Energy Balance (SEB) fluxes within urban settings, often leaves such predictions unvetted. Furthermore, many features of urban microclimate are determined at scales $<$ 1 km (Hunt et al. 2012; Ching 2013).

The capability of atmospheric modeling in urban environments is influenced by land-atmosphere coupling (F. Chen et al. 2011). The SEB is intimately related to the

Atmospheric Surface-Layer (ASL), or region closest to the ground, which provides, via a Surface-Layer Scheme (SLS), the interconnection between the ground, or Land Surface Model (LSM), and lower atmosphere, or, the Planetary Boundary Layer (PBL). In particular, SEB closure has been examined in the context of urban climate and remains a challenging issue (Arnfield 2003; Foken 2008). In the context of SEB modeling, the role of vegetation, moisture, latent heat flux, and anthropogenic forcing are important areas of active research (Arnfield 2003; Ching 2013). C. S. B. Grimmond et al. 2010 conducted an extensive inter-model comparison of off-line urban canopy models and found that not all models correctly account for SEB closure. A systematic evaluation of the modeled SEB is thus needed before addressing the above applications.

Parameterizations of urban processes within atmospheric models typically presume that the city is entirely sub-grid to the ASL. This modeling assumption means that the built environment should be contained within the surface layer, or first full model level (C. S. B. Grimmond et al. 2010). One main concern is that anthropogenic waste heat and momentum modifications are only supplied to the first model level. However, one method often employed within studies of the ASL or of lower PBL profiles is to add extra model levels near the ground. Hence, there is a trade-off between explicitly resolving fine structure in the ASL, especially within the urban boundary layer, also in conjunction with flow dominated by complex terrain (Fernando 2010). Furthermore, parameterizations of the ASL often employ Monin-Obukhov Similarity Theory (MOST) (Monin and Obukhov 1954), wherein horizontal homogeneity is assumed, meaning that individual buildings and land uses at sub-grid scales are not explicitly resolved. This assumption can break down in settings with inhomogeneous Land Use And Land Cover (LULC). Micro-scale LULC variations may become important when comparing with neighborhood-scale flux-tower measurements (Foken 2008; Nordbo et al. 2013).

Forecasting at smaller scales has become computationally possible by advances in technology and in numerical technique, such as nesting (Skamarock and Klemp 2008). Yet theoretical issues regarding turbulence closure and parameterization of PBL eddies remain a challenge as resolution approaches the so-called *Terra-Incognita* (Wyngaard 2004). At scales finer than the Terra-Incognita ($\lesssim$ 1 km), large eddy simulation are typically employed (e.g. Moeng et al. 2007). Recently, model development efforts have been focused on enabling transiting the Terra-Incognita (F. Chen et al. 2011; Mirocha, Kosović, and Kirkil 2014) Yet computational feasibility often limits applications to research. Furthermore, there has been limited assessment of model error at Terra-Incognita scales.

In this study we explore SEB, computational feasibility, model stability and sensitivity to parameterization, when nesting from global analysis data to a resolution of 333 m. This study addresses questions of model feasibility and accuracy within a hot arid city, probing the limits of current model physics parameterization schemes, computational capability, and input data, evaluated in a manner consistent with available observations of SEB. Model SEB terms were evaluated with flux-tower observations located in an arid urban residential neighborhood (Chow et al. 2014), assessing for a range of seasonal and diurnal input radiative forcing, and physically explaining errors. Multiple customized high-resolution urban LULC data sets were incorporated to evaluate parameterization of urban LULC appropriate to fine-resolution modeling. Two turbulence closure model PBL schemes, Yonsei-University (YSU, Hong, Noh, and Dudhia 2006) and Mellor-Yamada-Janjic (MYJ, (Janjic 2001)), were investigated with a data and model combination probing the limitation of approaching Terra-Incognita.

5.2 Methods

The influence of resolution is explored by employing spatially and temporally nested computational domains. Modified input parameterizations of LULC are employed to represent urbanization specific for Phoenix derived from observed data. A comparative analysis is then conducted between two types of model turbulence closure and four urban physical parameterization schemes for varied representations of the Phoenix urban canopy.

5.2.1 Flux Tower Observations and Study Period

Micro-meteorological data were obtained from an eddy flux-tower installed in a residential West Phoenix neighborhood (33.484°N, 112.143°W). Observed values were post-processed into half-hourly block-averaged (from 10 Hz) turbulent and radiative data, along with related temperature and three-dimensional wind data. The instruments were installed at 22.1 m above ground level. Further details can be obtained from Chow et al. 2014 regarding site characteristics, instruments employed, data quality, correction procedures, and calculation of flux source areas. Turbulent flux footrpint lengths are $\approx .5 - 1$ km for unstable to stable surface-layers, respectively, and the radiative flux source area is $\approx .5$ km in diameter.

A range of cloud-free dry-period SEB forcing conditions were examined by selecting time frames during winter and pre-monsoon summer with available SEB observations. These periods are: the 60-hour period from December 23 (Winter 2011), and the 72-hour period from June 17 (Pre-monsoon Summer 2012).

5.2.2 Numerical Simulations

The Weather Research and Forecasting (WRF) model (Skamarock et al. 2008) was evaluated using observations described above. Simulations were conducted using one-way nested domains where multiple domains were run concurrently with no feedback to parent domains. The outer domain and soil moisture were initialized with Final operational global analysis (FNL) data. These data are provided at one-degree spatial and six-hour temporal resolution, at 27 vertical pressure levels. Radiative processes are represented by the RRTM scheme for longwave (Mlawer et al. 1997) and the Dudhia scheme for shortwave (Dudhia 1989). Physical processes involving moisture were modeled using the 3-class single-moment microphysics scheme (Hong, Dudhia, and Chen 2004). The Kain-Fritsch cumulus parameterization (Kain 2004) was used for just the outer domain.

We utilize the Noah land-surface model (LSM) described in Chen and Dudhia 2001, which determines skin temperature and supplies heat, momentum, and moisture fluxes into the atmosphere in response to radiation, precipitation, humidity, and surface-layer temperature and winds, for the dominant non-urban LULC. The geographic non-urban LULC classifications and terrain elevations were obtained from nearest neighbor interpolation of the MODerate-resolution Imaging Spectroradiometer (MODIS) 20-category 30-arcsecond data modified for the Noah LSM. Vegetation fraction values were obtained from static terrestrial data provided in WRF.

5.2.2.1 Model Resolution

Five nested domains, referred to as D1 through D5, were configured with horizontal resolution (Δ_H) of 27, 9, 3, 1, and .333 km, respectively, and are represented schematically

in Figure 34. Also shown are terrain for all domains, and dominant LULC for D5, which was configured to contain the entire Phoenix Metropolitan area. All domains used a vertical grid with 40 vertical levels with increased grid resolution near the ground and a model top of 50 mbar. The first three domains were started synchronously. However, the starting times for D4 and D5 are delayed by 6 hours each to allow for spin-up. The D1 timestep for Winter simulations was 150 s. Summer simulations required a reduction to as low as 90 s due to model stability. Attribution of reducing the child domain timesteps by a factor of 3 from the parent domain, for D2 through D4, and by a factor of 5 for D5, led to stabilize the fine-scale domain simulation. The D1 timestep was further constrained to ensure that the D2 timestep would evenly divide the $\Delta_t = 300$ s output history interval.

5.2.2.2 Urban LULC Parameterizations

The categorical urban LULC fields from the 30-meter resolution 2006 U.S. Geological Survey National Land Cover Database (NLCD) (Fry et al. 2011) were used to derive representative urban LULC for the Phoenix Metropolitan area. Three urban LULC classes were identified as Commercial/Industrial (C/I), High-Intensity Residential (HIR), and Low-Intensity Residential (LIR). The C/I was derived from developed high-intensity, HIR from developed medium-intensity, and LIR from developed low-intensity and developed open space. Grid-scale urban LULC were then obtained by nearest neighbor interpolation and made a higher priority when combining with the MODIS LULC classes. To obtain the final LULC product for each domain (Fig. 34), any grid-cells still classified as urban/built-up by MODIS were replaced with LIR. Urban schemes are applied for the dominant urban LULC within each model grid-cell to which an urban LULC was attributed.

We compare the role of urban parameterization for the bulk urban scheme (hereafter,

		Urban LULC Class		
Parameter Description	**Units**	**C/I**	**HIR**	**LIR**
Urban fraction[1] default values	-	0.865	0.429	0.429
Urban fraction[1] PHX-A values	-	0.95	0.60	0.73
Urban fraction[1] PHX-B values[2]	-	0.95	0.85	0.70
Roof level (building height)	m	10.0	4.7	3.9
Standard deviation of roof height[3]	m	8.0	2.7	1.0
Roof (i.e., building) width	m	31.7	25.7	17.6
Road width	m	98.9	39.2	108.0
Anthropogenic heat	W m^{-2}	30.0	35.0	20.0
Volumetric heat capacity of roof[4,6]	MJ m^{-3} K^{-1}	1.32	1.32	1.32
Volumetric heat capacity of building wall[5,6]	MJ m^{-3} K^{-1}	2.11	1.52	1.52
Volumetric heat capacity of ground (road)[6]	MJ m^{-3} K^{-1}	1.94	1.94	1.94
Thermal conductivity of roof[4,6]	J m^{-1} s^{-1} K^{-1}	0.83	0.83	0.83
Thermal conductivity of building wall[6]	J m^{-1} s^{-1} K^{-1}	1.51	0.19	0.19
Thermal conductivity of ground (road)[6]	J m^{-1} s^{-1} K^{-1}	0.75	0.75	0.75

Table 3: Description of modifications made to UCM urban physics option parameters (Kusaka and Kimura 2004) from default values following S. Grossman-Clarke et al. 2010 for urban LULC classes Commercial/Industrial (C/I), High-Intensity Residental (HIR), and Low-Intensity Residental (LIR). Notes: [1] - f_{urb}, fraction of the urban landscape which does not have natural vegetation, [2] - Modified f_{urb} following M. Georgescu et al. 2011, [3] - Susanne Grossman-Clarke et al. 2005, [4] - Assume brick roof, [5] - Assume concrete wall for C/I; dense wood for HIR and LIR, [6] - Value from T. Oke 1987,

'bulk'), described in Liu et al. 2006, versus the Urban Canopy Model (UCM) described in Kusaka and Kimura 2004. The bulk scheme calculates fluxes from a single flat surface. However, the UCM accounts for unresolved simplified infinite urban canyons, with building morphology and materials, roads, and interactions between roads, roofs and walls of buildings, with 20 parameters for each urban LULC class.

We test three UCM cases by applying the calibrated LULC parameterizations. First, we test a baseline case (hereafter, 'default'), then we examine two other cases using modified morphological and material values for Phoenix (hereafter, 'PHX-A' and 'PHX-B', see Table 3). Only parameters which were changed from default values are given in Table 3,

all of which remain fixed for PHX-A and PHX-B, except for the urban fraction, f_{urb}, also given in Table 3 for all cases. The HIR class, which varies the most between PHX-A and PHX-B, also happens to be the LULC designation for the flux-tower footprint neighborhood. Thus, the differences between the three UCM cases will provide a simple variation of parameters.

The f_{urb} value represents the computational grid-cell fraction attributed to the dominant urban LULC. For comparison, f_{urb} values for the three UCM cases are also presented in Table 3. The f_{urb} values are held constant for all domains for their respective urban LULC class when that class is the dominant LULC in a given model grid cell. Unlike the implementation of UCM, which employs 3 urban LULC classes with $f_{\mathrm{urb}} \in (0, 1]$, the bulk scheme employs a single developed/built-up urban LULC class with f_{urb}=1.0. Furthermore, f_{urb} is used as a coefficient of the UCM scheme output variables, with the non-urban variable (with coefficient $1 - f_{\mathrm{urb}}$) derived from the Noah model. These sub-grid fractional contributions are then aggregated to compute a single value for each grid cell.

The UCM scheme assumes that the built environment is subgrid to the first vertical model level. Our choice of 40 vertical levels provides for $z_1 \approx 55$ m for the first model layer thickness, satisfying the subgrid condition for 99% of the buildings within the 16.7 km^2 core downtown Phoenix study area (Burian, Velugubantla, and Brown 2002), where 73% are < 5 m tall, and another 20% are between 5-10 m. While there are a few other built-up urban cores within the greater Phoenix metropolitan area, the predominant LULC is < 10 m tall residential.

5.2.2.3 Physical Parameterizations of Atmospheric Turbulence

The role of planetary boundary layer (PBL) scheme, which parametrizes vertical mixing processes of unresolved turbulent motion, was examined for two methods of turbulence closure. Each PBL scheme depends upon a specific surface-layer scheme (SLS) to connect the LSM to the first atmospheric model level, and hence will be influenced by feedback with the SEB. The non-local scheme of Yonsei-University (YSU, Hong, Noh, and Dudhia 2006), explicitly treats entrainment between the free atmosphere and top of the boundary layer, in addition to a non-local gradient flux term to account for large eddies. YSU couples with the MM5 SLS (Zhang and Anthes 1982). The higher-order local closure scheme of Mellor-Yamada-Janjic (MYJ), requires the Eta SLS (Janjic 2001). Both SLSs employ MOST, and assume a horizontally homogeneous and stationary constant flux layer. Horizontal sub-grid mixing was achieved with a 2nd-order diffusion parametrization and a Smagorinsky 1st order closure scheme.

5.2.3 Methods Used for Comparing Observations and Model Simulations

5.2.3.1 Physical Metrics Used for Evaluation

For WRF model evaluation, we use the following relations, with variables described in Table 4,

$$\begin{aligned} G_{SW}^{\uparrow} &= \alpha G_{SW}^{\downarrow}, \\ G_{LW}^{\uparrow} &= \varepsilon \sigma \mathrm{T_0}^4, \\ Q^{*} &= G_{SW}^{\downarrow} - G_{SW}^{\uparrow} + G_{LW}^{\downarrow} - G_{LW}^{\uparrow} \\ \langle Q_H \rangle &= \Delta\Sigma Q_H / \Delta_t, \\ \langle Q_E \rangle &= \Delta\Sigma Q_E / \Delta_t. \end{aligned} \tag{5.1}$$

Here $\sigma = 5.67040 \times 10^{-8}$ J s^{-1} m^{-2} K^{-4}, is the Stefan-Boltzman constant, and Δ_t is the 5-minute history output interval. Top-to-bottom are the upward radiative fluxes for shortwave, $G_{SW}^{\uparrow}$, and longwave, $G_{LW}^{\uparrow}$, and the net radiation Q^{*}. Lastly, are fluxes of sensible, $\langle Q_H \rangle$, and latent, $\langle Q_E \rangle$, heat, for which accumulated quantities were used for comparison with time-averaged observations rather than instantaneous values. All quantities have units of W m^{-2}.

The SEB relation for the effective residual or storage, ΔQ_s, is,

$$\Delta Q_s = Q^{*} - \langle Q_H \rangle - \langle Q_E \rangle. \tag{5.2}$$

When explicitly partitioning the anthropogenic forcing, Q_F, and ground heat flux, Q_G, one could write, $\Delta Q_s = \Delta Q_s' + Q_F + Q_G$, with a reduced residual $\Delta Q_s'$. However, for comparison with observations, Q_F is combined with the storage term ΔQ_s. The present analysis also considers Q_G as being a component of the residual term ΔQ_s because of the disparity in spatial scale between observation footprints of Q_G and the turbulent flux terms. Anthropogenic forcing, Q_F, was derived following Susanne Grossman-Clarke et al. 2005.

For making a fair comparison between observations and simulations, instantaneous values were output from WRF with $\Delta_t = 300$ s and were averaged to the same 30-minute periods. Percent differences, P_D, were calculated between 30-minute diurnally averaged values for observation, O, and simulation, S, as,

$$P_D = 100 \times \frac{O - S}{.5(O + S)}, \tag{5.3}$$

with variance estimated from standard deviation of averaged values, and propagated to estimate statistical uncertainty in each 30-minute interval of P_D. Furthermore, the scale of P_D, which can be both positive and negative and vary quite widely, are presented logarithmically in Figures 2-7 (described later) as,

$$\text{Scale}(P_D) = sign P_D \times \log_{10} \lceil |10^s P_D| \rceil, \tag{5.4}$$

where the coefficient will preserve the sign of P_D. We set the scaling factor $s = 0$ within the ceil function, $\lceil \cdot \rceil$, since we are interested in visually inspecting values of order of magnitude with $|P_D| > 10^0$. Note that simulations more closely match observations with a smaller value of $|P_D|$.

5.2.3.2 Diagnostic Temperature

The diurnal variation, and percent differences between observations and model cases described in Section 5.25.2.2 are shown for the diagnostic temperature at 2-meters above ground, $\mathrm{T_{2m}}$. Values of $\mathrm{T_{2m}}$ are calculated within WRF by the relation,

$$\mathrm{T_{2m}} = \mathrm{T_0} - \frac{Q_H}{\rho c_p C_H}. \tag{5.5}$$

Here Q_H and C_H are sensible heat flux and heat exchange coefficient, respectively, which are taken from the previous timestep, $\mathrm{T_0}$ is the skin temperature, ρ is the air density, and c_p

Variable	Output Name	Units	Description
ΣQ_H	ACHFX	J m^{-2}	Accumulated surface sensible heat flux
ΣQ_E	ACLHF	J m^{-2}	Accumulated surface latent heat flux
α	ALBEDO	-	Surface albedo
ε	EMISS	-	Surface emissivity
$G^{\downarrow}_{LW}$	GLW	W m^{-2}	Downward long wave flux at ground surface
Q_G	GRDFLX	W m^{-2}	ground energy flux, positive-release
Q_H	HFX	W m^{-2}	Surface sensible heat flux
Q_E	LH	W m^{-2}	Surface latent heat flux
z_{PBL}	PBLH	m	Boundary layer height
$G^{\downarrow}_{SW}$	SWDOWN	W m^{-2}	Downward short wave flux at ground surface
$\mathrm{T_{2m}}$	T2	K	2-meter temperature
$\mathrm{T_0}$	TSK	K	Surface skin temperature
u^*	UST	m s^{-1}	Friction velocity

Table 4: Description of WRF output variables used for flux analysis in Eq. 5.1 or elsewhere.

is the specific heat at constant pressure. The heat exchange parameter is defined by, $C_H = u^*\theta^*/(\Delta\theta)$, where $\Delta\theta = \mathrm{T_0} - \mathrm{T_{2m}}$. The friction velocity, u^*, and turbulent temperature scale, θ^*, in turn, make use of MOST integrated stability functions for momentum and heat. Stability profiles are empirical relationships which act as fits to surface and first model level values consistent with gradient flux relationships (see Section 5.25.2.25.2.2.3), and so are influenced by model bias at both levels. In particular, a bias in any of the terms contributing to $\mathrm{T_{2m}}$ could lead to error in derived values, and in some cases can cancel yielding a derived $\mathrm{T_{2m}}$ which may be more accurate than the individual parameters from which it was obtained.

5.2.3.3 Model Evaluation Across Resolution and Parameterization Configurations

A metric of model error is needed to enable intercomparison between the different cases of model horizontal grid resolution, Δ_H, and model parameterization configuration, p. For this purpose, we examine the diurnal mean absolute percent difference between observations and simulations, M, defined for a variable x by,

$$M(x;\Delta_H,p) = N_k^{-1} \sum_{k=1}^{N_k} \left| P_D(x(k;\Delta_H,p)) \right| . \tag{5.6}$$

The sum is over the $k = 1,\ldots,N_k$=48 thirty-minute time intervals in the diurnal period, and P_D is as given by Eq. 5.3, for the model grid point containing the observation location.

5.3 Results and Discussion

Here we address the main research questions pertaining to how well current WRF performs in a hot dry city (Phoenix) and where further improvement is needed, as validated with observations of SEB components. Inspection of 30-minute averaged time-series of observed values (not shown) exhibit a regular diurnal quality for the chosen study period, wherein local flow processes are dominant over mesoscale forcing, and justifying the use of diurnal averages. The diurnal maxima of net radiative forcing varies by a factor of nearly two between the seasons.

A further distinction between the three default urban LULC classes and those employed by S. Grossman-Clarke et al. 2010, is that the latter values are representative of commercial-industrial, mesic residential, and xeric residential, respectively. Furthermore, soil moisture values were initialized in our cases from NCEP FNL data with no prescription for modifications to incorporate effects of irrigation, as conducted with the previous studies

of S. Grossman-Clarke et al. 2010, and M. Georgescu et al. 2011. Rather, the present analysis is focused on examining the importance of f_{urb} values along with adapting the urban morphological and material parameters for Phoenix. The flux-tower footprint is a neighborhood with little vegetation and irrigation, and few water bodies (e.g. swimming pools) (Chow et al. 2014). Furthermore, the NLCD data were from 2006, with neglegible LULC modifications in the footprint area at the time of our study and more recent Quickbird derived LULC (Figure 2 and Table 1 Chow et al. 2014).

The diurnally averaged variables simulated by the 1 km resolution domain for WRF model configurations defined in Section 5.25.2.2 are compared with observed temperature and corresponding percent difference diurnal variation in (Fig. 35). Likewise, the radiation flux components are presented for $G^{\downarrow}_{LW}$ (Fig. 85), $G^{\uparrow}_{SW}$ (Fig. 37), and $G^{\uparrow}_{LW}$ (Fig. 38), and the friction velocity u^* is presented (Fig. 39). Similarly, the SEB flux quantities for just Pre-monsoon Summer 2012 are presented for $\langle Q_H \rangle$ and $\langle Q_E \rangle$ (Fig. 40), and for Q^* and ΔQ_s (Fig. 41). Influence of resolution and configuration on model errors derived with Eq. 5.6 are presented in Figure 42 for Pre-monsoon Summer 2012, for variables Q^*, $\langle Q_H \rangle$, $\langle Q_E \rangle$, ΔQ_s, $\mathrm{T_2m}$, $G^{\uparrow}_{LW}$, $G^{\downarrow}_{LW}$, $G^{\uparrow}_{SW}$, and $G^{\downarrow}_{SW}$, for Δ_H= 9, 3, and 1 km, and for model configurations of bulk, PHX-A, and PHX-B, with either MYJ-Eta or YSU-MM5. Results for the 333 m resolution domain are only presented for model configurations MYJ-Eta bulk, YSU-MM5 PHX-A and PHX-B for Summer 2012 (Fig. 42), and YSU-MM5 PHX-B for Winter 2011 (Fig. 43), because of the excessive computational time needed at this resolution.

5.3.1 Influence of Modifying Turbulence Parameterization, Urban Land Use and Land Cover, and Urban Representation Input Data

The influence of local versus non-local closure schemes on bias for T_{2m} is apparent in Figure 35. All cases perform well during mid-day unstable conditions. However, only cases MYJ-Eta with bulk and YSU-MM5 with UCM for PHX-A/B perform well at all times of day and for both seasons. Here, the notation "PHX-A/B" is used to represent UCM for either PHX-A or PHX-B. Also, the YSU-MM5 cases are warmer at night than corresponding MYJ-Eta cases, and with a higher z_{PBL} and lower stabilty (not shown), agreeing with previous studies comparing local and non-local schemes (e.g. Xie et al. 2012). The role of f_{urb} is present at night (Fig. 35a,b) , with PHX-B consistently warmer than PHX-A, for a given PBL-SLS. Here, the UCM scheme with MYJ-Eta reduces T_{2m} underestimation error by ≈50%. For instance, (Fig. 35a) shows that PHX-A MYJ-Eta underestimates T_{2m} by ≈ 8 °C between 0 to 6 local time, while PHX-B MYJ-Eta underestimated T_{2m} by ≈ 4 °C during the same period. The bulk scheme evaluates well compared to the UCM scheme with regard to T_{2m}, and YSU-MM5 for both PHX-B and bulk show quite similar T_{2m} for both seasons. However, this performance for bulk (Fig. 35) does not persist for the SEB terms (Fig. 40a,c) , and for e.g. $G^{\uparrow}_{LW}$ (Fig. 38a) .

A PBL-SLS dependence is also present for $G^{\downarrow}_{LW}$ (Fig. 85), which may be due to feedback from the surface modifying the column temperature profile where the atmosphere is too cold. This explaination would agree with previous studies which have shown a influence of PBL-SLS between local and non-local schemes on derived temperature profiles (Shin and Hong 2011) and on SLS-LSM coupling strength (Chen and Zhang 2009). The systematic $G^{\downarrow}_{LW}$ under-prediction bias could also be related to the afternoon 3-11% over-prediction bias in $G^{\downarrow}_{SW}$ (not shown), and the lack of accounting for urban air pollutants,

and a repartitioning of $G_{SW}^{\downarrow}$ into $G_{LW}^{\downarrow}$ by photochemically active species. These issues will be addressed in a future paper, and may further explain the $G_{LW}^{\downarrow}$ bias between models which use the same Dudhia and RRTM radiation schemes. The influence of bias in $G_{SW}^{\downarrow}$ is present in $G_{SW}^{\uparrow}$ (Fig. 37) owing to Eq. 5.1, which is clearly also influenced by the LSM and urban scheme, since the same magnitude bias is not present.

For $G_{SW}^{\uparrow}$ (Fig. 37), the cases with UCM have smaller error than bulk during mid-day, attributable to differences in α. The bulk scheme has f_{urb}=1, but no accounting for buildings, roads, or other surfaces as with UCM, and so only the 'Urban and Built-Up' LULC where α=0.15 is attributed. Meanwhile, the three UCM cases use input values of α for road, roof and wall, unlike the bulk scheme. The Noah LSM then accounts for f_{urb}, and non-urban fraction (1-f_{urb}) contributions to α. Thus differences between PHX-A and PHX-B are due solely to f_{urb} since α is identical for these two cases. Differences between default and the PHX-A/B cases are due to constituent values of α, along with building size and road width.

The modeled $G_{LW}^{\uparrow}$ (Fig. 38) has an afternoon under-prediction bias near 10%, and inter-parameterization bias is significantly reduced the most during Pre-monsoon Summer 2012 afternoon unstable period, yet still under-predicted (Fig. 38d) . Furthermore, and more significantly for UCM cases than for bulk, the $|P_D|$ of YSU-MM5 tends to be smaller than MYJ-Eta overnight, but not during afternoon unstable periods. This result occurs for both seasons (Fig. 38c,d) , and is more pronounced for the winter period (Fig. 38c) , which has longer stable conditions than during the summer period (not shown).

Evaluation of terms in Eq. 5.5 can reveal issues with model bias which are masked by bias cancelation within T_{2m}. T_0 is examined with $G_{LW}^{\uparrow}$ (Fig. 38) as per Eq. 5.1. Bias of $G_{LW}^{\uparrow}$ depends on f_{urb} in nocturnal periods. Also, bias in $G_{LW}^{\uparrow}$ has a PBL-SLS dependence, with the role of f_{urb} either reduced during the day, or the role of PBL-SLS stability class

becoming a factor. There are several feedbacks for T_0, including stability profiles, $\langle Q_H \rangle$, and C_H. These variables are an aggregate of the UCM representation of the underlying urban fabric and the Noah contribution.

A sensitivity to f_{urb} is apparent within $G^{\uparrow}_{LW}$ (Fig. 38), which, based upon (Eq. 5.1), is most sensitive to T_0, and otherwise first order to f_{urb} through flux aggregation. For this particular neighborhood, the PHX-A/B shows improved results over the default case. The bulk scheme yields a systematic 10-20% bias below observations which persists all day and for both seasons. Employing UCM for Phoenix reduces error compared to bulk, though not as significantly for Pre-monsoon Summer 2012 mid-day periods. The tendency in terms of $|P_D|$, where P_D uses Eq. 5.3, is that PHX-B $\leq$ PHX-A $\leq$ bulk, for a given PBL-SLS case, except during mid-day Pre-monsoon Summer 2012 where they are statistically indistinguishable. Thus, at night, the higher f_{urb} PHX-B is warmer than PHX-A, seen both for T_0 via $G^{\uparrow}_{LW}$ (Fig. 38), and for $T_{2\text{m}}$ (Fig. 35).

The previously discussed $G^{\downarrow}_{SW}$ bias (not shown) should lead to an over-predicted T_0, but $G^{\uparrow}_{LW}$ has an under-prediction bias (Fig. 38). By examination of $\langle Q_H \rangle$ during nocturnal Pre-monsoon Summer 2012 (Fig. 40), modeled values employing YSU-MM5 deviate from the MYJ-Eta cases, with the YSU-MM5 cases tending to have increased $\langle Q_H \rangle$ compared to both observations and the MYJ-Eta cases. The inter-PBL-SLS case difference in T_0 for a fixed urban case (Fig. 38) must arise in $T_{2\text{m}}$ owing to Eq. 5.5. However, $\langle Q_H \rangle$ (Fig. 40) also indicates overestimated daytime heating for the larger f_{urb} case PHX-B, and an overestimation of $\langle Q_E \rangle$ (Fig. 40) arises from the lower f_{urb} case PHX-A. These results indicates that the UCM scheme is missing physical mechanisms by which T_0 was increased (with coefficient f_{urb}), or the bias is arising from the non-urban "natural" contribution. One approach to reduce T_0 bias is to explore models beyond UCM that incorporate other afternoon processes that would increase $G^{\uparrow}_{LW}$ by modifying the effective T_0. Alternately,

Wang et al. 2011 demonstrated that T_0 is most sensitive to uncertainties in urban geometry, thermal properties of surface materials, and roughness lengths, which suggests other values in Table 3 may lead to systematic bias.

The u^* term within C_H, is another source of bias for T_{2m}, and compares well with observations (Fig. 39). The UCM cases have lower u^* than for bulk, owing to increased roughness length. Afternoon magnitude of u^* for PHX-B is less than u^* for PHX-A, owing to f_{urb}. Both PHX-A/B cases were closer to observations than bulk during daytime and especially during Pre-monsoon Summer 2012. However, nocturnal periods were poorly represented by all cases as observations show intermittent increases in u^*, as in simulations, but a relation between events cannot be determined without more detailed observations. Stable nocturnal period dynamics are notoriously poorly modeled, a shortcoming which is suspected to be contributing to these errors in u^*.

For the $\langle Q_H \rangle$ term as a component of bias in T_{2m} (Eq. 5.5), stable nocturnal periods show a bias dependent upon PBL-SLS for $\langle Q_H \rangle$ (Fig. 40), which is much larger than the f_{urb} influence on $\langle Q_H \rangle$. Here, YSU-MM5 has an increased bias, typically under-predicting observed $\langle Q_H \rangle$ compared to MYJ-Eta, which often over-predicted observations. Negative $\langle Q_H \rangle$ values indicate a release of heat from the surface, and so the bias due to PBL-SLS would lead to a warmer T_{2m} for YSU-MM5 than for MYJ-Eta. These PBL-SLS dependent differences in $\langle Q_H \rangle$ reduce during mid-day unstable periods, where f_{urb} becomes the dominant parameter for $\langle Q_H \rangle$ (Fig. 40), and UCM case differences are low for T_{2m} (Fig. 35).

Figure 40a shows the $\langle Q_H \rangle$ diurnal cycle dependence on both urban land surface representation and PBL-SLS, with increased divergence of P_D between PBL-SLS cases during stable nocturnal periods with YSU-MM5 under-predicting observations (Fig. 40b) . During afternoon period, both PHX-A/B cases show close agreement with observations,

with the lower f_{urb} PHX-A having better agreement during late-afternoon, while both yield comparable predictions at night. The late-afternoon difference can be understood by the larger f_{urb} leading to increased heat transfer from the atmosphere to the urban canopy. A similar argument based upon f_{urb} applies to the default UCM case, which under-predicts daytime observations; and the bulk case, which over-predicts daytime observations.

The role of f_{urb} apparent in $\langle Q_E \rangle$ bias (Fig. 40c) where moisture arises from the "natural" (i.e. non-urban) LULC via the Noah scheme. This explaination is clearly demonstrated by the bulk scheme reporting $\langle Q_E \rangle$=0. There is no significant difference between the two PBL-SLS schemes noted for $\langle Q_E \rangle$ or $\langle Q_H \rangle$. Moreover, the agreement with observations for $\langle Q_E \rangle$ indicate that the larger f_{urb} (lower non-urban fraction) PHX-B gives better results than PHX-A, opposite to what was concluded by examining $\langle Q_H \rangle$. This contradiction suggests that the contribution of vegetation is being over-represented within the non-urban component and yields a point of caution encountered in modeling arid cities, especially given that the soil moisture was initialized too low (.1 m^3 m^{-3} in top layer) compared to observed values (lowest value long after rain events approaches .1 m^3 m^{-3}, Chow et al. 2014), and no irrigation was applied.

Q^* (Fig. 41), exhibits mixed bias during daylight and nocturnal periods, also dependent upon which PBL-SLS and urban representation were employed. Similar results are present in the Winter period simulations, but with a shift that reduces mid-day over-prediction bias and increasing nocturnal under-prediction bias (not shown). Cases and times where the bias errors in Q^* (Fig. 41-42) are comparable to or smaller than the bias in the individual radiative flux terms is a result of bias error cancelation (e.g. MYJ-Eta PHX-B at night for $G_{LW}^{\uparrow}$, $G_{LW}^{\downarrow}$, and Q^*), which influences the evaluation of variables composed of differences between terms. Thus, assessing Q^* in absentia of considering the constituent radiative flux components will not provide a robust model evaluation. Furthermore, it is

difficult to disentangle potential sources of model error within the radiation forcing by solely examining bias in Q^*. For instance, an overestimation bias in solar focing by the $G_{SW}^{\downarrow}$ term, and an underestimation bias in radiative cooling by the $G_{LW}^{\uparrow}$ term, may both lead to an overestimation of energy at the surface, and may be related to an overestimation of convective cooling by the $\langle Q_H \rangle$ term.

For ΔQ_s (Fig. 41), the Pre-monsoon Summer 2012 PHX-B configuration is more consistent all day than other cases, with bulk being furthest from observations. Afternoon observed values are between PHX-A and PHX-B, indicating an intermediate f_{urb} would more closely reproduce ΔQ_s. Furthermore, the bulk case with MYJ-Eta was seen to reduce errors in the pre-dawn period compared to YSU-MM5. Also, PHX-A with lower f_{urb} value often had lower $|P_D|$ during nighttime compared to PHX-B.

The combination of terms in Eq. 5.2 used to derive ΔQ_s (Fig. 41) result in mixed performance between urban representation. The ordering of modeled ΔQ_s bias correlates with the f_{urb}, with the observed values of ΔQ_s being between PHX-A and PHX-B. Choice of PBL-SLS has small significance in ΔQ_s, due to the $\langle Q_H \rangle$ and Q^* terms, as insignificant variations arose within $\langle Q_E \rangle$ (Fig. 40). Partial bias canceling is obscuring the $G_{LW}^{\uparrow}$ and $G_{LW}^{\downarrow}$ bias contributions to error within Q^*. Bias canceling is more complex within ΔQ_s which is also influenced by $\langle Q_H \rangle$ and $\langle Q_E \rangle$ terms (Fig. 41). Hence, assessing ΔQ_s, along with SEB closure, can be challenging without exploring bias in all terms. Similar conclusions are drawn for SEB terms $\langle Q_H \rangle$, $\langle Q_E \rangle$,ΔQ_s, and Q^* during Winter 2011 (not shown).

Figure 42 and Figure 43 show the influence of model parameterization on mean percent difference model bias error metric $M(\cdot)$ for the entire diurnal cycle derived using Eq. 5.6 along with standard deviation errorbars with value of 1σ for the variance of the 30-minute diurnal mean P_D values. From these data, the effect of Δ_H on the error metric $M(.)$ Eq. 5.6 is small compared to the variance (Fig. 5.6). These figures demonstrate that

the largest influence of bias canceling between terms which comprise T_{2m} in Eq. 5.5, with variables T_0 and $\langle Q_H \rangle$, for which we have already examined diurnal P_D at 1 km resolution. Examining Figure 42, $M(T_{2m})$ is typically similar for $M(G_{LW}^{\uparrow})$, while one order of magnitude less than $M(\langle Q_H \rangle)$. Bias of other terms from which T_{2m} is derived (not shown) would modify the $\langle Q_H \rangle$ term component bias, and the magnitude of this bias canceling effect. Bias canceling within Q^* is most apparent in cases where $M(G_{LW}^{\uparrow})$ increases, yet, $M(Q^*)$ decreases, as with the bulk scheme. Figure 42 shows the tendency for $M(Q^*;\text{bulk}) \lesssim M(Q^*;\text{PHX-A/B})$ for a given season and PBL-SLS, yet, $M(Q^*;\text{PHX-A/B}) \lesssim M(Q^*;\text{bulk})$, with $M(G_{LW}^{\downarrow})$, $M(G_{SW}^{\downarrow})$, and $M(G_{SW}^{\uparrow})$, largely unchanged for a given season and PBL-SLS. Furthermore, Figure 42 is useful for assessing where models perform poorly, by seeking variables and cases with large values of M.

5.3.2 Effect of Model Spatial Resolution

Figure 42 also shows the influence of model domain resolution (Δ_H) on $M(\cdot)$. From these data, the effect of Δ_H on $M(\cdot)$ is insignificant, for all of the variables examined, aside from T_{2m} for Summer YSU-MM5 PHX-A, where 333 m showed minor improvement over coarser resolutions (Fig. 42e) . However, small differences ($< 1\sigma$) in the mean values are observed between the different Δ_H for some variables (Fig. 42). From this insignificant convergence or divergence with varying Δ_H, we infer that surface layer variables are not significantly sensitive to the aforementioned Terra-Incognita resolution-dependent issues with turbulence closure at the temporal and spatial resolution of observations. We hypothesize that evaluation of models at fine-scales is limited when model resolution surpasses resolution of either the observation footprint or mixing length scales within physical parameterization schemes.

5.4 Conclusion

We have performed an evaluation of the WRF model through a comparison of model simulations with observational data derived from a flux-tower within a high-intensity residential LULC neighborhood within the Phoenix metropolitan area for a range of diurnal and seasonal solar forcing during calm weather periods. An analysis of diurnal and seasonal model errors was performed for T_{2m}, along with the radiative flux components and the SEB terms. Evaluation of WRF simulations with observations was performed for horizontal model grid resolutions, Δ_H, ranging from 9 km to 333 m. We determined that it is computationally feasible to perform real-time simulations with 5 nested domains to Δ_H=333 m for 40 vertical levels using modern cluster architecture.

Diagnostic values such as T_{2m} are derived by an evaluation of the stability profile. Given the diurnal nature of surface-layer stability, and the fact that the profiles change their form with stability, bias may appear in one stability regime but not in another. Therefore, although a particular model may compare well with observed T_{2m} for a given stability regime, this evaluation is incomplete and possibly misleading without detailed SEB comparisons, as was demonstrated by the bulk cases. Furthermore, T_{2m} is influenced by bias canceling between the T_0, $\langle Q_H \rangle$, and C_H variables. For this reason, we show that solely evaluating model performance based upon diagnostic variables, such as T_{2m}, is not sufficient, and can in fact lead to incorrect conclusions on model evaluation. We also show that model evaluation can benefit by enabling more detailed assessment of model errors when considering the individual downward, in addition to upward (C S B Grimmond et al. 2011), shortwave and longwave radiation components, as opposed to just evaluating net radiation. Errors in Q^* may be hidden, since longwave and shortwave net radiation

components may also give rise to bias canceling between individual components, with each term having different mechanisms of bias.

Little effect was produced with decreasing Δ_H in our analysis despite entering the Terra-Incognita. This scale independence indicates that the modeled SEB terms are dominated by the local representation of the land surface and radiative forcing over any resolution-dependent turbulence dynamics influence. Furthermore, since the model does not change surface flux profile relationships at finer-scales, any resolution-dependent dynamics which may be present within the simulation above the surface layer must have weakly coupled feedback to the surface layer. Detection of Δ_H sensitivity within our analysis is limited by the averaging time, and footprint of observations, which at .5-1 km is near the larger scale of the described Terra-Incognita regime. Lastly, these results suggest that simulation at Δ_H=333 m seems to not clearly improve results with the parameterizations examined.

Our results indicate that YSU-MM5 tends to perform better than MYJ-Eta, and that UCM performs better than bulk for SEB terms and $G^{\uparrow}_{LW}$. The UCM shows sensitivity to choice of f_{urb} value, which for some variables (e.g. $\langle Q_E \rangle$, $\langle Q_H \rangle$, ΔQ_s) had larger daytime influence than PBL scheme. UCM (for PHX-A/B) and the bulk scheme, combined with YSU-MM5, give similar results for $\mathrm{T_{2m}}$. The bulk with MYJ-Eta also performed well. However, when evaluating the diurnal cycle of other variables (e.g. $G^{\uparrow}_{SW}$, $G^{\uparrow}_{LW}$, u^*, $\langle Q_H \rangle$, $\langle Q_E \rangle$), it is clear that UCM performs better than bulk during daytime. This conclusion regarding bulk versus UCM cannot be drawn when only examining the mean diurnal error, suggesting that evaluating the diurnal cycle is needed for improved model assessment of SEB. Our results also indicate that evaluation or consideration of model configuration for arid cities needs to include SEB terms not just $\mathrm{T_{2m}}$. All model configurations should represent urban heat island, since they all have urban representation. However, we did not

analyze for this effect. Decreasing Δ_H below 1 km does not substantially improve simulation results with the PBL-SLS and urban parameterizations tested. This null result might be due to PBL scheme mixing and smoothing of small scales. Thus, a better parameterization adapted for sub-kilometer grid-scales needs to be tested, and suggests that if improvement is sought at finer scales, that parameterizations need to be adapted for these scales. However, further investigation of parameterization (such as employing turbulent kinetic energy closure) needs to be performed before any definitive conclusion regarding the benefit of finer-scale resolution on T_{2m} and SEB terms can be achieved.

Application of irrigation could provide starting points for improvement of $\langle Q_E \rangle$, $\langle Q_H \rangle$, and $G_{LW}^{\uparrow}$. It would be necessary to prescribe irrigation for both mesic residential classes and in agricultural areas. However, availability of necessary gridded water use input data may be problematic. Scenarios exploring the limiting case of maintaining or periodically recharging to maximum field capacity, or basing soil moisture upon vegetation wilting point, may provide alternative means to supplement available input water-use data. In particular, the impact from a water management perspective could be explored by imposing irrigation either with a constant daily input or with a seasonal daily input, following the work of Volo et al. 2013 for both xeric and mesic LULCs.

Evaluation of fine-scale modeling is ultimately limited by simultaneously controlling for: 1) model physics parameterization and fundamental turbulence theory, 2) input data parameterization, 3) model resolution and filters, 4) observation resolution and siting, 5) anthropogenic influence. The 5th limiting factor contains aspects of the first two factors. Salient anthropogenic factors include LULC modifications, particularly urbanization (buildings, impervious surfaces, modified landscapes, etc.) and cropland. With some specific aspects that are anticipated to play an important role in improving model predictions, and in need of further investigation, being, irrigation of croplands and

vegetation; energy input and waste heat within the urban area; representation of urban parameters within models from values readily derived from observations; pollutants and air quality influencing radiative forcing and to a smaller degree air temperature. Model resolution was not seen to have a significant impact on SEB terms for the observation footprint considered.

Acknowledgment

This work was supported by the National Science Foundation (NSF) under EaSM grants EF-1049251 awarded to Arizona State University (ASU) and EF-1049224 to University of California Riverside, and by NSF grant DMS 1419593 awarded to ASU. Flux tower data is available from Central Arizona-Phoenix Long-Term Ecological Research (site manager Phil Torrant) with funding provide by grant CAP3: BCS-1026865 and by NSF via EaSM grant EF-1049251. We also thank for their input on this work T. Volo, E. Vivoni, F. Salamanca, S. Earl, and the anonymous reviewers. We thank the WRF group at the National Center for Atmospheric Research for providing the WRF code.

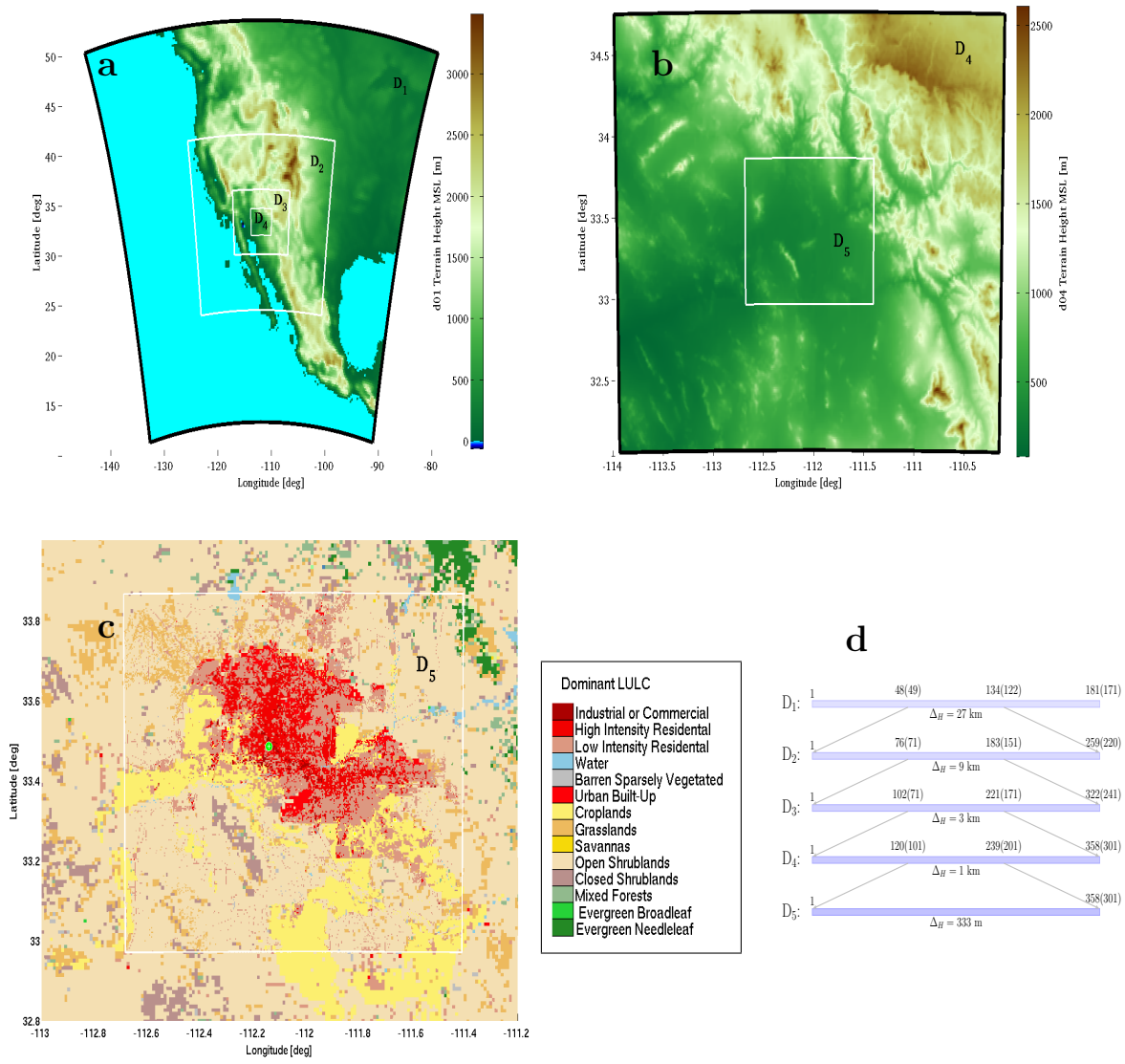

Figure 34: WRF Domain nest positions (with D1 center at 33.5 °N, 112 °W) overlaid on terrain height above mean sea level [m] for D1 to D4 (a), and, D5 within D4 (b). Dominant LULC (c) given in legend (bottom middle) at grid resolution of D4 to D5, and the West Phoenix flux-tower location (green circle, 33.484°N, 112.143°W). A schematic indicating nesting by horizontal grid index, denoted by indices for East-West with North-South within parenthesis, for D1 to D5 with resolution Δ_H indicated (d).

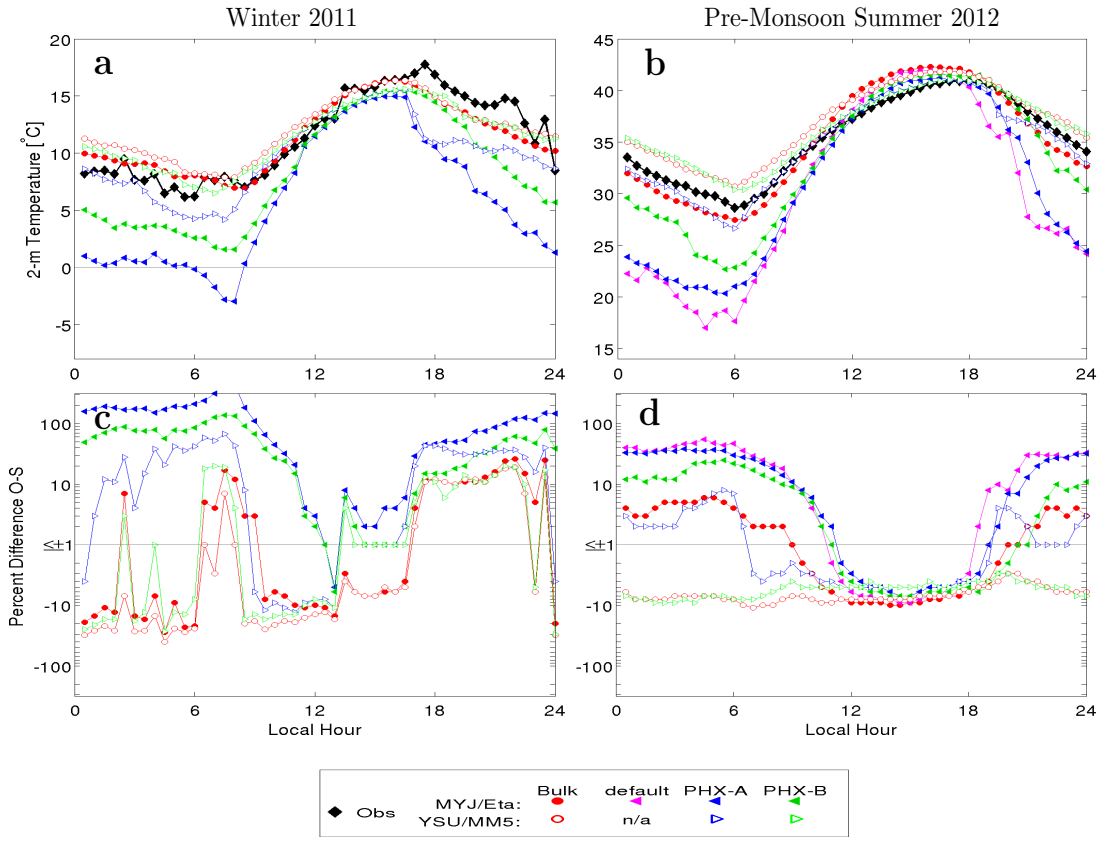

Figure 35: Comparison of surface layer 2-meter temperature, T_{2m}, between observed and simulated values, for D4 (Δ_H=1 km) as 30-minute and diurnally averaged values (a,b), and percent differences of simulations from observations (c,d), for Winter 2011 (a,c) and Pre-monsoon Summer 2012 (b,d). Shown are observed values (black diamonds), PBL-SLS for MYJ-Eta (solid symbols) and YSU-MM5 (open symbols), with bulk urban scheme (red circles), and UCM urban scheme (triangles) for configurations of default (magenta, Pre-monsoon Summer 2012 MYJ-Eta only), PHX-A (blue), and PHX-B (green), summarized in the legend (bottom). Note that percent difference ordinate scale is limited to $\pm$120% and has been made logarithmic preserving sign following Eq. 5.4.

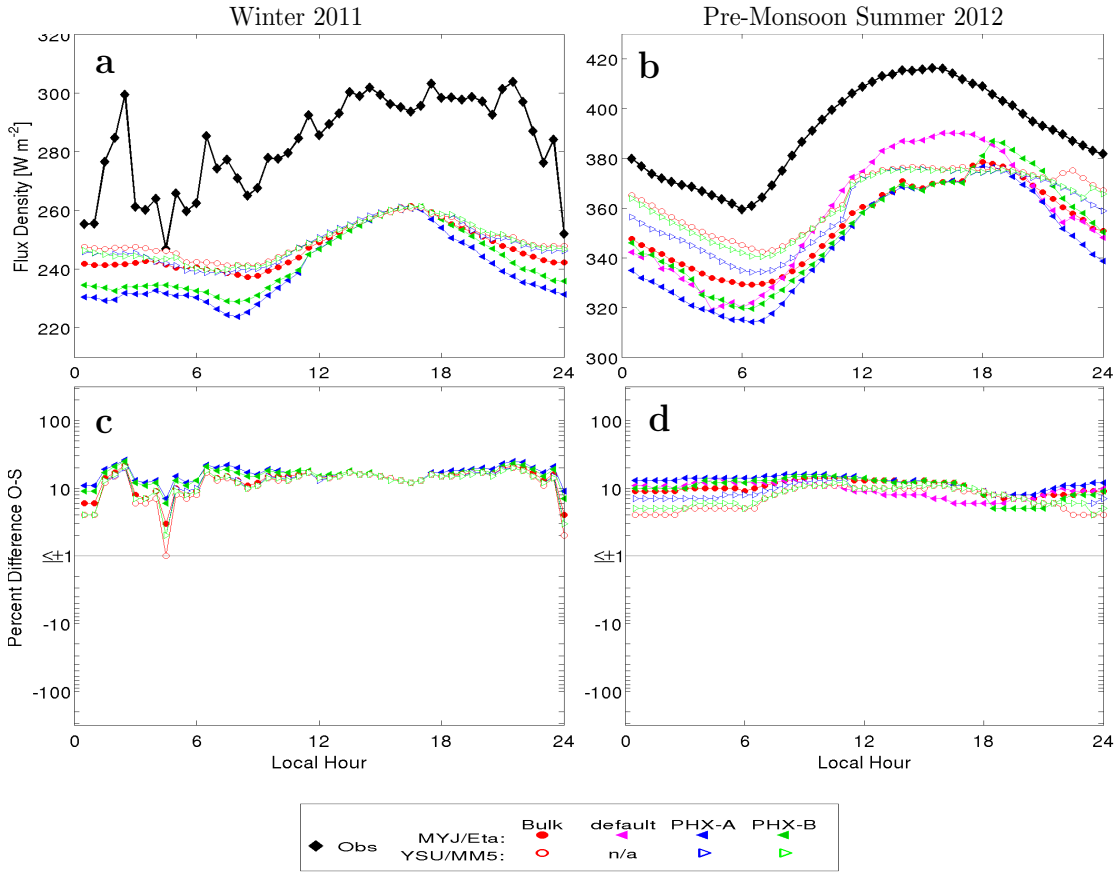

Figure 36: Same as in Figure 35 but for $G_{LW}^{\downarrow}$.

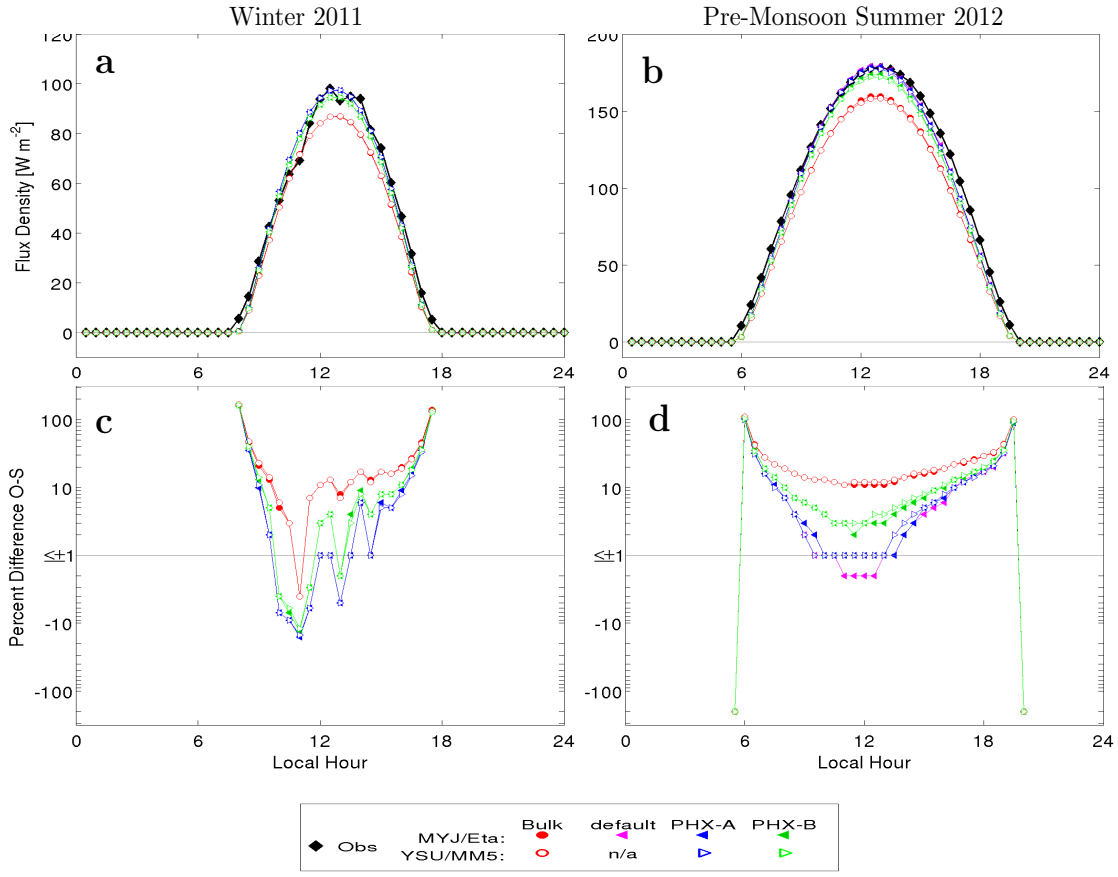

Figure 37: Same as in Figure 35 but for $G_{SW}^{\uparrow}$.

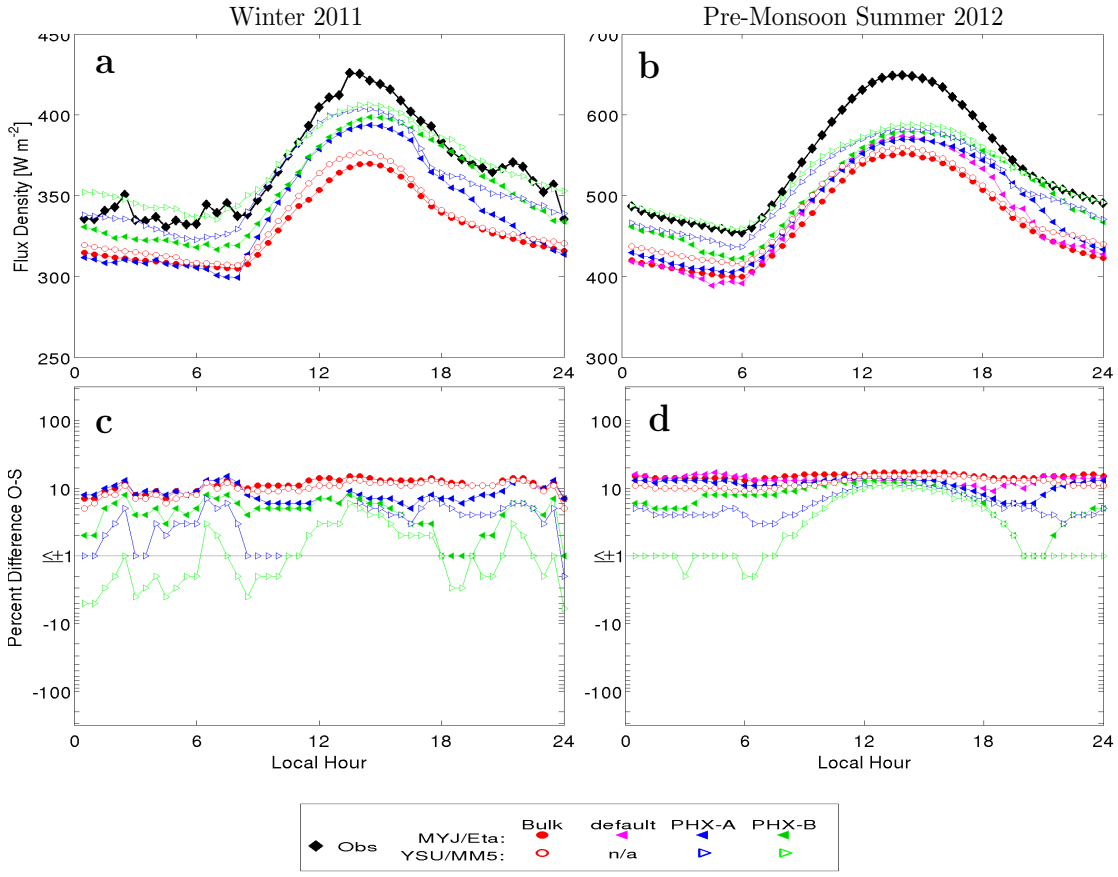

Figure 38: Same as in Figure 35 but for $G_{LW}^{\uparrow}$.

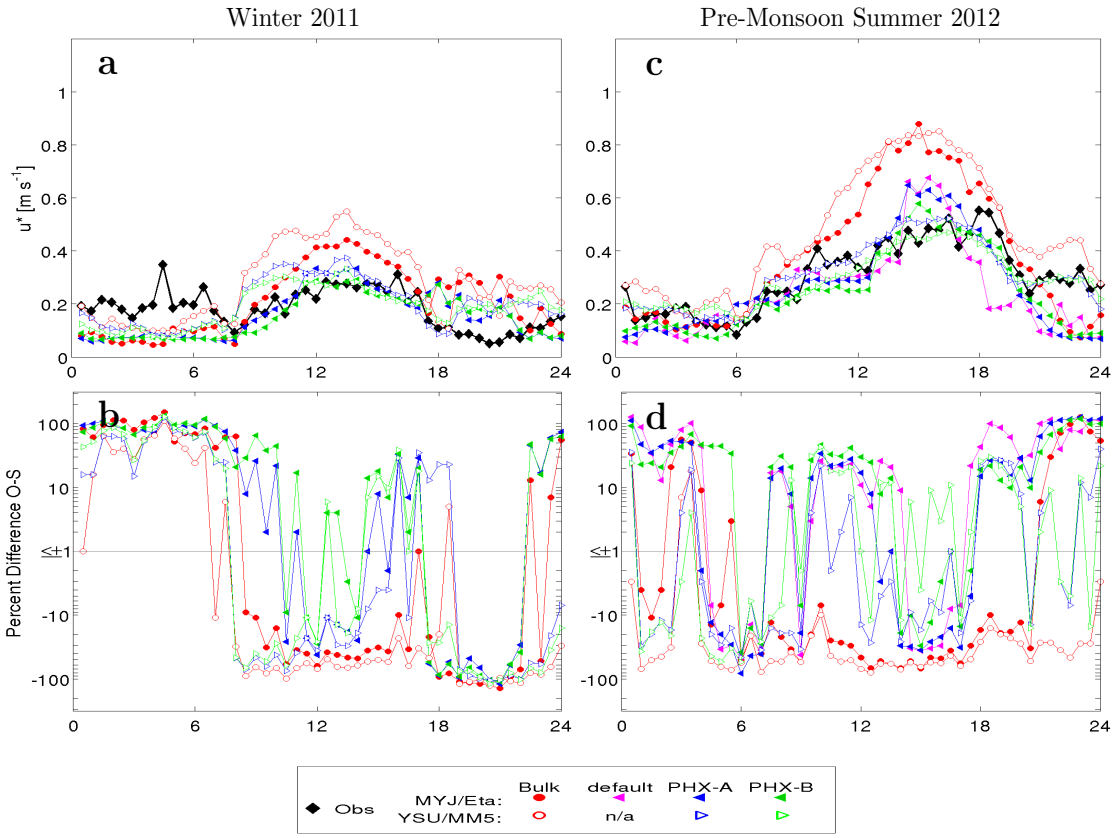

Figure 39: Same as in Figure 35 but for u^*.

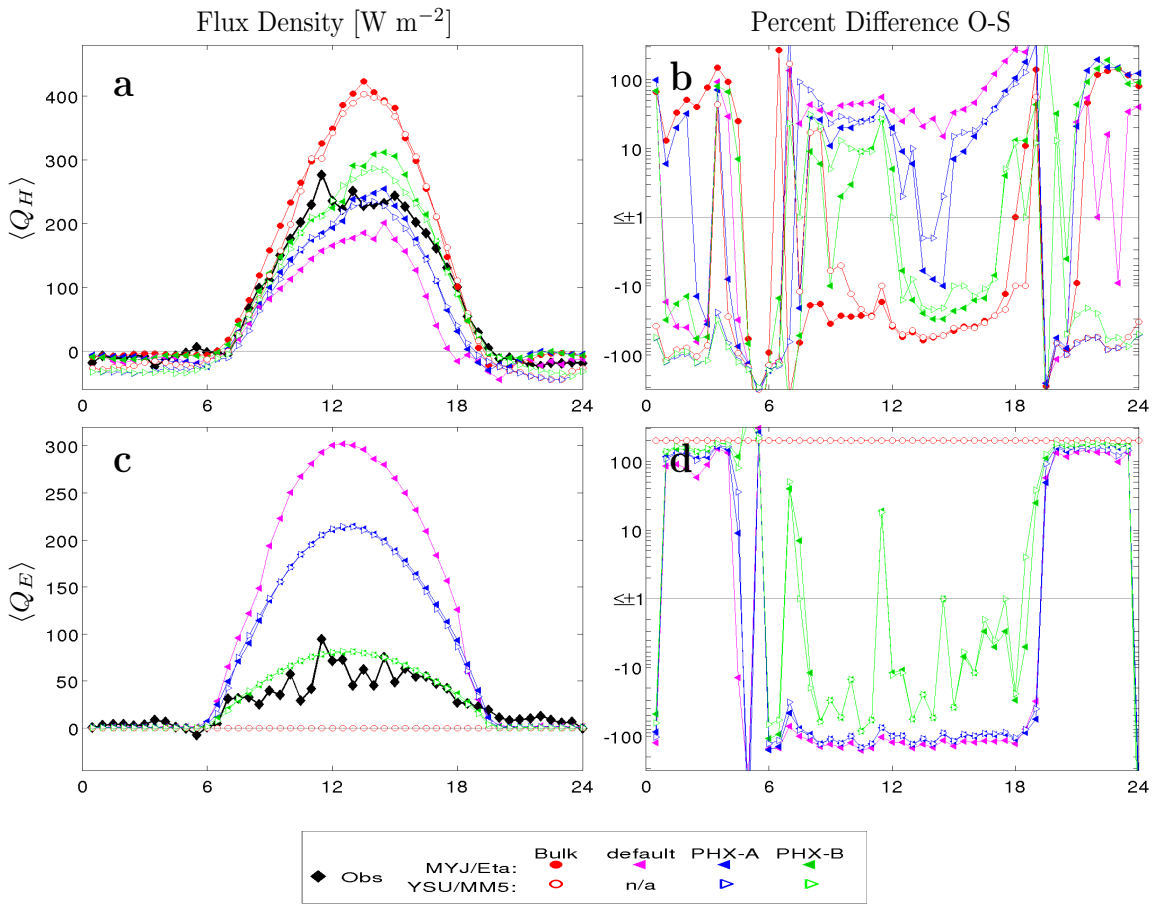

Figure 40: Same as Figure 35 but only for during Pre-monsoon Summer 2012 and for 30-minute and diurnally averaged observed and simulated values (a,c), and percent difference of simulations from observations (b,d), for $\langle Q_H \rangle$ (a,b), and $\langle Q_E \rangle$ (c,d).

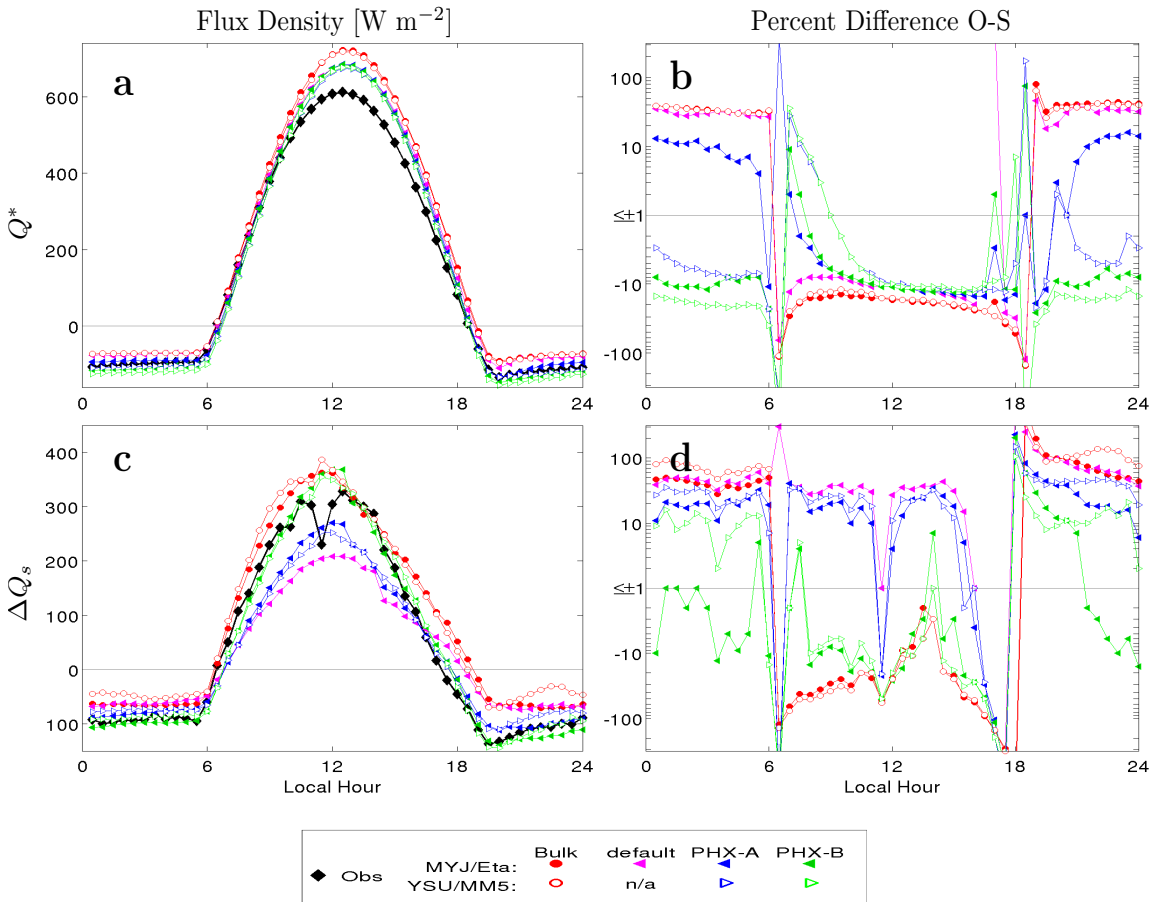

Figure 41: Similar to Figure 40 but for Q^* (a,b), and ΔQ_s (c,d), top to bottom, respectively.

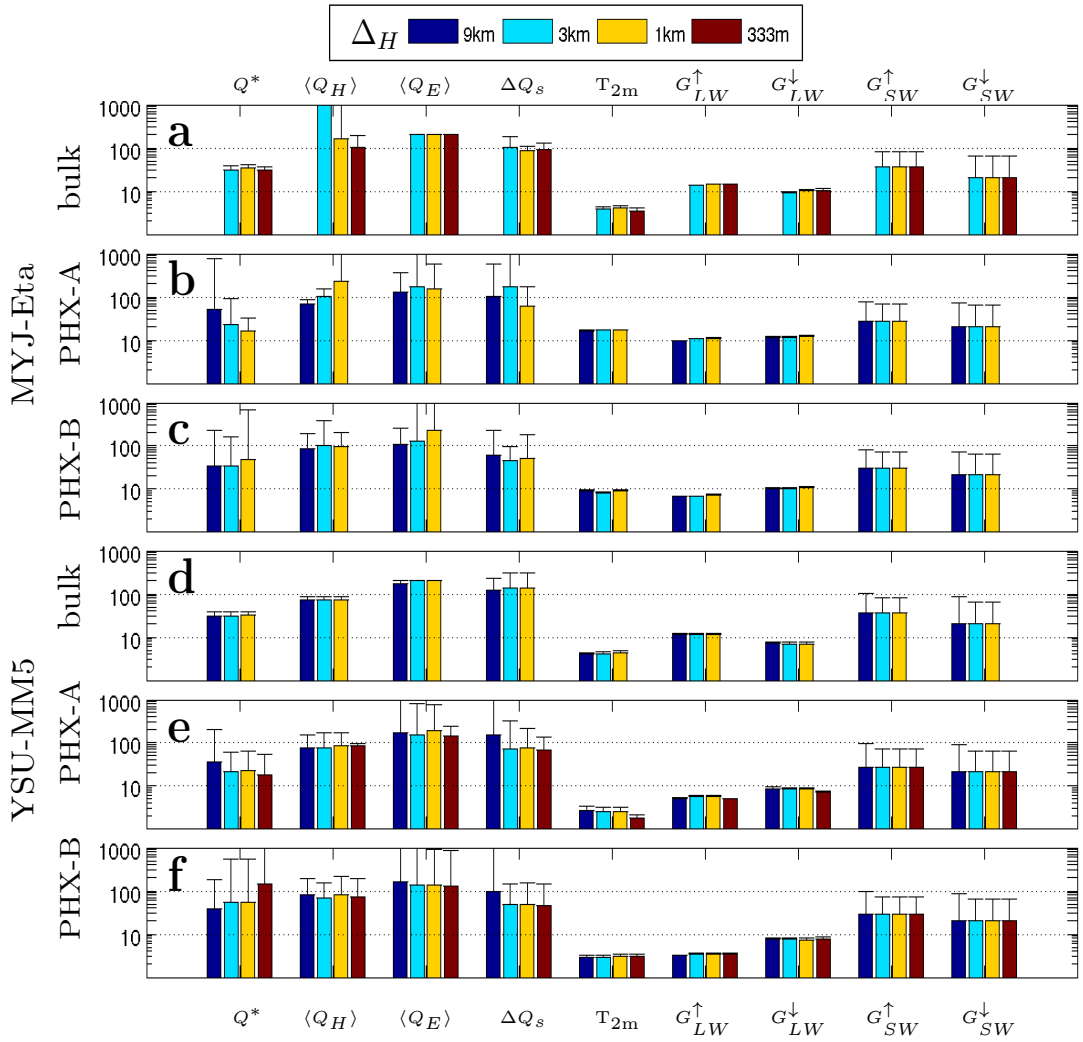

Figure 42: Error metric M (Eq. 5.6) as diurnal mean absolute percent difference between observations and simulations, for Pre-monsoon Summer 2012, for horizontal grid resolutions, Δ_H, of 9, 3, 1 km, and 333 m when available, for model configurations MYJ-Eta bulk (a), MYJ-Eta PHX-A (b), MYJ-Eta PHX-B (c), YSU-MM5 bulk (d), YSU-MM5 PHX-A (e), and YSU-MM5 PHX-B (f), and for variables Q^*, $\langle Q_H \rangle$, $\langle Q_E \rangle$, ΔQ_s, T_{2m}, $G^{\uparrow}_{LW}$, $G^{\downarrow}_{LW}$, $G^{\uparrow}_{SW}$, $G^{\downarrow}_{SW}$, left-to-right, respectively, for pre-monsoon summer 2012. Note that 9 km MYJ bulk output was only reported hourly and is excluded from this analysis.

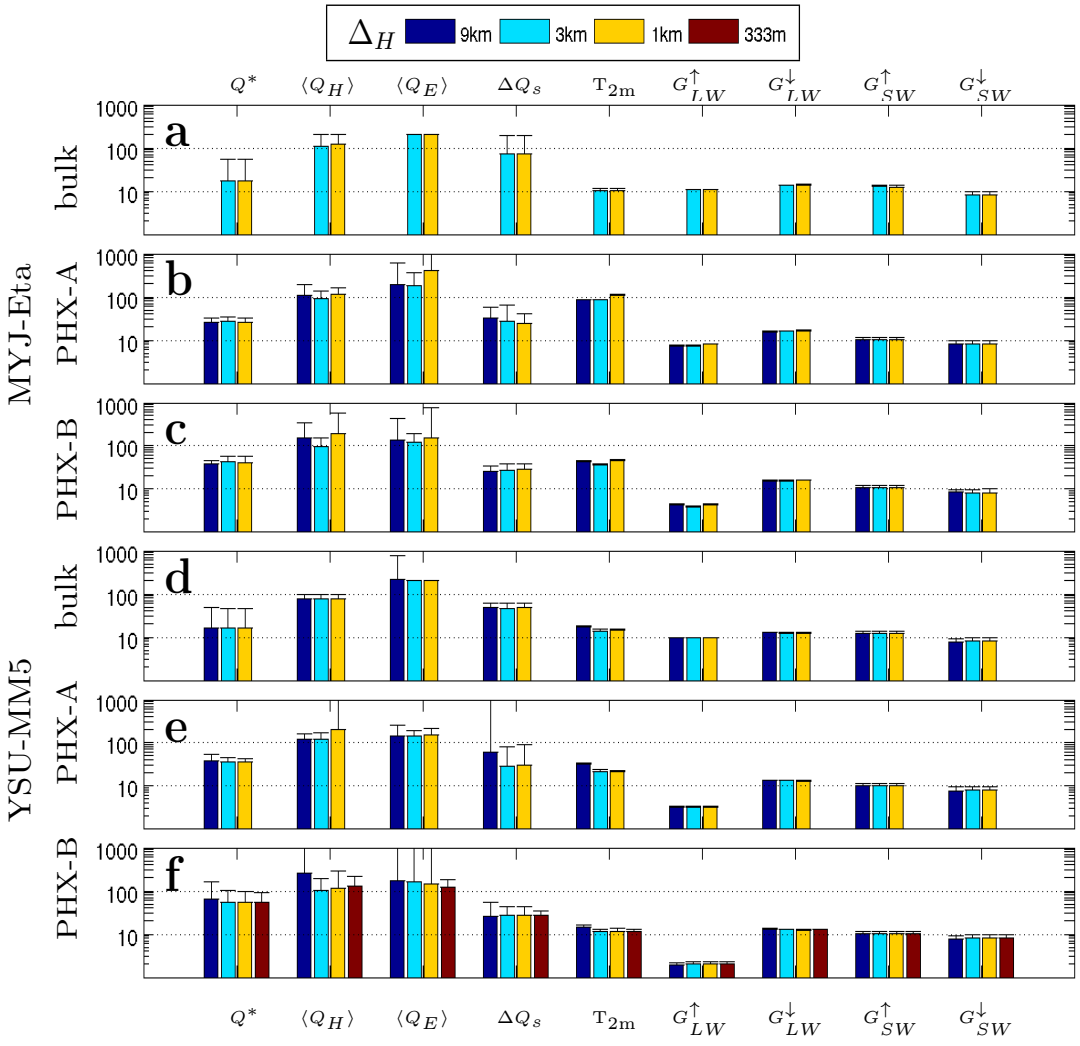

Figure 43: Same as for Figure 42 but for Winter 2011.

REFERENCES

ADEQ. 2000. *Final serious area ozone state implementation plan for Maricopa County.* Technical report. Arizona Department of Environmental Quality.

———. 2001. *Phoenix area PM10 Nonattainment - Agricultural Best Management Practices.* Technical report. Arizona Department of Environmental Quality.

Arizona, Republic. 2014. "Valley dust problems ease: County's air quality improving; EPA poised to relax scrutiny." *Arizona Republic,* no. Jan. 16: 1, 3.

Arnfield, A John. 2003. "Two decades of urban climate research: a review of turbulence, exchanges of energy and water, and the urban heat island." *Int. J. Climatol.* 23 (1): 1–26. doi:10.1002/joc.859.

Arya, S. Pal. 1988. *Introduction to micrometeorology.* 303. San Diego: Academic Press, Inc., San Diego.

Attenborough, K., K.M. Li, and K. Horoshenkov. 2007. *Predicting outdoor Sound.* London: Taylor / Francis, London, 441 p.

Babisch, Wolfgang, Bernd Beule, Marianne Schust, Norbert Kersten, and Hartmut Ising. 2005. "Traffic noise and risk of myocardial infarction." *Epidemiology* 16 (1): 33–40.

Babisch, Wolfgang, Wim Swart, Danny Houthuijs, Jenny Selander, Gösta Bluhm, Göran Pershagen, Konstantina Dimakopoulou, et al. 2012. "Exposure modifiers of the relationships of transportation noise with high blood pressure and noise annoyance." *The Journal of the Acoustical Society of America* 132 (6): 3788–3808. doi:10.1121/1.4764881.

Banta, Robert M., Lisa S. Darby, Jerome D. Fast, James O. Pinto, C. David Whiteman, William J. Shaw, and Brad W. Orr. 2004. "Nocturnal Low-Level Jet in a Mountain Basin Complex. Part I: Evolution and Effects on Local Flows." *J. Appl. Meteor.* 43:1348–1365. doi:10.1175/JAM2142.1.

Bao, J-W., S. A. Michelson, P. O. G. Persson, I. V. Djalalova, and J. M. Wilczak. 2008. "Observed and WRF-Simulated Low-Level Winds in a High-Ozone Episode during the Central California Ozone Study." *J. Appl. Meteor. Climatol.* 47 (9): 2372–2394. doi:10.1175/2008JAMC1822.1.

Barnosky, Anthony D., Elizabeth A. Hadly, Jordi Bascompte, Eric L. Berlow, James H. Brown, Mikael Fortelius, Wayne M. Getz, et al. 2012. "Approaching a state shift in Earth's biosphere." *Nature* 486:52–58. doi:10.1038/nature11018.

Beljaars, Anton. 1995. “The parametrization of surface fluxes in large-scale models under free convection.” *Quart. J. Roy. Meteor. Soc.* 121 (522): 255–270.

Berglund, Birgitta, Thomas Lindvall, and Dietrich H. Schwela. 1999. *Guidelines for community noise.* Geneva: World Health Organization.

Boer, L.C. den, and A. Schroten. 2007. *Traffic noise reduction in Europe.* Netherlands: C.E. Delft.

Bou-Zeid, Elie, Jan Overney, Benedict D Rogers, and Marc B Parlange. 2009. “The effects of building representation and clustering in large-eddy simulations of flows in urban canopies.” *Boundary-Layer Meteor.* 132 (3): 415–436.

Bowman, J.J., T.B.A. Senior, and P.L.E. Uslenghi, eds. 1987. *Electromagnetic and Acoustic Scattering by Simple Shapes.* Revised. New York: Hemisphere Publishing Corporation, New York, 728p.

Bracher, Astrid, M Sinnhuber, A Rozanov, and JP Burrows. 2005. “Using a photochemical model for the validation of NO 2 satellite measurements at different solar zenith angles.” *Atmos. Chem. Phys.* 5 (2): 393–408.

Brazel, A. J., H. J. S. Fernando, J. C. R. Hunt, N. Selover, B. C. Hedquist, and E. Pardyjak. 2005. “Evening Transition Observations in Phoenix, Arizona.” *J. Appl. Meteor.* 44:99–112. doi:10.1175/JAM-2180.1.

Brazel, AJ, and WG Nickling. 1986. “The relationship of weather types to dust storm generation in Arizona (1965–1980).” *J. Climate* 6 (3): 255–275.

Bremmer, Pamela, Jacqueline F. Byers, and Ermalynn Kiehl. 2003. “Noise and the Premature Infant: Physiological Effects and Practice Implications.” *J. Obstetric, Gynecologic, & Neonatal Nursing* 32 (4): 447–454.

Bronzaft, A.L. 1981. “The effect of a noise abatement program on reading ability.” *Journal of Environmental Psychology* 1 (3): 215–222.

Bronzaft, Arline L. 2011. “The Noise From Wind Turbines: Potential Adverse Impacts on Children’s Well-Being.” *Bulletin of Science, Technology & Society* 31 (4): 291–295.

Bronzaft, Arline L., and Dennis P. McCarthy. 1975. “The effect of elevated train noise on reading ability.” *Environment and Behavior* 7 (4): 517–527.

Burian, Steven J, Srinivas Pradeep Velugubantla, and Michael J Brown. 2002. *Morphological analyses using 3D building databases: Phoenix, Arizona.* Technical report. LA-UR-02-6726, Los Alamos National Laboratory, Los Alamos, New Mexico.

Businger, J, JC Wyngaard, Y Izumi, and Edward F Bradley. 1971. “Flux-profile relationships in the atmospheric surface layer.” *J. Atmos. Sci.* 28 (2): 181–189.

Byun, Daewon, and Kenneth L Schere. 2006. “Review of the governing equations, computational algorithms, and other components of the Models-3 Community Multiscale Air Quality (CMAQ) modeling system.” *Applied Mechanics Reviews* 59 (1/6): 51.

C. Steele. 2001. “A critical review of some traffic noise prediction models.” *Appl. Acoust.* 62:271–287.

Chandler-Wilde, S.N., and D.C. Hothersall. 1995. “Efficient calculation of the Green function for acoustic propagation above a homogeneous impedance plane.” *J. Sound Vib.* 180 (5): 705–724. doi:10.1006/jsvi.1995.0110.

Chen, Fei, Robert Bornstein, CSB Grimmond, Ju Li, Xudong Liang, ALBERTO Martilli, SHIGUANG Miao, James Voogt, and Yingchun Wang. 2012. “Research priorities in observing and modeling urban weather and climate.” *Bull. Amer. Meteor. Soc.* 93 (11): 1725–1728. doi:10.1175/BAMS-D-11-00217.1.

Chen, Fei, and Jimu Dudhia. 2001. “Coupling and advanced land surface-hydrology model with the Penn State-NCAR MM5 modeling system. Part I: Model implementation and sensitivity.” *Mon. Wea. Rev.* 129 (4): 569–585. doi:10.1175/1520-0493(2001)129<0569:CAALSH>2.0.CO;2.

Chen, Fei, Hiroyuki Kusaka, Robert Bornstein, Jason Ching, C. S. B. Grimmond, Susanne Grossman-Clarke, Thomas Loridan, et al. 2011. “The integrated WRF/urban modelling system: development, evaluation, and applications to urban environmental problems.” *Int. J. Climatol.* 31 (2): 273–288. doi:10.1002/joc.2158.

Chen, Fei, and Ying Zhang. 2009. “On the coupling strength between the land surface and the atmosphere: From viewpoint of surface exchange coefficients.” *Geophys. Res. Lett.* 36 (10): L10404. doi:10.1029/2009GL037980.

Chen, Yingying, Kun Yang, Degang Zhou, Jun Qin, and Xiaofeng Guo. 2010. “Improving the Noah land surface model in arid regions with an appropriate parameterization of the thermal roughness length.” *J. Hydrometeor.* 11 (4): 995–1006.

Ching, J. K. S. 2013. “A perspective on urban canopy layer modeling for weather, climate and air quality applications.” *Urban Climate* 3:13–39. doi:10.1016/j.uclim.2013.02.001.

Ching, Jason, Michael Brown, Timothy McPherson, Steven Burian, Fei Chen, Ron Cionco, Adel Hanna, Torrin Hultgren, David Sailor, Haider Taha, et al. 2009. "National urban database and access portal tool." *Bulletin of the American Meteorological Society* 90 (8): 1157–1168.

Chow, Winston T. L., Dean Brennan, and Anthony J Brazel. 2012. "Urban heat island research in Phoenix, Arizona: Theoretical contributions and policy applications." *Bull. Amer. Meteor. Soc.* 93 (4): 517–530. doi:10.1007/s00704-010-0293-8.

Chow, W.T.L., T.J. Volo, E.R. Vivoni, G.D. Jenerette, and B.L. Ruddell. 2014. "Seasonal Dynamics Of A Suburban Energy Balance In Phoenix, Arizona." *Int. J. Climatol.* In Press. doi:10.1002/joc.3947.

Clain, G., J.-L. Baray, R. Delmas, P. Keckhut, and J.-P. Cammas. 2010. "A lagrangian approach to analyse the tropospheric ozone climatology in the tropics: Climatology of stratosphere–troposphere exchange at Reunion Island." *Atmos. Environ.* 44 (7): 968–975. doi:10.1016/j.atmosenv.2009.08.048.

Clements, Andrea L, Matthew P Fraser, Nabin Upadhyay, Pierre Herckes, Michael Sundblom, Jeffrey Lantz, and Paul A Solomon. 2013. "Characterization of Summertime Coarse Particulate Matter in the Desert Southwest–Arizona, USA." *Journal of the Air & Waste Management Association,* no. just-accepted.

Cohen, Barney. 2004. "Urban growth in developing countries: a review of current trends and a caution regarding existing forecasts." *World Development* 32 (1): 23–51. doi:10.1016/j.worlddev.2003.04.008.

Coutts, Andrew M, Jason Beringer, and Nigel J Tapper. 2007. "Impact of increasing urban density on local climate: spatial and temporal variations in the surface energy balance in Melbourne, Australia." *J. Appl. Meteor. Climatol.* 46 (4): 477–493.

Crutzen, Paul J. 2002. "Geology of mankind." *Nature* 415 (6867): 23–23. doi:10.1038/415023a.

Dahlback, Arne, and Knut Stamnes. 1991. "A new spherical model for computing the radiation field available for photolysis and heating at twilight." *Planet. Space Sci.* 39 (5): 671–683. doi:10.1016/0032-0633(91)90061-E.

Davies, Huw C. 1983. "Limitations of some common lateral boundary schemes used in regional NWP models." *Mon. Wea. Rev.* 111 (5): 1002–1012. doi:10.1175/1520-0493(1983)111<1002:LOSCLB>2.0.CO;2.

De Bruin, HAR, RJ Ronda, and BJH Van De Wiel. 2000. “Approximate solutions for the Obukhov length and the surface fluxes in terms of bulk Richardson numbers.” *Boundary-Layer Meteor.* 95 (1): 145–157.

De Young, Raymond. 1999. “Tragedy of the commons.” In *Encylopedia of Environmental Science,* edited by David E. Alexander and Rhodes W. Fairbridge, 601–602. Http://hdl.handle.net/2027.42/83704. Dordrecht: Kluwer Academic Publishers. doi:10.1007/1-4020-4494-1_328.

Delany, M. E., and E. N. Bazley. 1970. “Acoustical properties of fibrous absorbent materials.” *Appl. Acoust.* 3 (2): 105–116. doi:10.1016/0003-682X(70)90031-9.

Di Sabatino, S., E. Solazzo, P. Paradisi, and R. Britter. 2008. “A Simple Model for Spatially-averaged Wind Profiles Within and Above an Urban Canopy.” *Boundary-Layer Meteor.* 127 (1): 131–151. doi:10.1007/s10546-007-9250-1.

Dragani, R., G. Redaelli, G. Visconti, A. Mariotti, V. Rudakov, A. R. MacKenzie, and L. Stefanutti. 2002. “High-resolution stratospheric tracer fields reconstructed with lagrangian techniques: a comparative analysis of predictive skill.” *J. Atmos. Sci.* 59:1943–1958.

Dritschel, David G. 1988. “Contour surgery: A topological reconnection scheme for extended integrations using contour dynamics.” *J. Comput. Phys.* 77 (1): 240–266. doi:10.1016/0021-9991(88)90165-9.

Dudhia, Jimy. 1989. “Numerical study of convection observed during the Winter Monsoon Experiment using a mesoscale two-dimensional model.” *J. Atmos. Sci.* 46 (20): 3077–3107. doi:10.1175/1520-0469(1989)046<3077:NSOCOD>2.0.CO;2.

Dyer, A.J., and B.B. Hicks. 1970. “Flux-gradient relationships in the constant flux layer.” *Quart. J. Roy. Meteor. Soc.* 96:715–721.

Embleton, Tony F. W. 1996. “Tutorial on sound propagation outdoors.” *J. Acoust. Soc. Am.* 100 (1): 31–48. doi:10.1121/1.415879.

Engling, Guenter, and András Gelencsèr. 2010. “Atmospheric Brown Clouds: From Local Air Pollution to Climate Change.” *Elements* 6.

Eskridge, R.E., and J.C.R. Hunt. 1979. “Highway modeling, Part 1: Prediction of velocity and turbulence fields in the wake of vehicles.” *J. Appl. Meteor.* 18 (4): 387–400. doi:10.1175/1520-0450(1979)018<0387:HMPIPO>2.0.CO;2.

Etzel, Ruth A. 1997. “American Academy of Pediatrics, Committee on Environmental Health. Noise a hazard for the fetus and newborn.” *Pediatrics* 100 (4): 724–726. doi:10.1542/peds.100.4.724.

F. de Roo and I. Noordhoek. 2003. “Harmonoise WP2-reference sound propagation model.” *Fortschritte Der Akustik* 29:354–355.

Fernando, H. J. S. 2008. “Polimetrics: the quantitative study of urban systems (and its applications to atmospheric and hydro environments).” *Environ. Fluid Mech.* 8 (5-6): 397–409. doi:10.1007/s10652-008-9116-1.

———. 2010. “Fluid Dynamics of Urban Atmospheres in Complex Terrain.” *Annu. Rev. Fluid Mech.* 42:365–389. doi:10.1146/annurev-fluid-121108-145459.

Fernando, Harindra J S, Brett Verhoef, Silvana Di Sabatino, Laura S Leo, and Seoyeon Park. 2013. “The Phoenix evening transition flow experiment (TRANSFLEX).” *Boundary-Layer Meteor.* 147 (3): 443–468. doi:10.1007/s10546-012-9795-5.

Fernando, Harindra, Marko Princevac, and Ronald Calhoun. 2007. “Atmospheric Measurements.” In *Springer Handbook of Experimental Fluid Mechanics,* edited by Cameron Tropea, Alexander L. Yarin, and John F. Foss, 1157–1178. Springer Berlin Heidelberg. 10.1007/978-3-540-30299-5_17.

Fernando, HJS, SM Lee, J Anderson, M Princevac, E Pardyjak, and S Grossman-Clarke. 2001. “Urban fluid mechanics: Air circulation and contaminant dispersion in cities.” *Environ. Fluid Mech.* 1 (1): 107–164. doi:10.1023/A:1011504001479.

Fernando, HJS, MC Mammarella, G Grandoni, P Fedele, R Di Marco, R Dimitrova, and P Hyde. 2012. “Forecasting PM< sub> 10</sub> in metropolitan areas: Efficacy of neural networks.” *Environmental Pollution* 163:62–67.

Foken, Thomas. 2008. “The energy balance closure problem: An overview.” *Ecolog. Appl.* 18 (6): 1351–1367. http://www.jstor.org/stable/40062260.

Forman, Richard T. T., and Robert D. Deblinger. 2000. “The Ecological Road-Effect Zone of a Massachusetts (U.S.A.) Suburban Highway.” *Conserv. Biol.* 14 (1): 36–46. http://www.jstor.org/stable/2641902.

Fry, J., G. Xian, S. Jin, J. Dewitz, C. Homer, L. Yang, C. Barnes, N. Herold, and J. Wickham. 2011. “Completion of the 2006 National Land Cover Database for the Conterminous United States.” *Photogramm. Eng. Remote Sens.* 77 (9): 858–864.

Gauvreau, B., M. Bérengier, P. Blanc-Benon, and C. Depollier. 2002. “Traffic noise prediction with the parabolic equation method: Validation of a split-step Pade approach in complex environments.” *J. Acoust. Soc. Am.* 112 (6): 2680–2687.

Georgescu, M., M. Moustaoui, A. Mahalov, and J. Dudhia. 2011. “An alternative explanation of the semiarid urban area “oasis effect”.” *J. Geophys. Res.* 116:D24113. doi:10.1029/2011JD016720.

Georgescu, M, M Moustaoui, A Mahalov, and J Dudhia. 2013. “Summer-time climate impacts of projected megapolitan expansion in Arizona.” *Nat. Clim. Change* 3 (1): 37–41. doi:10.1038/NCLIMATE1656.

Gilbert, K. E., and X. Di. 1993. “A fast Green’s function method for one-way sound propagation in the atmosphere.” *J. Acoust. Soc. Am.* 94:2343–2352.

Gilbert, K.E., and M.J. White. 1989. “Application of the parabolic equation to sound propagation in a refracting atmosphere.” *J. Acoust. Soc. Am.* 85 (2): 630–637. doi:10.1121/1.397587.

Goines, L., and L. Hagler. 2007. “Noise pollution: A modern plague.” *Southern Medical Journal* 100:287–294.

Golden, Jay S. 2004. “The built environment induced urban heat island effect in rapidly urbanizing arid regions–a sustainable urban engineering complexity.” *Environ. Sci.* 1 (4): 321–349. doi:10.1080/15693430412331291698.

Granados, J. A. T. 1998. “Reducing automobile traffic: an urgent policy for health promotion.” *Rev. Panam Salud Publica* 3:227–241.

Grell, G.A., J. Dudhia, and D. R. Stauffer. 1994. *A description of the Fifth-Generation Penn State/NCAR Mesoscale Model (MM5).* NCAR Technical Note NCAR/TN-398+STR, pp. 121. December.

Grell, Georg A, Steven E Peckham, Rainer Schmitz, Stuart A McKeen, Gregory Frost, William C Skamarock, and Brian Eder. 2005. “Fully coupled “online” chemistry within the WRF model.” *Atmos. Environ.* 39 (37): 6957–6975.

Grimm, Nancy B, Stanley H Faeth, Nancy E Golubiewski, Charles L Redman, Jianguo Wu, Xuemei Bai, and John M Briggs. 2008. “Global change and the ecology of cities.” *Science* 319 (5864): 756–760. doi:10.1126/science.1150195.

Grimmond, C S B, M Blackett, M J Best, J-J Baik, S E Belcher, J Beringer, S I Bohnenstengel, et al. 2011. “Initial results from Phase 2 of the international urban energy balance model comparison.” *Int. J. Climatol.* 31 (2): 244–272. doi:10.1002/joc.2227.

Grimmond, C. S. B., M. Blackett, M. J. Best, J. Barlow, J.-J. Baik, S. E. Belcher, S. I. Bohnenstengel, et al. 2010. “The International Urban Energy Balance Models Comparison Project: First Results from Phase 1.” *J. Appl. Meteor. Climatol.* 49:1268–1292. doi:10.1175/2010JAMC2354.1.

Grimmond, C S B, and Timothy R Oke. 1999. “Aerodynamic properties of urban areas derived from analysis of surface form.” *J. Appl. Meteor. Climatol.* 38 (9): 1262–1292. doi:10.1175/1520-0450(1999)038<1262:APOUAD>2.0.CO;2.

Grossman-Clarke, S., J.A. Zehnder, T. Loridan, and C.S.B. Grimmond. 2010. “Contribution of Land Use Changes to Near-Surface Air Temperatures during Recent Summer Extreme Heat Events in the Phoenix Metropolitan Area.” *J. Appl. Meteor. Climatol.* 49:1649–1664. doi:10.1175/2010JAMC2362.1.

Grossman-Clarke, Susanne, Joseph A Zehnder, William L Stefanov, Yubao Liu, and Michael A Zoldak. 2005. “Urban modifications in a mesoscale meteorological model and the effects on near-surface variables in an arid metropolitan region.” *J. Appl. Meteor. Climatol.* 44 (9): 1281–1297. doi:10.1175/JAM2286.1.

Gryning, Sven-Erik, Ekaterina Batchvarova, Burghard Brümmer, Hans Jørgensen, and Søren Larsen. 2007. “On the extension of the wind profile over homogeneous terrain beyond the surface boundary layer.” *Boundary-Layer Meteor.* 124 (2): 251–268.

Haines, M M, S A Stansfeld, J Head, and R F S Job. 2002. “Multilevel modelling of aircraft noise on performance tests in schools around Heathrow Airport London.” *J. Epidemiol. Community Health* 56 (2): 139–144.

Halfwerk, W., L.J.M. Holleman, C.M. Lessells, and H. Slabbekoorn. 2011. “Negative impact of traffic noise on avian reproductive success.” *J. Appl. Ecol.* 48:210–219.

Hardin, Garrett. 1968. “The tragedy of the commons.” *Science* 162 (3859): 1243–1248. doi:10.1126/science.162.3859.1243.

Hart, Jaime E., Stephanie E. Chiuve, Francine Laden, and Christine M. Albert. 2014. “Roadway Proximity and Risk of Sudden Cardiac Death in Women.” *Circulation.* doi:10.1161/CIRCULATIONAHA.114.011489.

Hatch, L., C. Clark, R. Merrick, S. Van Parijs, D. Ponirakis, K. Schwehr, M. Thompson, and D. Wiley. 2008. "Characterizing the relative contributions of large vessels to total ocean noise fields: a case study using the Gerry E. Studds Stellwagen Bank National Marine Sanctuary." *Atmos. Environ.* 42:735–752.

Hemida, Hassan, and Chris Baker. 2010. "Large-eddy simulation of the flow around a freight wagon subjected to a crosswind." *Computers & Fluids* 39 (10): 1944–1956. doi:10.1016/j.compfluid.2010.06.026.

Hildebrand, John A. 2009. "Anthropogenic and natural sources of ambient noise in the ocean." *Marine Ecol. Prog. Ser.* 395:5–20.

Hole, Lars R., and Gard Hauge. 2003. "Simulation of a morning air temperature inversion break-up in complex terrain and the influence on sound propagation on a local scale." *Appl. Acoust.* 64 (4): 401–414. doi:10.1016/S0003-682X(02)00104-4.

Holtslag, A. A. M., and H. A. R. de Bruin. 1988. "Applied Modeling of the Nighttime Surface Energy Balance over Land." *J. Appl. Meteor.* 27 (June): 689–704. doi:10.1175/1520-0450(1988)027<0689:AMOTNS>2.0.CO;2.

Hong, Song-You, Jimy Dudhia, and Shu-Hua Chen. 2004. "A Revised Approach to Ice Microphysical Processes for the Bulk Parameterization of Clouds and Precipitation." *Mon. Wea. Rev.* 132 (1): 103–120. doi:10.1175/1520-0493(2004)132<0103:ARATIM>2.0.CO;2.

Hong, Song-You, Ying Noh, and Jimy Dudhia. 2006. "A New Vertical Diffusion Package with an Explicit Treatment of Entrainment Processes." *Mon. Wea. Rev.* 134 (9): 2318–2341. doi:10.1175/MWR3199.1.

Hsu, NC, R Gautam, AM Sayer, C Bettenhausen, C Li, MJ Jeong, S-C Tsay, and BN Holben. 2012. "Global and regional trends of aerosol optical depth over land and ocean using SeaWiFS measurements from 1997 to 2010." *Atmos. Chem. Phys.* 12 (3): 8465–8501.

Hu, Xiao-Ming, John W. Nielsen-Gammon, and Fuqing Zhang. 2010. "Evaluation of Three Planetary Boundary Layer Schemes in the WRF Model." *J. Appl. Meteor. Climatol.* 49 (9): 1831–1844. doi:10.1175/2010JAMC2432.1.

Hunt, Julian C., Yulia V. Timoshkina, Sylvia I. Bohnenstengel, and Stephen Belcher. 2012. "Implications of climate change for expanding cities world-wide." *Proc. Inst. Civil Eng. - Urban Design Planning* 166 (DP4): 241–254. doi:10.1680/udap.10.00062.

Hygge, S. 2011. “Noise and cognition in children.” Edited by J.O. Nriagu. *Encyclopedia of Environmental Health* 4:146–151.

Hygge, Staffan, Gary W. Evans, and Monika Bullinger. 2002. “A Prospective Study of Some Effects of Aircraft Noise on Cognitive Performance in Schoolchildren.” *Psychological Science* 13 (5): 469–474.

Iglesias Merchan, Carlos, Luis Diaz-Balteiro, and Mario Soliño. 2014. “Noise pollution in national parks: Soundscape and economic valuation.” *Landscape and Urban Planning* 123:1–9.

Ising, H, B Kruppa, et al. 2004. “Health effects caused by noise: evidence in the literature from the past 25 years.” *Noise and Health* 6 (22): 5.

J. Chambers, H. Saurenman, R. Bronsdon, L. Sutherland, K. Gilbert, R. Waxler, and C. Talmadge. 2006. “Effects of temperature induced inversion conditions on suburban highway noise levels.” *Acta Acust. Acust.* 92:1060–1070.

J. Wang and J. Angell. 1999. “Air Stagnation Climatology for the United States (1948-1998).” *NOAA/Air Resources Laboratory, Atlas No. 1, Silver Spring, MD.*

Janjic, Z.I. 1994. “The step-mountain Eta coordinate model: Further developments of the convection, viscous sublayer, and turbulence closure schemes.” *Mon. Wea. Rev.* 122 (5): 927–945. doi:10.1175/1520-0493(1994)122<0927:TSMECM>2.0.CO;2.

———. 1996. “The surface layer in the NCEP Eta Model.” In *Eleventh Conference on Numerical Weather Prediction,* 354–355. Norfolk, VA: American Meteorological Society, August.

———. 2001. *Nonsingular Implementation of the Mellor-Yamada Level 2.5 Scheme in the NCEP Meso model.* Technical report 437. December. NCEP Office Note, December.

Jiménez, Pedro A, Jimy Dudhia, J Fidel González-Rouco, Jorge Navarro, Juan P Montávez, and Elena García-Bustamante. 2012. “A revised scheme for the WRF surface layer formulation.” *Mon. Wea. Rev.* 140 (3): 898–918. doi:10.1175/MWR-D-11-00056.1.

K. Attenborough. 2002. “Sound propagation close to the ground.” *Annu. Rev. Fluid Mech.* 34:51–82. doi:10.1146/annurev.fluid.34.081701.143541.

Kain, J. S. 2004. “The Kain-Fritsch convective parameterization: An update.” *J. Appl. Meteor.* 43 (1): 170–181. doi:10.1175/1520-0450(2004)043<0170:TKCPAU>2.0.CO;2.

Kalma, Jetse D, Tim R McVicar, and Matthew F McCabe. 2008. “Estimating land surface evaporation: A review of methods using remotely sensed surface temperature data.” *Surveys Geophys.* 29 (4-5): 421–469. doi:10.1007/s10712-008-9037-z.

Kato, S., and N.G. Loeb. 2003. “Twilight irradiance reflected by the Earth estimated from clouds and the Earth’s radiant energy system (CERES) measurements.” *J. Climate* 16:2646–2650.

Kaufman, Y. J., D. Tanré, B. N. Holben, S. Mattoo, L. A. Remer, T. F. Eck, J. Vaughan, and B. Chatenet. 2002. “Aerosol radiative impact on spectral solar flux at the surface, derived from principal-plane sky measurements.” *J. Atmos. Sci.* 59:635–646.

Klemp, J. B., W. C. Skamarock, and J. Dudhia. 2007. “Conservative split-explicit time integration methods for the compressible nonhydrostatic equations.” *Mon. Wea. Rev.* 135 (8): 2897–2913. doi:10.1175/MWR3440.1.

Kusaka, Hiroyuki, and Fujio Kimura. 2004. “Coupling a Single-Layer Urban Canopy Model with a Simple Atmospheric Model: Impact on Urban Heat Island Simulation for an Idealized Case.” *J. Meteor. Soc. Japan* 82 (1): 67–80. doi:10.2151/jmsj.82.67.

Latha, K. Madhavi, and K.V.S. Badarinath. 2005. “Shortwave radiative forcing efficiency of urban aerosols-a case study using ground based measurements.” *Chemosphere* 58:217–220.

Lee, Sang-Mi, Harindra J.S. Fernando, Marko Princevac, Dragan Zajic, Michela Sinesi, Jennifer L. Mcculley, and James Anderson. 2003. “Transport and Diffusion of Ozone in the Nocturnal and Morning Planetary Boundary Layer of the Phoenix Valley.” *Environ. Fluid Mech.* 3 (4): 331–362. doi:10.1023/A:1023680216173.

Lee, Sang-Mi, and HJS Fernando. 2013. “Dispersion of an Urban Photochemical Plume in Phoenix Metropolitan Area.” *Atmos. Environ.* 80:152–160. doi:10.1016/j.atmosenv.2013.07.066.

Li, Y.L., S.J. Franke, and C.H. Liu. 1993. “Wave scattering from a ground with a Gaussian bump or trough in an inhomogeneous medium.” *J. Acoust. Soc. Am.* 94 (2): 1067–1075.

Lienhart, Hermann, and Stefan Becker. 2003. “Flow and turbulence structure in the wake of a simplified car model.” *Soc. Automot. Eng.* 112 (6): 785–796.

Lihoreau, Bertrand, Benoit Gauvreau, Michel Bérengier, Philippe Blanc-Benon, and Isabelle Calmet. 2006. “Outdoor sound propagation modeling in realistic environments: Application of coupled parabolic and atmospheric models.” *J. Acoust. Soc. Am.* 120 (110): 110–119. doi:10.1121/1.2204455.

Liu, Yubao, Fei Chen, Thomas Warner, and Jeffrey Basara. 2006. "Verification of a mesoscale data-assimilation and forecasting system for the Oklahoma City area during the Joint Urban 2003 field project." *J. Appl. Meteor. Climatol.* 45:912–929.

Loridan, Thomas, Fredrik Lindberg, Oriol Jorba, Simone Kotthaus, Susanne Grossman-Clarke, and CSB Grimmond. 2013. "High Resolution Simulation of the Variability of Surface Energy Balance Fluxes Across Central London with Urban Zones for Energy Partitioning." *Boundary-Layer Meteor.* 147 (3): 493–523. doi:10.1007/s10546-013-9797-y.

Luber, George, and Michael McGeehin. 2008. "Climate change and extreme heat events." *Am. J. Prev. Med.* 35 (5): 429–435. doi:10.1016/j.amepre.2008.08.021.

M. West and Y. Lam. 2000. "Prediction of sound fields in the presence of terrain features which produce a range dependent meteorology using the generalised terrain parabolic equation (GT-PE) model." *Proceedings of Inter-Noise 2000* 2:943.

Madsen, P. T., M. Wahlberg, J. Tougaard, K. Lucke, and P. Tyack. 2006. "Wind turbine underwater noise and marine mammals: implications of current knowledge and data needs." *Marine Ecol. Prog. Ser.* 309:279–295.

MAG. 2007. *Eight-hour ozone plan for the Maricopa Nonattainment Area.* Technical report. Maricopa Association of Governments.

———. 2008. *PM-10 Source Attribution and Deposition Study.* Technical report. Maricopa Association of Governments.

———. 2013. *2013 Carbon monoxide maintenance plan for the Maricopa County area.* Technical report. Maricopa Association of Governments.

Mahalov, A., and M. Moustaoui. 2010. "Characterization of atmospheric optical turbulence for laser propagation." *Laser Photonics Rev.* 4 (1): 144–159. doi:10.1002/lpor.200910002.

Mahalov, A., M. Moustaoui, and V. Grubišić. 2011. "A numerical study of mountain waves in the upper troposphere and lower stratosphere." *Atmos. Chem. Phys.* 11 (11): 5123–5139. doi:10.5194/acp-11-5123-2011.

Mahalov, Alex, and Mohamed Moustaoui. 2009. "Vertically nested nonhydrostatic model for multiscale resolution of flows in the upper troposphere and lower stratosphere." *J. Comput. Phys.* 228 (4): 1294–1311. doi:10.1016/j.jcp.2008.10.030.

Mateshvili, Nina, Didier Fussen, Filip Vanhellemont, Christine Bingen, Erkki Kyrölä, Iuri Mateshvili, and Giuli Mateshvili. 2005. "Twilight sky brightness measurements as a useful tool for stratospheric aerosol investigations." *J. Geophys. Res.: Atmos.* 110 (D9). doi:10.1029/2004JD005512.

Mattick, Carolyn S, Eric Williams, and Braden R Allenby. 2009. "Energy and civilization: A history of energy production and consumption in a global cultural, technological and economic context." In *Sustainable Systems and Technology, 2009. ISSST'09. IEEE International Symposium on,* 1–6. IEEE. doi:10.1109/ISSST.2009.5156766.

McGregor, Peter K, Andrew G Horn, Marty L Leonard, and Frank Thomsen. 2013. "Anthropogenic noise and conservation." In *Animal Communication and Noise,* 409–444. Springer. doi:10.1007/978-3-642-41494-7_14.

Mellor, G.L., and T. Yamada. 1982. "Development of a turbulence closure model for geophysical fluid problems." *Rev. Geophys. Space Phys.* 20 (4): 851–875.

Michalakes, J., J. Dudhia, D. Gill, T. Henderson, J. Klemp, W. Skamarock, and W. Wang. 2004. "The Weather Research And Forecast Model: Software Architecture And Performance." In *Use Of High Performance Computing In Meteorology,* edited by Walter Zwieflhofer and George Mozdzynski, 156–168. Proceedings of the Eleventh ECMWF Workshop. Available online at http://wrf-model.org/wrfadmin/docs/ecmwf_2004.pdf. Reading, UK: European Centre for Medium-Range Weather Forecasts, World Scientific, 25-29 October.

Minguez, M., R. Pasquetti, and E. Serre. 2008. "High-order large-eddy simulation of flow over the "Ahmed body" car model." *Phys. Fluids* 20, 095101 (9): 095101. doi:10.1063/1.2952595.

Mirocha, Jeff, Branko Kosović, and Gokhan Kirkil. 2014. "Resolved Turbulence Characteristics in Large-Eddy Simulations Nested within Mesoscale Simulations Using the Weather Research and Forecasting Model." *Mon. Wea. Rev.* 142 (2): 806–831. doi:10.1175/MWR-D-13-00064.1.

Mitchell Jr, J Murray. 1971. "The effect of atmospheric aerosols on climate with special reference to temperature near the Earth's surface." *J. Appl. Meteorol* 10 (4): 703–714.

Mlawer, Eli J., Steven J. Taubman, Patrick D. Brown, Michael J. Iacono, and Shepard A. Clough. 1997. "Radiative transfer for inhomogeneous atmospheres: RRTM, a validated correlated-k model for the longwave." *J. Geophys. Res.* 102 (D14): 16663–16682. doi:10.1029/97JD00237.

Moeng, CH, Jimy Dudhia, Joe Klemp, and Peter Sullivan. 2007. "Examining two-way grid nesting for large eddy simulation of the PBL using the WRF model." *Mon. Wea. Rev.* 135 (6): 2295–2311. doi:10.1175/MWR-D-13-00064.1.

Moeng, Chin-Hoh. 1984. "A large-eddy-simulation model for the study of planetary boundary-layer turbulence." *J. Atmos. Sci.* 41 (13): 2052–2062. doi:10.1175/1520-0469(1984)041<2052:ALESMF>2.0.CO;2.

Monaghan, Andrew J., Leiqiu Hu, Nathaniel A. Brunsell, Michael Barlage, and Olga V. Wilhelmi. 2014. "Evaluating the impact of urban morphology configurations on the accuracy of urban canopy model temperature simulations with MODIS." *J. Geophys. Res.: Atmos.* n/a–n/a. doi:10.1002/2013JD021227.

Monin, A S, and A M Obukhov. 1954. "Basic laws of turbulent mixing in the surface layer of the atmosphere." *Trudy Geofiz. Inst. Acad. Nauk SSSR* 24 (151): 163–187.

Moreno, E. L., N. Bazoglu, G. Mboup, and R. Warah. 2008. *State of the World's Cities 2008/2009: Harmonious Cities.* Edited by R. Warah. London: UN-HABITAT.

Moudon, Anne Vernez. 2009. "Real Noise from the Urban Environment: How Ambient Community Noise Affects Health and What Can Be Done About It." *Am. J. Prev. Med.* 37 (2): 167–171. doi:10.1016/j.amepre.2009.03.019.

NCEP. *NCEP FNL National Center for Environmental Prediction (NCEP) Final (FNL) operational model global tropospheric analyses, continuing from July 1999.* National Center for Atmospheric Research, Research Data Archive, ds083.2, http://rda.ucar.edu.

Nelson, Jon P. 1982. "Highway Noise and Property Values: A Survey of Recent Evidence." *J. Transport Econ. Policy* 16 (2): 117–138. http://www.jstor.org/stable/20052643.

Nordbo, Annika, Leena Järvi, Sami Haapanala, Joonas Moilanen, and Timo Vesala. 2013. "Intra-city variation in urban morphology and turbulence structure in Helsinki, Finland." *Boundary-Layer Meteor.* 146 (3): 469–496. doi:10.1007/s10546-012-9773-y.

Oke, Timothy R. 1974. "Review of urban climatology 1968-1973," 132 pp. Tech. Note No. 134, WMO No. 383. World Meteorol. Organiz., Geneva.

———. 1979. "Review of urban climatology, 1973-1976," 114 pp. Tech. Note No. 169, WMO No. 539. World Meteorol. Organiz., Geneva.

———. 1982. "The energetic basis of the urban heat island." *Quart. J. Roy. Meteor. Soc.* 108 (455): 1–24. doi:10.1002/qj.49710845502.

Oke, T.R. 1987. *Boundary Layer Climates.* 435. Routledge, London.

Ostashev, V. E., F. Gerdes, V. Mellert, and R. Wandelt. 1997. “Propagation of sound in a turbulent medium. II. spherical waves.” *J. Acoust. Soc. Am.* 102:2571–2578.

Ostashev, V. E., V. Mellert, R. Wandelt, and F. Gerdes. 1997. “Propagation of sound in a turbulent medium. I. plane waves.” *J. Acoust. Soc. Am.* 102:2561–2570.

Ostashev, V. E., D. K. Wilson, L. Liu, D. F. Aldridge, N. P. Symons, and D. Marlin. 2005. “Equations for finite-difference, time-domain simulation of sound propagation in moving inhomogeneous media and numerical implementation.” *J. Acoust. Soc. Am.* 117:503–517.

Ostashev, Vladimir E. 1997. *Acoustics in moving inhomogeneous media.* London: E& FN SPON, London, 259p.

Ovenden, N. C., S. R. Shaffer, and H. J. S. Fernando. 2009. “Impact of meteorological conditions on noise propagation from freeway corridors.” *J. Acoust. Soc. Am.* 126, no. 1 (July): 25–35. doi:10.1121/1.3129125.

P. Chevret, P. Blanc-Benon, and D. Juve. 1996. “A numerical model for sound propagation through a turbulent atmosphere near the ground.” *J. Acoust. Soc. Am.* 100:3587–3599.

Parsons, E.C.M., Sarah J. Dolman, Michael Jasny, Naomi A. Rose, Mark P. Simmonds, and Andrew J. Wright. 2009. “A critique of the UK’s JNCC seismic survey guidelines for minimising acoustic disturbance to marine mammals: Best practise?” *Marine Pollut. Bull.* 58 (5): 643–651.

Parsons, E.C.M., Sarah J. Dolman, Andrew J. Wright, Naomi A. Rose, and W.C.G. Burns. 2008. “Navy sonar and cetaceans: Just how much does the gun need to smoke before we act?” *Marine Pollut. Bull.* 56 (7): 1248–1257.

Passchier-Vermeer, W., and W. F. Passchier. 2000. “Noise exposure and public health.” *Environ. Health Perspect.* 108 (1): 123–131.

Paul, Patrick J, and Christopher P Colyer. 2011. “The Maricopa County PM-10 5% Plan: An Overview of EPA’s Proposed Disapproval.” *Ariz. St. LJ* 43:879.

Paulson, C.A. 1970. “The mathematical representation of wind speed and temperature profiles in the unstable atmospheric surface layer.” *J. Appl. Meteor.* 9:857–861.

Pierce, Allan D. 1981. *Acoustics – An Introduction to its physical principles and applications.* McGraw-Hill, Inc.

Piringer, M, and A Kaiser. 2008. “Investigating a valley atmosphere with a Sodar/RASS and comparison to a flatland site.” *IOP Conference Series: Earth and Environmental Science* 1 (1): 012006.

Prusa, Joseph M, Piotr K Smolarkiewicz, and Andrzej A Wyszogrodzki. 2008. “EULAG, a computational model for multiscale flows.” *Computers Fluids* 37 (9): 1193–1207.

Pry, Mark E., and Fred Andersen. 2011. *Arizona Transportation History.* Final Report FHWA-AZ-11-660. Arizona Department of Transportation, December.

R. Sack and M. West. 1995. “A parabolic equation for sound propagation in two dimensions over any smooth terrain profile: The generalised terrain parabolic equation (GT-PE).” *Appl. Acoust.* 45:113–129.

Ramanathan, V., P. J. Crutzen, J. T. Kiehl, and D. Rosenfeld. 2001. “Aerosols, Climate, and the Hydrological Cycle.” *Science* 294.

Rasmussen, K. 1985. “On the effect of terrain profile on sound propagation outdoors.” *J. Sound Vib.* 98 (1): 35–44.

Reynolds, Osborne. 1875a. “On the Refraction of Sound by the Atmosphere.” *Proc. R. Soc. Lond.* 24 (164-170): 164–167. doi:10.1098/rspl.1875.0020.

———. 1875b. “X. Proceedings of Learned Societies.” *Philosophical Magazine Series 4* 50 (328): 62–77. doi:10.1080/14786447508641260.

Rheindt, F. E. 2003. “The impact of roads on birds: Does song frequency play a role in determining susceptibility to noise pollution?” *J. Ornithol.* 144 (3): 295–306.

Robertson, J. S., W. L. Seigmann, and M. J. Jacobson. 1995. “Low-frequency sound propagation modeling over a locally reacting boundary with the parabolic approximation.” *J. Acoust. Soc. Am.* 98:1130–1137.

Robertson, J.S. 1999. “Sound propagation over a large wedge: A comparison between the geometrical theory of diffraction and the parabolic equation.” *J. Acoust. Soc. Am.* 106 (1): 113–119.

Rosenzweig, Cynthia, William Solecki, Stephen A Hammer, and Shagun Mehrotra. 2010. “Cities lead the way in climate-change action.” *Nature* 467 (7318): 909–911. doi:10.1038/467909a.

Sailor, D.G., and L. Lu. 2004. “A top-down methodology for developing diurnal and seasonal anthropogenic heating profiles for urban areas.” *Atmos. Environ.* 38:2737–2748. doi:10.1016/j.atmosenv.2004.01.034.

Salamanca, F, M Georgescu, A Mahalov, M Moustaoui, and M Wang. 2014. "Anthropogenic heating of the urban environment due to air conditioning." *J. Geophys. Res.: Atmos.* doi:10.1002/2013JD021225.

Salamanca, Francisco, Alberto Martilli, Mukul Tewari, and Fei Chen. 2011. "A Study of the Urban Boundary Layer Using Different Urban Parameterizations and High-Resolution Urban Canopy Parameters with WRF." *J. Appl. Meteor. Climatol.* 50 (5): 1107–1128.

Salomons, E. M. 1998. "Improved Green's function parabolic equation method for atmospheric sound propagation." *J. Acoust. Soc. Am.* 104:100–111. doi:10.1121/1.423260.

Salomons, E.M. 2001. *Computational Atmospheric Acoustics.* 1–348. Dordrecht: Kluwer Academic Publishers, Dordrecht, Boston, pp. 348.

Schaller, Robert R. 1997. "Moore's law: past, present and future." *Spectrum, IEEE* 34 (6): 52–59. doi:10.1109/6.591665.

Scofield, L., and P. Donavan. 2005. "Early Results of the Arizona Quiet Pavement Program." *Proceedings of the 80th Meeting of the Association of Asphalt Paving Technologists, Long Beach, CA.*

Serre, Eric, Matthieu Minguez, Richard Pasquetti, Emmanuel Guilmineau, Gan Bo Deng, Michael Kornhaas, Michael Schäfer, Jochen Fröhlich, Christof Hinterberger, and Wolfgang Rodi. 2013. "On simulating the turbulent flow around the Ahmed body: A French–German collaborative evaluation of LES and DES." *Computers & Fluids* 78 (5): 10–24. doi:10.1016/j.compfluid.2011.05.017.

Seto, Karen C, Michail Fragkias, Burak Güneralp, and Michael K Reilly. 2011. "A meta-analysis of global urban land expansion." *PLoS ONE* 6 (8): e23777. doi:10.1371/journal.pone.0023777.

Shaffer, S. R., N. C. Ovenden, H. J. S. Fernando, M. Moustaoui, and A. Mahalov. 2014. "Simulating meteorological profiles to study noise propagation from freeways." *Appl. Acoust.* In Review.

Shaw, William J., J. Christopher Doran, and Richard L. Coulter. 2005. "Boundary-layer evolution over Phoenix, Arizona and the premature mixing of pollutants in the early morning." *Atmos. Environ.* 39 (4): 773–786. doi:10.1016/j.atmosenv.2004.08.055.

Shin, Hyeyum Hailey, and Song-You Hong. 2011. "Intercomparison of planetary boundary-layer parametrizations in the WRF model for a single day from CASES-99." *Boundary-Layer Meteor.* 139 (2): 261–281. doi:10.1007/s10546-010-9583-z.

Skamarock, W. C. 2004. “Evaluating High-Resolution NWP Models Using Kinetic Energy Spectra.” *Mon. Wea. Rev.* 132 (12): 3019–3032. doi:10.1175/MWR2830.1.

Skamarock, W. C., and J. B. Klemp. 2008. “A time-split nonhydrostatic atmospheric model for weather research and forecasting applications.” *J. Comput. Phys.* 227 (7): 3465–3485. doi:10.1016/j.jcp.2007.01.037.

Skamarock, W. C., J. B. Klemp, J. Dudhia, D. O. Gill, D. M. Barker, M.G. Duda, X.-Y. Huang, W. Wang, and J. G. Powers. 2008. *A description of the Advanced Research WRF version 3.* NCAR Technical Note NCAR/TN-475+STR, pp. 113. June.

Smith, Bruce D, and Melinda A Zeder. 2013. “The Onset of the Anthropocene.” *Anthropocene* 4:8–13. doi:10.1016/j.ancene.2013.05.001.

Smolarkiewicz, Piotr K, and Georg A Grell. 1992. “A class of monotone interpolation schemes.” *J. Comput. Phys.* 101 (2): 431–440. doi:10.1016/0021-9991(92)90018-T.

Sorooshian, Armin, Anna Wonaschütz, Elias G Jarjour, Bryce I Hashimoto, Bret A Schichtel, and Eric A Betterton. 2011. “An aerosol climatology for a rapidly growing arid region (southern Arizona): Major aerosol species and remotely sensed aerosol properties.” *J. Geophys. Res.* 116 (D19): D19205.

Stansfeld, Stephen A, and Mark P Matheson. 2003. “Noise pollution: non-auditory effects on health.” *British Med. Bull.* 68 (1): 243–257.

Stewart, John, Francis McManus, Nigel Rodgers, Val Weedon, and Arline Bronzaft. 2011. *Why noise matters: A worldwide perspective on the problems, policies and solutions.* Oxford, UK: Earthscan Publications.

Strang, EJ, and HJS Fernando. 2001. “Entrainment and mixing in stratified shear flows.” *J. Fluid Mech.* 428 (1): 349–386.

Stull, R.B. 1988. *An introduction to boundary layer meteorology.* 1–666. Dordrecht: Kluwer Academic Publishers, Dordrecht, Boston, London, pp. 666.

Sun, Jielun, Larry Mahrt, Robert M. Banta, and Yelena L. Pichugina. 2012. “Turbulence Regimes and Turbulence Intermittency in the Stable Boundary Layer during CASES-99.” *J. Atmos. Sci.* 69 (1): 338–351. doi:10.1175/JAS-D-11-082.1.

Tennekes, H., and J.L. Lumley. 1972. *A first course in turbulence.* Cambridge, MA: The MIT Press.

Trenberth, K. E., J.T. Fasullo, and J. Kiehl. 2009. “Earth’s global energy budget.” *Bull. Amer. Meteor. Soc.* 90:311–323.

Volo, Thomas J, Enrique R Vivoni, Chris A Martin, Stevan Earl, and Benjamin L Ruddell. 2013. "Modeling soil moisture, water partitioning and plant water stress under irrigated conditions in desert urban areas." *Ecohydrology* In Press. doi:10.1002/eco.1457.

Vörösmarty, Charles J, Pamela Green, Joseph Salisbury, and Richard B Lammers. 2000. "Global water resources: vulnerability from climate change and population growth." *Science* 289 (5477): 284–288. doi:10.1126/science.289.5477.284.

Vörösmarty, Charles J, PB McIntyre, Mark O Gessner, David Dudgeon, A Prusevich, P Green, S Glidden, Stuart E Bunn, Caroline A Sullivan, C Reidy Liermann, et al. 2010. "Global threats to human water security and river biodiversity." *Nature* 467 (7315): 555–561. doi:10.1038/nature09440.

Votsi, Nefta-Eleftheria P., Evangelia G. Drakou, Antonios D. Mazaris, Athanasios S. Kallimanis, and John D. Pantis. 2012. "Distance-based assessment of open country Quiet Areas in Greece." *Landscape and Urban Planning* 104 (2): 279–288.

Wang, Zhi-Hua, Elie Bou-Zeid, Siu Kui Au, and James A Smith. 2011. "Analyzing the sensitivity of WRF's single-layer urban canopy model to parameter uncertainty using advanced Monte Carlo simulation." *J. Appl. Meteor. Climatol.* 50 (9): 1795–1814. doi:10.1175/2011JAMC2685.1.

Ward, L. M., and P. Suedfeld. 1973. "Human responses to highway noise." *Environ. Res.* 6:306–326.

Wayson, R. L., M. Martin, A. M. Edwards, and R. Wasko. 1995. "The AAMA traffic noise model: a better approach." *SAE Trans.* 104:2402–2410.

Webb, EK. 1970. "Profile relationships: The log-linear range, and extension to strong stability." *Quart. J. Roy. Meteor. Soc.* 96 (407): 67–90.

Webster, Mort David, M Babiker, Monika Mayer, John M Reilly, Jochen Harnisch, Robert Hyman, Marcus C Sarofim, and Chien Wang. 2002. "Uncertainty in emissions projections for climate models." *Atmos. Environ.* 36 (22): 3659–3670. doi:10.1016/S1352-2310(02)00245-5.

West, M., K. Gilbert, and R. Sack. 1992. "A tutorial on the parabolic equation (PE) model used for long range sound propagation in the atmosphere." *Appl. Acoust.* 37 (1): 31–49. doi:10.1016/0003-682X(92)90009-H.

Whiteman, C. David. 2000. *Mountain Meteorology: Fundamentals and Applications.* 355. New York: Oxford University Press, New York, Oxford, pp. 355.

WHO. 2007. *Night Noise Guidelines for Europe.* Bonn: WHO, regional Office for Europe: World Health Organization.

Wicker, L.J., and W. C. Skamarock. 2002. "Time splitting methods for elastic models using forward time schemes." *Mon. Wea. Rev.* 130 (8): 2088–2097. doi:10.1175/1520-0493(2002)130<2088:TSMFEM>2.0.CO;2.

Wiley, William D. 2011. "Maricopa County Air Quality Department: Challenges and Solutions." *Ariz. St. LJ* 43:943.

Willmott, Cort J, Steven G Ackleson, Robert E Davis, Johannes J Feddema, Katherine M Klink, David R Legates, James O'Donnell, and Clinton M Rowe. 1985. "Statistics for the evaluation and comparison of models." *J. Geophys. Res.: Oceans* 90 (C5): 8995–9005. doi:10.1029/JC090iC05p08995.

Wilson, D. K. 2000. "A turbulence spectral model for sound propagation in the atmosphere that incorporates shear and buoyancy forcings." *J. Acoust. Soc. Am.* 108:2021–2038.

Wilson, D. K., J. G. Brasseur, and K. E. Gilbert. 1999. "Acoustic scattering and the spectrum of atmospheric turbulence." *J. Acoust. Soc. Am.* 105:30–34.

Wyngaard, J. 2004. "Toward Numerical Modeling in the "Terra Incognita"." *J. Atmos. Sci.* 61 (14): 1816–1826. doi:10.1175/1520-0469(2004)061<1816:TNMITT>2.0.CO;2.

Wyszogrodzki, Andrzej A, Shiguang Miao, and Fei Chen. 2012. "Evaluation of the coupling between mesoscale-WRF and LES–EULAG models for simulating fine-scale urban dispersion." *Atmos. Res.* 118:324–345. doi:10.1016/j.atmosres.2012.07.023.

X. Di and K. E. Gilbert. 1994. "The effect of turbulence and irregular terrain on outdoor sound propagation." *Proceedings of the Sixth Symposium on longrange sound propagation:* 315–333.

Xie, Bo, Jimmy C. H. Fung, Allen Chan, and Alexis Lau. 2012. "Evaluation of nonlocal and local planetary boundary layer schemes in the WRF model." *J. Geophys. Res.: Atmos.* 117 (D12103): 26. doi:10.1029/2011JD017080.

Zaremba, Laura L., and John J. Carroll. 1999. "Summer Wind Flow Regimes over the Sacramento Valley." *J. Appl. Meteor.* 38 (10): 1463–1473. doi:10.1175/1520-0450(1999)038<1463:SWFROT>2.0.CO;2.

Zhang, Dalin, and Richard A. Anthes. 1982. “A High-Resolution Model of the Planetary Boundary Layer - Sensitivity Tests and Comparisons with SESAME-79 Data.” *J. Appl. Meteor.* 21:1594–1609. doi:10.1175/1520-0450(1982)021<1594:AHRMOT>2.0.CO;2.

Zib, Behnjamin J, Xiquan Dong, Baike Xi, and Aaron Kennedy. 2012. “Evaluation and intercomparison of cloud fraction and radiative fluxes in recent reanalyses over the Arctic using BSRN surface observations.” *J. Climate* 25 (7): 2291–2305.

Zilitinkevich, SS. 1995. “Non-local turbulent transport: Pollution dispersion aspects of coherent structure of convective flows.” *Air Pollution III* 1:53–60.

Zirbel, K., P. Balint, and E.C.M. Parsons. 2011. “Navy sonar, cetaceans and the US Supreme Court: A review of cetacean mitigation and litigation in the US.” *Marine Pollut. Bull.* 63 (1–4): 40–48.

APPENDIX A

ADDITIONAL ADOT FIELD EXPERIMENT DATA

A.1 ADOT Field Experiment

Supplementary material for Chapter 2 field experiments, for microphones, ultra-sonic anemometers, SODAR-RASS, balloon-tethersonde, and other data collected at ADOT field experiments in Oct, Nov 2006, and Apr 2007.

A field experiment Ovenden, Shaffer, and Fernando 2009; Shaffer et al. 2014 was conducted during the morning hours of November 7 and 8, 2006 along the Phoenix Loop 202 highway in Mesa, Arizona near coordinates 33.48240°N, 111.76338°W, shown in Figure 25. One aim of the study was to capture effects of sound propagation from a straight freeway segment during morning transition from stable to unstable conditions. Measuring equipment employed included a SOund Detection And Ranging (SODAR) with Radio Acoustic Sounding System (RASS) and sonic anemometers situated on a meteorological tower and two tripods. A cross-section of the Nov. 2006 setup and terrain height is presented in Figure 44.

A.1.1 Acoustic Data

Microphone data collection and analysis was performed by Illingworth & Rodkin, Inc. (I&R), with placements summarized in Table 5. I&R provided 5-minute time-averaged Sound Pressure Level (SPL) measurements, L_{eq,f_n}, in 27 third-octave spectral bands from 25 Hz to 20 kHz, along with L_{eq}, L_{max}, L_{50} and L_{90} total values in 5-minute averages, shown in Figure 45-48. Standard one-third octave bands can be found in Table 2.1 of Pierce 1981. Of these acoustic data, we observe that only 17 frequency bands are relevant when applying A-weighting to account for human sensitivity to sound, as typical for studies of noise

ID	Distance [ft]	Height AGL [ft]
1	50	12
2	50	5
3	100	5
4	250	5

Table 5: Summary of microphone placement during November field experiment. Distance is from the center of near travel lane, which is 12 feet from the edge of pavement.

pollution, defined as undesirable sound to humans. This approach yields less than 1% error in the total A-weighted SPL field and speeds computations by neglecting larger frequencies.

A.1.2 Meteorological Data

Meteorological data obtained from the SODAR-RASS and sonic anemometers during the entire measurement periods on November 7 and 8, 2006, local standard time in Arizona (UTC-7) are presented. Shown in Figures 49-54 are time-series plots of vertical profiles for temperature, U (East-West), V (North-South) and W (vertical) velocity components, along with horizontal wind direction and speed, respectively. The change in wind direction with time and height, presence and dialy breakup of temperature inversion and presence of early morning shear and a low-level jet is evident. Unfortunately, only error estimates in the W component and the total backscatter were retained in the data files, so uncertainties in U, V and T are unavailable. Further data corruption could have occurred due to anomolously loud roadway events and were not accounted for, but might be inferred from L_{90} values.

The Scientech SODAR-RASS was employed to sample vertical profiles of air velocity and temperature, which were recorded in 20 minute time averaged values with 20 meter vertical resolution between roughly 40 meters and 360 meters above ground level

ID	Manufacturer	Structure	Distance [ft]	Height AGL [m]
1	RM Young 81000	met tower	100	6.8
2	RM Young 81000	met tower	100	13.8
3	RM Young 81000	tripod 1	50	1.8
4	Campbell Scientific	tripod 2	250	2.2

Table 6: Summary of placement of sonic anemometers during field experiemnt. The structure is as described in Figure 44, and distance is from edge of pavement. Sonic 4 was only used on November 8th.

(AGL). Using directed pulsed acoustic signals, the SODAR obtains horizontal velocities via doppler shifts, and when combined with electromagnetic signal source and receiver dishes, the RASS enables sampling temperature, and combined with SODAR the vertical velocity component Fernando, Princevac, and Calhoun 2007 Piringer and Kaiser 2008. Being a source of acoustic contamination, the SODAR-RASS was positioned several hundred feet away from the microphones, displaced parallel to the roadway. Furthermore, data corruption is suspected to have occurred due to anomolously loud events from the roadway interfering with measurement signal-to-noise ratio. Equipment difficulties caused for other periods to lack data.

Sonic anemometers were placed on separate towers alongside microphone locations at 50, 100 and 250 feet from the center of the near lane of traffic and at various heights above ground, summarized in table 6. They were operated at 20 Hz during roughly 0700 and 1100 local standard time. The data were then post-processed into 5 and 15 minute time-averaged values for observed and derived quantities.

Sonic anemometer data are presented Figures 55 - 71, with the sonic positions as summarized in Table 6. The initial ordering of sonics in Table 6 was arbitrary, though perhaps they should be sorted by height above ground. However, distance from road may also be important as mentioned below. There are several features that stand out and several

points of further analysis for careful interpretation of these data. The first is the change in horizontal wind direction at 11 am LST more noticably on Noveber 7th. Features such as wind speed and temperature trends could be examined from WRF data quite readily, though one must understand the comparison being made between 5-minute time-averaged point (3 cm diameter sampling volume) measurements and an instantaneous realization of rectangular pancake 20 meters in height and at grid resolutions of 111, 333 or 1000 meters on a side (when comparing with WRF).

The difference between sonic positions from the roadway may be important as seen in the rms values, Figures 61-64, Reynolds stresses and turbulent fluxes in Figures 66 - 70, and TKE in Figure 71. In comparing sonic number 3 and 4 (Nov 8th only) which are at similar heights 2 m agl, but at 50 ft and 250 ft, respectively, from the roadway. For instance, between roughly 8:15 and 9:05 the u_{rms} (Fig. 61), v_{rms} (Fig. 62), and the stresses $\overline{u'v'}$ (Fig. 65), and the $\overline{u'w'}$ (Fig. 66), together with TKE (Fig. 71), deviations are present which might be indicative of roadway influences. Comparisons with observed timeseries of traffic intensity or a more careful analysis of the ADOT observations of travel velocity and vehicle flux might be of use. A simple model of a wake behind a bluff body Ahmed car model Lienhart and Becker 2003, only here we have more complex boundary layer flow with mean wind, shear and inversion etc. so short of performing a full LES analysis (e.g. Serre et al. 2013, Hemida and Baker 2010, Minguez, Pasquetti, and Serre 2008) perhaps some scaling arguments could be used to infer confirmation of this possible explanation for these observations. Also note that the rms temperature (and heat flux) is greater closer to the roadway. See also, analysis performed in Eskridge and Hunt 1979. More detailed analysis needs to be performed on these topics.

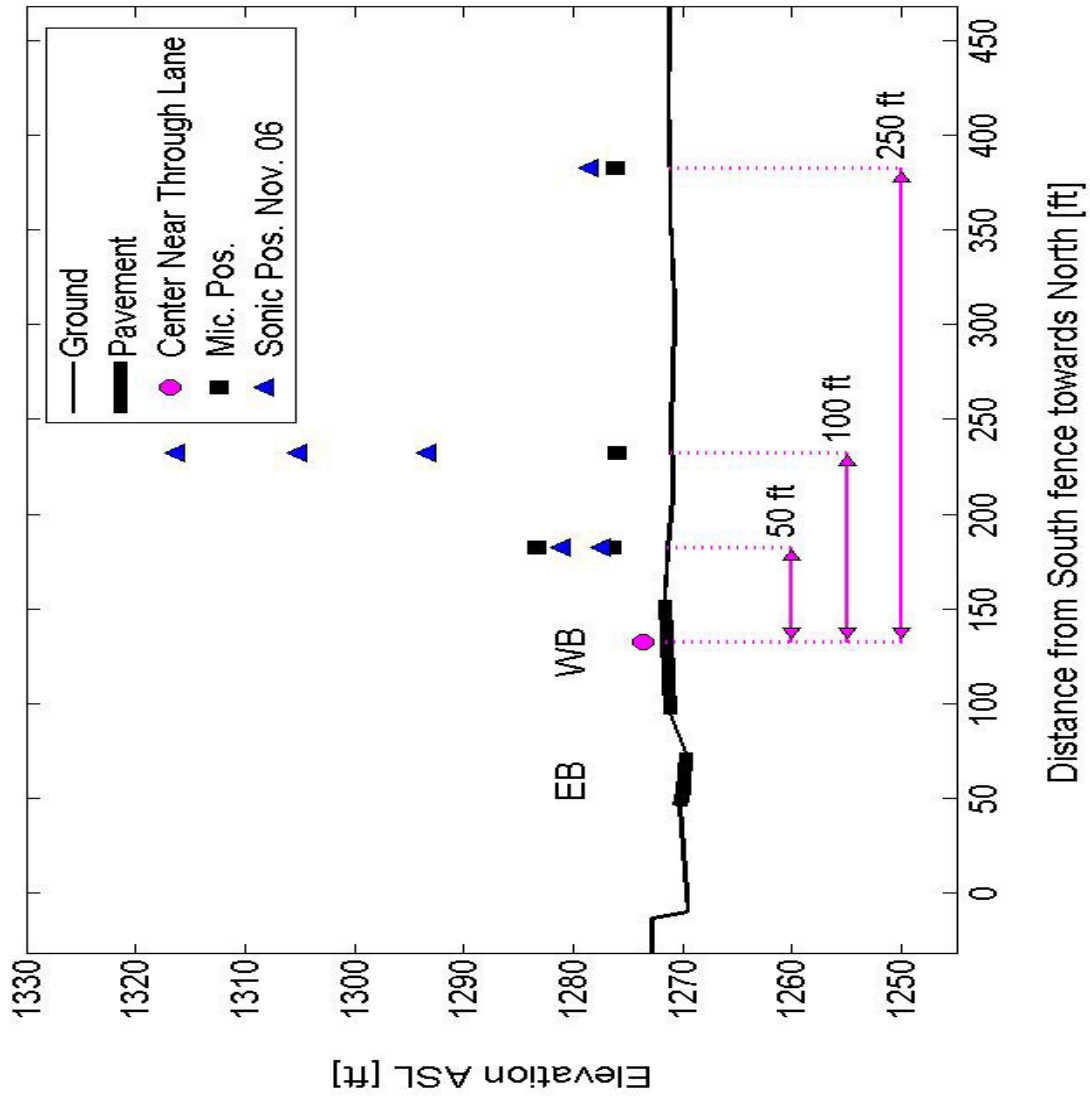

Figure 44: Schematic of ADOT experimental setup for November 2006.

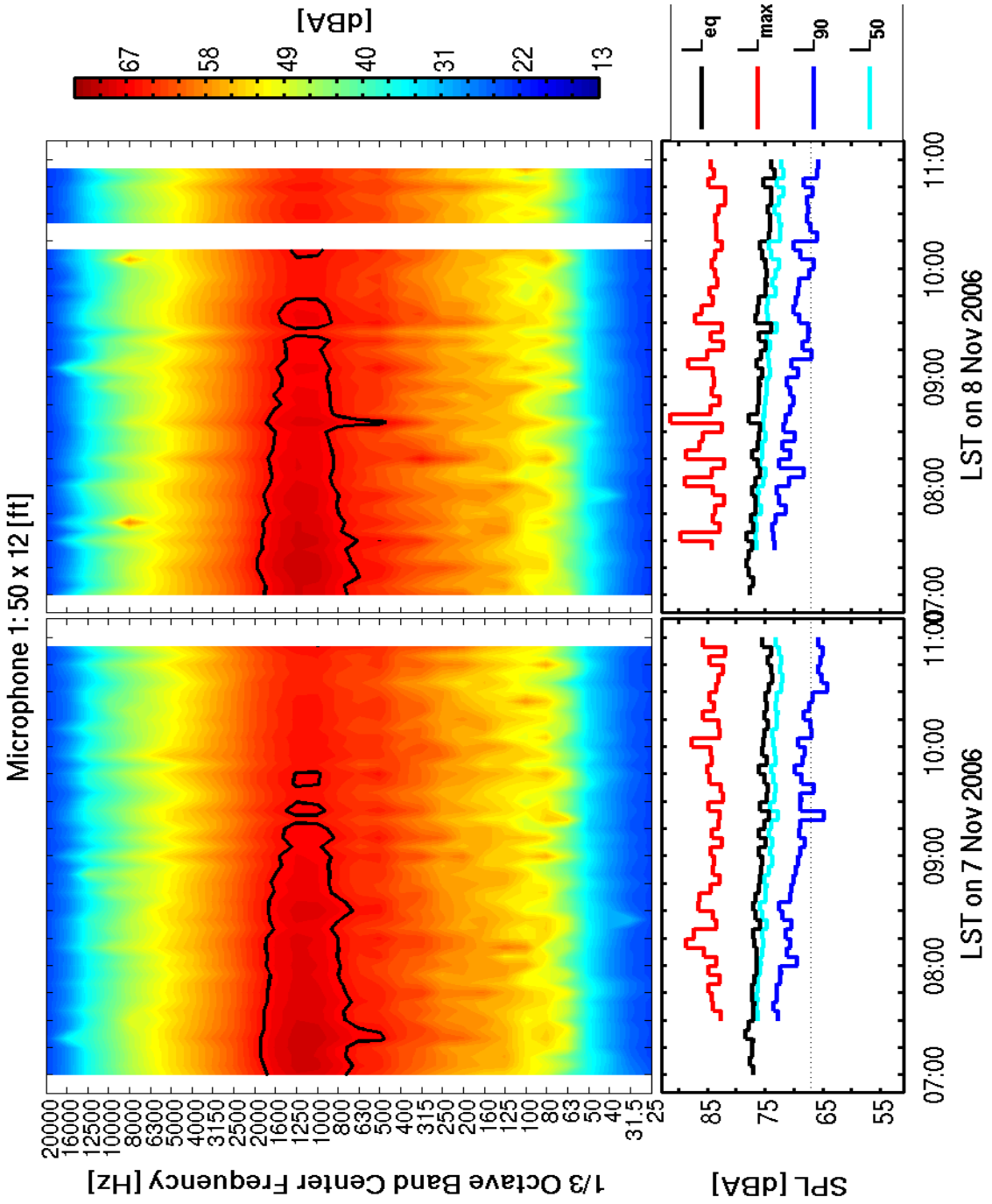

Figure 45: Time series of microphone 1 measurements for one-third octave spectrogram (25 Hz to 20 kHz) with values ranging from (13,73) dBA interpolated contours, and a 67 dBA black contour showing individual frequencies that are above the L_{eq} threshold (top), and timeseries of $_{eq}$, L_{max}, L_{90}, and L_{50} 5-minute average values (bottom), during the Nov. 2006 observation periods for Nov 7th (left), and Nov. 8th (right), local time.

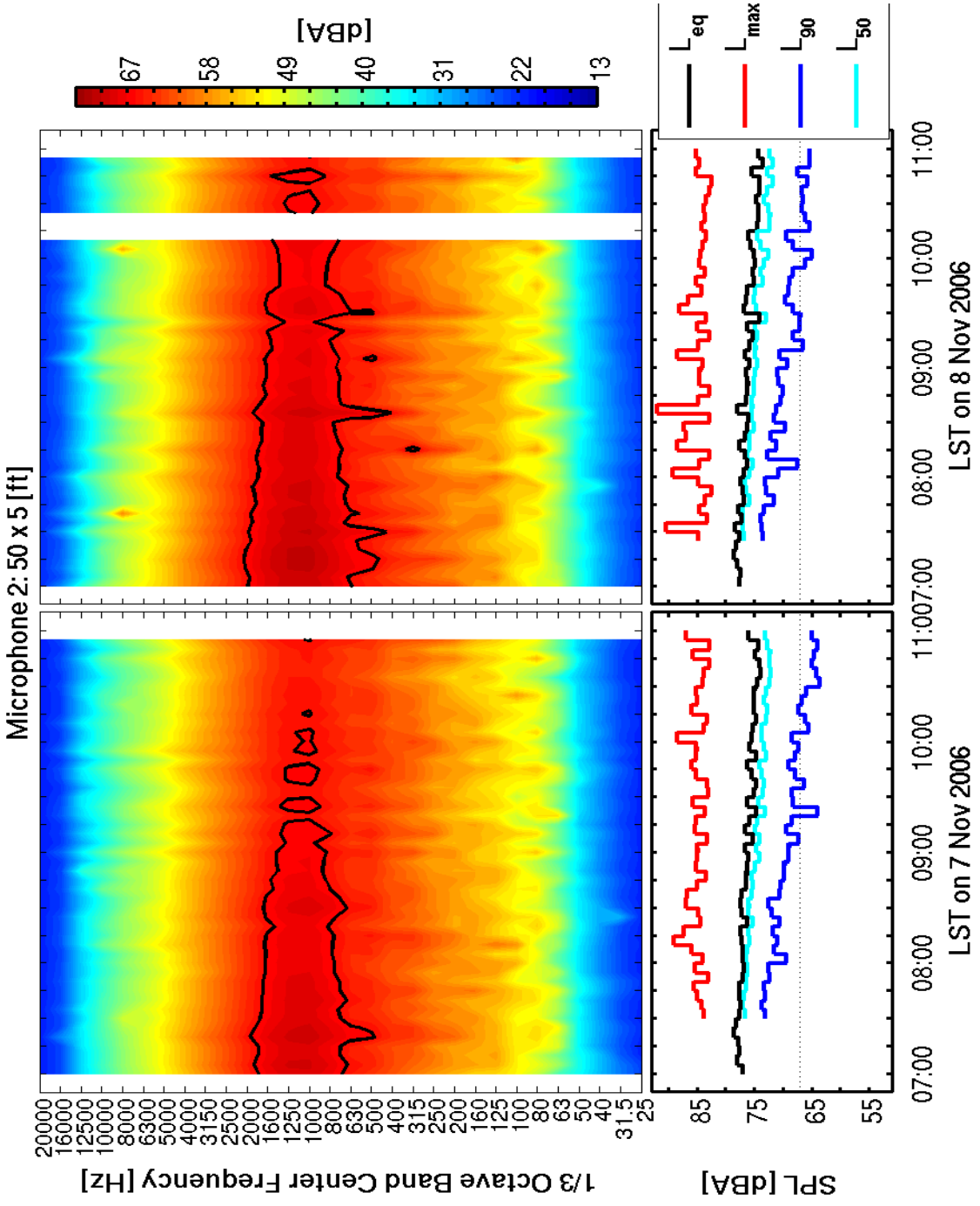

Figure 46: Same as Figure 45 but for microphone 2.

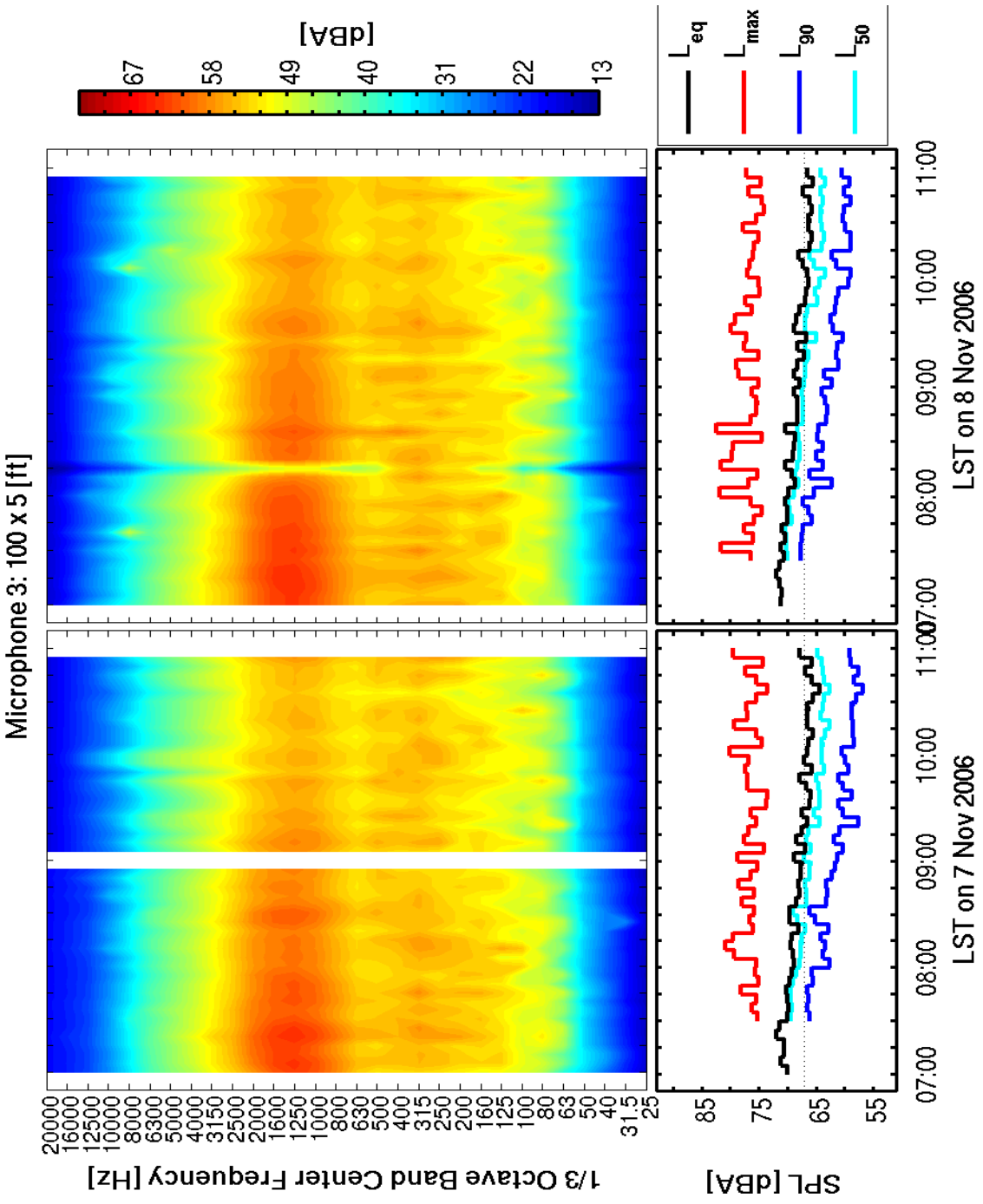

Figure 47: Same as Figure 45 but for microphone 3.

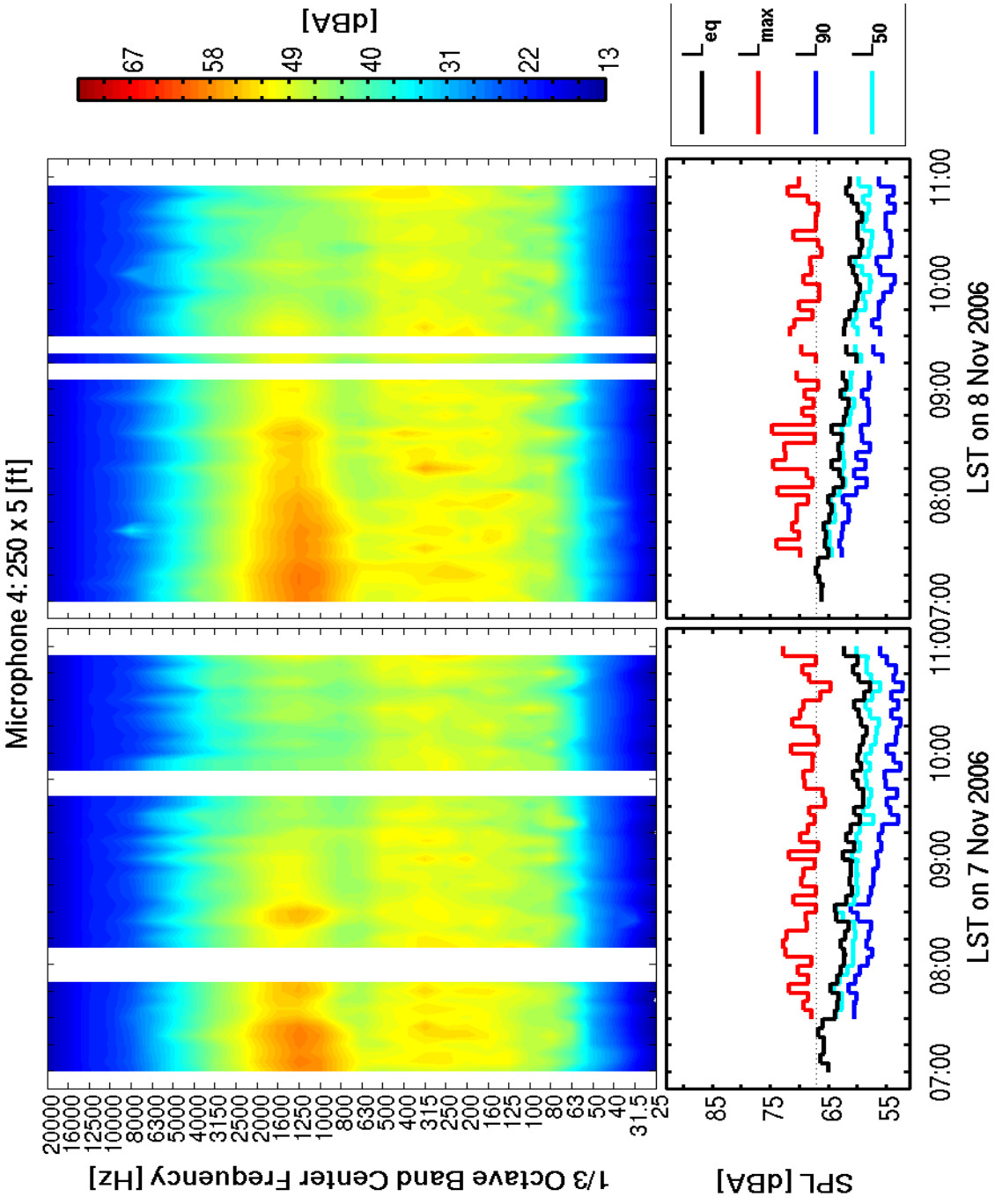

Figure 48: Same as Figure 45 but for microphone 4.

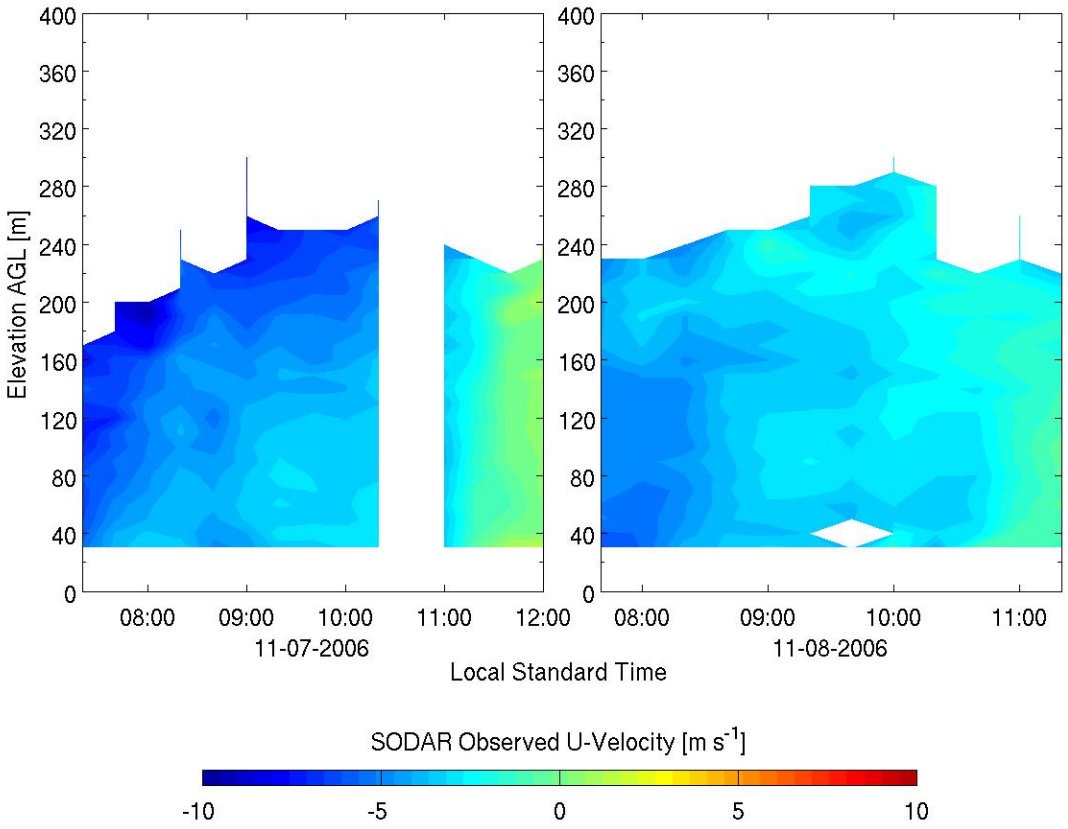

Figure 49: Observed time-series of SODAR-RASS vertical profiles during the two observational periods on Nov 7th (left panel) and Nov 8th (right panel) for U velocity component. Positive values are towards the East. Ragged top is due to variations in range of SODAR-RASS.

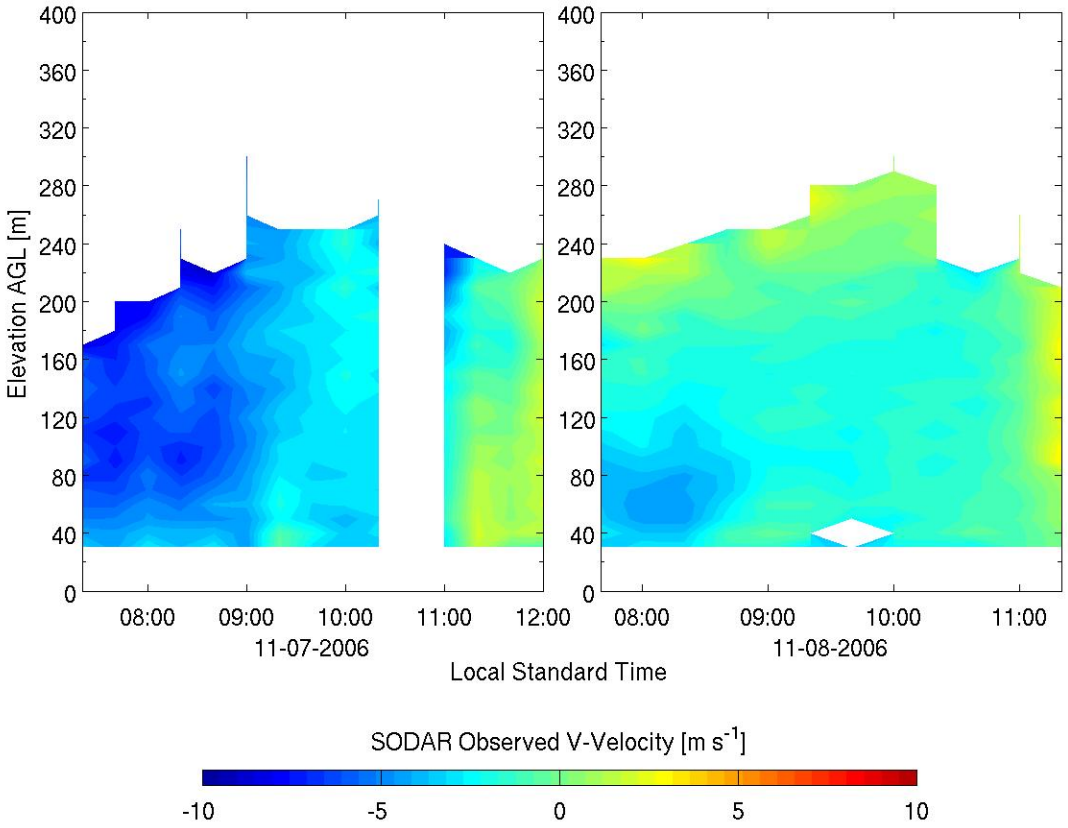

Figure 50: Same as for Figure 49 but for V velocity component. Positive values are towards the north.

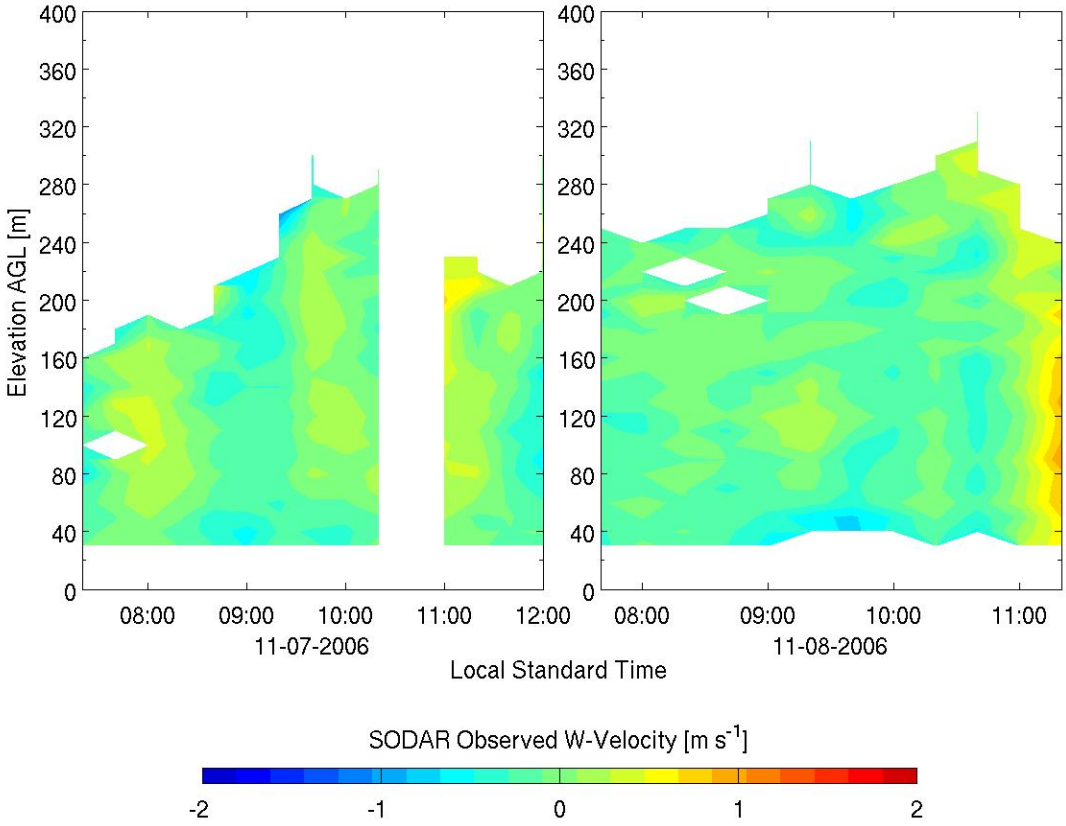

Figure 51: Same as for Figure 49 but for W velocity component. Positive values are up.

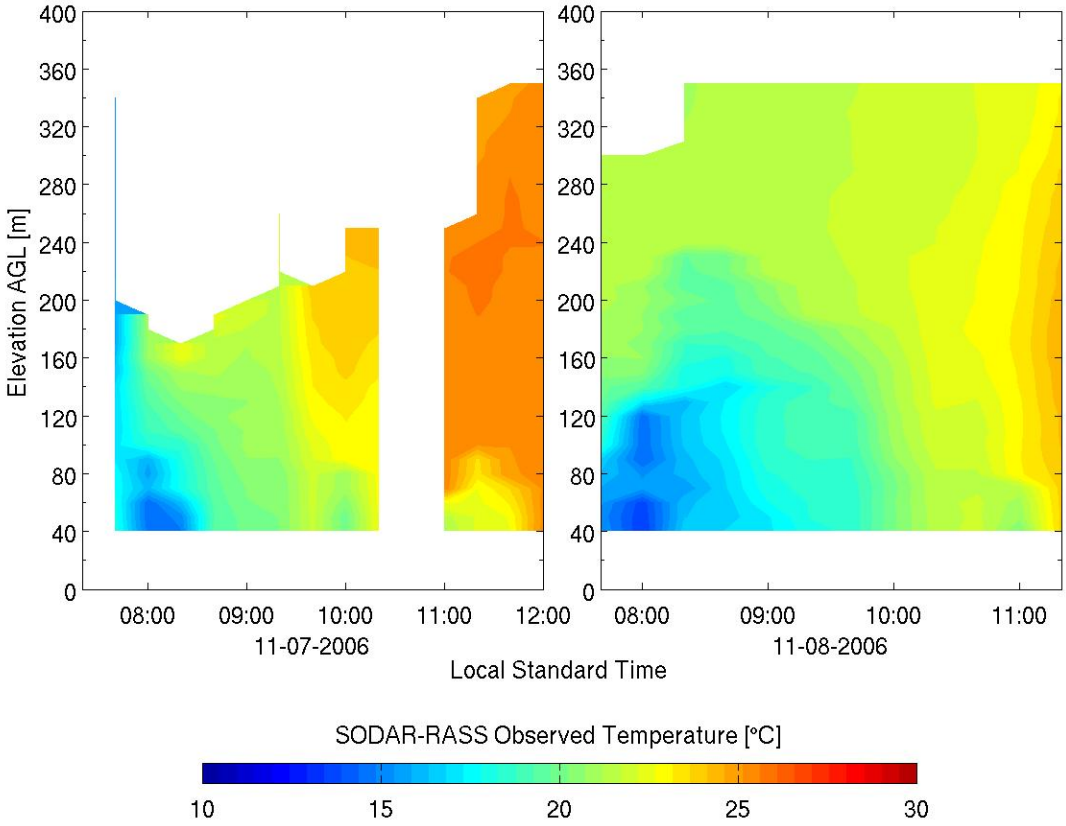

Figure 52: Same as for Figure 49 but for temperature.

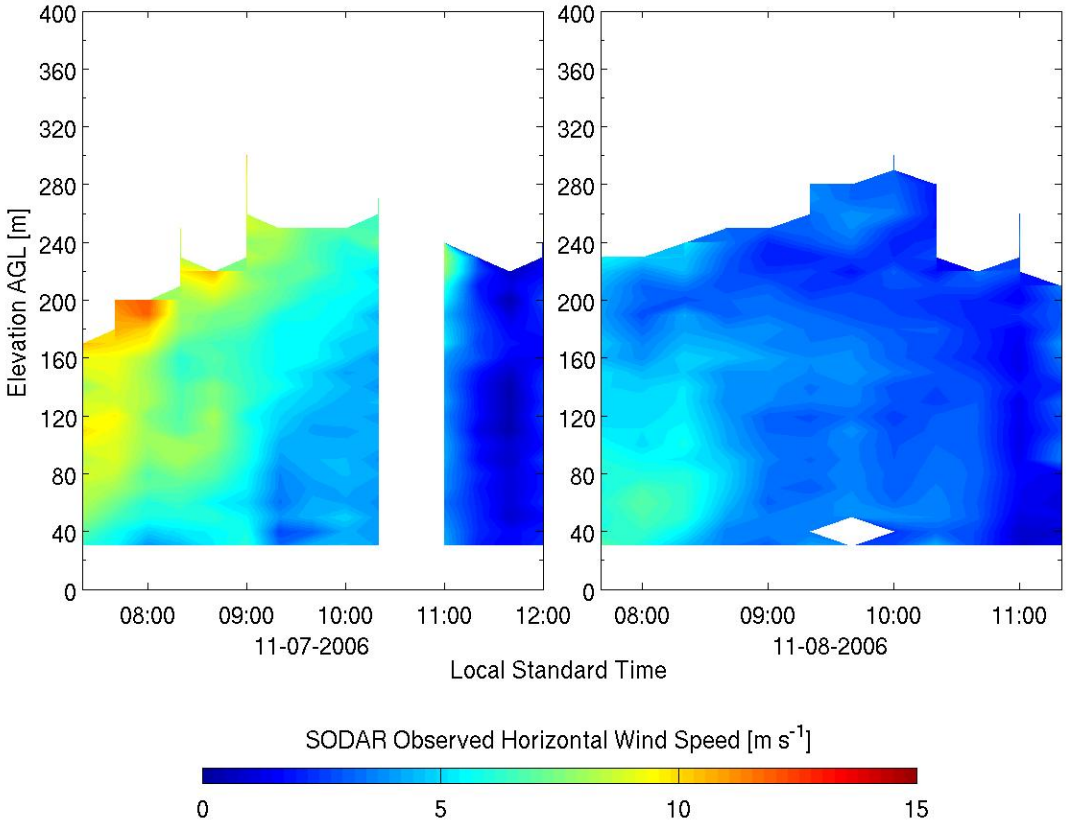

Figure 53: Same as for Figure 49 but magnitude of horizontal wind speed.

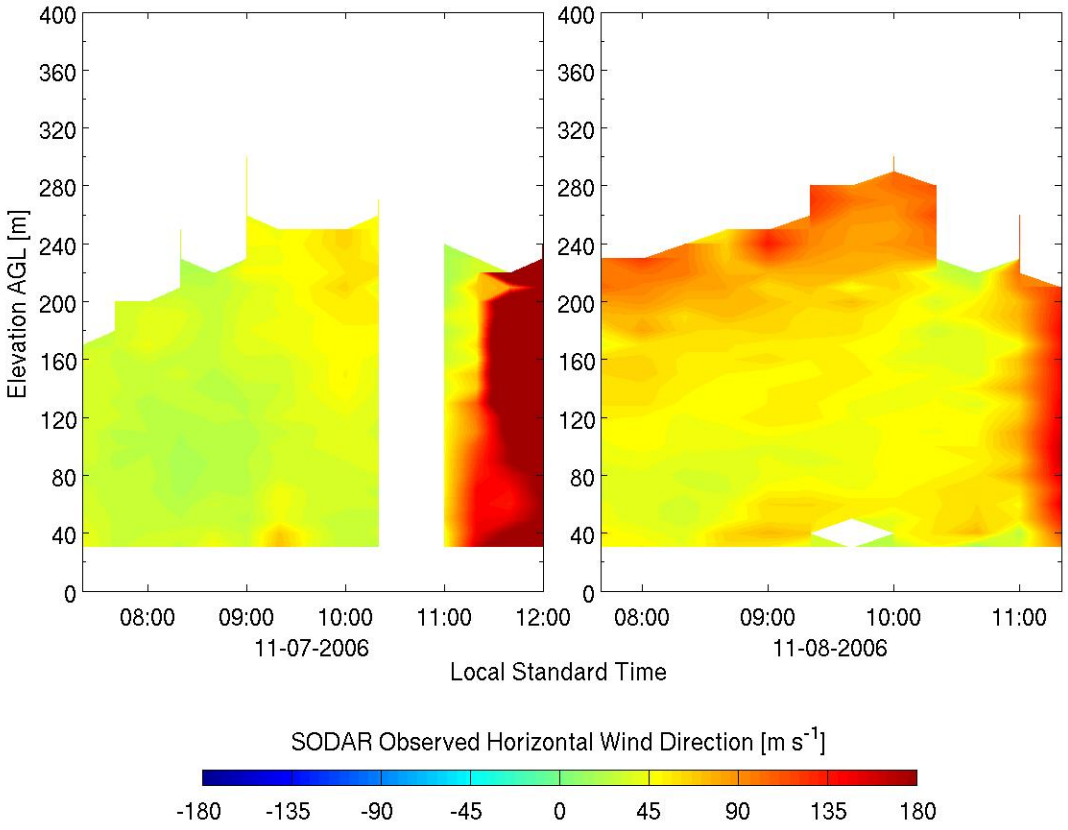

Figure 54: Same as for Figure 49 but for direction of horizontal wind speed. Here East is 0° and North is 90°.

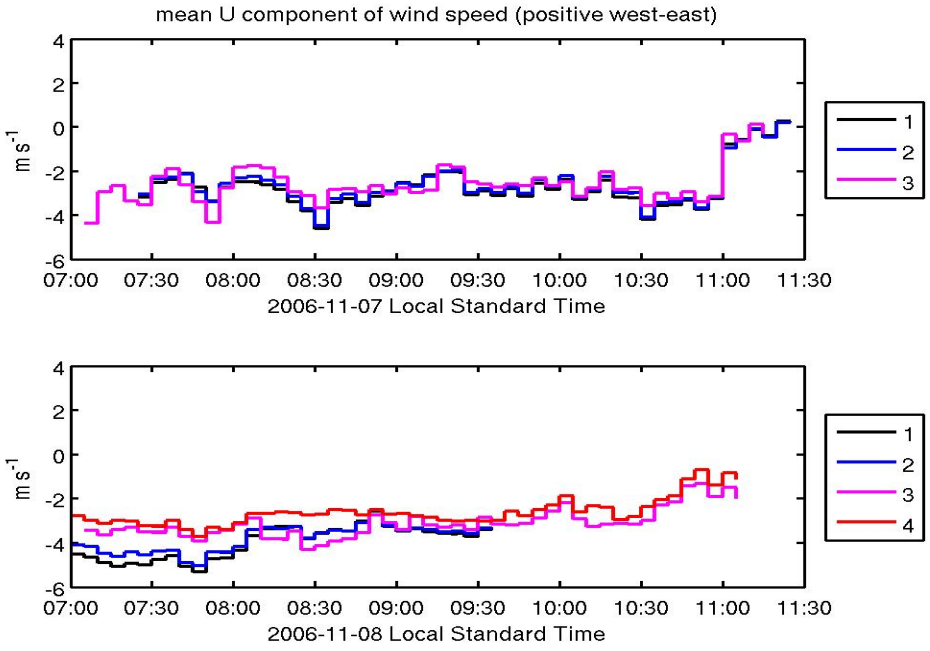

Figure 55: Observed time-series of sonic anemometer data, with ID corresponding to instrument in Table 6, during the two observational periods on Nov 7th (top) and Nov 8th (bottom) for 5-minute time-averaged mean values of U velocity component, positive towards east.

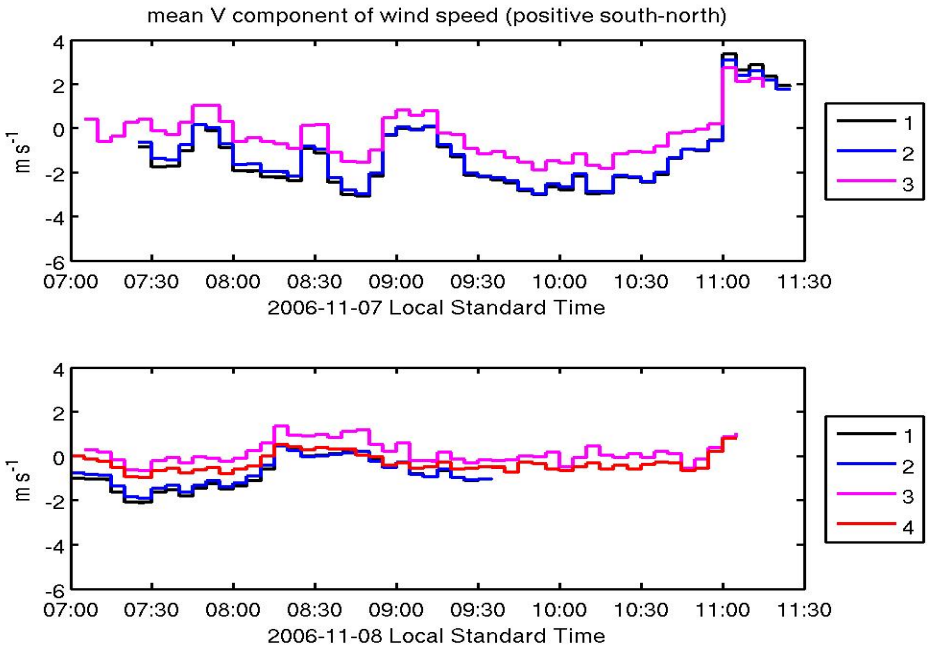

Figure 56: Same as for Figure 55, but for V velocity component. Positive is towards north.

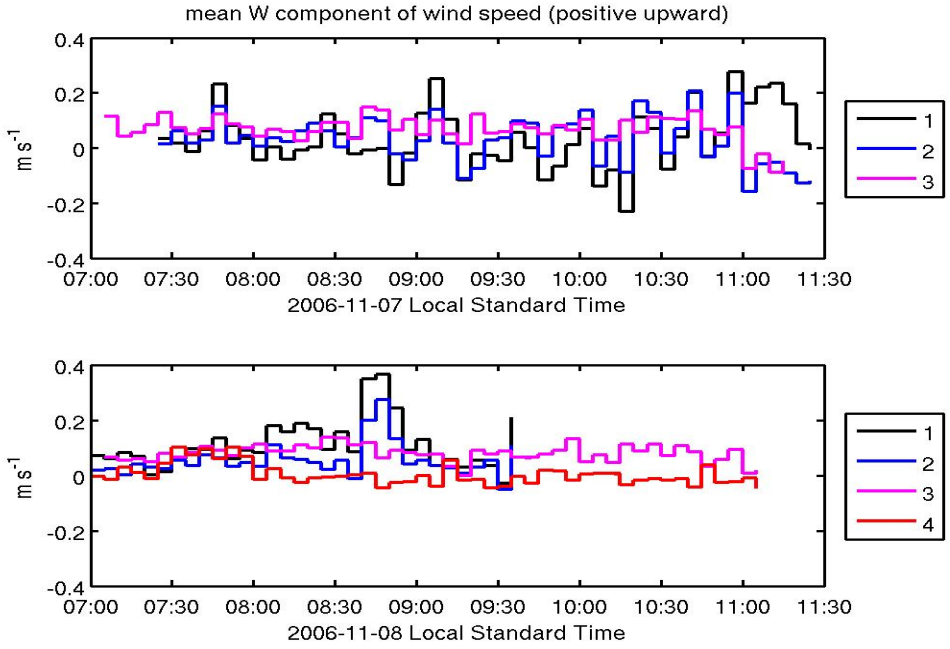

Figure 57: Same as for Figure 55, but for W velocity component. Positive is upward.

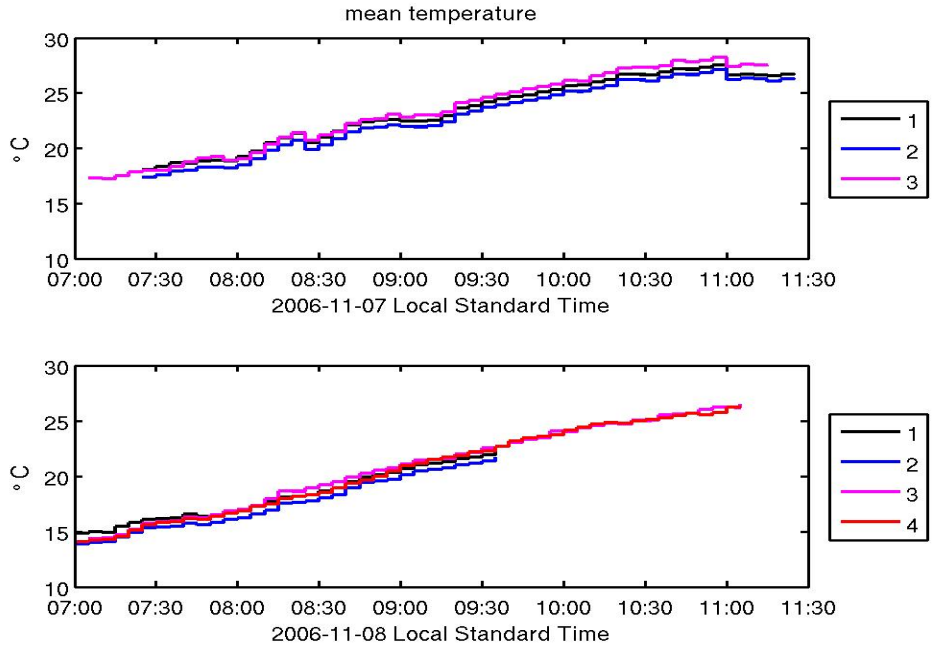

Figure 58: Same as for Figure 55, but for temperature.

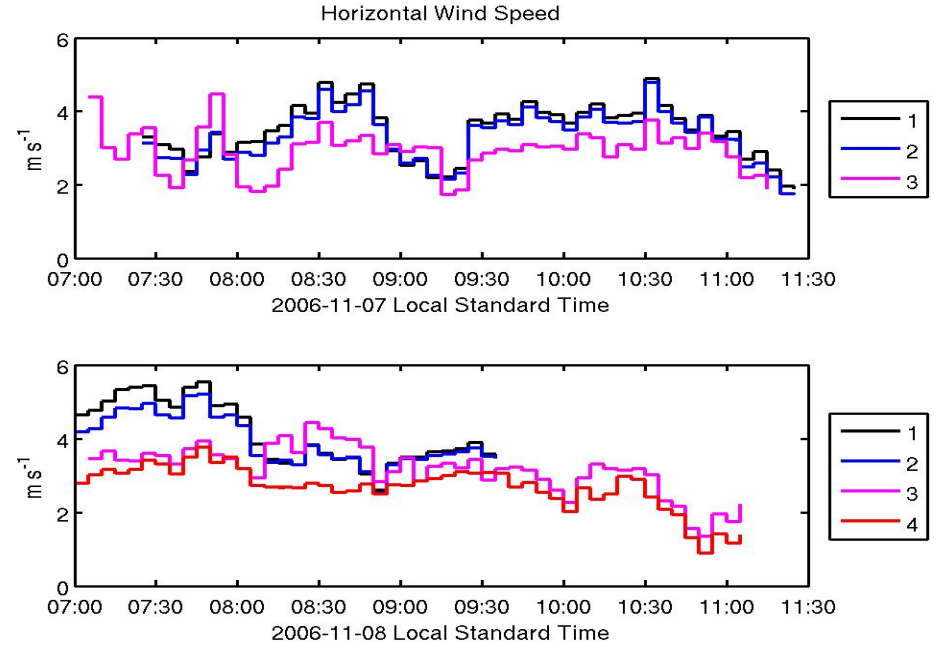

Figure 59: Same as for Figure 55, but for horizontal wind speed.

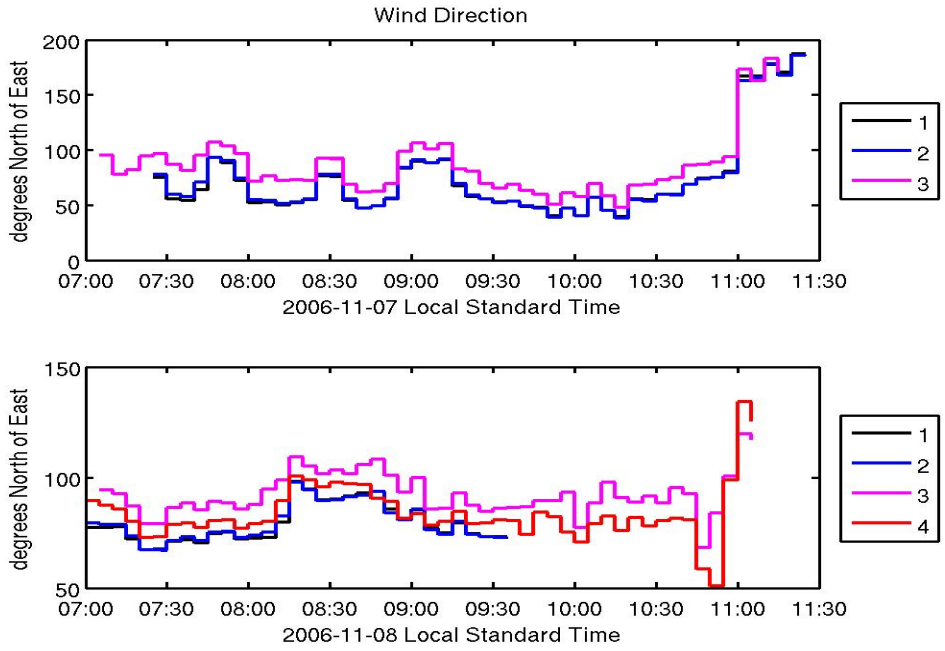

Figure 60: Same as for Figure 55, but for horizontal wind direction where East is 0° and North is 90°.

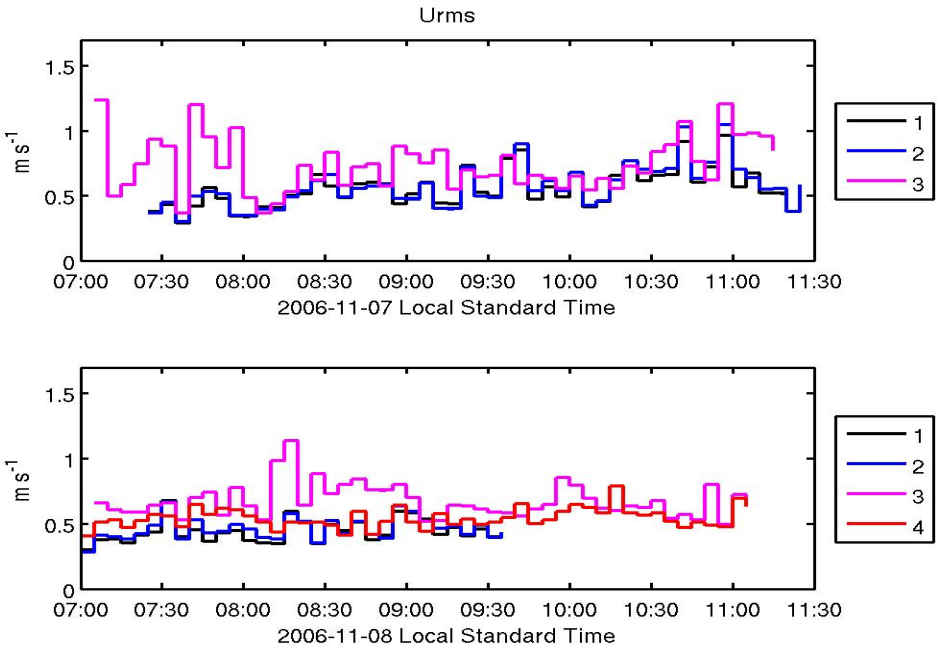

Figure 61: Same as for Figure 55, but for u_{rms}, RMS of u-velocity component.

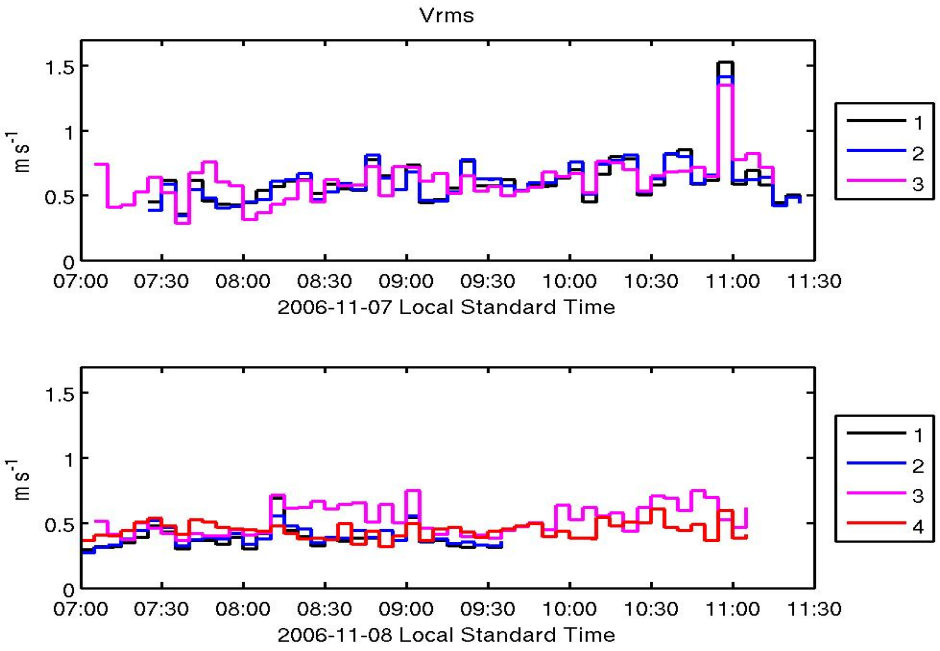

Figure 62: Same as for Figure 55, but for v_{rms}, RMS of v-velocity component.

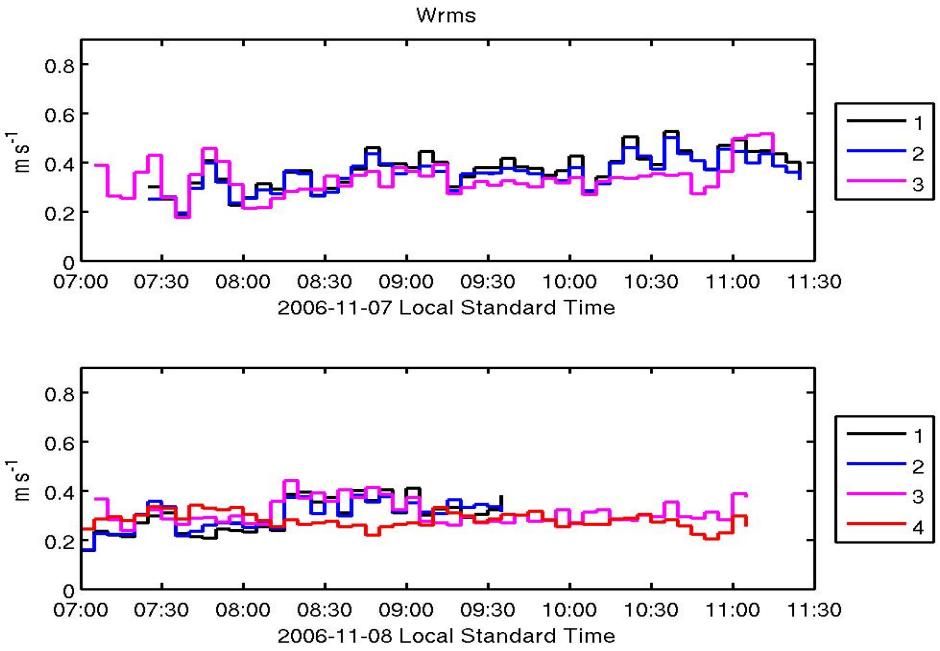

Figure 63: Same as for Figure 55, but for w_{rms}, RMS of w-velocity component.

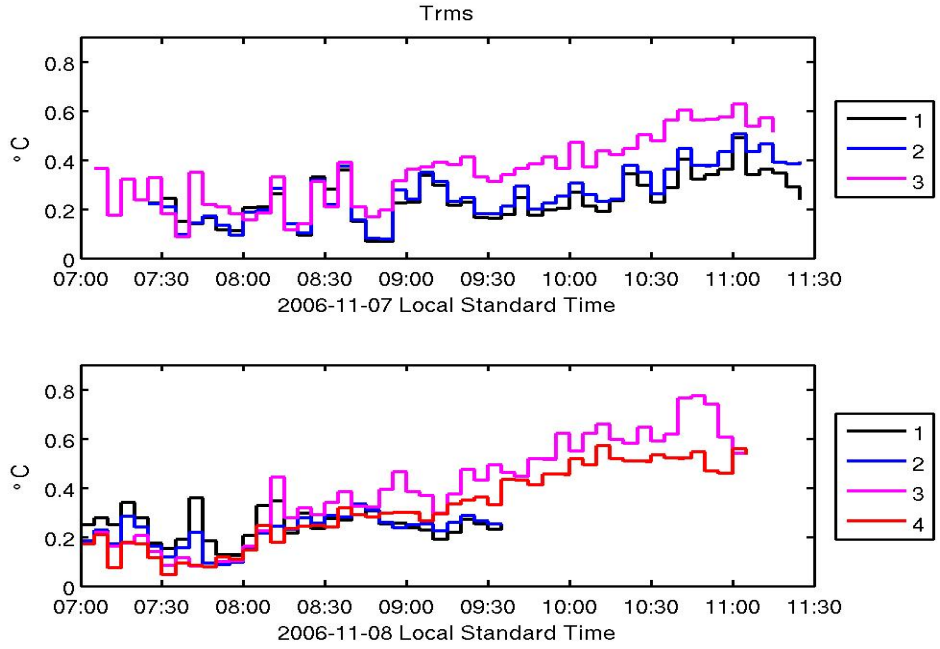

Figure 64: Same as for Figure 55, but for θ_{rms}, RMS of virtual potential temperature.

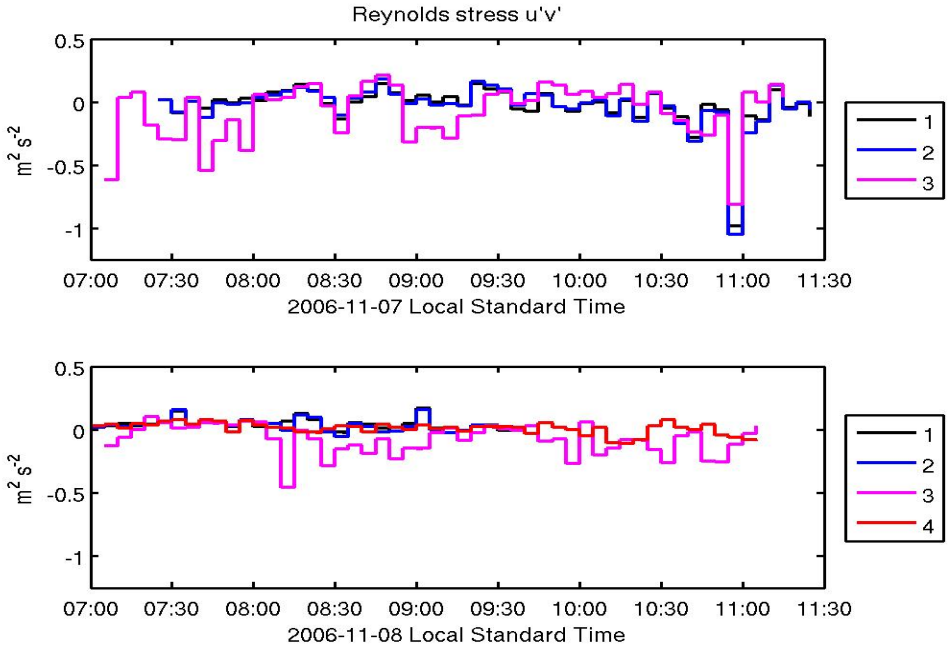

Figure 65: Same as for Figure 55, but for Reynolds stress $\overline{u'v'}$.

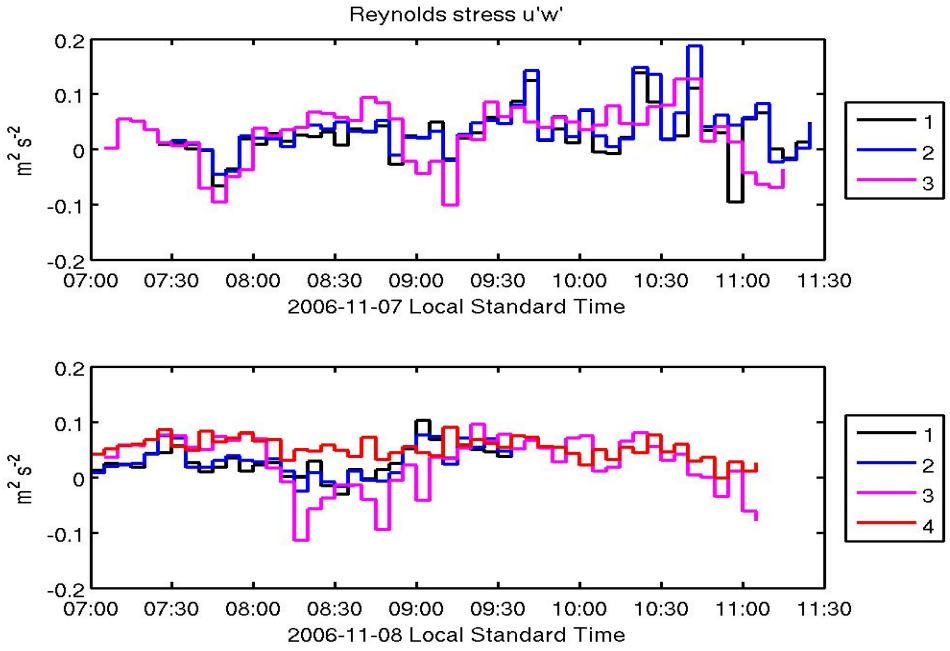

Figure 66: Same as for Figure 55, but for Reynolds stress $\overline{u'w'}$.

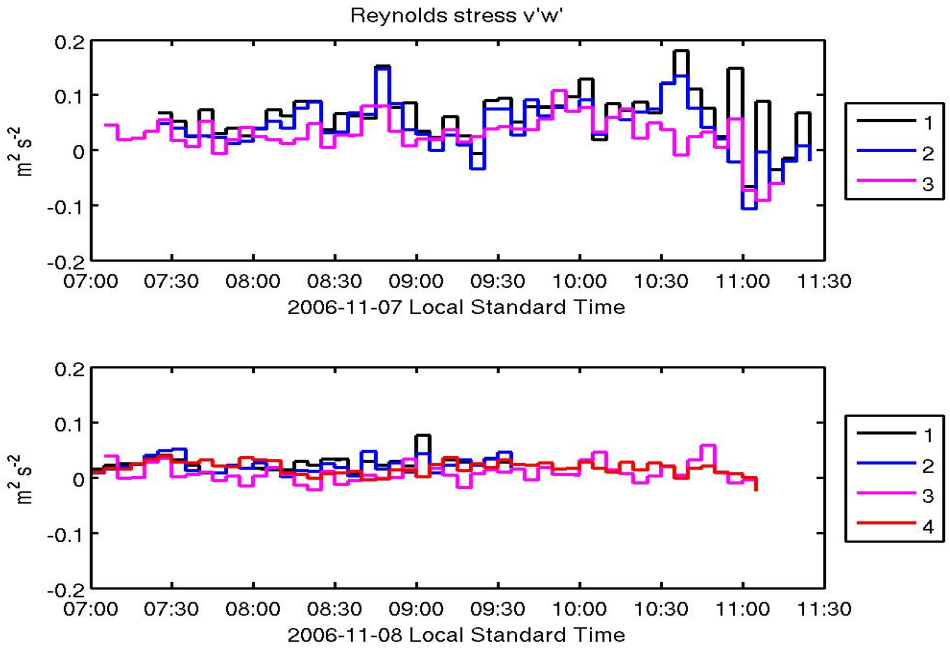

Figure 67: Same as for Figure 55, but for Reynolds stress $\overline{v'w'}$.

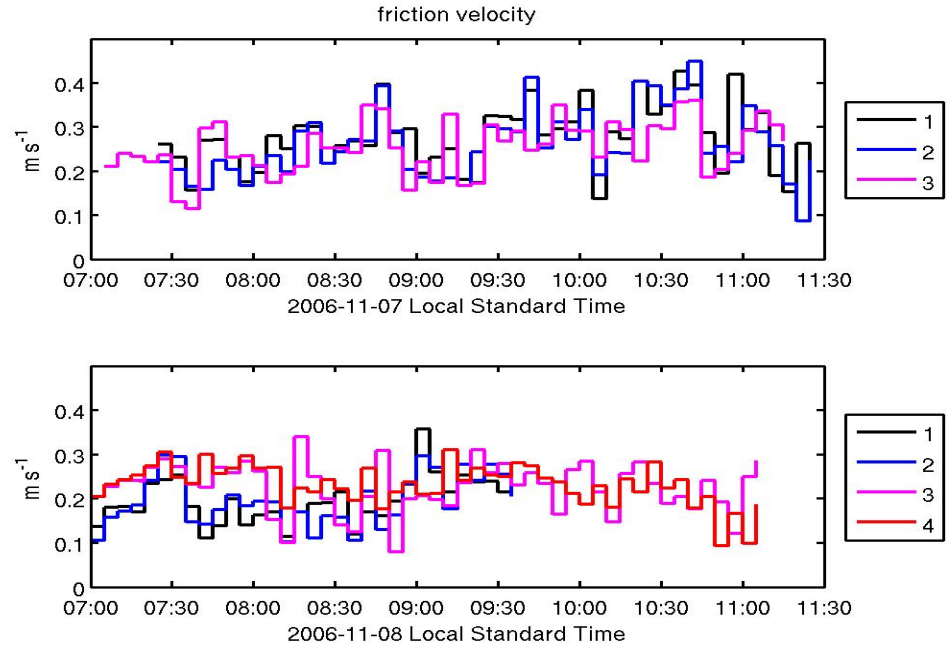

Figure 68: Same as for Figure 55, but for friction velocity $u*$.

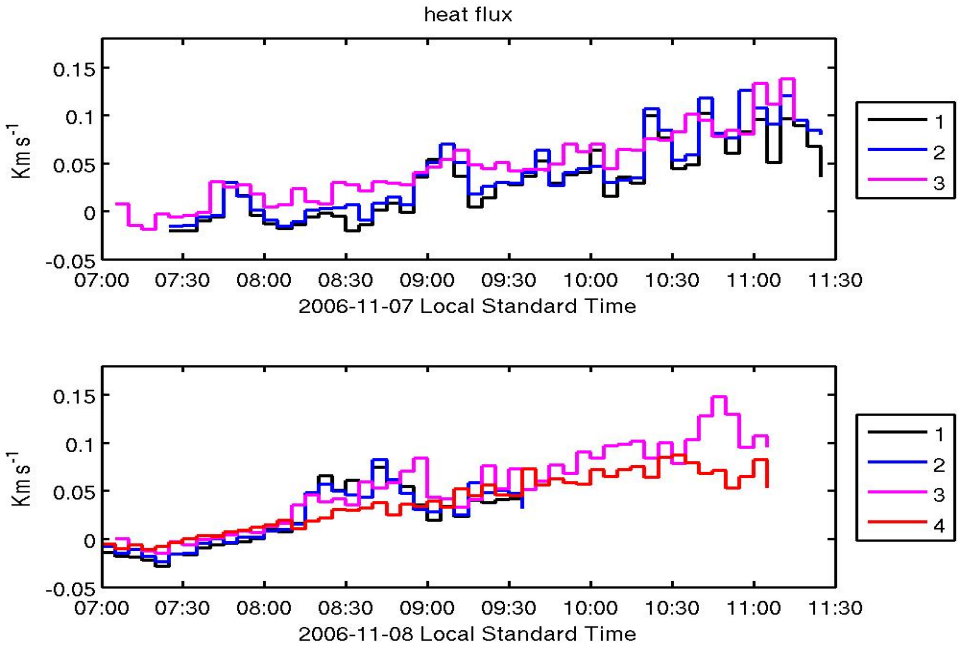

Figure 69: Same as for Figure 55, but for heat flux $\overline{w'\theta'}$.

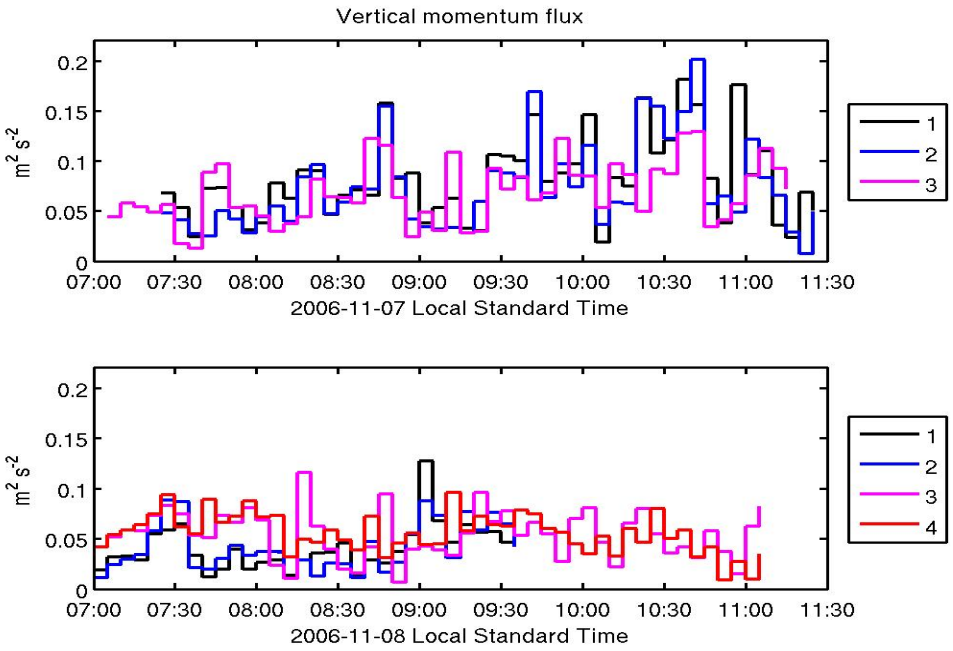

Figure 70: Same as for Figure 55, but for vertical momentum flux $(\overline{v'w'}^2 + \overline{u'w'}^2)^{\frac{1}{2}}$.

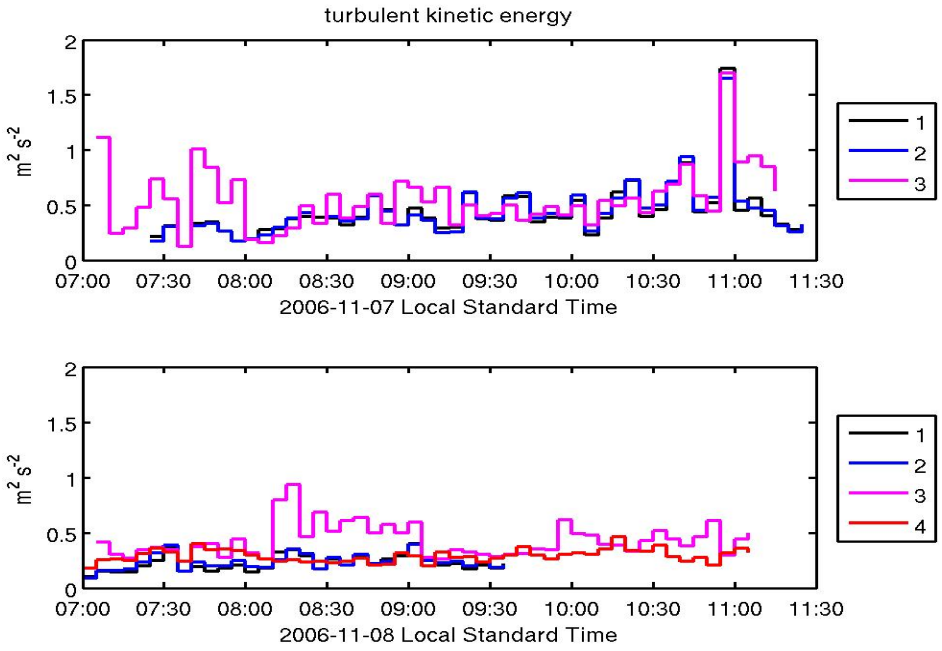

Figure 71: Same as for Figure 55, but for turbulent kinetic energy.

APPENDIX B

PRELIMINARY INVESTIGATION OF EFFECTS FROM A 2D ACOUSTIC REFRACTION FIELD VIA A LAGRANGIAN METHOD

B.1 Introduction

We demonstrate our method of deriving realizations from ARW-WRF v3.2 of effective acoustic index of refraction field fluctuations for studies of highway noise pollution in Phoenix, Arizona. A 44 hour simulation period beginng on 7 November 2006 at 00 UTC is used along with several cases of model parameterizations that influence the boundary layer. Using a six-minute output frequency for the 1 km domain we implement a Lagrangian technique of reverse-time domain filling (RDF) which enables deriving the spatial variation in the potential temperature field on a known grid at higher resolution than the WRF grid. This is achieved for under two hour trajectories by invoking the adiabatic approximation for conservation of potential temperature. The result is then used in an acoustic model via a range dependent effective sound speed profile using the velocity profile obtained from the WRF output. We use a one-way parabolic equation (PE) approximation to the Helmholtz equation with a Green's function solution for a line-source above a flat locally-reacting impedance plane to obtain the starting field for a Crank-Nicolson scheme. The acoustic field of a 400 HZ source is computed both with and with RDF, at 8am local time on 7 November, during the period of morning katabatic flow from balleys abutting Four Peaks to the Northeast. The site location and times were chosen to coincide with field experiment measurements from previous work by the authors.

B.2 WRF Model Setup

For the preliminary study, we use similar configurations as presented in Section 4.3.2 for cases 1, 3, 4, and 5 given in Table 7 of Section **??** to which the reader is referred for further detail outside of the following brief description. A summary table of the cases

used here is given in figure 7. As indicated in the timeline of figure 73, these experiments utilize model restarts to enable an hourly output rate for much of the simulation time that was not going to be needed for RDF or other analysis, and an much higher output rate of every six minutes during the observational and analysis times. Model nesting for the four domains and the 2-way feedback used for all four domains is indicated in figure 72, centered on Phoenix Arizona as indicated in figure 72. Vertical refinement was applied on the 4th domain using hourly data and a 12 hour spin-up period. Initial resolution was 60 vertical levels and increased to 180 levels with a refinement factor of 3 in using `ndown`. The model timestep for d01 was set to 120 seconds, hence the 6-minute output frequency as parent-child timestep ratio of 3 was used for all domains. The vertically refined domain used a 2 second timestep. For the two land-use methods, the maps of 1 kilometer 4th domain are presented in figure 74 indicating differences in classification along with the inclusion of urban data from NLCD.

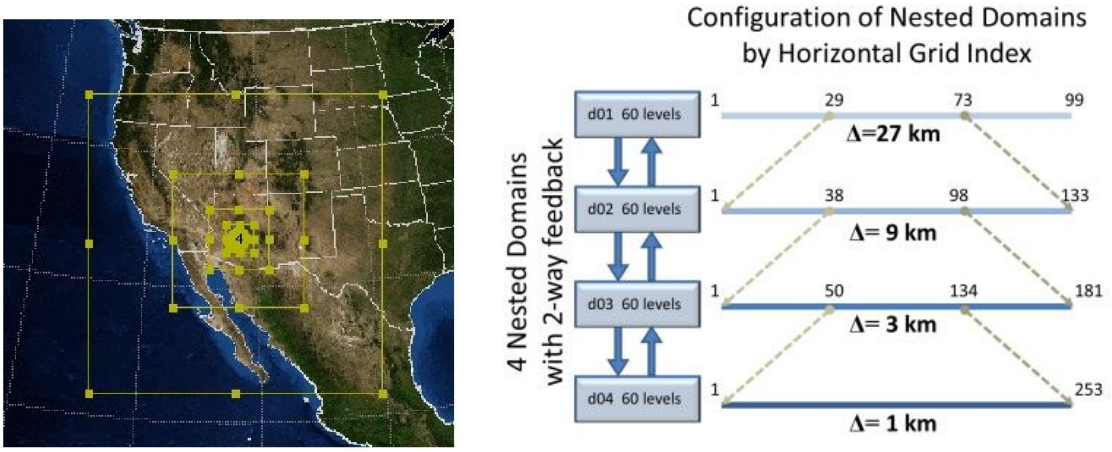

Figure 72: (left) Schematic (from WRF Domain Wizard) showing 4 nested domains overlaid on map of western United States. (middle and right) Schematics showing domain nesting, resolution and feedback. Horizontal grid indices and vertical levels are indicated.

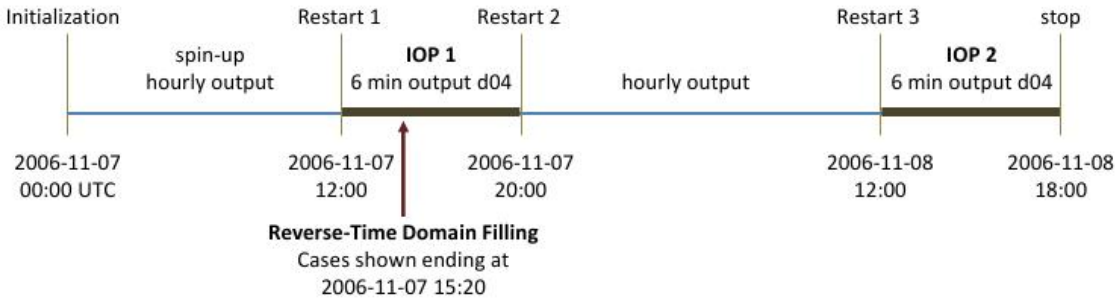

Figure 73: Schematic timeline of simulation showing key aspects: model initialization, model restart times, observational periods, analysis time of reverse-time domain filling and frequency of WRF model output.

Case ID	Urban	Land Surface	Surface Layer	Boundary Layer	Land Use
A	UCM	5-layer	MM5	YSU	USGS
B	bulk	5-layer	MM5	YSU	MODIS+NLCD
C	UCM	5-layer	MM5	YSU	MODIS+NLCD
D	bulk	Noah	Eta	MYJ	MODIS+NLCD

Table 7: Definitions of Case ID for WRF model parameterization options used in this study.

B.3 Acoustic Model

The acoustic model we use is a range-update version of what is presented in Section 4.2 with a modified schematic presented in figure 75. The PE model equation here reads,

$$\left(\frac{\partial}{\partial y}+i\sqrt{\mathscr{H}}\right)\left(\frac{\partial}{\partial y}-i\sqrt{\mathscr{H}}\right)p_c=0,$$

where

$$\mathscr{H}=\frac{1}{c_{eff}^2(y,z)}\frac{\partial}{\partial z}\left[c_{eff}^2(y,z)\frac{\partial}{\partial z}\right]+\frac{\omega^2}{c_{eff}^2(y,z)}$$

Where we retain only the factor $\left(\frac{\partial}{\partial y}-i\sqrt{\mathscr{H}}\right)$ for propagation in the positive y direction, here rotated to be South, transverse to the highway and in the downwind direction for comparison with OSF09. Again, grid spacing is $\Delta_y=\Delta_z=\lambda_f/10$. The key to this section is

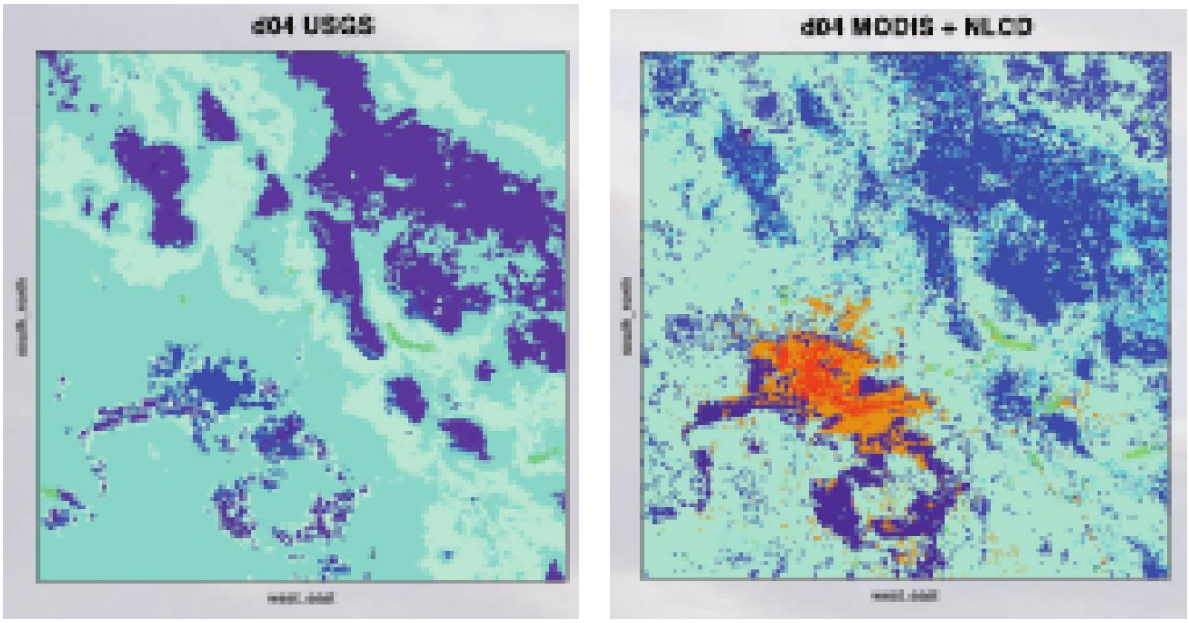

Figure 74: Map of dominant land-use index for USGS (left) and Modis with NLCD urban (right). Blue indicates urban areas in USGS and orange to red are used for NLCD. Also forest in USGS (purple) is miscategorized in some Phoenix valley locations, as seen in the cropland (purple) of MODIS, where MODIS forest is blue.

the slowly varying with range effective sound speed field,

$$c_{eff}(y,z) = c_{ad}(y,z) + V_S(z)$$

where we plan to use one profile from WRF for the representative velocity field in the South direction, $V_S(z)$, and to use a mesh with 30 meter grid spacing of 10 vertical by 20 horizontal, for a 300 meter high by 600 meter in range grid of points in temperature from which to construct the adiabatic sound speed $c_{ad}(y,z)$. We use the same conversions as presented in Section 4.3.3 to obtain the sound speed, which here is interpolated from the 30 meter grid to obtain input profiles that are updated with each range step in the PE model.

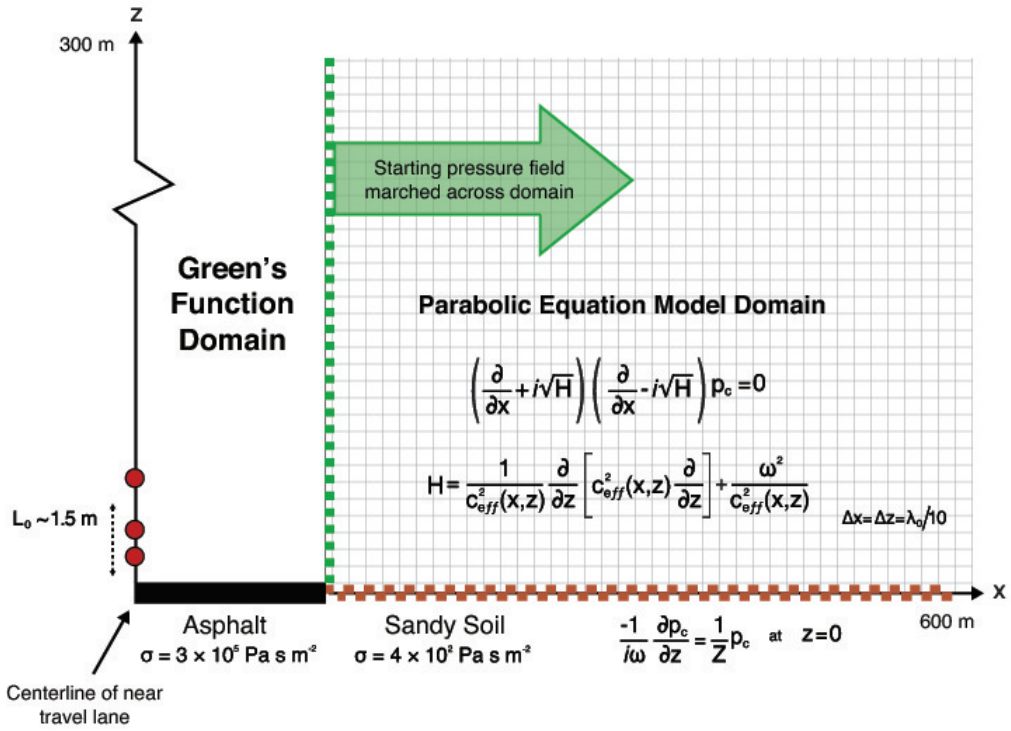

Figure 75: Schematic of range-update PE model, but rotated to propagate in the $+x$ direction instead of $+y$, with z vertical. A Green's function solution for a monochromatic line source above an impedance plane in a homogeneous stationary atmosphere of constant temperature to find the starting pressure field at the edge of the asphalt. The pressure field is then marched across the PE domain, taking updates in $C_{efF}(z)$ at each range step to recompute H. An attenuating layer at the top is used to avoid reflections. A 1-parameter ground impedance model is used with flow porosity representative of sandy soil for the complex normal impedance ground boundary condition. The domain height is 300 meters and the range id 600 meters.

B.4 Lagrangian Reverse-Time Domain Filling

B.4.1 Method

We use a Lagrangian technique called reverse-time domain filling (RDF) which has been applied in several previous studies for other applications in the atmospheric sciences

Clain et al. 2010; Dritschel 1988; Dragani et al. 2002. Our approach to using the technique is now described and applied to the vertically refined fourth domain with one kilometer horizontal resolution shown in Section B.5 with trajectory results shown below. We will use capital notation for the WRF domain grid, and lower-case for the higher resolution grid to which we seek to fill with an initially unknown potential temperature field – without simply spatially interpolating the temperature. From the WRF output files, we have velocities, $\vec{U}$, potential temperature, Θ, at the specified output times, T, all at the resolution of the domain with positions, $\vec{X}(T)$, which are time-dependent due to the η-coordinate depending upon pressure which is also a prognostic variable. Let $\vec{x}(t_0)$ be a regular grid with individual points $\vec{x}_i(t_0)$, at time $t_0 = T_0$, with much higher resolution than $\vec{X}(T_0)$. We seek to determine temperature data $\theta(\vec{x}(t_0), t_0)$, at this higher resolution for use in deriving a range dependent effective sound speed field $c_{eff}(\vec{x}(t_0), t_0)$ for an acoustic model which depends on spatial scales not resolved by the meso-scale model which produced the coarse grid data. Furthermore, the acoustic model uses the frozen-field approach since $\mathscr{O}(U) \ll \mathscr{O}(c_{eff})$ over a propagation distance $\mathscr{L}_D$. Or, more properly stated in terms of timescales, the eddy timescale within the acoustic domain of height $\mathscr{H}_D$ in the PBL, $\mathscr{T}_{eddy} \sim \mathscr{H}_D/U$, is related to the acoustic timescale, $\mathscr{T}_{acoustic} \sim \mathscr{L}_D/c_{eff}$, by $\mathscr{O}(\mathscr{T}_{acoustic}) \ll \mathscr{O}(\mathscr{T}_{eddy})$.

Using the adiabatic approximation for short times, $t \ll \mathscr{T}_{ad}$,

$$\frac{d\theta}{dt} = 0,$$

stating that potential temperature is conserved within the flow where $\mathscr{T}_{ad}$ is an adiabatic timescale describing time thermal diffusion and other parcel heating processes. By using the Lagrangian perspective definition,

$$\frac{d\vec{X}}{dT} = \vec{U}\left(\vec{X}(T), T\right),$$

we seek to solve for,

$$\frac{d\vec{x}_i}{dt} = \vec{u}_i\left(\vec{x}_i(t), t\right),$$

where $\Delta t \ll \Delta T$ and we are neglecting shear in considering advection of an infintesimal fluid parcel Ω_i with initial coordinates $\vec{x}_i(t_0)$. We set $\Delta T = N\Delta t$ with $N \gg 1$. For our case, $\Delta T = 6$ minutes, the interval in WRF output files and $\Delta t = 4$ seconds, the advection timestep with a 4th order Runge-Kutta (RK4) method using evaluation-timesteps of 2 and 4/3 seconds. We take a 30 meter resolution grid in the y–z plane at $t_0 = T_0 = T_A$ as the analysis time (for T_A being, for instance, 15:20 Z on 11-07-2006 for case A in OSF09 described in Section 4.3.1 table 1) where we desire to compute the sound field using the 2-D range-update PE model described in B.3. Reverse-time advection is performed for a total time $M\Delta T$, $M \in \mathbb{N}$ where we advect back for 2 hours giving $M = 20$. Any parcel that impacts the ground or otherwise leaves the domain is stopped and evaluated at the timestep before it would have left.

First, we determine monotonic cubic spline coefficients (using Matlab function `pchip`) for the WRF model output times T_k, $k = 2, \ldots, -M-3$. For accuracy in temporal interpolation we use a set of six WRF output fields bracketing the current interval ΔT for interpolating the velocity field to perform RK4 backwards advection for each set of N timesteps of increment $-\Delta t$. In the following, we use the notation of a hat to denote the spatially interpolated field (using Matlab function `ppval` with the piecewise monotonic cubic-spline polynomial coefficients). We first interpolate at the bracketing WRF times $T_{\{J\}} \in \{T_{J-3}, \ldots, T_{J+2}\}$, where $J \in 1, \ldots, M$ is the current interval between WRF output files, obtaining the coarse-time velocities at the fine-grid positions,

$$\vec{U}\left(\vec{X}(T_{\{J\}}), T_{\{J\}}\right) \xrightarrow[\vec{x}_i(t_j)]{\text{“spline”}} \hat{\vec{U}}\left(\vec{x}_i(t_j), T_{\{J\}}\right),$$

for the timestep t_j, $j \in 1, \ldots, N$ or at RK4 evaluation-timesteps. We next interpolate in time

using the 6 bracketing times,

$$\hat{\vec{U}}\left(\vec{x}_i(t_j), T_{\{J\}}\right) \xrightarrow[t_j]{\text{“spline”}} \vec{u}_i\left(\vec{x}_i(t_j), t_j\right),$$

which is then used to obtain new positions $\vec{x}_i(t_{j-1})$. When $j-1=-N$, the $J=J-1$ is updated. Lastly, when $t_j = T_M$, advection is stopped and the temperature field is constructed by,

$$\theta(\vec{x}_i(t_0)) = \theta(\vec{x}_i(t_{end})) \xleftarrow[\vec{x}_i(t_{end})]{\text{“spline”}} \Theta(\vec{X}(t_{end}), t_{end}).$$

Here, we use the notation t_{end} to denote the end-point of the trajectory of an individual parcel with initial coordinates $\vec{x}(t_0)$.

In the above notation, we intend that,

$$\mathscr{C} \xrightarrow[\mathscr{E}]{\text{“spline”}} \mathscr{F},$$

is to be interpreted as meaning the interpolation of coarse-grid data, $\mathscr{C}$, onto the evaluation-grid, $\mathscr{E}$, yielding the fine-grid data, $\mathscr{F}$. Or, that $\mathscr{C}(\mathscr{E}) = \mathscr{F}$ by monotonic cubic-spline interpolation of the data in $\mathscr{C}$. The analogous relation is to hold for $\leftarrow$.

B.4.2 Results for Trajectories and $\theta(\vec{x}(t_0), t_0)$

To conserve memory used for holding variable data and free space for parcel data, we use only a subset of the 252 km^2 1 km horizontal resolution vertically refined fourth domain d04R when computing trajectories. Hence, the following figures 77 and 78 only show this subset, and figure 76 shows a further zoomed subset of this domain. This section demonstrates the results of the reverse-time trajectory calculations and temperature retrieval. Shown in 76 is a snapshot is taken at the analysis time T_A of 15:20 Z on 11-07-2006 corresponding to the end of the 20 minute interval for case A in OSF09, which is used in

the following analysis for the temperature fields from the 4 WRF namelist configuration cases listed in figure 7.

Shown in figure 77 is a time progression of the trajectories for a single namelist case from the release point, tracing backwards in time up the valleys adjacent to the Four Peaks mountain grouping confirming morning katabatic drainage flow. Differences in the parameterizations can be seen with all four cases tested thus far in figure 78. Shown in figure 79 is the initial raw retrieved from RDF of perturbation potential temperature in Kelvin with initial grid points overlaid as white "x" marks, here for namelist case B. Note that this was plotted with default `contourf` package method and distorts what would be a smoother transition if it were first spline interpolated. Next, we show in figure 80 the retrieved temperature fields in Kelvin from converting the raw perturbation potential temperature alongside what would otherwise have been derived for range-dependence if the adjacent WRF profiles were interpolated (here again using the `contourf` plot interpolation and patching which looks messy and is deceptive in how it plots).

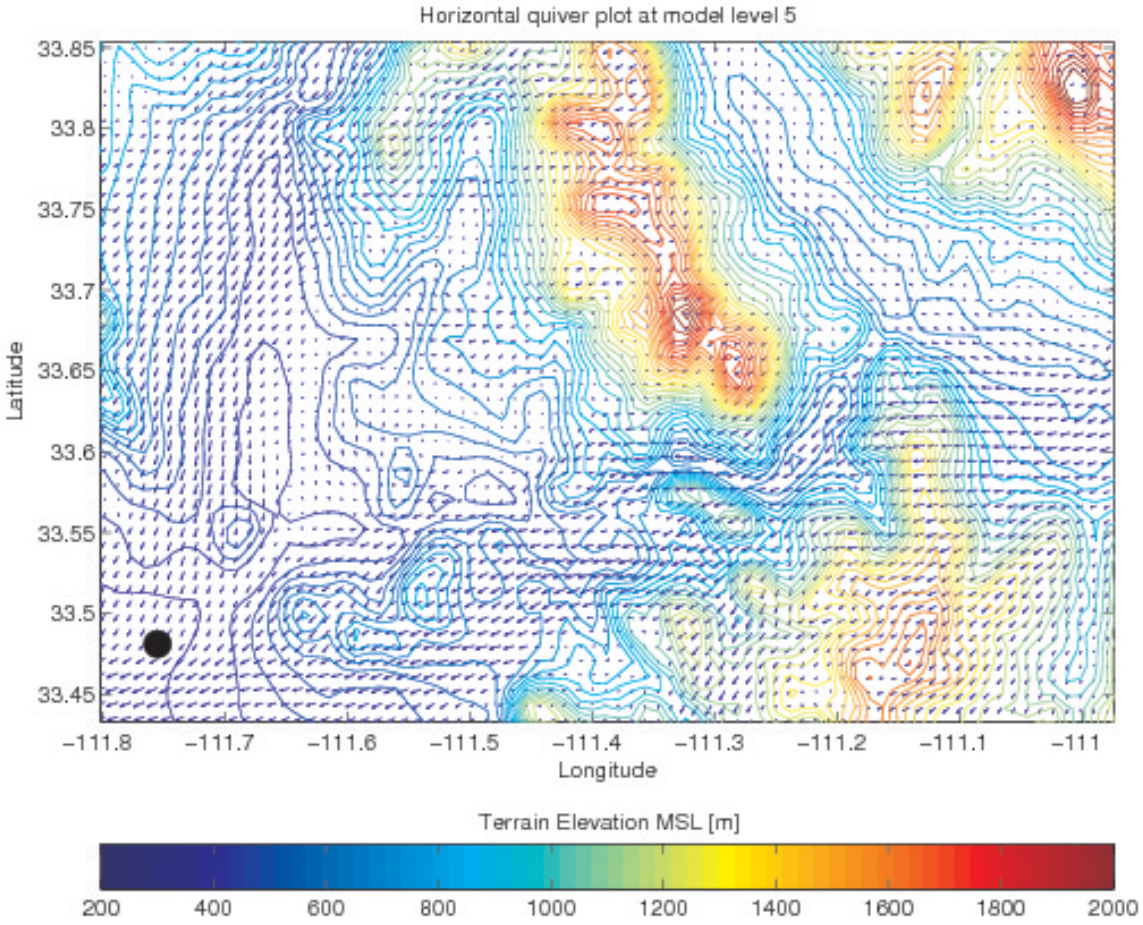

Figure 76: Zoom into d04R showing terrain elevation in colored contours with height in meters indicated by the colorbar at bottom. This snapshot is taken at the analysis time T_A of 15:20 Z on 11-07-2006 corresponding to the end of the 20 minute interval for case A in OSF09. The field experiment point and $\vec{x}(t_0)$ location is indicated with the black dot in the lower left. Horizontal velocity vectors are also shown for the 5th model level ($\approx$120 meters agl) with 1 km horizontal spacing. The Four Peaks mountain range is clearly visible as the high elevation grouping in the center of the image and Roosevelt lake is in the valley to the east of these peaks. The Superstition mountain range is in the bottom right of the frame.

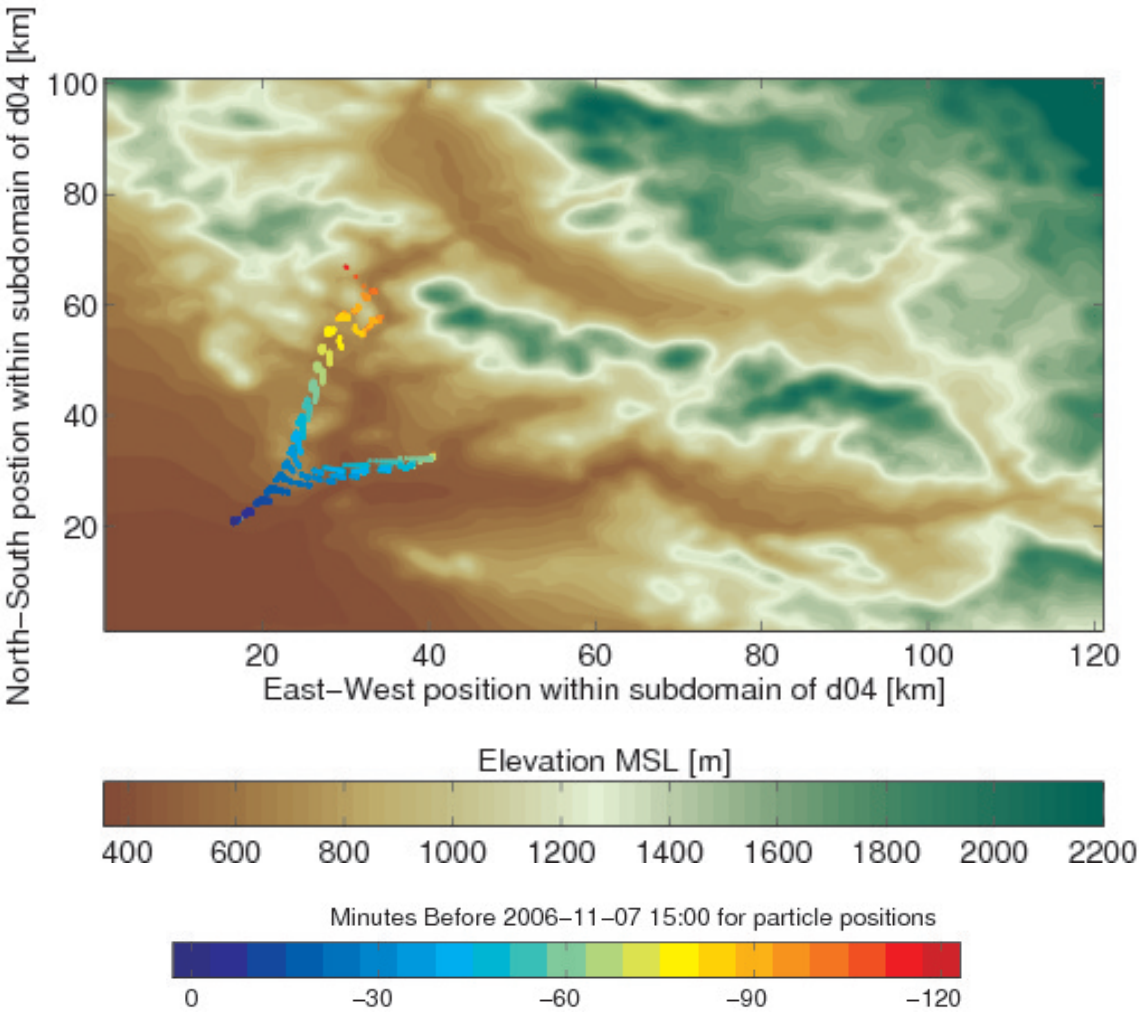

Figure 77: Filled contour map indicating terrain elevation in meters and blue-to-red colorbar indicating time in minutes before the analysis time of 11-07-2006 at 15:00 Z for parcel positions every 6 minutes, provided they haven't hit the ground, for namelist case B.

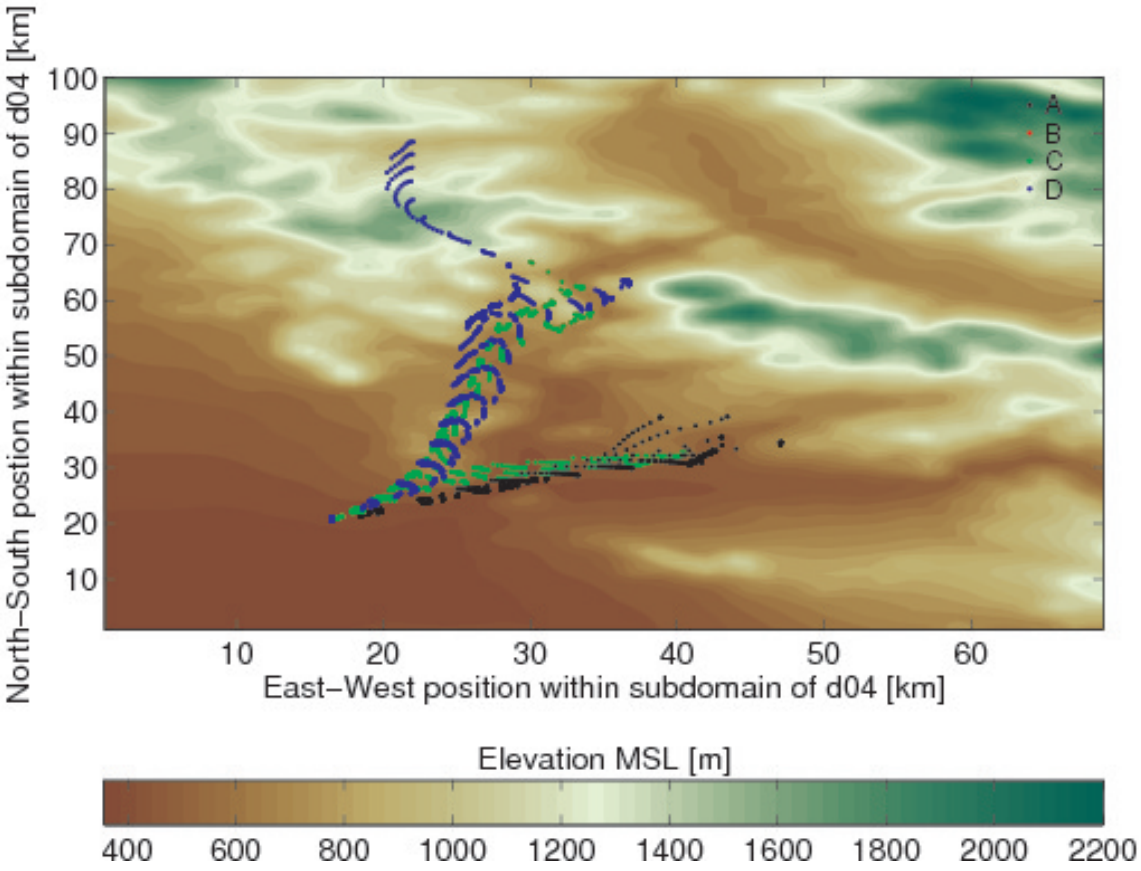

Figure 78: Same as figure 77 but instead of coloring trajectories by time, they are colored by namelist case with case A (blue), case B (red), case C (green) and case D (black). Note that case B is exactly under case C since the only difference was in use of urban canopy model, but these trajectories are not influenced by any urban effects for this analysis time.

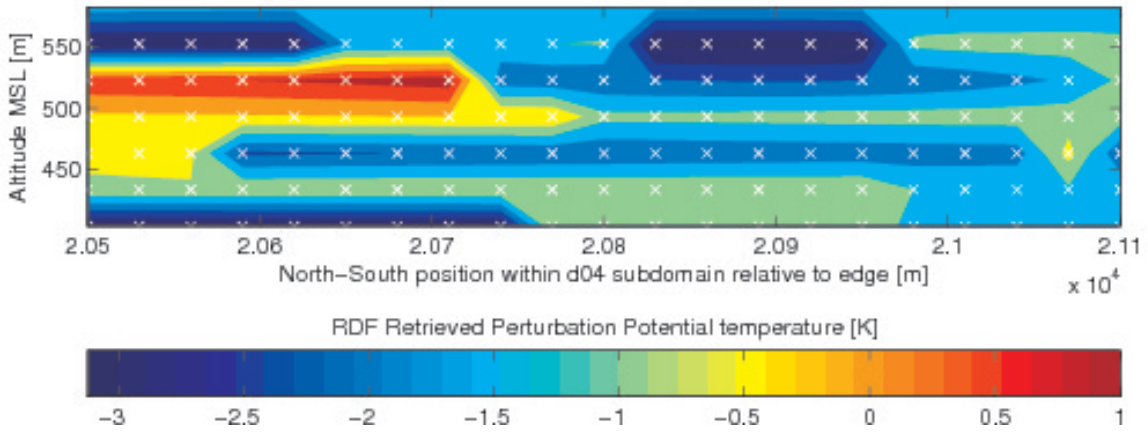

Figure 79: Initial raw retrieved RDF perturbation potential temperatures in Kelvin plotted with default contourf package with initial grid points overlaid as white "x" marks, here for namelist case B.

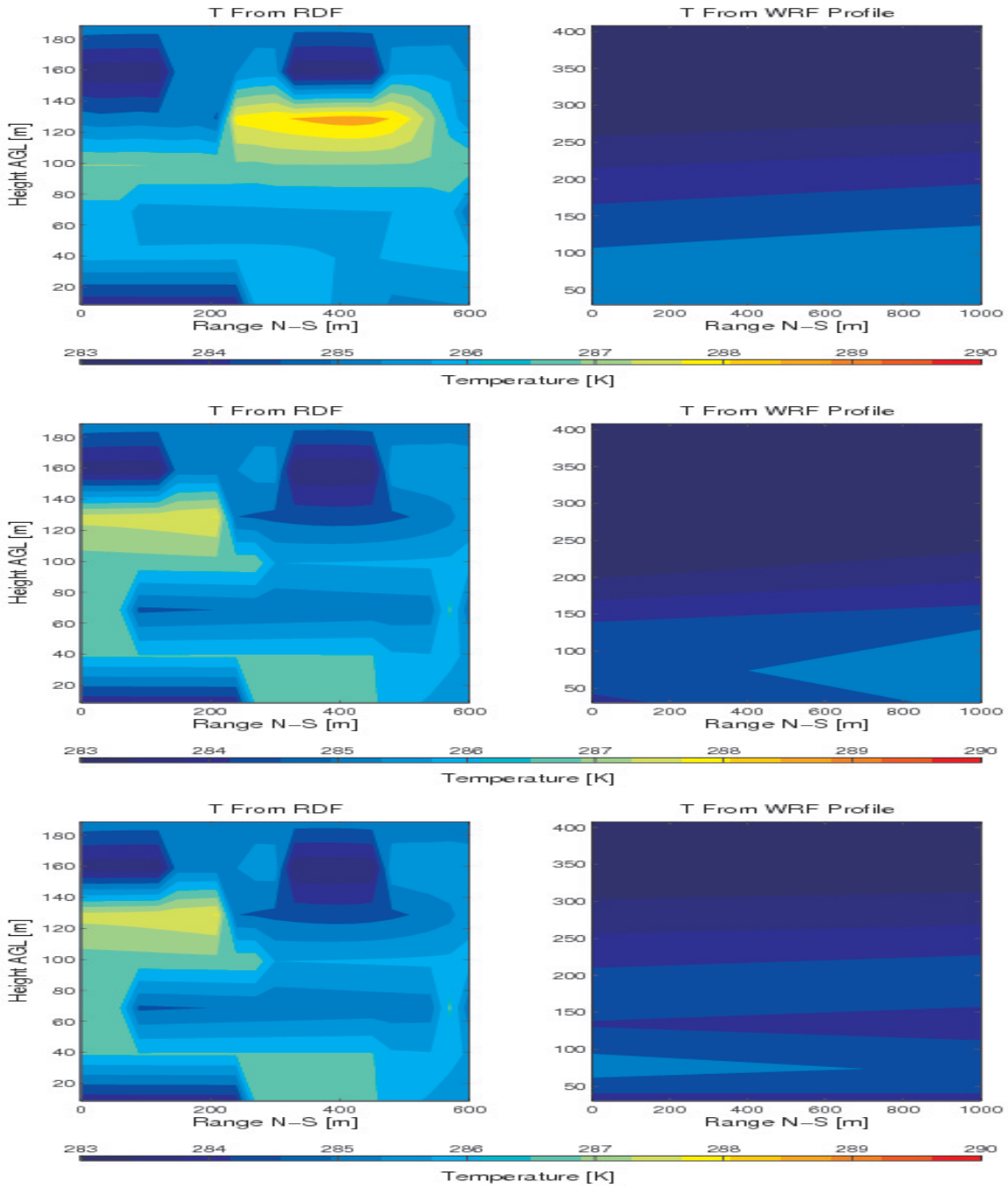

Figure 80: (left panels) RDF temperature fields converted to Kelvin in the GTPE computational grid coordinates (using default contourf plot) only shown to 200 meters AGL because the attenuating layer begins at this height. (right panels) The 1 km horizontally spaced, vertically refined WRF grid (d04R) temperature profiles of the 2 nearest North-South grid coordinates interpolated (with the default contourf plotting). For namelist case A (top row) case B or C (middle row) and case D (bottom row).

B.5 RUPE Model Results

Unfortunately, the GTPE model was run for a plane-wave incident source and not for the OSF09 intended highway line-source and this needs to be revisited.

B.6 Future Work

This work was prelimiary proof of concept and more validation and verification needs to be performed. The RUPE model was modified from previous work considering a Gaussian temperature bump, to injest the new temperature perturbation field, but the wrong switch option on starting field changed some other settings. This was run in batch mode under deadline. A correct field case was computed but the output field has not yet been plotted as other pressing deadlines arose.

Below are some specific points to consider. Re-run and plot for correct acoustic source field, of course. Modify temperature field figures to plot higher-resolution interpolated data, then plot using `contourf` patching and interpolating method. I'm not sure if I confused cases B,C and D temperature fields when collating the figures when making plots for figure 80, but judging from the trajectories it seems unlikely that B/C and D would be the same. There are also some code improvements and parallelizations that could be implemented. I specifically need to ensure that I use `pchip` and not `csape` when interpolating. The point of interpolating before entering the time loop has yet to be implemented, and in fact, all of the wrfout times could be pre-processed in parallel or as a sub-process of the wrf job script if faster results are needed.

Of course, linking this method with the general terrain method is a goal but there are several idealized assumptions made in the process and the simulation can no longer be

considered as “real”. It would be nice to check these temperature field results against what is retrieved with d05R and d06R discussed in Section **??** and for all the namelist cases outlined in Section **??**, using resolutions of those domains with a 3D initial grid. We could in essence, compare the retrieved temperature fields against those produced by incorporating a child (or several) domain(s) into the nest from which we interpolate the velocity field.

A means of applying this to the velocity field was also considered, where WRF solves the flux-form Navier-Stokes equations for velocities,

$$\frac{d\vec{U}}{dt} = F_{\vec{U}}$$

and applies sub-grid models. If we were to modify the registry to provide auxiliary output of $F_{\vec{U}}$ and other needed fields at given timesteps and implement similar sub-grid models, it seems that in principle we might be able to devise a scheme to obtain $\vec{u}_i(\vec{x}_i(t),t)$. This was deferred until the temperature retrievals were completed.

APPENDIX C

APPENDIX FOR CHAPTER 5

C.1 Observed Fluxes

Seasonal (during 2012) and diurnal variation of incident shortwave forcing, along with the persistent katabatic and anabatic diurnal consistency of horizontal winds, are demonstrated in Figure 81, for observations averaged to 30-minutes during mid-December 2011 to January 2013. Observations during the study period are presented in Figure 82, showing 30-minute time-series (denoted by, $< \cdot >_{30}$) for net radiation, Q^*, fluxes of sensible and latent heat, $\langle Q_H \rangle$ and $\langle Q_E \rangle$, SEB residual ΔQ_s, anthropogenic forcing Q_F, along with the individual downward and upward radiation components for shorwave $G^{\downarrow}_{SW}$, $G^{\uparrow}_{SW}$, and longwave, $G^{\downarrow}_{LW}$, $G^{\uparrow}_{LW}$. Diurnally averaged 30-minute time-series (denoted by, $< \cdot >_{30,D}$), of the aforementioned quantites are also shown.

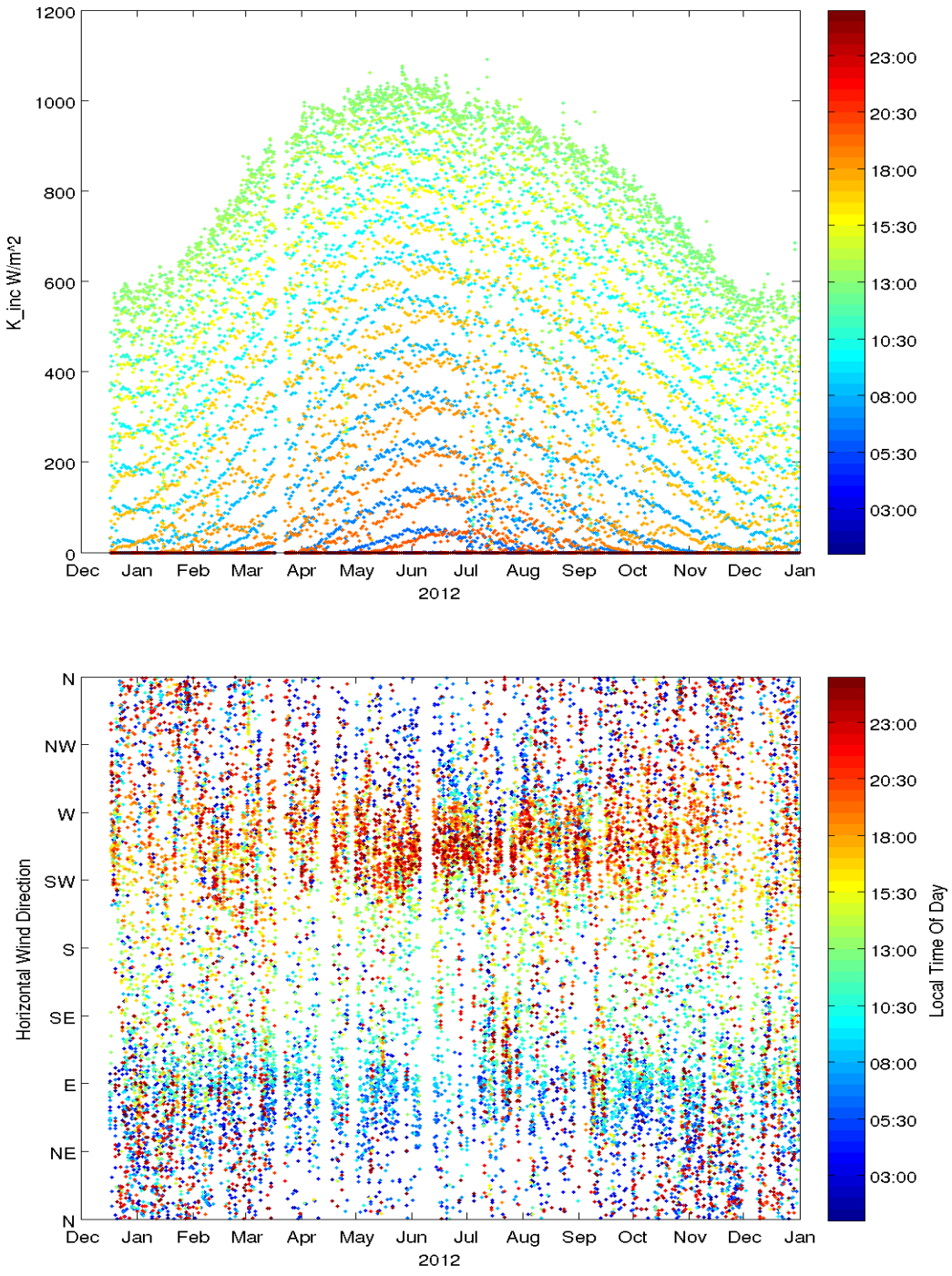

Figure 81: West Phoenix 22.1 meter flux tower observed diurnal (colorbar) and seasonal variation of 30-minute averaged downward shortwave radiation (top) and horizontal wind direction (bottom).

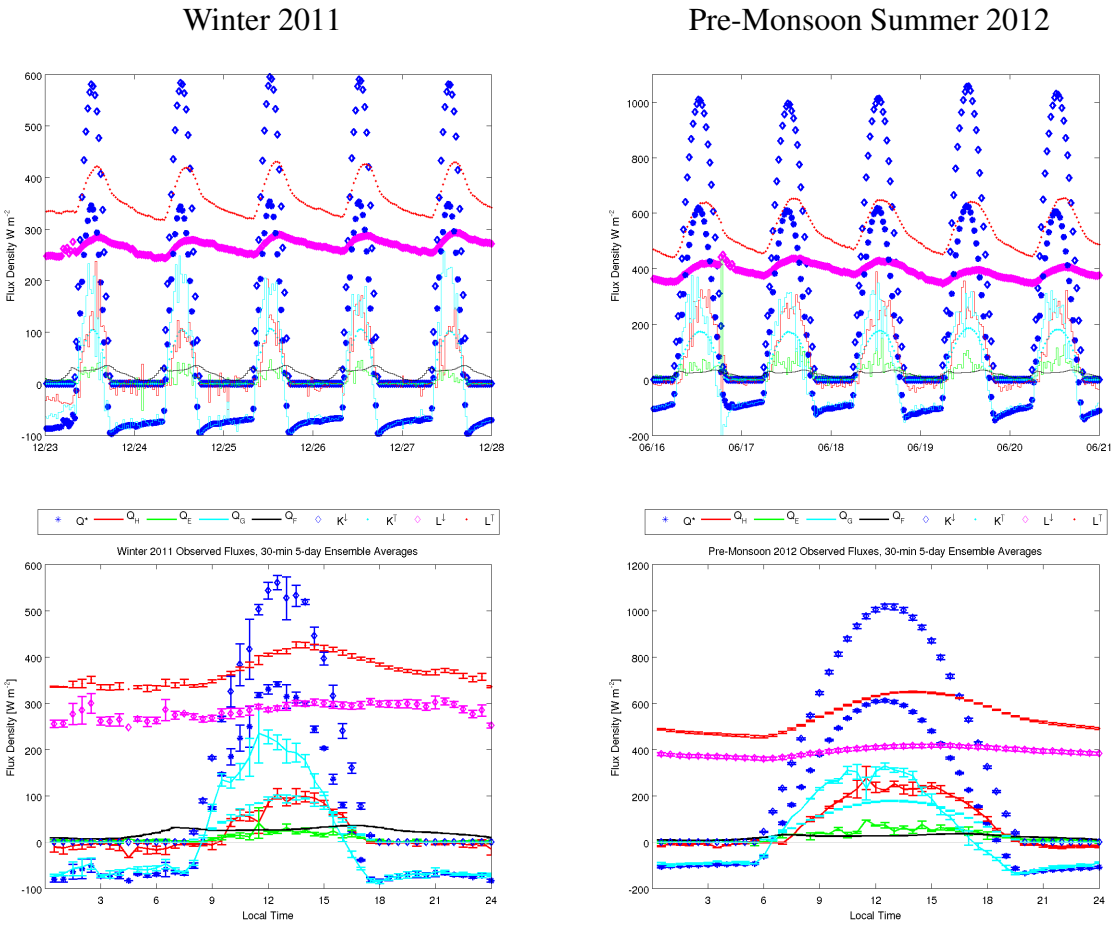

Figure 82: Observed surface fluxes combined for Winter 2011 (left) and Pre-monsoon summer 2012 (right), as a time-series during the analysis period (top), and diurnally averaged over a 5 day period (bottom).

C.2 Additional Model Evaluation

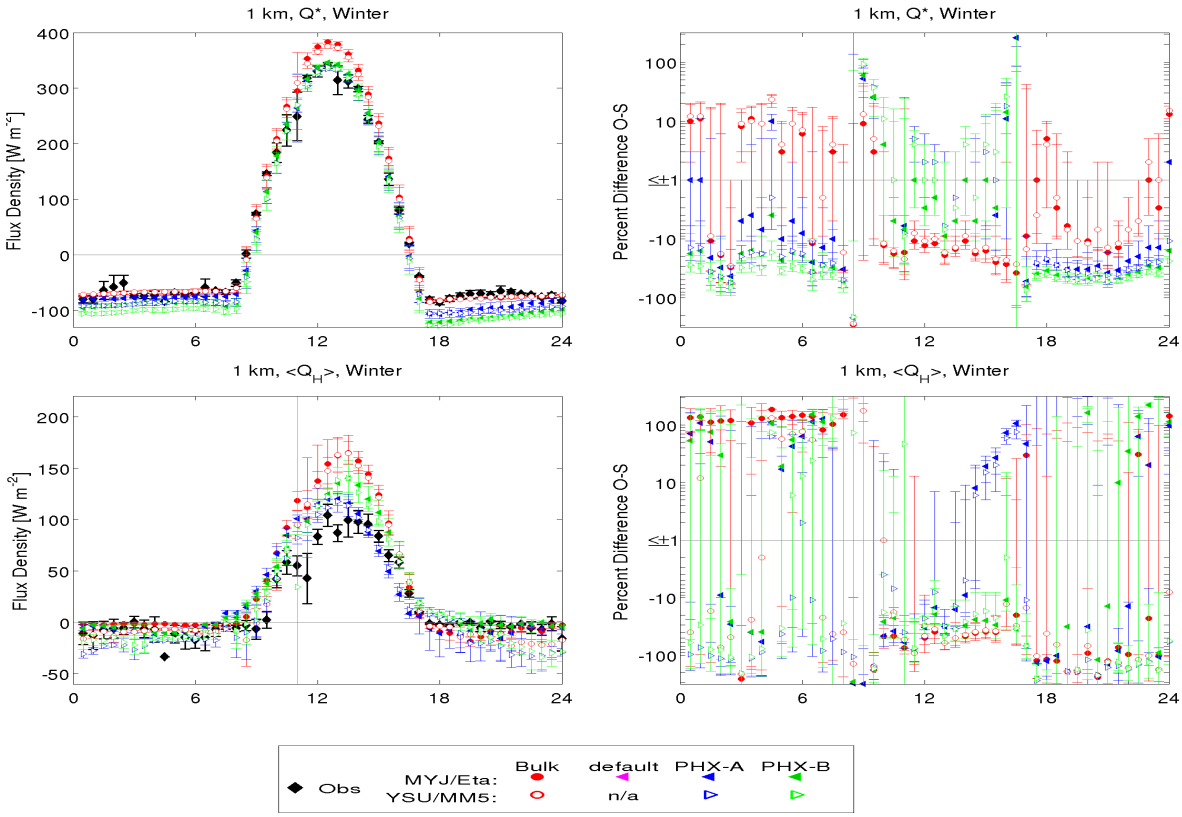

Figure 83: Diurnally averaged to 30-minute intervals during winter 2011 from D4 (Δ_H=1 km), showing comparison between observations and simulations (left), and percent difference of simulations from observations (right), for Q^* and $\langle Q_H \rangle$, top to bottom, respectively. See Figure 40 and 41 for pre-monsoon summer 2012.

C.2.1 Remark on Bias Canceling

When considering the bias error of a single measurement-and-prediction pair, for e.g. Q^*, as,

$$\mathrm{BE}(Q^*) = (Q^*)_{\mathrm{obs}} - (Q^*)_{\mathrm{sim}}, \tag{C.1}$$

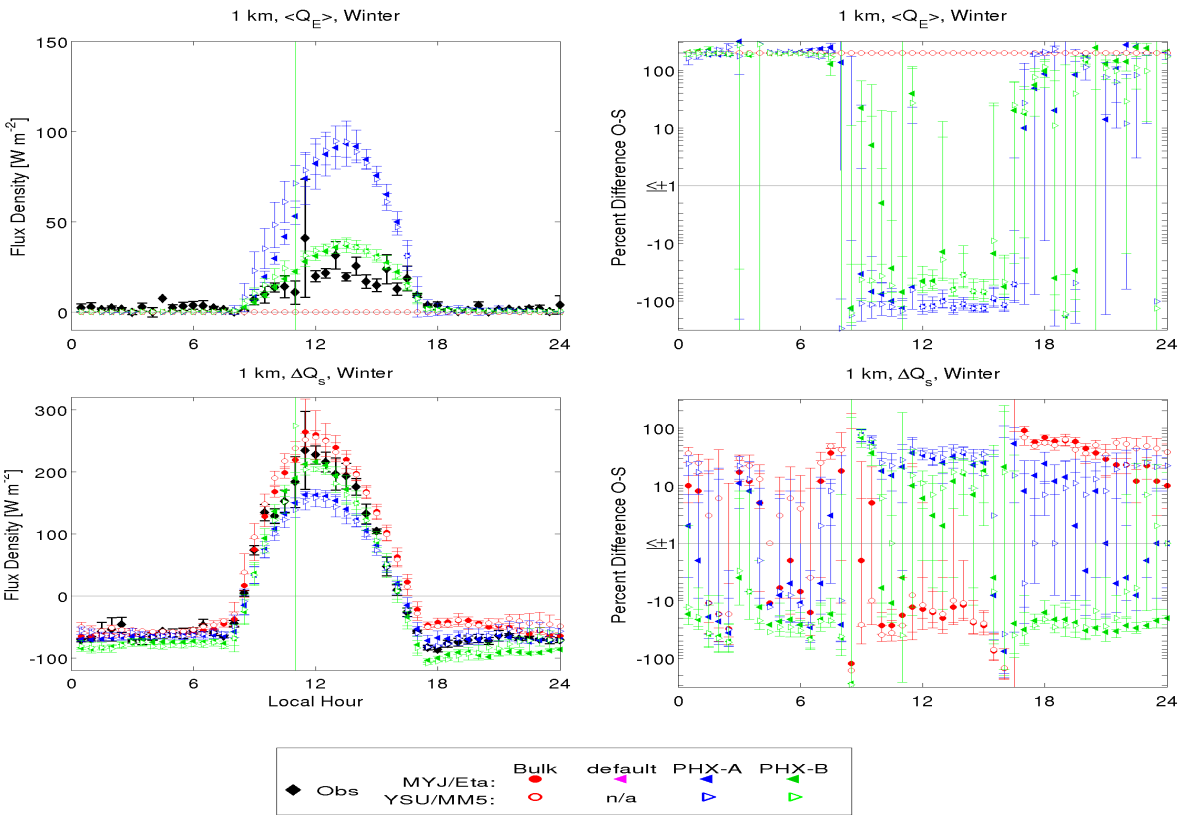

Figure 84: Diurnally averaged to 30-minute intervals during winter 2011 from D4 (Δ_H=1 km), showing comparison between observations and simulations (left), and percent difference of simulations from observations (right), for $\langle Q_E \rangle$ and ΔQ_s, top to bottom, respectively. See Figure 40 and 41 for pre-monsoon summer 2012.

it is straightforward to show that the bias error, for Q^* in this case, can be written as,

$$\mathrm{BE}(Q^*) = \mathrm{BE}(G_{SW}^{\downarrow}) - \mathrm{BE}(G_{SW}^{\uparrow}) + \mathrm{BE}(G_{LW}^{\downarrow}) - \mathrm{BE}(G_{LW}^{\uparrow}). \tag{C.2}$$

So the bias error in Q^* may be reduced in comparison to the bias of constituent radiative flux terms depending upon the sign of each term. Therefore, assessing net radiation in absentia of considering the constituent shortwave and longwave, upward and downward components, is not sufficient to evaluate model agreement with physical reality. Furthermore, it is difficult to disentangle potential sources of model error within the radiation forcing by solely examining bias in Q^*.

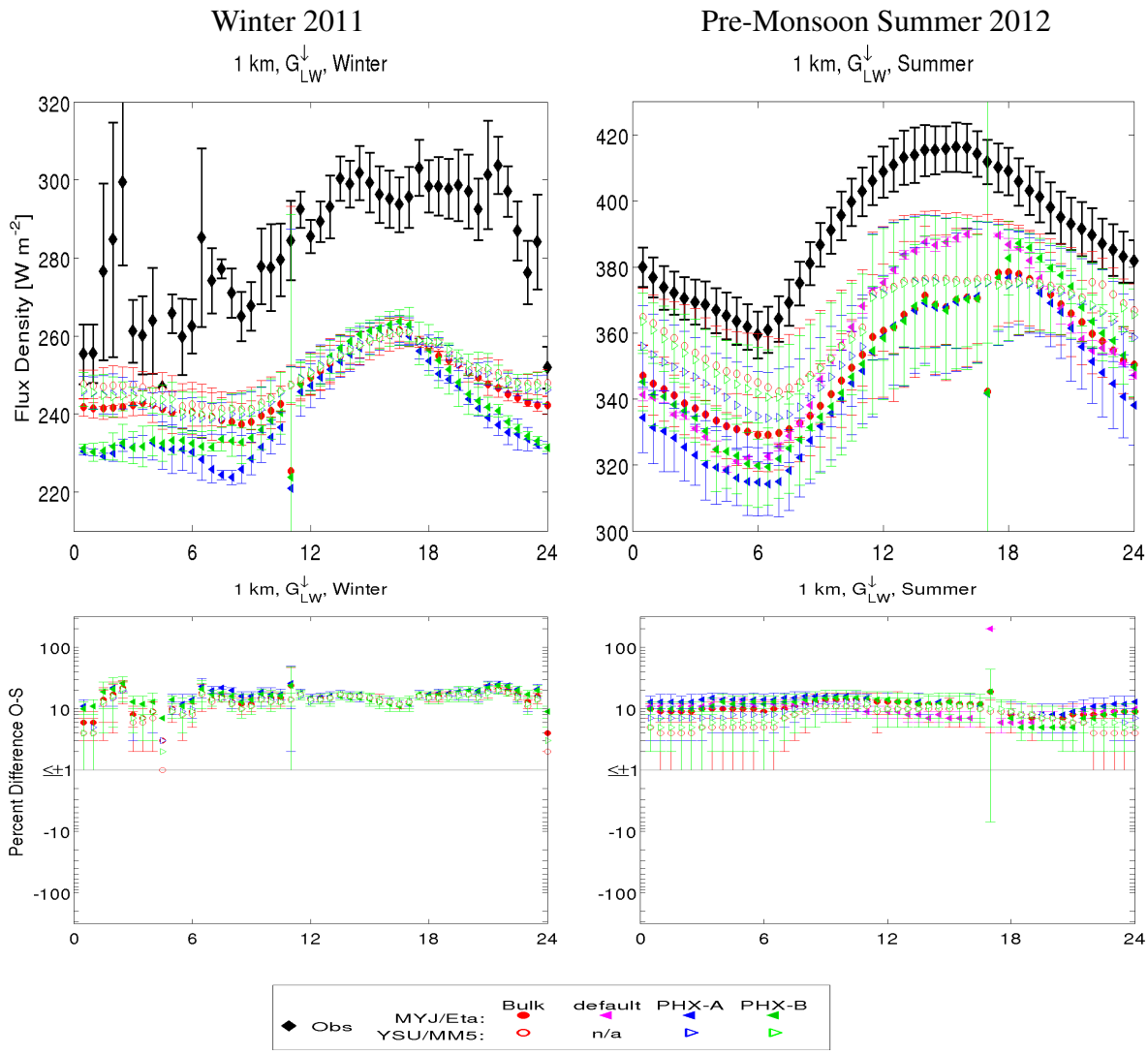

Figure 85: Comparison of downward longwave radiation component, $G_{LW}^{\downarrow}$, between observed and diagnostic simulated values, from D4 (Δ_H=1 km) as 30-minute and diurnally averaged values (top) and percent differences (bottom) for winter 2011 (left) and pre-monsoon 2012 (right).

C.2.2 Downward Radiation

A systematic underestimation bias of 3-20%, especially during mid-day, is shown in Figure 85 for the downward longwave flux, $G_{LW}^{\downarrow}$. Model-level air temperature is an input

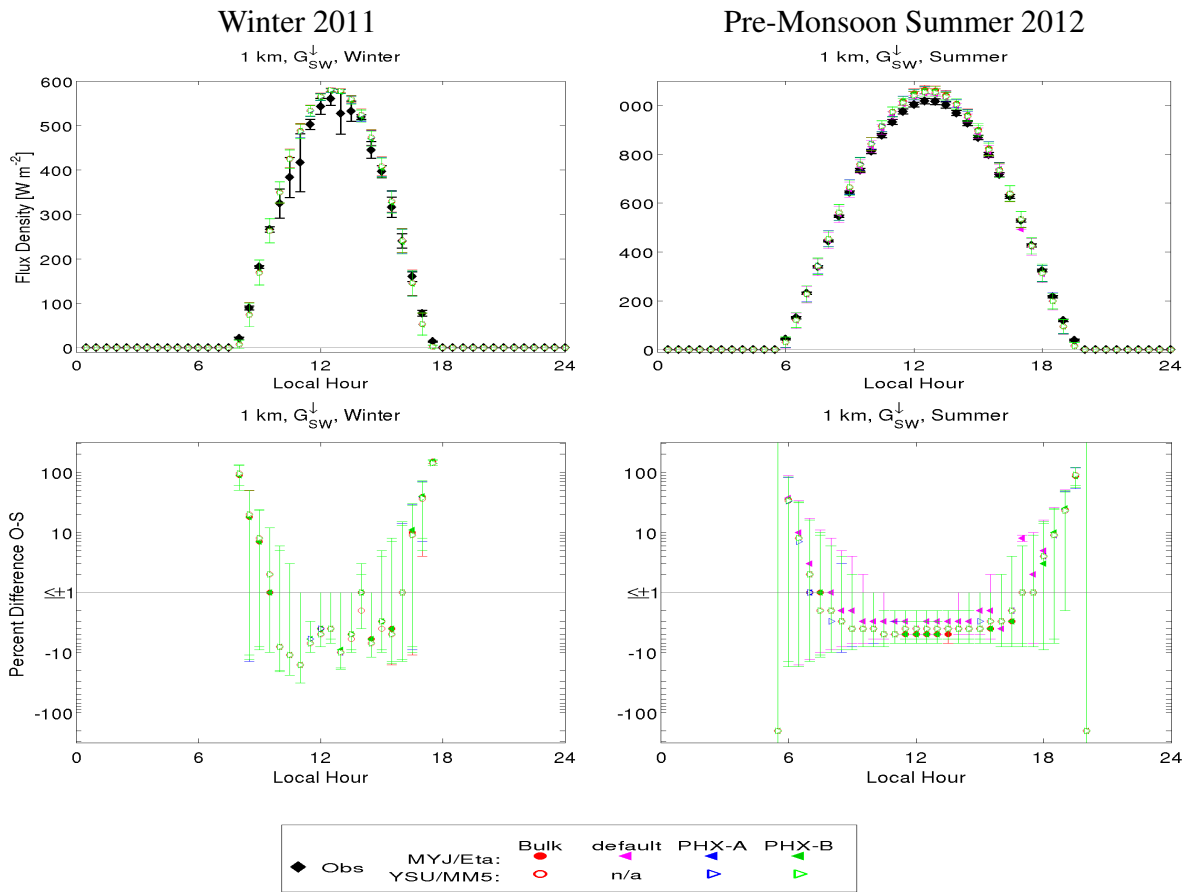

Figure 86: Same as in Figure 85 but for $G^{\downarrow}_{SW}$.

for the frequency integrated Plank function when calculating the longwave radiation convergence and heating profile (Dudhia 1989). Thus we infer that the longwave bias from observations is because the air aloft was too cool, however we lack observed profiles of temperature to test this hypothesis. Interparameterization differences in $G^{\downarrow}_{LW}$ may be explained by examining potential temperature profiles controlling for PBL/SLS and UCM. A similar potential temperature bias has been noted between PBL schemes in other studies, with YSU being warmer than MYJ in Xie et al. 2012, and Shin and Hong 2011 show a warm (with YSU warmer than MYJ) and dry bias from observations, where the shape and interparameterization variability are due to PBL scheme differences.

The downward shortwave radiation $G^{\downarrow}_{SW}$, presented in Figure 86, shows afternoon model overestimation bias of 3-5% in pre-monsoon summer, and 4-10% in winter. Simulated radiation would not account for atmospheric heating from repartitioning of shortwave flux due to pollutants in the observed UBL, since the simulations did not account for polluted air. Furthermore, a column moisture content bias would lead to longwave absorption and heating bias. Additional heating from other urban heat island sources and anthropogenic waste heat sources are also expected to contribute to the UBL temperature and radiation flux components, as discussed in Arnfield 2003. We hypothesize that an atmospheric moisture content bias could result from a combination of soil moisture initialization bias along with no irrigation, reducing regional evapotranspiration, or by input meteorological data bias. Atmospheric temperature bias could arise from not having aerosol heating, which would increase $G^{\downarrow}_{LW}$ and reduce $G^{\downarrow}_{SW}$, discussed in further detail below, with the reduced $G^{\downarrow}_{SW}$ influencing Q^{*} and surface forcing. Note that the $G^{\downarrow}_{SW}$ overprediction bias, seen in Figure 86, should produce a warmer surface, but the cold bias based upon $G^{\uparrow}_{LW}$ implies that the LSM is not producing a large enough skin temperature, as already discussed.

Examining $G^{\downarrow}_{LW}$ in Figure 85 there is more inter-parameterization divergence over night, for both seasons, and the variance during summer is much larger than for winter. It is suspected that summertime convection and wintertime stability play a role in model values, owing to differing rates of vertical transport from the surface, which shuts off in stable conditions. These differences are also manifest in z_{PBL} in Figure 88 as the PBL responds to surface values. When there is divergence between PBL cases, YSU is closer to observations than MYJ. The $G^{\downarrow}_{LW}$ for the higher f_{urb} value of PHX-B is also closer to observations than the corresponding PHX-A cases. Also, the bulk cases perform quite competitively in both seasons, especially during the evening periods.

C.2.2.1 Twilight

Increased bias error for all WRF cases near twilight hours is exibited for $G_{SW}^{\downarrow}$ in Figure 86 (and $G_{SW}^{\uparrow}$ in Figure 37 owing to albedo times $G_{SW}^{\downarrow}$). Astronomical twilight, defined by the center of the Sun at 108 degrees from zenith, for the study periods was, 0601 and 1956 for winter, and 0335 and 2124 for summer, all LST. While negligible in regards to total radiative forcing when accounting for Earth's global radiation budget (Kato and Loeb 2003), twilight seems to explain the increase to 20-60% underestimation error for $G_{SW}^{\downarrow}$ during the periods near sunrise and sunset, with observations being 12–30 W m^{-2} above simulations. This is largely due to the plane-parallel approximation used in the short wave radiative transfer model ([ )][Eqn. C12]Dudhia1989 that neglects all downward shortwave radiation for solar zenith angles greater than 90°. This small bias could have implications for atmospheric photochemistry for solar zenith angles near 90 degrees, or high latitudes which have long twilight periods (Mateshvili et al. 2005), particularly in polar regions (Kato and Loeb 2003; Bracher et al. 2005; Zib et al. 2012). One possible correction is to consider spherical geometry for high zenith angles by employing Chapman functions as demonstrated by Dahlback and Stamnes 1991.

C.2.2.2 Air Quality

It is well established that Maricopa County has been in non-attainment for federal air quality standards, in particular O_3, NO_x, and PM_{10} (Wiley 2011; Paul and Colyer 2011), resulting in photochemical influence of the polluted airshed (Lee and Fernando 2013). Uncertainties due to unresolved flow and upscale processes from urban airsheds and induced dynamics (e.g. UHI and urban thermal plumes), particularly concerning the role of

aerosol forcing (Mitchell Jr 1971), is a key uncertainty in short-term regional weather and long-term global climate modeling and for assessing the global energy budget (Trenberth, Fasullo, and Kiehl 2009; Ramanathan et al. 2001; Engling and Gelencsèr 2010). Accounting for pollutants necessitates employing an atmospheric chemistry module, such as WRF-CHEM (Grell et al. 2005), or CMAQ (Byun and Schere 2006), along with a detailed emission source inventory, to properly address these issues. WRF-CHEM with advanced Noah-like surface treatment meets the description of suggested work offered by T. R. Oke 1974 as a "future" boundary-layer model suitable for addressing this problem.

A consequence of the hypothesis of qir quality causing a repartitioning of downward fluxes for shortwave into longwave, would be a method to study the impact of pollutants within the UBL on the radiation components of the SEB. The order of magnitude for aerosol direct effect short-wave radiative forcing has been reported for typical urban brown-cloud as -80 W m^{-2} (Kaufman et al. 2002), or -62.5 W m^{-2} per 0.1 increase in aerosol optical depth (AOD) (Latha and Badarinath 2005). Not including such attenuation could explain part of the $\approx 5\%$ overestimation bias error in downward shortwave radiation due to not accounting for aerosols expected to be present in the Phoenix airshed (Lee et al. 2003; Clements et al. 2013). These data would indicate that daytime maximum AOD for Phoenix range between .03-.06 and .05-.09, for winter and pre-monsoon summer, respectively, based on ranges of mid-day shortwave bias. These low values are not unexpected based upon seasonal satellite data presented by Hsu et al. 2012; Sorooshian et al. 2011 showing $\lesssim$ 0.1-0.2 for the region, neglecting the sporadic summertime dust storm events (Brazel and Nickling 1986) which were not present during the selected quiescent study periods.

With a population of approximately 4 million, Maricopa County, in the south-central Arizona Sonoran Desert, consists of 26 different cities, with the largest being the City of Phoenix. The urbanized portions of this region are generally flat, although

numerous mountain ranges ring the urban area, with especially high ones to the east and northeast, as seen in e.g. Figure 34. A recent study by Lee and Fernando 2013 investigates the photochemical influence of the polluted Maricopa County airshed, but does not examine the influence on the SEB and ground-level net radiation terms. In the absence of synoptic frontal passages, prevailing daytime winds, as shown in Figure 81 at the study location, are from the west and southwest, reversing during the night, both directions being a consequence of topographically induced air flows: (1) an interstate, regional valley-to-mountain daytime flow from the west and southwest, augmented by continental westerlies; and (2) a more localized, county-scale nocturnal drainage from the east and northeast (Fernando 2010).

Despite concerted regulatory efforts at reducing metropolitan emissions of air pollutants (e.g. ADEQ 2000); despite innumerable technical analyses conducted by governmental agencies, universities, and private-sector scientists to better understand how the dynamics of horizontal and vertical air flow affect pollutant concentrations (e.g. ADEQ 2001; MAG 2007, 2008; H. Fernando et al. 2012); and despite remarkable improvements in air quality exemplified by the elimination of violations of the standard for carbon monoxide MAG 2013; much remains to be learned. With air pollutant emission densities highest in the urban core, with the well-known air pollution meteorology of arid climates, and with the general air flow patterns just described; the general outlines of the proximate causes of elevated concentrations of particulate matter (both airborne particles 10 microns and smaller (PM_{10}) and 2.5 microns and smaller ($PM_{2.5}$)) and ground-level ozone are clear enough. For example, the west-central portion of the urban region serves as a reservoir or "sink" of chemically inert, ground-level pollutants such as PM_{10} and carbon monoxide. Visibility is conspicuously degraded on a daily basis in winter mornings, with an unsightly "brown cloud" hovering over the central part of the urban region, slowing ascending and

diffusing with the rising mixing height until dissipated by the mid-afternoon thermals. For the photochemically reactive pollutant ozone, formed by the action of sunlight on emissions of volatile organic compounds and oxides of nitrogen (mostly from vehicular traffic), the air flow patterns tend to produce the highest concentrations in late summer afternoons along the eastern fringe of the metropolitan area. Early morning accumulations of the ozone precursors and of airborne particulates can be attributed to the frequent stagnant conditions of light to calm winds and a pronounced surface temperature inversion.

Since air pollution monitoring began in the 1970s metropolitan Phoenix, Arizona (in Maricopa County), has failed to attain the federal air quality standards for ozone and particulate matter Wiley 2011; Paul and Colyer 2011. Notwithstanding the recent announcement that the U.S. EPA intends to accept Maricopa County's 2012 for reducing particulates, and thereby declare the area to be in attainment with the PM_{10} standard (EPA publication in the Federal Register is anticipated by mid 2014 (Arizona 2014)), this arid region will continue to face difficulties in achieving and maintaining this standard. For example, in the 2010 - 2012 period on which the attainment status is to be based, 27 days had PM_{10} concentrations that exceeded the health standard. All of these were classified as "natural exceptional events", thereby except from having to meet the standards. Such a blanket classification for a month's worth of days with unhealthful concentrations of PM_{10} is tantamount to asserting that most if not all of the airborne particulates on these high-wind days originate naturally. A less sanguine but perhaps more realistic viewpoint would admit that major portions of this airborne dust arise from the actions of turbulent winds on such disturbed land surfaces as agricultural fields, major construction sites, unpaved roads, and heavily grazed desert cattle lands.

Improvement of numerical modeling tools such as the WRF, the subject of this paper, is paramount in acquiring a better understanding and ultimately substantial

improvement of air quality in the Phoenix region. The reason for this is that the WRF routinely provides the meteorological fields necessary for physico-chemical Eulerian air quality models employed in regulatory and other technical analyses of the air pollution problems inherent in metropolitan Phoenix. Achieving the national health standards for air pollution depends on a cost-effective reduction of air pollutant emissions, itself an immense regulatory and technical effort dependent on a more complete understanding of the atmospheric dynamics at work in the region.

However, in order to draw conclusions on this point, further observations and simulations are needed. It is recommended to run WRF-CHEM with similar parameterizations and to investigate the impact on these variables for different reasonable estimates of air-quality.

C.2.3 Atmospheric Surface Layer Stability

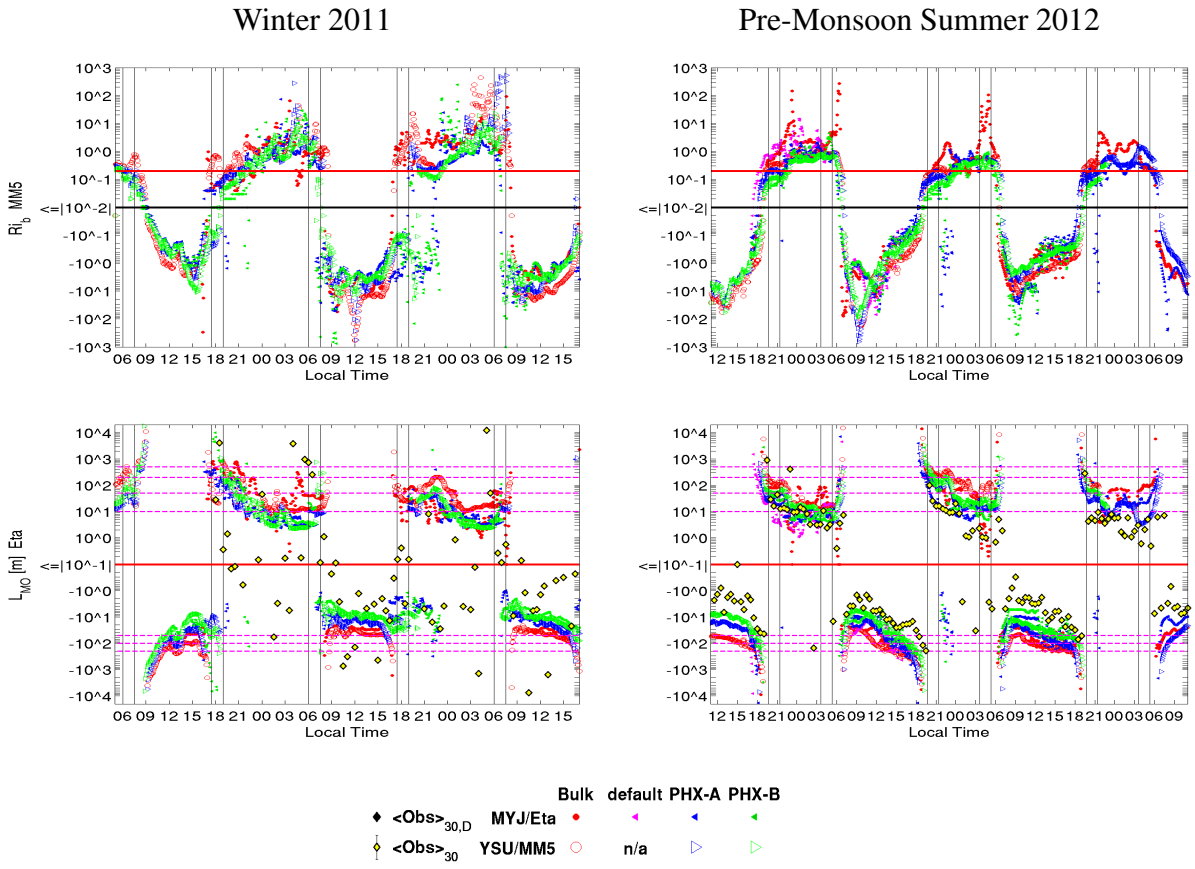

Figure 87: Time series from West Phoenix in D4 (Δ_H=1 km) during simulation periods for Winter 2011 (left), and Pre-Monsoon Summer 2012 (right), for bulk Richardson number, $\mathrm{Ri_b}$, used for MM5 SLS (top), and Obukhov length, L_{MO}, in meters, used for Eta SLS (bottom), with the boundary between stable and unstable regimes (red lines) and the following stability sub-classification limits, as described in the text, denoted: within $\mathrm{Ri_b}$, the MM5 defined boundary between three unstable regimes (black line, $<, =, >$); for L_{MO}, following Gryning et al. 2007 (magenta dashed). Observations are shown for values averaged to 30-minutes ($<>_{30}$, black points), and averaged to 30-minutes diurnally over 5 days ($<>_{30,D}$, black and yellow points). Twilight periods are indicated for solar zenith angles of 90°and 108°(vertical lines).

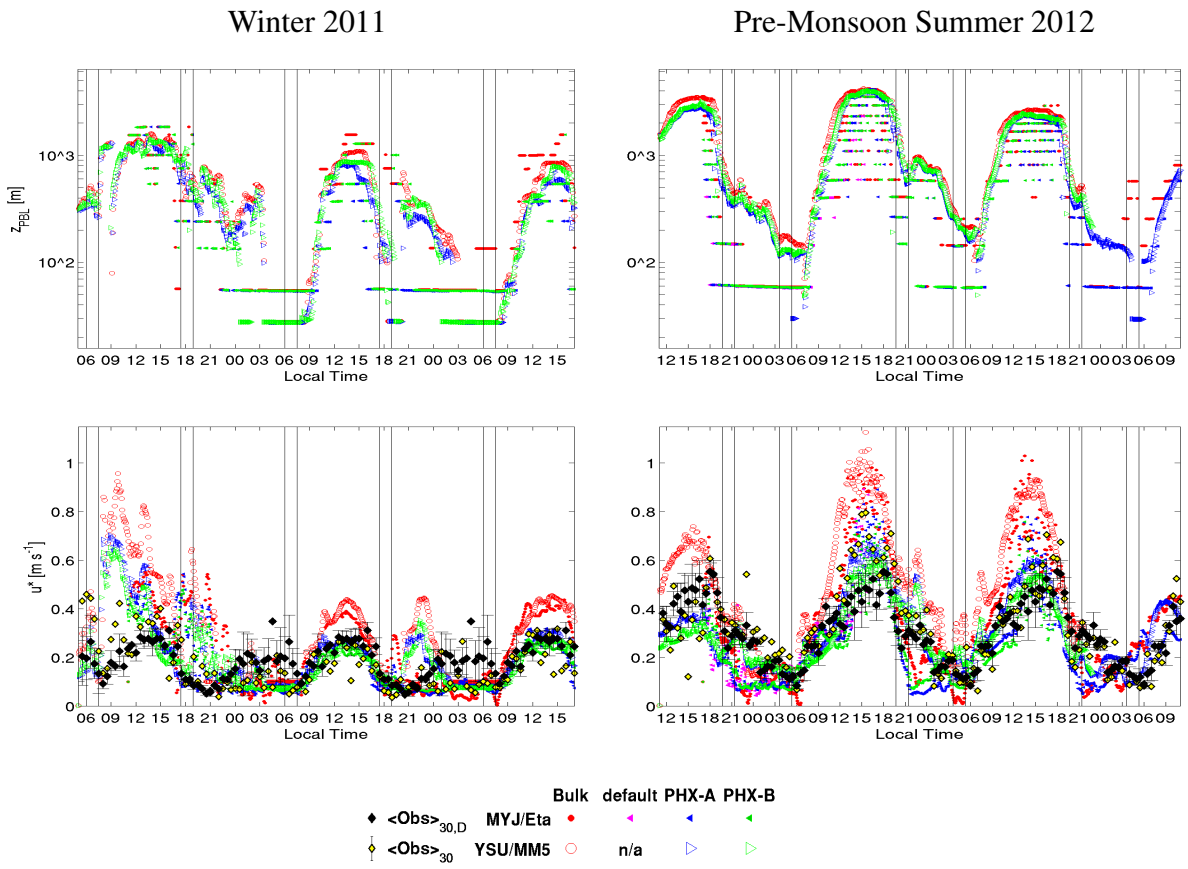

Figure 88: Same as for Figure 87, but showing height of mixed layer z_{PBL} (top), and friction velocity u^* (bottom).

C.2.3.1 Definitions

Surface layer profiles directly influence diagnostic surface layer parameters, such as 2-meter temperature, $\mathrm{T_{2m}}$, and 10-meter winds, U_{10} and V_{10}, along with the surface-atmosphere flux coupling through sensible and latent heat fluxes, and the friction velocity, u^*. By determining the stability regime, and changes thereof within the diurnal period, we can seek a physical explanation for errors in the modeled SEB parameters. Figure 87 presents the time-series for the last 48-hours of each simulation period of

5-minute output frequency instantaneous values for the bulk Richardson number, $\mathrm{Ri_b}$, Obukhov length, L_{MO}. Shown in Figure 88 are the depth of mixed layer or PBL height, z_{PBL}, and friction velocity, u^*. For observed data, we can only derive L_{MO} and u^* based upon the 22.1 m A.G.L. measurements, which are also shown on Figure 87, and, Figure 88, respectively. The observed L_{MO} was derived from 30-minute averaged values as per Equation C.5 given later. The friction velocity is a scaling parameter useful for assessing Reynolds' stress of turbulent shear in the surface layer by $\tau = \rho u^{*2}$, with the air density, ρ, and is used in SLS scaling relationships for turbulent fluxes. The boundary layer height (depth) is another scaling parameter which indicates the portion of the atmosphere directly influenced by the surface layer (Stull 1988; Zhang and Anthes 1982).

The MM5 SLS employs the bulk Richardson number of the surface layer following Zhang and Anthes 1982, which can be written in terms of WRF variables as,

$$\mathrm{Ri_b} = \frac{g z_{\mathrm{SL}}}{\theta_0} \frac{\Delta\theta}{\Delta U_H^2} = \frac{g z_{\mathrm{SL}}}{\mathrm{T}_0} \times \frac{\mathrm{T_{2m}} - \mathrm{T}_0}{U_{10}^2 + V_{10}^2}, \tag{C.3}$$

where $g = 9.81$ m s^{-2} is gravitational acceleration, $z_{\mathrm{SL}} = z_U^2 / z_\theta$ is the height of the surface layer in terms of the heights of diagnostic variables, $z_U = 10$ m, for horizontal wind components U_{10} and V_{10}, and $z_\theta = 2$ m, for temperature $\mathrm{T_{2m}}$, respectively, with $\Delta\theta/\theta_0 = (\mathrm{T_{2m}} - \mathrm{T}_0)/\mathrm{T}_0$, for T_0 being the surface skin temperature, and converting T_0 and $\mathrm{T_{2m}}$ to virtual potential temperature. The Richardson number is the dimensionless ratio of buoyancy to horizontal shear forces, presuming the vertical coordinate dominates variations. When discretized for a volume, such as the surface layer, $\mathrm{Ri_b}$ is taken as bulk value. The four stability regimes are defined by,

1. $\mathrm{Ri_b} \geq 0.2$, nighttime stable conditions,
2. $0.2 > \mathrm{Ri_b} > 0$, damped mechanical turbulence,
3. $\mathrm{Ri_b} = 0$, forced convection, and,

4. $\mathrm{Ri_b} < 0$, free convection.

The MM5 SLS is implemented in WRF based on stability functions given in Paulson 1970, Dyer and Hicks 1970, and Webb 1970, for four stability regimes following Zhang and Anthes 1982, and with a convective velocity following Beljaars 1995.

The Eta SLS (Janjic 2001), in turn, defines based upon the Obukhov stability parameter,

$$\zeta = \frac{z_{\mathrm{PBL}}}{L_{MO}}. \tag{C.4}$$

The stability regime is then defined by,

1. $\zeta \geq 0$, stable, use profiles of Holtslag and de Bruin 1988, and,

2. $\zeta < 0$, unstable, use profiles of Paulson 1970.

The Obukhov stability parameter and stability functions are derived iteratively and are determined for stable and unstable conditions following Holtslag and de Bruin 1988 and Paulson 1970, respectively. The Obukhov length, L_{MO}, can be written in terms of WRF output variables as,

$$\frac{1}{L} = \frac{-\kappa g}{c_p}\frac{H_1}{\rho\theta_a u_*^3} = \frac{-\kappa g R_{\mathrm{air}}}{c_p}\frac{\mathrm{HFX}}{\mathrm{PSFC}\times(\mathrm{UST})^3}, \tag{C.5}$$

by using $\rho = \mathrm{PSFC}/(R_{\mathrm{air}}\times \mathrm{T2})$, where $\kappa = 0.4$ is the von Kármán constant, $R_{\mathrm{air}} = 287.058$ J kg^{-1} K^{-1} and $c_p = 1003.5$ J kg^{-1} K^{-1}, are the dry air values for gas constant and specific heat at constant pressure, respectively. The Obukhov length arises from applying MOST to the turbulent kinetic energy (TKE) budget equation for the surface layer, and is related to the height at which the TKE production by mechanical shear stress begins to be dominated by buoyancy. Note that L_{MO} can be related to the Richardson number and the boundary layer height (Businger et al. 1971; Arya 1988; Stull 1988; De Bruin, Ronda, and Van De Wiel 2000). Since $z_{\mathrm{PBL}} > 0$, we do not show ζ, but rather just z_{PBL} and L_{MO}

separately, although ζ is employed within the stability profiles. Also denoted for L_{MO} in Figure 87 are seven sub-classes of stability following Gryning et al. 2007, which are,

1. $10 < L_{MO} < 50$, very stable,
2. $50 < L_{MO} < 200$, stable,
3. $200 < L_{MO} < 500$, near neutral, stable,
4. $|L_{MO}| > 500$, neutral,
5. $-500 < L_{MO} < -200$, near neutral, unstable,
6. $-200 < L_{MO} < -100$, unstable,
7. $-100 < L_{MO} < -50$, very unstable,

in units of meters. Note that Gryning et al. 2007 does not designate a sub-class in the region for which $-50 < L_{MO} < 10$.

A further discussion of the dynamics of evening transition within a field experiment in Phoenix are discussed in H. J. S. Fernando et al. 2013. They calculate a gradient Richardson number, $\mathrm{Ri_g}$, from observations at 3.4 and 7 m AGL, which are used to describe critical values following the laboratory study of Strang and Fernando 2001. Regimes are identified as: for $\mathrm{Ri_g} < 0.25$ expect strong mixing due to Kelvin-Helmholtz instabilities; a transition for $0.25 \leq \mathrm{Ri_g} \leq 1$ with interacting Kelvin-Helmholtz and internal modes as buoyancy becomes more important; and for $\mathrm{Ri_g} > 1$ they expect weak sporadic mixing due to Hölmböe instabilities. While some effects are not anticipated to be identified within the WRF simulations owing to vertical resolution requirements, similar effects may be present within our tower measurements, such as increases in $\mathrm{Ri_b}$ and u^*, following the decrease leading up to sunset from mid-day unstable periods. H. J. S. Fernando et al. 2013 describe

such events within the evening transition as being due to katabatic flow from adjacent terrain causing a “paint-stripper” effect, as dense air undercuts as it descends nearby terrain features progressing into the valley. In their examination of u^* and $\mathrm{Ri_b}$ values they discuss the varied timing of such events, or pulses, in terms of the timing of transition front arrivals from varied terrain locations and directions.

C.2.3.2 Interparameterization Comparison of Surface Layer Stability

Figure 88 shows that z_{PBL} for MYJ is shallower than for YSU, especially during the summer period. This result agrees with previous studies by Xie et al. 2012 and Hu, Nielsen-Gammon, and Zhang 2010, which have demonstrated that local mixing schemes, such as MYJ, tend to produce shallower PBL heights than non-local schemes, such as YSU. The sensitivity of coupling strength between the LSM and PBL are demonstrated by Chen and Zhang 2009 as being due to heat and moisture exchange coefficients. Y. Chen et al. 2010 explain the influence of bias in thermal roughness length, as being obtained from incorrect vegetation assumptions in the Noah LSM for an arid desert location within Arizona, which in turn modify other terms, such as $\langle Q_H \rangle$ and $G^{\uparrow}_{LW}$.

In Figure 88, it is also apparent that MYJ restricts z_{PBL} to be on a model level and YSU imposes $\min z_{\mathrm{PBL}} = \frac{1}{2} z_1$. Periods of this limit occurring in YSU z_{PBL} also coincide with the YSU imposed minimum of $u^* = 0.1$ m s^{-}1. Influence of these limits during stable periods is discussed in Jiménez et al. 2012. During stable periods following sunset while the MYJ scheme is found to have z_{PBL}=z_1 (Figure 88), the YSU scheme indicates an increase in z_{PBL}, coinciding with an increase in u^* and $\mathrm{Ri_b}$, indicating damped mechanical turbulence. The observed values of u^* match quite well with the PHX UCM cases, seen in Figure 88.

Examining the stability classifications based upon $\mathrm{Ri_b}$ and L_{MO} in Figure 87, it appears that during winter evening and morning transition periods, the bulk scheme would remain stable for several hours longer than the UCM cases, especially for the evening transition. The bulk scheme also produced more stable conditions at night, and more unstable conditions during the day, based upon the magnitudes of $\mathrm{Ri_b}$ and L_{MO}, for both SLS schemes. Later we discuss that the latent heat flux $\langle Q_H \rangle$ and residual ΔQ_s for bulk are

also much larger than for UCM cases, and the residual ΔQ_s peaks earlier than the UCM cases. Daytime bulk u^* values are much higher than for the UCM scheme cases than bulk, which is due to building roughness modification imposed by the UCM on u^*, which is also proportional to urban fraction.

The u^* and z_{PBL} values shown in Figure 88 for MM5 tend to increase following sunset, for both seasons, whereas the Eta scheme values remain low, indicative of calmer conditions during the evening transition for the Eta scheme. Furthermore, the larger UF PHX-B case has lower u^* values than the PHX-A case, showing the influence of surface drag over an increased urban fraction. Also during the same periods for the UCM cases, the MM5 scheme tends to produce more periods of stable $\mathrm{Ri_b}$, but the Eta scheme L_{MO} indicates episodic unstable periods following sunset, as seen in Figure 87. The bulk scheme tends to remain stable during these periods. The difference in stability between the UCM SLS cases is more pronounced in the winter, and for UCM cases more than bulk cases.

C.2.4 Diagnostic Horizontal Wind Components

Comparisons for the 22.1 m A.G.L. observed horizontal wind components are shown in Figure 89 with U_{10} and V_{10}, and the prognostic variables U and V destaggered and at the first half-mass height z_1 in Figure 90. The diagnostic wind components are obtained by similarity theory,

$$U_{10} = U(z_1)\psi(10)/\psi(z_1), \tag{C.6}$$

where $U(z_1)$ is the velocity component on the first prognogistic level z_1, and $\psi(z) = \ln(z/z_0) - \Psi_m(z)$, is the similarity function evaluated at height z with roughness length z_0, and integrated stability function for momentum ψ_m. A similar relation is used for

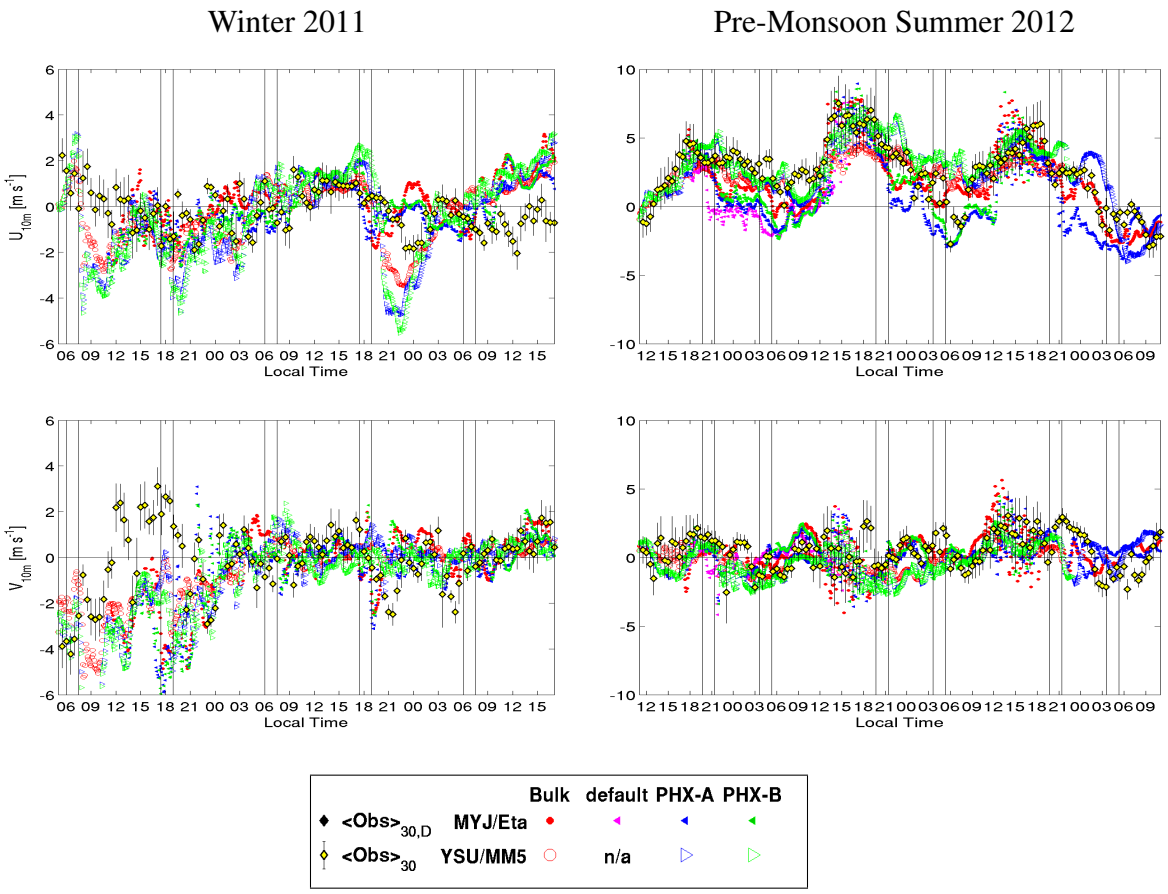

Figure 89: Same as for Figure 87, but comparison between observed horizontal wind component measured at 22.1 m A.G.L. and diagnostic 10-meter horizontal velocity components for positive to east U_{10} (top), positive to north V_{10} (second row).

V_{10}. Given in Table 8 are root-mean-square errors, partitioned following Willmott et al. 1985, for the wind component time-series given in Figure 89. Linear model bias is contained within the systematic component,

$$RMSE_s^2 = \sum_{j=1}^{N} \omega_j |\hat{S}_j - O_j|^2 / \sum_{j=1}^{N} \omega_j, \tag{C.7}$$

while model precision is contained within unsystematic component,

$$RMSE_u^2 = \sum_{j=1}^{N} \omega_j |\hat{S}_j - S_j|^2 / \sum_{j=1}^{N} \omega_j, \tag{C.8}$$

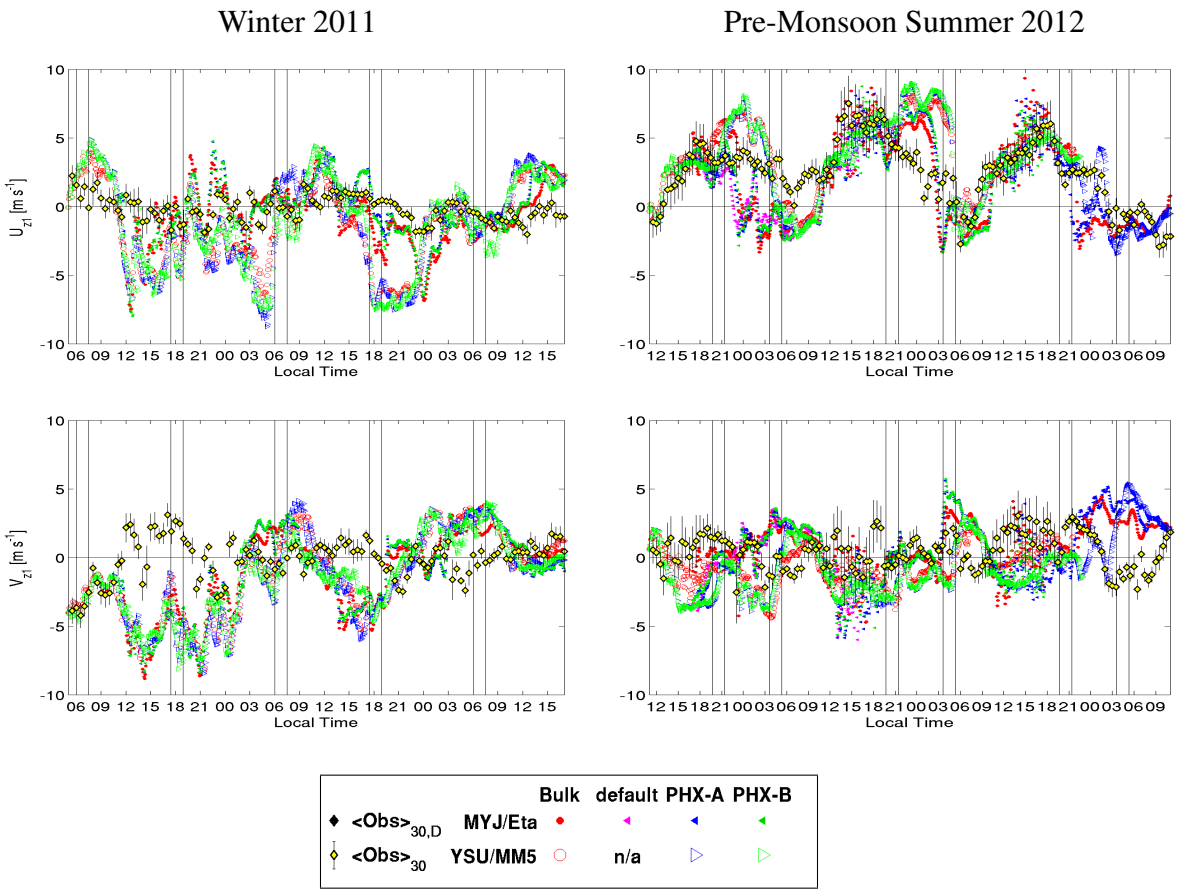

Figure 90: Same as for Figure 87, but comparison between observed horizontal wind component measured at 22.1 m A.G.L. and prognostic velocity components destaggered and at first half-mass level $z_1(\approx 27$ m) for U (top), and V (bottom).

where the weighting factor $\omega_j \approx 1$ for a uniform sampling of both observation and comparison data (our case at 1 km and 30 minute averages), and $\hat{S}_j$ is the ordinary least-squares estimator of S_j from simulation prediction, S, versus observation, O, comparison. These values satisfy the relation, $RMSE^2 = RMSE_u^2 + RMSE_s^2$. From this analysis we see that the wind components are well represented, with values ranging from .13 - 3 m s^{-1}, with more typical values between 1 - 2 m s^{-1}, for both systematic and unsystematic measures for the model parameterization cases tested, and including spinup periods.

	Winter 2011							
	MYJ/Eta				YSU/MM5			
	U_{10}	V_{10}	$U(z_1)$	$V(z_1)$	U_{10}	V_{10}	$U(z_1)$	$V(z_1)$
bulk $RMSE_s$	1.02	1.54	0.59	2.40	0.66	1.24	1.29	2.01
bulk $RMSE_u$	1.08	1.45	1.96	2.81	1.27	1.24	2.83	2.98
default $RMSE_s$	-	-	-	-	-	-	-	-
default $RMSE_u$	-	-	-	-	-	-	-	-
PHX-A $RMSE_s$	0.71	1.76	0.13	2.58	0.67	1.18	1.15	2.14
PHX-A $RMSE_u$	1.02	1.45	2.01	2.93	1.83	1.77	3.27	3.09
PHX-B $RMSE_s$	0.72	1.82	0.15	2.56	0.62	1.28	1.20	2.14
PHX-B $RMSE_u$	1.09	1.57	2.02	2.94	1.95	1.77	3.15	2.72
	Pre-Monsoon Summer 2012							
	MYJ/Eta				YSU/MM5			
	U_{10}	V_{10}	$U(z_1)$	$V(z_1)$	U_{10}	V_{10}	$U(z_1)$	$V(z_1)$
bulk $RMSE_s$	0.92	1.12	0.83	1.68	1.42	1.14	0.91	1.63
bulk $RMSE_u$	1.32	1.02	2.26	1.57	0.77	0.73	2.12	1.32
default $RMSE_s$	3.00	1.32	2.47	1.99	-	-	-	-
default $RMSE_u$	1.27	0.86	1.52	1.91	-	-	-	-
PHX-A $RMSE_s$	1.93	1.25	1.09	2.00	0.66	1.25	0.39	2.28
PHX-A $RMSE_u$	1.54	0.99	2.26	2.17	1.57	1.14	2.37	2.03
PHX-B $RMSE_s$	1.46	1.06	0.97	1.71	0.99	1.22	0.80	2.30
PHX-B $RMSE_u$	1.49	1.06	2.49	1.95	1.24	1.08	2.43	1.63

Table 8: Root-mean-square-error for systematic ($RMSE_s$) and unsystematic ($RMSE_u$) values, in m s^{-1}, following Willmott et al. 1985, for 30-minute average time-series of observations and simulations, for the seasons, PBL/SLS, and urban cases given in column or row labels, of the data presented in Figure 89.

C.2.5 Possible Additional Anthropogenic Forcing in T_{2m}

By inspecting the winter evening period (between 1900-2200) observed in Figure 35, we possibly observe a human behavior not captured by the UCM. The effect, most apparent in T_{2m} and $G^{\uparrow}_{LW}$, is hypothesized to originate from building waste heat. There is no corresponding increase in T_{2m} in the simulations, which have a steady cooling rate during this period. This is the time of day when most residents arrive home after work and

turn on or increase home heating. The observed T_{2m} increase mostly attenuates when people typically go to bed around 2200. Strongly stable nocturnal periods do not rule out advection of non-local urban heat island thermal plumes, so more detailed tower footprint analysis may be needed. It should be possible to investigate scenarios of human behavior via increased indoor temperature with the BEP+BEM model Francisco Salamanca et al. 2011. This peak in AH forcing is expected to be shifted to afternoon periods during the summertime, at peak indoor cooling during peak daytime temperatures (F Salamanca et al. 2014).

C.3 Computational Feasibility of Urban WRF Modeling Below 1 km

The model was run on the Arizona State University Saguaro computer cluster maintained by the Advanced Computing Center. Details of relevant architecture employed include: Intel Xeon E5440 2.83 GHz processors with 8 cores and 16 GB RAM per compute node, 16 nodes per chassis connected via DDR IB using PowerEdgeM600 (hereafter Harpertown); and, Intel Xeon x5570 2.93 GHz processors with 8 cores and 24 GB RAM per compute node, 16 nodes per chassis connected via DDR IB using PowerEdgeM610 (hereafter Nehalem). Model performance for several configurations was assessed with several requested cluster architectures, summarized in Table 9.

The ratio of numerical time step to computational time was calculated from the timing data reported in the log file for each domain for many of the simulations performed. The reported value for a specific domain, Dn, includes overhead from processes on the child domain, Dn-1, along with input and output tasks that take place between time steps. Model parameterization tasks also have their associated frequency of occurrence. These varied events, along with cluster related processes, contrive for a distribution of reported output times on each domain. Rather than attempting a proper accounting for these tasks, a simplified approach was employed to first correct each domain timing estimate by removing the cumulative child timing since the last parent output. Then an estimate for the most probable time on domain without overhead of child processes was used to calculate speedup based upon the timestep on that domain. Based upon this method, the most probable timing on some child domains could be larger than each specific process, resulting in an over-estimate of the speedup on the parent domain. So the results reported in Table 9 should be speculatively examined for parent domains.

From the analysis of most probable speedup times, and assessing only the maximum

Processor	Cluster Topology	Urban Scheme	PBL Scheme	Winter Δ_t(D1) [sec]	Winter D2 9 km 3:1	Winter D3 3 km 3:1	Winter D4 1 km 3:1	Winter D5 333 m 5:1	Summer Δ_t(D1) [sec]	Summer D2 9 km 3:1	Summer D3 3 km 3:1	Summer D4 1 km 3:1	Summer D5 333 m 5:1
Nehalem	16 x 8	bulk	YSU	135	129.9	35.5	16.2	-	100	147.1	39.8	20.8	-
Nehalem	32 x 8	bulk	MYJ	150	208.3	61.7	26.7	-	112.5	232.6	63.3	17.5	5.8
Nehalem	16 x 8	UCM	MYJ	150	256.4	70.4	29.6	-	-	-	-	-	-
Nehalem	16 x 8	UCM	YSU	135	204.1	55.2	22.2	-	100	138.9	38.5	16.3	-
Nehalem	16 x 8	UCM	YSU	-	-	-	-	-	100	175.4	47.6	13.0	4.0
Nehalem	32 x 8	UCM	MYJ	150	113.6	32.3	15.5	-	112.5	161.3	42.4	16.8	-
Nehalem	32 x 8	UCM	MYJ	-	-	-	-	-	112.5	263.2	74.1	20.5	7.1
Nehalem	32 x 8	UCM	MYJ	-	-	-	-	-	112.5	222.2	62.1	17.2	5.7
Nehalem	32 x 8	UCM	MYJ	-	-	-	-	-	112.5	263.2	74.1	20.7	7.0
Nehalem	32 x 8	UCM	YSU		-	-	-	-	100	185.2	53.2	15.5	6.7
Harpertown	32 x 8	UCM	MYJ	150	217.4	58.1	22.7	-	-	-	-	-	-
Harpertown	32 x 8	UCM	MYJ	150	217.4	59.2	22.9	-	-	-	-	-	-
Harpertown	32 x 8	UCM	YSU	-	-	-	-	-	112.5	9.5*	2.4*	∞*	-
Harpertown	48 x 8	UCM	YSU	135	158.7	46.7	33.1	-	-	-	-	-	-
Harpertown	64 x 8	UCM	MYJ	150	277.8	78.7	47.6	-	-	-	-	-	-
Harpertown	64 x 8	UCM	MYJ	150	113.6	32.3	15.5	-	-	-	-	-	-

Table 9: Summary of speedup, the ratio of numerical time step to computational time, as determined by most-probable time on domain D_N, subtracting overhead of child domain D_{N-1}. Results are sorted by processor type, cluster topology, namelist configurations of urban and PBL scheme, along with season. For the experiments reported we give time step on first domain, $\Delta_t(D1)$, domain resolution and parent:child time step ratio. Note that not all parallel combinations were tested. We tested several model configurations, with max_dom=4,5. Unavailable data is denoted by a '-', and failings of the most-probable time-on-domain method are denoted by a '*', where parent estimates are befuddled by a poorly estimated child domain value.

domain (D4 in winter, D4 or D5 in summer), we see that 5 concurrent domains to Δ_H=333 m is real-time feasible with a most-probable speedup of at least 4 on 128 Nehalem processors, and at least 5.7 on 256 Nehalem processors. For just four domains, half of the Nehalem processors are required for a similar speedup as provided on the Harpertown processors. Speedup is varied for large processor numbers on the Harpertown architecture, likely owing to communication tasks between model tiles and distribution across more remote nodes. From these data and analysis it is difficult to draw conclusions regarding time requirements between the different physics options tested.

APPENDIX D

APPLICATION AND EVALUATION OF SUBGRID LAND USE INFORMATION FOR URBAN CLIMATE MODELING

In Preparation. To be submitted to *Monthly Weather Review*,

S.R. Shaffer; M. Moustaoui; B.L. Ruddell; A. Mahalov

A method for representing grid-scale heterogeneous development density for urban climate models from probability distributions of sub-grid resoloution observed data is proposed. Derived values are evaluated in relation to normalized Shannon Entropy to provide guidance in assessing model input data. Mosaic urban fractional contribution is estimated by combining analysis on data products for continuous impervious surface area with categorical urban land use. The urban parameterization schemes of the Advanced Research Weather Research and Forecasting (ARW-WRF) model are adapted to take these derived heterogeneous development density data as input for the dominant urban class. Development density and urban land use are obtained from the 30-meter resolution National Land Cover Database (NLCD) products. The impact of increased realism of input data and parameterization obtained via heterogeneous urban fraction versus constant urban fraction is demonstrated by a test case using the urban canopy model. Comparisons are made between simulations employing a constant versus heterogeneous development density for the entire Phoenix metropolitan area. Modeled variables are evaluated with an eddy-covariance flux tower in West Phoenix. The proposed method has wider applicability than products which are only available for central business districts, such as the National Urban Database and Access Portal Tool.

APPENDIX E

A SEMI-IMPLICIT METHOD FOR INTEGRATION OF GLOBAL SHALLOW WATER AND ANELASTIC EQUATIONS

In Preparation. To be submitted to *Monthly Weather Review*,

M. Moustaoui; **S.R. Shaffer**; A. Mahalov; E. Kostelich

A new semi-implicit time stepping method is proposed. This method combines an implicit scheme that stably integrates fast propagating waves, with a recently developed scheme based on leapfrog and a fourth-order implicit time-filter for treating slow propagating waves. Formal accuracy and stability analysis demonstrate that this combined scheme has third-order accuracy for amplitude errors while damping non-physical modes inherent in the unfiltered leapfrog method. The method also stabilizes the computational modes in combined advection and damping or diffusion equations that are unconditionally unstable when using leapfrog. The formulation and the explicit implementation of this scheme using just one function evaluation per time-step are shown. The scheme gives a factor of three speed-up compared with the third-order Runge-Kutta (RK3) scheme, while maintaining $O(\Delta t^4)$ accuracy for amplitude errors. Comparative tests with RK3, including applications for nonlinear global spectral shallow water equations on the sphere, and anelastic (or Boussinesq) non-hydrostatic equations, demonstrate the ability of the proposed scheme to control computational modes and to give more accurate results compared to the semi-implicit time-filtered leapfrog schemes existing in the literature. This method has many applications including acoustic, electromagnetic, atmospheric, oceanic, and climate modeling.

APPENDIX F

SUMMARY OF PUBLICATIONS AND PRESENTATIONS

Peer Reviewed Journal Publications

Forthcoming - In Review

5. M. Moustaoui; **S.R. Shaffer**; A. Mahalov; E. Kostelich (Submitted, Nov. 2014). "A semi-implicit method for integration of global shallow water and anelastic equations," *Mon. Wea. Rev.*.

4. **S.R. Shaffer**; M. Moustaoui; B.L. Ruddell; A. Mahalov (Submitted, Nov. 2014). "Application and evaluation of subgrid land use information for urban climate modeling," *Mon. Wea. Rev.*.

Completed

3. **S.R. Shaffer**; W.T.L. Chow; M. Georgescu; P. Hyde; G.D. Jenerette; A. Mahalov; M. Moustaoui; B.L. Ruddell (Accepted, Oct. 2014). "Multi-scale modeling and evaluation of urban surface energy balance in the Phoenix metropolitan area." *J. Appl. Meteorol. Climatol.*.

2. **S.R. Shaffer**; N.C. Ovenden; H.J.S. Fernando; M. Moustaoui; A. Mahalov (Accepted, Oct. 2014). "Simulating meteorological profiles to study noise propagation from freeways," *Appl. Acoust.*.

1. N. Ovenden, **S.R. Shaffer** and H.J.S. Fernando (July 2009). "Impact of meteorological conditions on noise propagation from freeway corridors," *J. Acoust. Soc. Am.*, Vol. 126, No. 1, pp. 26-35.

Other Peer-Reviewed Publications

3. **S.R. Shaffer**, H.J.S. Fernando and N.C. Ovenden (2013). "Investigations of environmental effects on freeway acoustics", Arizona Dept. of Transportation, Final Report: Project ID - R060518P (JPA 06-014T), SPR 605-2. http://ntl.bts.gov/lib/47000/47600/47664/AZ605_2_.pdf

2. H.J.S. Fernando, N. Ovenden and **S.R. Shaffer** (2010). "Investigations of environmental effects on freeway acoustics", Arizona Dept. of Transportation, Final Report: Project ID - R060518P (JPA 06-014T).

1. **S.R. Shaffer** (May 2009). "Investigations of environmental effects on freeway acoustics", Arizona State University, M.S. Thesis.

Other Press Releases

1. "How the Weather Affects the Scale of Urban Noise Pollution." N.C. Ovenden, S.R. Shaffer, H.J.S. Fernando (5-24-2011) http://acoustics.org/pressroom/httpdocs/161st/Ovenden.html

Conference Presentations († - presenter)

6. **S.R. Shaffer**†, B.L. Ruddell, W.T.L. Chow, M. Moustaoui, A. Mahalov, M. Georgescu (2013). "Evaluation of WRF for fine scale surface energy balance modeling in Phoenix." Fall Meeting of American Geophysical Union, San Francisco, CA, Dec 12, A43A-0217.

5. **S.R. Shaffer**†, B.L. Ruddell, W.T.L. Chow, M. Moustaoui, A. Mahalov, M. Georgescu (2013). "Evaluation of WRF for fine scale surface energy balance modeling in Phoenix." 14th Annual WRF Users' Workshop, Boulder, CO, June 26, P66.

4. B.L. Ruddell†, E. Vivoni, M. Moustaoui, D. Jenerette, A. Mahalov, C. Martin, S. Harlan, T. Volo, **S.R. Shaffer**†, W. Chow (July 2012). "Assessing decadal climate change impacts on urban populations in the Southwestern USA", NSF EaSM PI Meeting, Arlington, VA. Grant No. 1049251, Theme 4 poster 11.

3. **S.R. Shaffer**†, N.C. Ovenden, M. Moustaoui, A. Mahalov, and H.J.S. Fernando (2011). "Coupling WRF with an acoustic propagation model to study highway noise pollution." 12th Annual WRF Users' Event, Boulder, CO, June 20-24, P.49.

2. N.C. Ovenden†, **S.R. Shaffer** and H.J.S. Fernando (May 2011). "Investigations of environmental and terrain effects on the propagation of freeway noise", 161st meeting of the Acoustical Society of America, Seattle, WA, Talk 2pNS3.

1. **S. Shaffer**†, M. Moustaoui† and A. Mahalov (June 2010). "Application of vertical nesting within ARW-WRF v3.2 to a study of highway noise pollution in Phoenix Arizona", 11th Annual WRF Users Event, Boulder, CO. Poster 67.

Seminar Presentations

6. "Towards a two-way parabolic equation model with terrain following coordinates", Center for Environmental Fluid Dynamics Seminar, Arizona State University, 24 April 2009.

5. “Investigations of environmental effects on freeway acoustics”, M.S. Thesis Defense, Arizona State University, 16 February 2009.

4. “Incorporating Turbulence into Traffic Noise Models”, Center for Environmental Fluid Dynamics Seminar, Arizona State University, 10 October 2008.

3. “Incorporating Turbulence into Traffic Noise Propagation Models”, Environmental Fluid Dynamics Program Seminar, Arizona State University, 28 March 2008.

2. “Case Studies of the Impact from Meteorological Conditions on Propagation of Freeway Noise”, Environmental Fluid Dynamics Program Seminar, Arizona State University, 14 September 2007.

1. “Modeling the Atmospheric Propagation of Freeway Noise”, Environmental Fluid Dynamics Program Seminar, Arizona State University, 13 April 2007.

BIOGRAPHICAL SKETCH

Born to Richard A. and Carolyn J. (Hayward) Shaffer, little brother of Michael A. Shaffer, uncle of Liliana Mary Shaffer, and very proud father of Evan Hayward Aballe Shaffer since late 2010, the "Thesis Baby". Mother's family operated a dairy farm in West Bridgewater, Massachusetts for 10 generations, with her's being the first to leave the farm. Inspired at an early age by grandparents Howard Manly and Mary Caroline (Harris) Hayward, and uncle Howard Wayne Hayward, in topics of conservation and stewardship of the land. (The remaining 74-acres of the former Hayward Dairy Farm were recently registered under Massachusetts' 1979 Agricultural Preservation Restriction Program.) Father was the first in his family to attend college, B.S. in Aeronautical Engineering from Embry Riddle Aeronautical University, Daytona Beach, Florida, 1972, M.S. in Mechanical Engineering from Wichita State University in Wichita Kansas, 1979, and worked with Pratt & Whitney for 30 years, initially in Connecticut. Beginning in 1997 at Manchester Community College in Connecticut, receiving Associate of Science degrees in General Studies in 2000, and Engineering Science in 2001. Moved to Tucson in 2001 and received a B.S. triple-majoring in Physics, Mathematics, and Astronomy in 2005 from the University of Arizona. Inspired by graduate fluid dynamics course at UofA in spring 2006 with Prof. Raymond Goldstein to continue studies in the topic. Moved to Tempe in summer 2006 to study with Prof. H.J.S. Fernando in the Center for Environmental Fluid Dynamics at Arizona State University. Joined a collaboration with Prof. Fernando and Prof. Nick Ovenden from University College London on the ADOT freeway noise field experiment in fall 2006 which became the topic of the M.S. thesis in Mechanical Engineering received in 2009. Transitioned to working with Prof. Alex Mahalov and Prof. Mohamed Moustaoui in 2010 to advance ideas for incorporating Weather Research and Forecasting modeling into acoustic work, along with other research topics. Worked with Prof. Alex Mahalov and Sue Mahalov at IntelliWare L.L.C. on various research topics related to applications of WRF modeling and atmospheric turbulence, beginning in 2010. Continued collaboration with Prof. Ovenden and Prof. Fernando on ADOT SPR-699 upon being awarded in 2013, which extends the SPR-605 studies by considering freeway walls. Other interests include: climbing rocks, gardening, commuting via bicycle, chasing a soccer ball, hiking, and photography.